Atomic scale thermodynamics of crystalline Li-Si compounds for batteries

Charbel Jose El Khoury

université PARIS-SACLAY

Atomic scale thermodynamics of crystalline Li-Si compounds for batteries

Etude thermodynamique à l'échelle atomique des composés cristallins Li-Si pour les batteries

Thèse de doctorat de l'université Paris-Saclay

École doctorale n°564 : physique en Île-de-France (PIF)
Spécialité de doctorat : Physique
Graduate School : Physique
Référent : Faculté des sciences d'Orsay

Thèse préparée dans l'unité de recherche
Service de Recherche en Corrosion et Comportement des Matériaux- SRMP
(Université Paris-Saclay, CEA),
sous la direction de **Fabien BRUNEVAL**, directeur de recherche, et
la co-direction de **Maylise NASTAR**, directrice de recherche.

Thèse soutenue à Paris-Saclay, le 22 septembre 2023, par

Charbel Jose EL KHOURY

Composition du jury

Membres du jury avec voix délibérative

Philippe MOREAU Professeur (Nantes Université)	Président
Anne HEMERYCK Chargée de recherche (HDR) (Université de Toulouse)	Rapporteur & Examinatrice
Jean-Marc JOUBERT Directeur de recherche (Université Paris-Est Créteil)	Rapporteur & Examinateur
Marion CHANDESRIS Directrice de recherche (Université Grenoble Alpes)	Examinatrice

THESE DE DOCTORAT

NNT : 2023UPASP098

université PARIS-SACLAY | ÉCOLE DOCTORALE Physique en Île-de-France (PIF)

Title : Atomic scale thermodynamics of crystalline Li-Si compounds for batteries
Keywords : Thermodynamics, Point defects, Si electrode, non-stoichiometry, Ab initio

Abstract : Silicon shows great promise as a high-capacity material for Li-ion battery negative electrodes, with a theoretical specific capacity ten times higher than graphite. In this study we model from first principle calculations the thermodynamic properties of the crystalline Li-Si compounds. We start by computing the lattice vibration contribution to the Gibbs free energy, and the formation energy of point defects in Li-Si crystalline compounds. With these we were then able to account for the off-stoichiometry of these compounds by means of statistical physics models. From these calculations we extract single phase and two-phase composition domains. We deduce properties such as the open circuit voltage and we construct the first reported phase diagram including off-stoichiometry. Moreover, we can explain why the nucleation of metastable crystalline $\mathrm{Li_{15}Si_4}$ phase may be favorable over other thermodynamically crystalline stable phases under room temperature lithiation.

Titre : Etude thermodynamique à l'échelle atomique des composés cristallins Li-Si pour les batteries
Mots clés : Thermodynamique, Défauts ponctuels, Si électrode, non-stoechiométrie, Ab initio

Résumé : Le silicium présente un grand potentiel en tant que matériau à haute capacité pour les électrodes négatives des batteries Li-ion, avec une capacité spécifique théorique dix fois supérieure à celle du graphite. Dans cette étude, nous modélisons à partir de calculs de premiers principes les propriétés thermodynamiques des composés cristallins Li-Si. Nous commençons par calculer la contribution des vibrations de réseau à l'énergie libre de Gibbs, ainsi que l'énergie de formation de défauts ponctuels dans les composés cristallins Li-Si. À l'aide de ces résultats, nous avons ensuite pu tenir compte de l'hors-stœchiométrie de ces composés au moyen de modèles de physique statistique. À partir de ces calculs, nous extrayons les domaines de composition à phase unique et à deux phases. Nous déduisons des propriétés telles que la tension de circuit ouvert et nous construisons le premier diagramme de phase rapporté incluant l'hors-stœchiométrie. De plus, nous pouvons expliquer pourquoi la nucléation de la phase cristalline métastable $\mathrm{Li_{15}Si_4}$ peut être favorable par rapport aux autres phases cristallines stables sur le plan thermodynamique lors de la lithiation à température ambiante.

Acknowledgements

I would like to express my gratitude to Maylise Nastar and Fabien Bruneval, my supervisors, for their invaluable guidance and mentorship, and boundless patience throughout the journey of this research. Your expertise has been instrumental in shaping this thesis. I can't be thankful enough to both of you for being available almost always, if not always. To emphasize how difficult thermodynamics can get I quote German physicist Arnold Sommerfeld who said "Thermodynamics is a funny subject. The first time you go through it,you don't understand it at all. The second time you go through it, you think you understand it,except for one or two points. The third time you go through it, you know you don't understand it...". However, thanks to you both Maylise (especially, on thermodynamics) and Fabien (for helping me make the connection with DFT), I was able to go from, what I would deem, 0% knowledge in thermodynamics to at least being able to achieve the results of this thesis!

I would also like to thank Magali Gauthier. Her collaboration with us was indispensable and important. Thanks for teaching me a lot about batteries and the corresponding experiments. I will never forget the little times we met to prepare samples for GITT experiments, and all the times you answered many of my questions regarding the experimental results.

I extend my deepest appreciation to Philippe Moreau, Anne Hemeryck, Jean Marc Joubert, and Marion Chandesris, the members of the defense jury, whose insightful feedback and rigorous evaluation enriched the quality of this thesis. Your expertise and critical analysis have been indispensable in refining my work. Thank you for taking your time reading and understanding this work. I also must admit that I enjoyed presenting my thesis work in front of you and answering every single one of your questions.

My lab mates at SRMP have been constant sources of inspiration. Your collaborative spirit and willingness to share knowledge have made this research experience truly enjoyable. It would be a long list if I were to name all of you, but rest assure that I will remember everyone of you and all the interesting conversations we had on a professional and personal level.

To my friends, both near and far, thank you for your unwavering encouragement and understanding during the highs and very difficult lows of this academic pursuit. Your support has been a very important pillar of strength. It would be really unfair to not name each one of you (in alphabetical order, so do not get sad): Alan, Alvaro, Andres, Charlotte, Daphné, Frederic, Lautaro, Masha, Mattia, Michael, Pablo, Patricia, Remik, Ricardo, Tony. I will say it again, thanks a lot; you played a crucial role in my mental strength, exactly in the moments I needed it most.

To my family, whom I owe an immeasurable debt of gratitude. Your unwavering belief in me, and your enduring love have been the driving force behind my academic journey. Working in this thesis made me realize much of the sacrifices you have to go through the day by day. Indeed, this thesis is as much a reflection of your dedication as it is mine.

Last but not least, my deepest and most heartfelt gratitude goes to a fellow Dr. whom I see as a role model and, fortunately, who also happens to be my fiancée, Pamela Camilos. Your unwavering belief in me, your sacrifices, and your unbeatable support played a pivotal and vital role in my academic journey. You were my rock and inspiration during the long hours of research and writing, and your love and understanding carried me through the most challenging times. Thank you for also playing an essential role in making my thesis defense one of the best presentations I have given. I am truly blessed to have you by my side.

I would like to leave a space here to express my personal thanks and appreciation to each of you, as words alone cannot capture the depth of my gratitude.

Contents

General introduction **9**

1 Bibliography **11**
1.1 Li-Si in batteries: state of the art . . . 12
1.1.1 A brief history of batteries: from Volta cell to Li-ions . . . 12
1.1.2 Notion of a battery . . . 13
1.1.3 Si as a negative electrode for next generation batteries . . . 14
1.1.4 Challenges linked to Si cycling . . . 14
1.1.5 Approaches taken to enhance Si cycling and their problems . . . 15
1.2 Characterization of alloying processes in Li-Si systems: state of the art . . . 16
1.2.1 Phase Diagrams . . . 16
1.2.2 Experimental limitations . . . 19
1.2.3 DFT and alloying processes . . . 20
1.2.4 Room temperature Si (de)lithiation cycling and $Li_{15}Si_4$ . . . 20
1.2.5 Nanosized Si anodes and alloying processes . . . 21
1.3 Methodology . . . 22
1.3.1 Thermodynamic definitions . . . 23
1.3.2 Density Functional Theory . . . 24
1.3.3 PHONOPY . . . 27
1.3.4 Statistical physics approximations . . . 31
1.3.5 Phase diagram . . . 33
1.3.6 CALPHAD . . . 35
1.3.7 Open circuit voltage . . . 36
1.3.8 Galvanostatic intermittent titration technique . . . 38
1.3.9 Classical nucleation theory and beyond . . . 41
1.4 Conclusion . . . 44

2 Perfectly ordered Li-Si line compounds **45**
2.1 Table of previously reported compounds in this work . . . 46
2.2 Discovered compounds . . . 47
2.2.1 Convex hull of stability at 0 K . . . 48
2.3 Vibrational contributions to thermodynamic properties . . . 52
2.3.1 Methodology . . . 52
2.3.2 Li . . . 53
2.3.3 Si . . . 56
2.3.4 $Li_{12}Si_7$ . . . 59
2.3.5 Line compounds nearby Li_7Si_3 . . . 62

2.3.6 $Li_{13}Si_4$ . . . 67
2.3.7 $Li_{17}Si_4$ . . . 70
2.4 Volume expansion . . . 73
2.5 Convex hull of stability at finite temperatures . . . 76
2.5.1 Enthalpies of formation at 300 K . . . 76
2.6 Open circuit voltage from two ordered-phase equilibrium . . . 76
2.7 Conclusion . . . 79

3 Non-stoichiometric and stoichiometric defects of Li-Si compounds 81
3.1 Low temperature expansion of the grand potential . . . 82
3.1.1 Including finite temperature effect from vibrational entropy in LTE . . . 82
3.1.2 Formation energies of point defects from E_c . . . 83
3.1.3 Point defects and off-stoichiometry . . . 83
3.1.4 Analytical calculation of off-stoichiometry properties: when point defects are interstitials and vacancies of the same species . . . 84
3.1.5 Methodology . . . 86
3.2 Off-stoichiometry studies of $Li_{12}Si_7$ . . . 87
3.2.1 Point defects . . . 87
3.2.2 Properties of $Li_{12}Si_7$ in single phase domain . . . 88
3.3 Off-stoichiometry studies of vacancy superstructures of Li_5Si_2 . . . 90
3.3.1 Origin of vacancy superstructure ordering . . . 91
3.3.2 Point defects in Li_7Si_3 . . . 93
3.3.3 Family of Li_5Si_2 vacancy superstructures . . . 94
3.3.4 Point defects in $Li_{43}Si_{18}$ . . . 96
3.3.5 Thermodynamic properties of the stable Li_5Si_2 superstructures in their single phase domain . . . 96
3.4 Off-stoichiometry studies of $Li_{13}Si_4$ . . . 99
3.4.1 Point defects . . . 99
3.4.2 Properties of $Li_{13}Si_4$ in single phase domain . . . 101
3.5 Off-stoichiometry studies of vacancy superstructures of $Li_{22}Si_5$ . . . 104
3.5.1 Point defects . . . 105
3.5.2 OCV of $Li_{21}Si_5$, $Li_{17}Si_4$, and $Li_{22}Si_5$ in their single phase domain . . . 108
3.5.3 Properties of $Li_{17}Si_4$ in single phase domain . . . 110
3.6 Discussion . . . 111
3.6.1 Prediction of Li-Si compounds . . . 111
3.6.2 Point defects . . . 112
3.6.3 Comparison with experimental values . . . 113
3.7 Conclusion . . . 113

4 Phase stability 115
4.1 Dilute solid solution of Li in Si . . . 116
4.1.1 Formation energy of Li interstitial in Si . . . 116
4.1.2 Li solubility limit in Si . . . 117
4.2 Two phase equilibria from LTE . . . 119
4.2.1 Studies at 690 K . . . 119
4.2.2 Studies at 300 K . . . 123
4.3 Li_7Si_3 as a disordered solid solution of $Li_{43}Si_{18}$ . . . 128
4.3.1 Li Sublattices . . . 129
4.3.2 Vacancy interaction energy model . . . 130

4.3.3 Mean Field Model of the Gibbs Free energy . . . 131
4.3.4 Li order-disorder transition temperature . . . 132
4.3.5 Thermodynamic stability of the Li-disordered solid solution . . . 133
4.3.6 Phase Diagram based on the solid solution model . . . 134
4.3.7 OCV and thermodynamic enhancement factor . . . 136
4.3.8 Heat Capacity . . . 139
4.4 The metastable $Li_{15}Si_4$ phase . . . 140
4.4.1 Phonon density of state . . . 141
4.4.2 Free energy, Isochoric Entropy, and Isochoric Heat Capacity . . . 141
4.4.3 Point defects in $Li_{15}Si_4$ . . . 143
4.4.4 Single phase domain properties of $Li_{15}Si_4$ . . . 144
4.5 Nucleation driving forces under applied voltage . . . 144
4.5.1 Constrained nucleation driving force . . . 145
4.5.2 Lithiation of Si . . . 147
4.5.3 (De)Lithiation starting from intermediary Li-Si compounds . . . 151
4.5.4 Confined-volume constrained nucleation . . . 155
4.6 Conclusion . . . 156

General conclusion **159**

A Effect of negative frequencies in Li thermodynamic properties **163**

B Gibbs free energy T dependent fits of ordered compounds from our studies **167**

C CIF files of this work **169**
C.1 CIF file of $Li_{12}Si_7$ . . . 169
C.2 CIF file of Li_7Si_3 . . . 170
C.3 CIF file of $Li_{13}Si_4$ . . . 171
C.4 CIF file of $Li_{22}Si_5$ . . . 172
C.5 CIF file of $Li_{21}Si_5$ . . . 175
C.6 CIF file of $Li_{17}Si_4$ . . . 178
C.7 CIF file of $Li_{15}Si_4$ . . . 182

D XRD diffraction patterns **185**

Résumé en français **187**

General introduction

Advancements in batteries play a crucial role in addressing several pressing global challenges. Firstly, an estimated 770 million people lack access to electricity, primarily in developing regions [1]. By improving battery technology, we can enhance energy storage and distribution systems, allowing for reliable power supply in remote areas, ultimately improving the quality of life and enabling economic growth for millions of individuals. Secondly, batteries have a significant impact on reducing greenhouse gas emissions. Countries seeking to shift from carbon-intensive electricity sources (an estimate of 45% of global emissions according to [2]) to clean and renewable forms, such as solar and wind, face a significant challenge in energy storage. The intermittent nature of renewable energy requires efficient methods to store excess power generated during peak periods and distribute it during times of low production. Improved batteries enable effective energy storage, ensuring a stable and consistent supply of clean electricity, even in regions lacking carbon-free methods of electricity generation. Furthermore, one of the major emissions currently stems from petrol-based city transportation (an estimate of 12% of global emissions according to [2]). Transitioning to electric vehicles (EVs) powered by efficient and long-lasting batteries is a key solution; especially in countries like France where carbon free sources of electricity (e.g. nuclear) are available. That is why, for example, the European Union seeks to completely ban petrol based cars to be sold by 2035 [3]. Advancements in battery technology enable increased EV range, faster charging times, and longer lifespan, making EVs a more viable and sustainable alternative to conventional petrol-powered cars.

The current best and most used technology used in EV's battery is the Lithium (Li) ion one [4]. However the performance of Li-ion batteries can be enhanced through the development of new electrode materials with high energy density. In the past two decades, it has been demonstrated that under certain conditions, silicon (Si) is a highly promising negative electrode material since it possesses a specific theoretical capacity ten times higher than that of graphite, the negative electrode material used in commercial batteries [5].

The lithiation of Si via electrochemical processes has been proved to be challenging due to various reasons. There is an enormous volumetric expansion up to 400% of Si when lithiated that is known to cause difficulties (e.g. pulverization of Si). This volume expansion is due to Li-Si phase transformations that can depend on Li content, mechanical constraints, electrochemical constraints, etc. Experimental studies have indicated that amorphous alloys exhibit superior cycling performance compared to their crystalline counterparts [6, 7]. These investigations have determined that the mechanisms responsible for capacity loss in amorphous anode materials differ from those observed in crystalline phases. In crystalline structures, the introduction of lithium leads to the formation of intermetallic phases, resulting in uneven expansion and cracking. On the other hand, although amorphous materials experience greater volume expansion upon lithiation [8], the deformation is uniform and reversible, which sharply contrasts with the behavior exhibited by crystalline phases. Moreover, the formation of crystalline phases like $Li_{15}Si_4$ can be problematic for the cycling of Si based anodes (e.g. loss of capacity over the electrochemical de/lithiation cycles).

Understanding the alloying processes of both crystalline and amorphous Si-Li compounds from an

atomic scale is key to avoid the previously mentioned problems. However, atomic characterization of these alloying processes has been rather difficult due to experimental limitations when it comes to determination of crystallographic structure (i.e. X-ray diffraction pattern inaccuracies due to Li [9]). Before even taking on the difficult task of modeling the amorphization or crystallization transitions, we find that there are still open questions in the literature concerning what are the thermodynamic stability of crystalline phases. Therefore, the literature lacks a generally-agreed-upon Li-Si phase diagram. In addition, it is important to highlight that the consideration of off-stoichiometry theoretical modeling has been neglected in the studies of Li-Si systems -to the best of our knowledge. This omission can lead to inaccuracies when creating phase diagrams and comparing them with experimental findings. Moreover, off-stoichiometry theoretical modeling is vital for accurately modeling diffusion and phase transformations in these systems.

In this thesis, we model from the atomic scale the thermodynamic properties of crystalline Li-Si compounds using Density Functional Theory (DFT) and statistical physics methods. We model point defects and the off-stoichiometry thermodynamic properties of Li-Si phases. By including the off-stoichiometry studies, this thesis aims to reproduce experimentally available data containing evidence of off-stoichiometry (e.g. open circuit voltage). This can also help deducing the stability of certain phases and therefore validate their existence. With the off-stoichiometry studies this thesis also aims to understand the phase transformation processes that Li-Si phases undergo whether they occur at equilibrium or constrained (i.e. applied voltage) thermodynamics.

The first chapter (bibliography) provides a brief overview of the functioning of Li-ion batteries and an overview of the materials that constitute them. It also presents the advantages and challenges associated with the use of Si in the battery. A state-of-the-art review of characterization of alloying processes, with the open questions in the literature, is presented as well. Lastly yet importantly, the bibliography ends with a methodology section where we explain most of the methods used in or required for understanding this thesis.

The second chapter consists of finite temperature studies of Li-Si line compounds. In this chapter, we introduce two phases ($Li_{43}Si_{18}$ and $Li_{44}Si_{18}$) that, to the best of our knowledge, are novel. This chapter also provides the finite temperature contribution to the Gibbs free energy coming from the lattice vibration in all the calculations of this thesis.

The third chapter is about off-stoichiometry studies of many of the known Li-Si compounds including finite temperature contributions to the Gibbs free energy (that we present in the previous chapter). This chapter also contains a detailed presentation of the studied point defects and their formation energies. In this chapter, we do quantitative comparisons with experimentally available data on off-stoichiometry properties, like open circuit voltage in function of Li content in the single phase domain of Li-Si phases at 690 K.

In the fourth and final chapter, we tackle the phase stability. In this chapter, we study the thermodynamic two-phase-equilibria between phases accounting for deviations from perfect stoichiometry. We then finish this chapter by a discussion section where we present how we can take advantage of the off-stoichiometry thermodynamic study to analyze precipitation driving forces of phases during lithiation, in particular, very well known $Li_{15}Si_4$ phase.

Finally, the conclusion brings together the main results obtained and discusses the perspectives of this thesis work.

Chapter 1

Bibliography

In the following chapter, we will start by giving a state of the art of Li batteries in general and the advantages and problems of adding Si for the production of next generation batteries. As one of the main goals of this thesis is to understand the alloying process of Li-Si compounds, we will also give a state of the art of what has been done in the literature to characterize the alloying processes of Li-Si compounds. Following the state of the art sections, we present a methodology section where we explain all the methods used during this thesis. Finally, we end with a conclusion where we summarize the open questions we tackle in this work.

1.1 Li-Si in batteries: state of the art

Before we head into the importance of incorporating Si for next generation batteries, it is crucial we give a brief history of batteries and explain how they work. Despite being a very good candidate for next generation batteries, Si still has some drawbacks that we will discuss and briefly mention what can possibly be done to tackle these problems.

1.1.1 A brief history of batteries: from Volta cell to Li-ions

To explore the history of Li-ion batteries, it is necessary to delve into the origins of the first electrochemical cell capable of generating electricity. In 1800, Alessandro Volta introduced a groundbreaking system known as the Voltaic pile, which converted chemical energy into electrical energy. This invention involved stacking metal discs made of zinc and copper, separated by felt, and immersed in a saline solution. Volta's work was prompted by a dispute with Galvani [10] concerning the frog experiment, where the frog's leg twitched upon contact with two metals. Through the Voltaic pile, Volta successfully disproved Galvani's theory of "animal electricity" and established the concept of "metallic electricity." This breakthrough paved the way for further advancements in battery technology, including the Daniell cell (1836) and the Leclanché Zn/MnO_2 cell (1866) [11]. It was Gaston Planté who later invented the first rechargeable battery, based on lead, in 1859. This lead-acid technology continues to be used in internal combustion engine vehicles. However, lead-based systems faced limitations in terms of energy and power. Consequently, alternative storage systems were developed, such as the Nickel-Cadmium (Ni-Cd) technology, which was developed in 1909 [12]. Ni-Cd batteries offer higher energy capacity and greater power output than lead-acid batteries. Nonetheless, the toxicity associated with cadmium has limited their usage. As a viable alternative, the Ni-MH (Nickel-Metal Hydride) technology, which is less harmful, has replaced Ni-Cd batteries.

In 1949, J. Hajek proposed the idea of using metallic lithium as the negative electrode in electrochemical batteries [13]. Lithium has gained significant interest due to its low atomic mass (6.94 g/mol) and highly reducing potential. However, the concept of lithium-metal batteries emerged only in the mid-1970s with the discovery of the first compounds capable of (de)intercalating lithium, such as TiS_2 [14]. Nevertheless, lithium-metal technology quickly encountered safety issues, including explosions (by air exposure) caused by short circuits resulting from the growth of lithium dendrites within the cells. To address this problem, two concepts were introduced in 1980. The first approach, called Li-polymer [15], involved using a polymer electrolyte instead of a liquid electrolyte in the cell to hinder dendrite formation. The second concept, proposed by D.W. Murphy [16] and B. Scrosati [17], was the Li-ion technology. This technology replaced the metallic lithium electrode with a low-potential lithium insertion compound to prevent dendrite formation. Ultimately, the first Li-ion batteries based on this principle were commercialized by SONY in 1991 and have since enjoyed increasing success.

The development of Li-ion technology has paved the way for various energy storage systems, both within the Li-ion domain and beyond (i.e. Li metal). Over time, Li-ion batteries have emerged as the most advanced and efficient option when compared to their main competitors. This can be observed in the Ragone plot in Fig. 1.1, which showcases the superior mass energy densities and power densities of Li-ion batteries in comparison to other technologies.

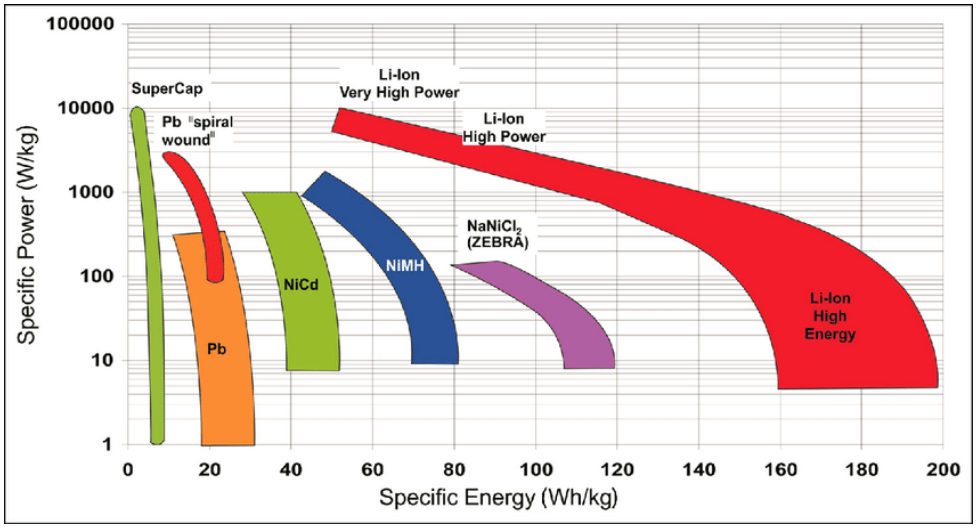

Figure 1.1: Ragone plot showing the performance in battery materials [4]. Conceptually, the horizontal axis describes how much energy is available per unit mass, while the vertical axis shows how quickly that energy can be delivered per unit mass.

1.1.2 Notion of a battery

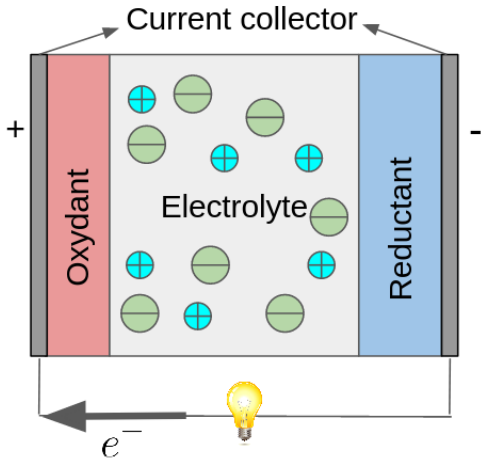

Figure 1.2: Schematic representation of an electrochemical cell. The sense of the current here indicates the discharging of the battery.

The fundamental operating principle of an electrochemical battery described here is applicable to all electrochemical energy storage technologies. In an electrochemical cell, chemical energy is directly converted into electrical energy through redox reactions. These reactions involve the exchange of electrons between an oxidizing species and a reducing species, resulting in a balanced overall reaction with respect to charges. In an electrochemical battery, the oxidizing and reducing species are spatially separated, allowing control of the overall reaction by enabling electron flow through an external circuit (electric

current) while ions migrate within the battery. Fig. 1.2 illustrates the principle of an electrochemical battery during discharge (i.e. when it supplies current). The battery comprises two electrodes containing electrochemically active species, a conductive ion electrolyte, current collectors, and an external circuit. During discharge, the material at the negative electrode undergoes oxidation, while the material at the positive electrode undergoes reduction. The negative electrode releases ions and electrons, whereas the positive electrode consumes them. The electrolyte facilitates ion conduction between the oxidizing and reducing species, while blocking the passage of electrons. Thus, electrons are collected by the current collector and transmitted from one electrode to the other through the external circuit, generating an electric current.

The fundamental properties of a battery are voltage, capacity, and energy density (per unit volume). Voltage refers to the difference in average potentials between the positive and negative electrodes, resulting from simultaneous redox reactions. Capacity represents the specific amount of charge exchanged during the electrochemical reactions, indicating the system's electricity quantity in terms of mass or volume. Energy density, obtained by multiplying the average potential and capacity, represents the amount of energy that the cell can deliver.

The Li-ion battery involves the reversible exchange of Li^+ ions and electrons between two electrodes. As mentioned earlier, Li-ion technology relies on the use of materials capable of inserting/removing lithium atoms into/out of their crystalline structure. An example of a typical commercial Li-ion battery consists of a negative electrode made of graphite, a positive electrode based on $LiCoO_2$, a liquid electrolyte that conducts Li^+ ions while acting as an electron insulator, two current collectors, and an external circuit.

The variety of positive electrodes for Li-ion batteries is very large and well described in several works [18] and out of the scope of this work. However for the negative electrode, the search for a good candidate that could be combined with Li metal as a positive electrode has regained popularity.

1.1.3 Si as a negative electrode for next generation batteries

Due to the previously mentioned limitations associated with the use of metallic lithium (needed for high capacity storage), the need for new materials for the negative electrode has emerged. Graphite, the most common material in Li-ion batteries, is now facing competition from other materials. Among them, we have the carbon materials (other than graphite) such as carbon nanotubes [19]. Regaining popularity, we have pure metals and semiconductors (such as Si) that show to be the best to replace graphite.

Silicon is the next candidate to replace graphite due to its high theoretical capacity of 4200 mAh/g (12 times more than that of graphite 370 mAh/g). Besides, Si constitutes 28% of Earth's crust making it the second most abundant element on Earth and playing an essential role in its very low cost. Additionally, Si is non toxic to work with. These are mainly the reasons why Si has gained particular interest in the last two decades [5]. However, Si unfortunately faces some challenges when lithiated.

1.1.4 Challenges linked to Si cycling

In practical applications, achieving reversible cycling of silicon has proven to be difficult. Early studies using micrometer-sized silicon revealed significant challenges such as poor cycling stability and low coulombic efficiency (i.e. the charge efficiency by which electrons are transferred in batteries) [20, 21, 22]. These issues are primarily attributed to two factors: the volumetric expansion of the silicon material during cycling and the formation of degradation compounds at the electrode/electrolyte interface [23].

Unlike graphite, the electrochemical reaction between Si and Li involves alloying through phase transformations rather than intercalation. As a result, when lithium atoms are inserted into the silicon structure, the material undergoes enormous volumetric expansion, that can reach up to 400% [24]. Conversely, during lithium extraction, the material undergoes contraction. The mechanical stresses resulting from these expansion and contraction cycles cause pulverization of the silicon particles, leading to the loss of

electron contacts between particles and between particles and the current collector (a process known as delamination) [20]. Consequently, some particles become disconnected, reducing their contribution to the cycling process and resulting in a decrease in the electrode's capacity. Fig. 1.3 shows the schematic representation of aforementioned mechanisms.

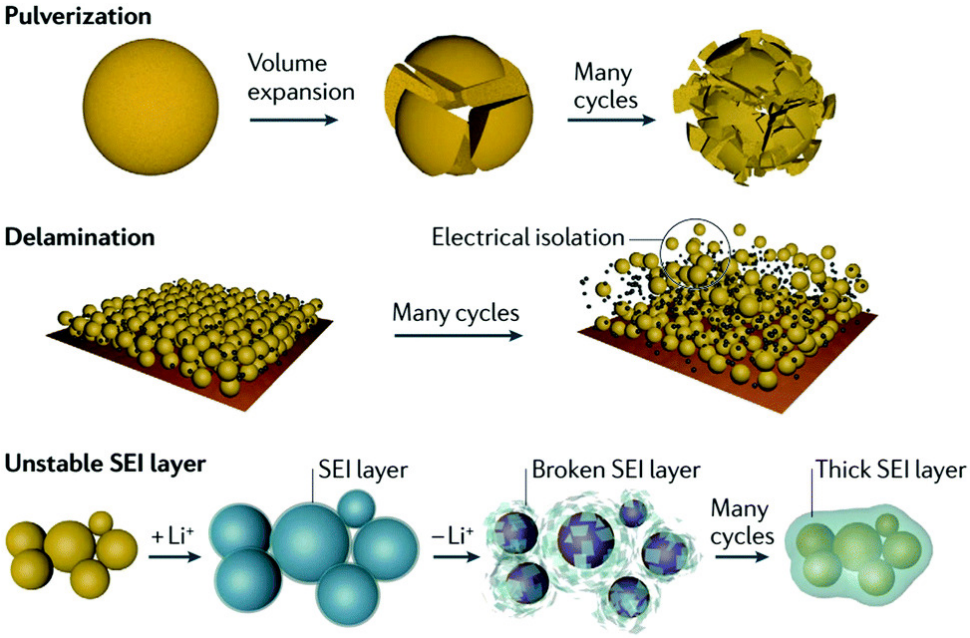

Figure 1.3: Schematic representation of Si cycling degradation mechanisms [25].

Fig. 1.3 shows the degradation of the electrolyte at the electrode surface which is another factor that impacts the performance of Si-based electrodes. In Li-ion batteries, the liquid electrolyte is only stable within a specific potential range. When the potential of the negative electrode falls below 1 V vs. Li/Li+, the electrolyte decomposition occurs at the electrode surface. This results in the formation of a solid layer called the solid electrolyte interface (SEI) on the material's surface. The formation of the SEI layer consumes ions and electrons, leading to a loss of capacity. While the SEI layer formed on graphite is stable and passive, the SEI layer formed on silicon is unstable due to the volumetric expansion of the material [26, 27, 28]. During the expansion or contraction of the material, the SEI layer breaks, exposing fresh surfaces to the electrolyte. This leads to continuous SEI formation throughout cycling, consuming ions and electrons and causing irreversible capacity losses (i.e. because of formation of thick SEI layer).

1.1.5 Approaches taken to enhance Si cycling and their problems

The ways to enhance Si cycling are numerous, as a matter of fact, we estimate over 1000 articles have been published the last decade on this matter. We briefly discuss below a few of the approaches that have been presented in the literature.

Composites

One of the early approaches to mitigate the volumetric expansion of silicon involves using a structure composed of a metallic matrix in which silicon particles are dispersed. The matrix serves to reduce the

volumetric expansion of the silicon particles, thereby reducing electrode pulverization. Even though successful in reducing electrode pulverization, Si/metal composites suffer from reduced capacity deliverance the more cycles they undergo [29].

Another set of composites are the Si/Carbon ones. Not new to the domain of batteries, carbon can also provide a good hosting matrix for Si particles. Carbon is a lightweight material that is highly tolerant to mechanical stresses. Most importantly, carbon can act as a buffer element for volumetric expansion the effect of the external pressure on the Si lithiation. Si/Carbon composites offer capacities greater than Si/metal ones, while also providing better performance in terms of reversibility [30].

Reduction of the Si particle size

The prevalent approach in the literature to improve the performance of silicon involves reducing particle size or nanostructuring the electrodes. Nanoscale particles or nanostructured materials offer several advantages, such as increased resistance to mechanical stresses and shorter diffusion paths for ions and electrons. However, there are challenges associated with nanomaterials, including increased parasitic reactions with the electrolyte and lower volumetric densities, resulting in lower volumetric capacities. Additionally, the synthesis of nanoparticles or nanostructures raises concerns regarding reproducibility, toxicity, complexity, and cost, which may impact their potential commercialization [31].

Stabilization of surface reactions

One of the latest approaches to optimizing the performance of Si-based electrodes is the control of degradation mechanisms at the electrode/electrolyte interface. As mentioned earlier, the continuous formation of the SEI occurs during cycling of Si. To stabilize the SEI formed on the surface of Si electrodes and reduce the resulting irreversibility, the addition of additives to carbonate-based electrolytes or the modification of the composition of conventional electrolytes have been considered. These approaches aim to improve the stability of the SEI layer and mitigate capacity losses during cycling [32].

1.2 Characterization of alloying processes in Li-Si systems: state of the art

Regardless of the approach taken to enhance the Si (de)lithiation cycling, Si will undergo an alloying process, as mentioned earlier, and the formation of Li-Si phases (crystalline or amorphous) will take place. Because of this, it is important that we understand the different approaches, experimental or theoretical, that the literature offers to characterize the alloying phenomena. Having insight of how the phases transform can give us a better understanding of the physics behind the alloying (e.g. the volume expansion).

1.2.1 Phase Diagrams

The Li-Si binary system was first studied at high temperatures (greater than 650 K) by S. Lai [33], and Sharma and Seefurth [34] in 70's. They had been the first ones to report open circuit voltage (OCV) plateaus that were, indeed, signature of two-phase-equilibria between what had been (and still is) believed to be crystalline phases. However, both their works reported phases that are different from that of the work of Wen and Huggins in 1981, despite having excellent agreement in the OCV plateau values [35]. Different from the former's work, the work of Wen and Huggins included x-ray diffraction (XRD) pattern comparison with previously reported XRD data of the well known $Li_{12}Si_7$, Li_7Si_3, $Li_{13}Si_4$ and $Li_{22}Si_5$. The first reported phase diagram by H. Okamoto [36] (similar to the one reported by Braga et al. 5 years

later [37]) was then based on the results of the previously mentioned works; especially, on the work of Wen and Huggins for the identification of phases.

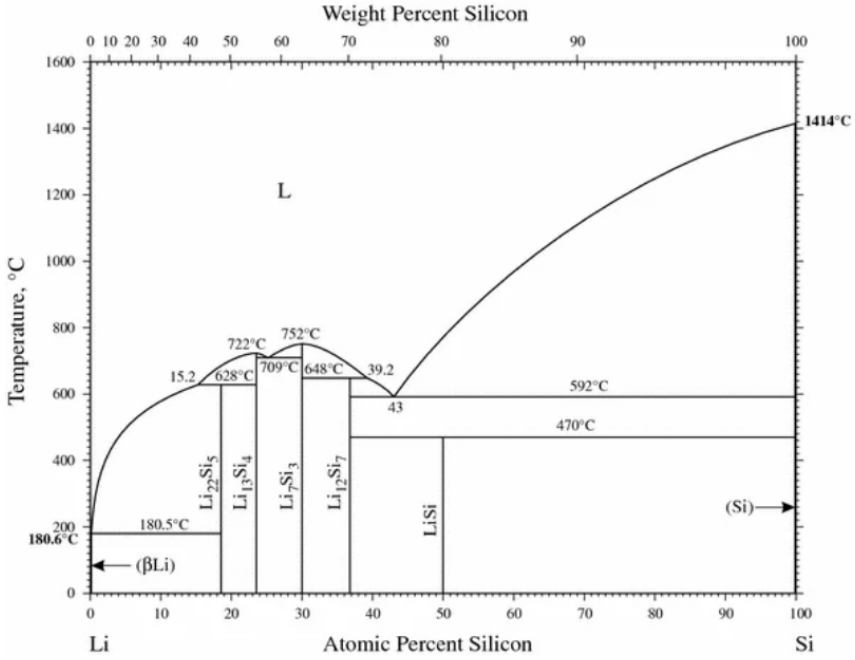

Figure 1.4: Phase diagram of Li-Si as reported by H. Okamoto in 2009 [38].

It was not until 2009 that H. Okamoto added LiSi to his previous phase diagram [38] (Fig. 1.4). The reason why LiSi was not previously observed, although the other alkali monosilicides (NaSi, KSi, RbSi, and CsSi) were known to exist, is because it requires high temperatures and pressure to be synthesized (773–973 K, 1–2.5 GPa) as reported by Stearns et al. in 2003 [39]. A work by Evers et al. has shown that, once present, this phase decomposes at 743 K into Si and $Li_{12}Si_7$ with thermal analysis [40]. This addition to the phase diagram was further validated by Density Functional Theory (DFT) calculations at 0 K and finite temperatures (using harmonic approximation) [41]. It is important to note that LiSi is a semiconductor with a narrow bandgap (0.057 eV) [39]; and to the best of our knowledge, there is no literature using hybrid functional DFT calculations for Li-Si compounds which could potentially change the theoretical stability of LiSi -please check Sec. 1.3.2 for more information on how hybrid functionals can affect the calculation of energies. For instance, a more recent phase diagram by the work of Wang et al. [42] does not consider LiSi in the phase diagram (Fig. 1.5a). Wang et al. were the first ones to assess their data from experimental measurements of heat capacity [43] using the CALPHAD approach.

Phase discovery methods such as Genetic Algorithm and minima hopping method, have led to the discovery of stable phase Li_5Si_2 at 0 K [44, 45, 46]. Moreover, DFT formation energies at 0 K have demonstrated that Li_7Si_3 is not stable against two-phase-equilibrium between $Li_{12}Si_7$ and Li_5Si_2 because it is above the convex hull [45]. Tipton et al. state that the phase around $x = 2.333$ in Li_xSi is indeed Li_5Si_2 but with high Li vacancy concentration due to low formation energy value of the latter [44].

Up to now, the identification of the highly lithiated phases is still problematic. Wen and Huggins declared it was the $Li_{22}Si_5$ phase [35]. However, based on experimental and theoretical studies, some authors were in agreement that the claimed $Li_{22}Si_5$ phase is indeed the $Li_{21}Si_5$ phase [41, 47]. One experimental study by Obrovac and Christensen strongly disagrees on $Li_{21}Si_5$ being the highly lithiated phase and rather claim that it is $Li_{15}Si_4$ at room temperature [48]. Thanks to Zeilinger and co-workers

we have one of the latest experimental insights in the relative stability of highly lithiated phases: $Li_{17}Si_4$ [49], $Li_{15}Si_4$ [50], $Li_{4.11}Si$ [51] and $Li_{13}Si_4$ [52]. They found $Li_{17}Si_4$ to be stable at room temperature up to 761 K, and $Li_{4.11}Si$ stable between 754 K and 892 K and they report the phase $Li_{15}Si_4$ to be metastable. The CALPHAD work of Braga et al. also reports one of the most recent phase diagrams [53]; their phase diagram is the closest in agreement with the experimental works done by Zeilinger et al. (Fig. 1.5b).

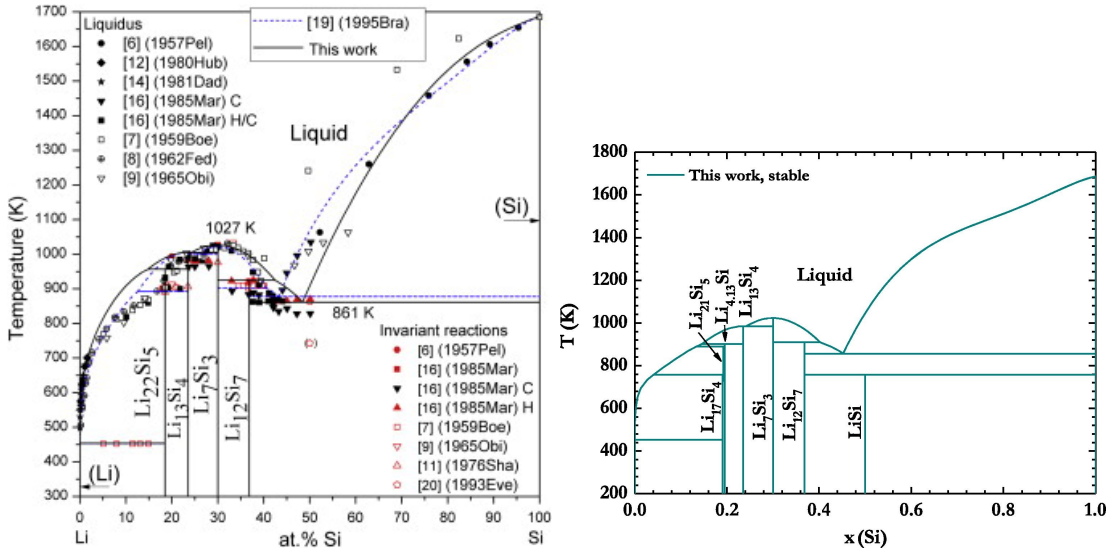

(a) Wang et al. phase diagram [42]

(b) Braga et al. phase diagram [53]

Figure 1.5: Recent phase diagrams in the literature assessed from experimental thermodynamic data (i.e. heat capacity and OCV measurements).

Regardless of the phase diagram that has been reported in the past for Li-Si systems, none considers the off-stoichiometry of compounds. The experiment of Wen and Huggins is the living proof that off-stoichiometry should be accounted for in these systems [35]. Wen and Huggins work has showed that the transitions between the plateaus of two-phase-equilibria are not vertical lines and span over finite composition ranges. Besides, heat capacity experiments have demonstrated that for the Li_7Si_3 nominal composition we obtain a first order phase transition around 210 K [43, 54]. By relying on Nuclear Magnetic Resonance (NMR) results, we expect this phase transition to be from a two-phase-equilibrium to a single phase. None of the given phase diagrams above is able to reproduce such first order phase transition phases are assumed to be line compounds.

As it can be observed from the previous figures and discussion, throughout the years, the phase diagram has changed. There is not really a consensus on the relative stability of phases in the binary Li-Si system. More importantly, there are still open questions regarding the phases with composition close to Li_7Si_3 and highly lithiated ones, they have one thing in common. They are very similar in stoichiometry which might be actually the reason why a general agreement has not been achieved concerning the Li-Si phase diagram. The stoichiometry and symmetry of the Si sublattice are so similar that the limitations would be the ones imposed by the experimental accuracy.

An even more recent experimentally assessed CALPHAD work by Liang et al. [55] yields an almost identical phase diagram to that of Braga et al. [53]. However, it has managed to reproduce the OCV voltage profile of the work of Wen and Huggins at 690 K [35] with the only difference being that they report LiSi even at 690 K even when Wen and Huggins do not. Nonetheless, they still do not reproduce

the single phase domain OCV as reported in [35].

1.2.2 Experimental limitations

In order to explain why there is no general agreement in the literature, it is important to understand the sources of experimental error in Li-Si systems.

XRD

When it comes to synthesizing Li-Si phases, the most common way to identify them is via XRD measurements [35, 43, 54]. Lithium's position in the crystal lattice can be difficult to establish due to its low XRD scattering factor. Zeilenger and coworkers have showed that the differences in XRD patterns among the $Li_{21}Si_5$, $Li_{17}Si_4$, and $Li_{22}Si_5$ phases are very difficult to distinguish [51] (Fig. 1.6). Morris et al. also explained that this could happen with Li_7Si_3 and Li_5Si_2 [45]. Overall, when it comes to phases having similar stoichiometries and lattices that differ over few Li sites, XRD can fail to identify the phases properly due to the proximity and similarities in peaks.

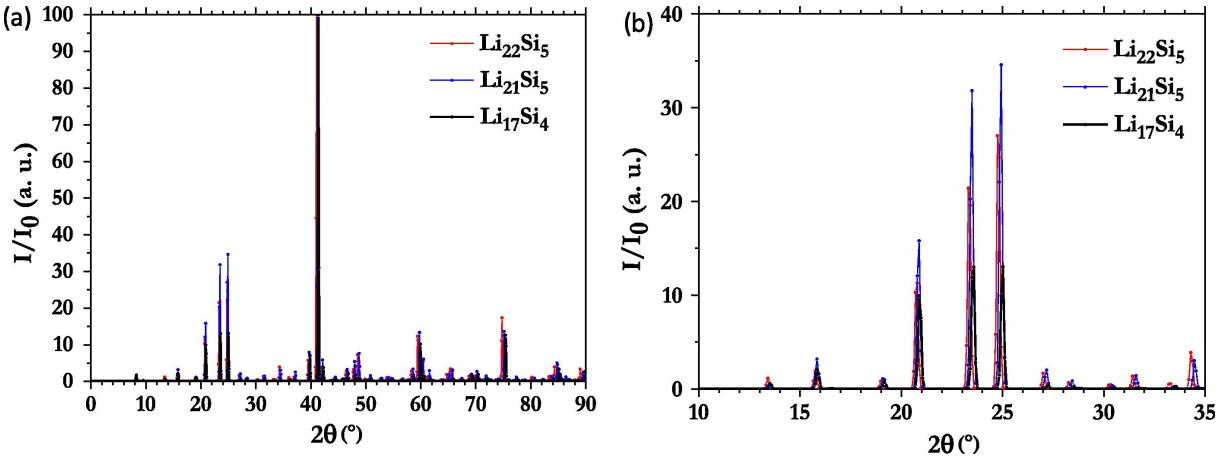

Figure 1.6: XRD diffraction patterns of $Li_{21}Si_5$, $Li_{17}Si_4$ and $Li_{22}Si_5$. Note that the right-hand panel is a zoomed representation of the left-hand figure. Image taken from the work of [51].

Low temperature characterization

Low temperature characterization poses limitations due to the limited atomic diffusion. The system's dynamic nature and potential deviations from equilibrium conditions introduce uncertainties in the observed phenomena and their interpretations. Consequently, calorimetry measurements commonly used to study phase transitions, may not capture phase transitions accurately at low temperatures. Moreover, we do not have voltage cycling profile with crystalline Li-Si phases at temperatures below 600 K (to be shown in the next section).

Lithiation composition

One of the most common ways to observe the alloying processes and phase transformation is via eletrochemical lithiation of phases. As discussed previously, the first alloying characterizations consisted of observing the OCV plateaus while lithiating Si at high temperatures. Wen and Huggins, used the Galvanostatic Intermittent Titration Technique (GITT, explained later in Sec. 1.3.8) to quantify the amount

of Li going in/out the Si electrode [35]. This method relies on the hypothesis that for each electron measured going in/out of the Si electrode, there is also a Li going in/out of the Si electrode from/towards the Li electrode. This condition on its own can be a source of inaccuracy in the evaluation of the real nominal composition in Li of the Si electrode. Thus, for phases with close-by stoichiometry, the error in composition that GITT could have is enough to predict one phase over the other.

1.2.3 DFT and alloying processes

Since the experimental data on crystalline phases are missing at room temperature and there are some uncertainties on the OCV-composition relationships, DFT methods can actually provide insight on the Li-Si phases stability. Table 1.1 shows a summary of the DFT work done and the method used. Notice how there is 0 K data using DFT generalized gradient approximation (GGA), but not hybrid functional (both explained later in Sec. 1.3.2). Previous references have also included finite temperature effects in most of the Li-Si phases with the harmonic or quasiharmonic approximations (explained in Sec. 1.3.3); however, they still miss some phases like Li_5Si_2. Moreover, they lack a direct comparison with the experimental open circuit voltage reported by Wen and Huggins at 690 K [35].

Reported phase	**DFT GGA**	**DFT Hybrid Functional**	**Harmonic**	**Quasiharmonic**
LiSi	[41]	N/A	[41]	N/A
$Li_{12}Si_7$	[41]	N/A	[41]	[56]
Li_7Si_3	[41]	N/A	[41]	[56]
Li_5Si_2	[44]	N/A	N/A	N/A
$Li_{13}Si_4$	[41]	N/A	[41]	[56]
$Li_{21}Si_5$	[53],[41]	N/A	[53],[41]	N/A
$Li_{17}Si_4$	[53]	N/A	[53]	N/A
$Li_{22}Si_5$	[41]	N/A	[41]	[56]

Table 1.1: Reported literature using DFT calculations, notice how for quasiharmonic approximation and the hybrid functional there is not a single reference that includes all the reported studies together.

1.2.4 Room temperature Si (de)lithiation cycling and $Li_{15}Si_4$

The potential profiles of Li-Si phases at room temperature are quite different from those obtained at 690-K (Fig. 1.7). At room temperature, lithiation of Si does not result in the formation of crystalline phases as observed at 690 K. The lithiation curve exhibits a single potential plateau corresponding to a two-phase-equilibrium process between crystalline silicon and an amorphous Li_xSi phase. Several research groups have determined the composition of the produced amorphous Li_xSi phase. The compositions reported include $Li_{3.5}Si$ from in situ X-ray diffraction (i.e. via the disappearance of Si brag peaks while lithiation) [57], $Li_{2.9}Si$ from electron energy loss spectroscopy (EELS) [58], and $Li_{3.1}Si$ from Auger spectroscopy [59]. Upon full lithiation, cycling of silicon at low potential leads to the crystallization of the $Li_{15}Si_4$ ($Li_{3.75}Si$) phase, as observed by Li and Dahn using X-ray diffraction [57].

Although not predicted to be a stable phase with DFT at 0 K and finite temperatures [41], there are plenty of experimental studies that agree on the formation of crystalline $Li_{15}Si_4$ upon electrochemical lithiation at room temperature.

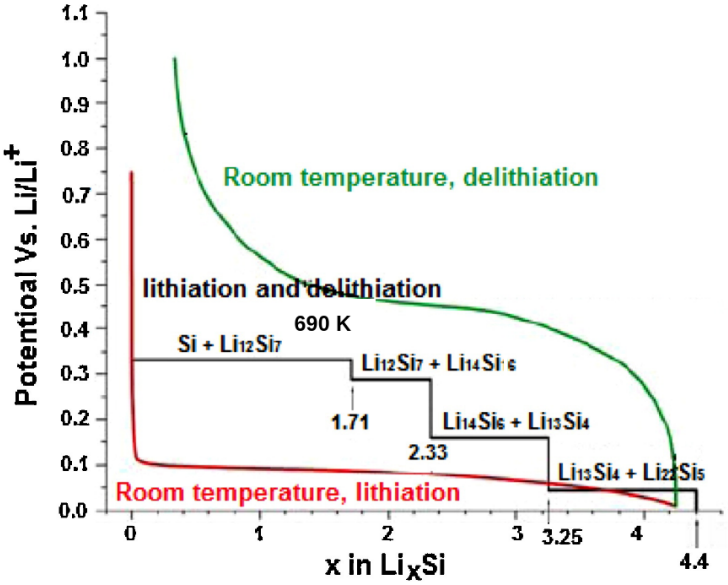

Figure 1.7: Potential profile at room temperature upon lithiation (in red) and delithiation (in green) [23] and 690 K (in black) [35]. Image adapted from [23].

The formation of the $Li_{15}Si_4$ phase at the end of lithiation plays a crucial role in the cycling performance of Si electrodes. Obrovac and Krause [60] demonstrated that limiting the lithiation potential of Si above 50 mV prevents the formation of the crystallized $Li_{15}Si_4$ phase and improves the cycling stability of the electrodes. The crystallization of the $Li_{15}Si_4$ phase has a detrimental effect on electrode cycling. The cycling performance of Si-based electrodes is significantly enhanced when alloying reactions involve only amorphous phases, with a lithiation potential maintained above 50-70 mV. Therefore, understanding the formation of $Li_{15}Si_4$ is considered essential.

A work, using in-situ scanning transmission electron microscopy, electron energy loss spectroscopy, and DFT, has shown that as the lithium concentration (x) increases in the amorphous Li_xSi, it undergoes a transformation into the crystalline $Li_{15}Si_4$ phase. The crystallization of $Li_{15}Si_4$ from amorphous Li_xSi is a congruent process that does not involve long-range atomic diffusion or phase separation (as if it were an ordering transition). As x increases, the electronic structure of amorphous Li_xSi approaches that of the crystalline phase with the same chemical composition [61]. However, we believe that it is not enough to explain why other crystalline phases would not form.

Additionally, McDowell et al. reported that $Li_{15}Si_4$ phase is formed as the terminal phase below 85°C [62], but the phase $Li_{21}Si_5$ forms at the end of lithiation at temperatures higher than 100°C. These authors also found that if Si is lithiated at room temperature but the voltage is held at 0 V vs Li/Li+ after lithiation, the $Li_{21}Si_5$ Bragg peaks begin to develop after about 24 hours suggesting that $Li_{15}Si_4$ is metastable with the ability to transform into the thermodynamically stable phase if given sufficient time [62, 43].

1.2.5 Nanosized Si anodes and alloying processes

Despite having increased resistance to mechanical stresses, Si nanoparticles still face plastic deformation when lithiated. Observations made using in situ transmission electron microscopy (TEM) show that the process of lithiation frequently involves the moving of a distinct and well-defined interface between Si that has been lithiated and the Si that remains unlithiated [63, 64]. The TEM images depicted in

Fig. 1.8 illustrate a core-shell configuration of a Si nanoparticle undergoing partial lithiation. This configuration involves a well-defined boundary, consisting of two distinct phases, separating a crystalline Si core from an amorphous Li_xSi (with $x \approx 3.75$) outer shell. The presence of such a sharply defined phase boundary indicates that the transition between the lithium-poor and lithium-rich phases is not a continuous transformation with changing composition. Instead, there exists a significant solubility gap between the two phases, which is evident through a sudden change in lithium concentrations across the boundary. Additionally, Fig. 1.8 reveals the formation of a surface crack, suggesting the occurrence of hoop tension in the surface layer during lithium insertion [64]. This hoop stress that develops at the surface can also have an effect on the precipitation driving forces (Sec. 1.3.9) and hysteresis (i.e. due to asymmetrical selection of phases during lithitation and delithiation).

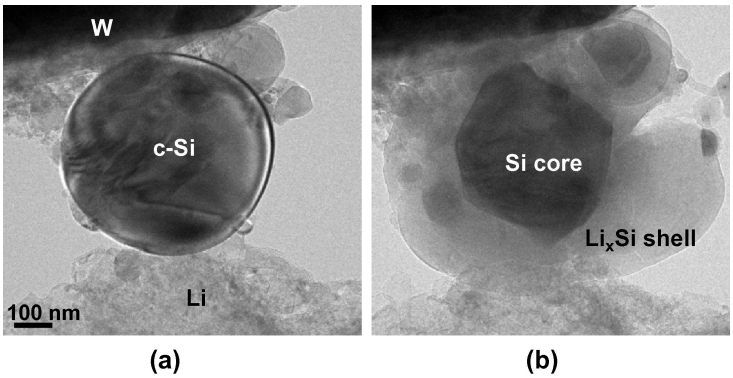

Figure 1.8: In situ TEM observation of lithiation and cracking in a Si nanoparticle, image taken from [64]. (a) The particle before lithiation. (b) The particle after lithiation, the surface crack can be observed.

A work by Bernard et al. has shown the influence of carbon coating (thin and thick), and initial atomic configuration (amorphous or crystalline) on Si nanoparticles electrochemical behaviours [65]. Bernard et al. show that the thickest carbon coating improves capacity retention. They also show that the initial atomic configuration of Si has little impact on cycling performance. They found that the lithiation of all particles show a very similar OCV profile; while the delithiation of thick coated carbon Si nanoparticles shows, relative to the other samples, the smallest hysteresis. They inferred this phenomena could be attributed to the effect of compressive stress by the carbon coating. They noticed that the thick carbon coating provided more stable SEI with lower resistance via impedance measurement. These results lead them to conclude that carbon coating has an effect on the lithiation kinetics. Despite affecting the lithiation kinetics, thick carbon coating does not promote the formation of crystalline phases, other than $Li_{15}Si_4$ -at least, that is what the OCV cycling profiles show.

1.3 Methodology

In this section, we present the modeling methods used in this work to investigate the thermodynamic properties of the Si-Li system. We emphasize here the potential links between the calculated properties and the observables from the experiment (e.g. the voltage, phase diagram, etc.). We start by simple thermodynamic definitions, we present Density Functional Theory and the statistical physics methods used to deduce the thermodynamic properties. We demonstrate how we include finite temperature contributions to the Gibbs free energy, and we briefly introduce the principles behind constructing a phase diagram. After having a concrete idea of the aforementioned, we can then show the relationship they have with the Open Circuit Voltage. Also, we can explain the principle behind the Galvanostatic

Intermittent Titration Technique and the method of analysis of the measured voltage. In the last part of the methodology section, we explain the thermodynamic formulation of nucleation.

1.3.1 Thermodynamic definitions

Thermodynamics deals with the study of energy transformations in physical systems. It is essential for the investigation of the voltage, phase stability, heat capacity, and selection of phases. Ahead, we present the definitions needed for the scope of this work.

Enthalpy

Enthalpy (H) of a system is defined as the sum of its internal energy (U) and the product of its pressure (p) and volume (V):

$$H = U + pV. \tag{1.1}$$

The internal energy is all the energy within a given system, including the kinetic energy of molecules and the energy stored in all of the chemical bonds between molecules. Its absolute value has no physical meaning and is systematically defined with respect to a reference energy.

Entropy

Entropy (S) is a thermodynamic property that quantifies the level of disorder of the system. It is related to the number of possible microstates that correspond to a given macrostate. In this work it is important that we account for the vibrational and configurational entropies.

Vibrational entropy arises from the vibrational motion of atoms or molecules within a system. The vibrational entropy quantifies the number of accessible vibrational states at a given temperature, and it increases with temperature due to the availability of more vibrational states.

Configurational entropy is the entropy arising from the different arrangements or configurations of the atoms of different species within a system. It is particularly relevant in systems with distinguishable arrangements such as crystalline structures or multi-component solids.

Gibbs Free Energy

Gibbs free energy (G) is the thermodynamic potential of the (N, P, T) thermodynamic ensemble. In other words, it quantifies the maximum useful work that can be extracted from a system at constant number of atoms, pressure, and temperature. The Gibbs free energy is given by the equation:

$$G = H - TS = U + pV - TS \tag{1.2}$$

We remark that at 0 K, the Gibbs free energy is equal to the 0 K enthalpy of the system. After the Euler theorem, the Gibbs free energy can also be expressed as function of chemical potential of species α (μ_α) [66]:

$$G = \sum_\alpha N_\alpha \mu_\alpha, \tag{1.3}$$

where N_α is the number of α species.

Helmholtz free energy

Helmholtz free energy (F) is another thermodynamic potential. Its variation describes the maximum work obtainable from a system -but unlike G- it occurs at constant volume, number of atoms and temperature. It is related to G by the Legendre transformation:

$$F = G - PV \tag{1.4}$$

Heat Capacity

Heat capacity is a thermodynamic property that measures the amount of heat energy required to raise the temperature of a system by a certain amount. It quantifies the system's ability to store thermal energy and is often denoted by the symbol C_p at isobaric conditions and C_v at isochoric conditions. Heat capacity can be deduced from the variation of H and S with temperature:

$$C_p = \frac{dH}{dT}, \tag{1.5}$$

$$C_p = -T\frac{dS}{dT}. \tag{1.6}$$

We can also find a relationship with the Gibbs free energy (at constant pressure and number of atoms):

$$dG = VdP - SdT + \sum_{\alpha} \mu_\alpha dN_\alpha$$

$$\frac{dG}{dT} = -S \tag{1.7}$$

therefore using Eq. 1.6 we can relate G to C_p as follows:

$$C_p = -T\frac{d^2G}{dT^2}. \tag{1.8}$$

When a system undergoes a process at constant volume, it means that there is no expansion work involved. It is important to note that the value of C_v is always lower than the value of C_p in Li-Si systems [53]. The heat capacity at constant volume in terms of enthalpy, entropy or free energy reads:

$$C_v = \left(\frac{\partial H}{\partial T}\right)_V = T\left(\frac{\partial S}{\partial T}\right)_V = T\left(\frac{\partial^2 F}{\partial T^2}\right)_V \tag{1.9}$$

1.3.2 Density Functional Theory

Density functional theory (DFT) is currently the most popular and efficient method used in the electronic structure calculations of the ground state of solids. Its formulation was developed through formalism by Hohenberg and Kohn in 1964 [67] and by Kohn and Sham in 1965 [68]. DFT has been primarily used since the 1970s for solid-state physics and chemistry studies. However, in the last two decades, it has become popular in materials science and, therefore, batteries (as shown in Sec. 1.1.3).

The objective of DFT is to simplify the complex problem of quantum many-body interactions. In this approach, we seek to obtain the physical characteristics of a system composed of N_n nuclei and N_e electrons by solving the Schrödinger equation:

$$\hat{H}\Psi\left(\mathbf{r}_1, \mathbf{r}_2, \ldots, \mathbf{r}_{N_e}, \mathbf{R}_1, \mathbf{R}_2, \ldots, \mathbf{R}_{N_n}\right) = E\Psi\left(\mathbf{r}_1, \mathbf{r}_2, \ldots, \mathbf{r}_{N_e}, \mathbf{R}_1, \mathbf{R}_2, \ldots, \mathbf{R}_{N_n}\right), \tag{1.10}$$

where $\hat{H}$ is the total Hamiltonian operator of the system, Ψ is the many-body wave function of the system, $\mathbf{r}_i$ and $\mathbf{R}_j$ correspond to the coordinates of the i$^{\text{th}}$ electron and j$^{\text{th}}$ nucleus respectively, and E is the total energy which is an eigenvalue of $\hat{H}$. The Hamiltonian of Eq. 1.10 reads, in atomic units, as:

$$H = -\frac{1}{2}\sum_{p=1}^{N_n}\frac{\nabla^2_{\mathbf{R}_p}}{M_p} - \frac{1}{2}\sum_{i=1}^{N_e}\nabla^2_{\mathbf{r}_i} + \frac{1}{2}\sum_{p=1}^{N_n}\sum_{q\neq p}^{N_n}\frac{Z_p Z_q}{|\mathbf{R}_p - \mathbf{R}_q|} + \frac{1}{2}\sum_{i=1}^{N_e}\sum_{j\neq i}^{N_e}\frac{1}{|\mathbf{r}_i - \mathbf{r}_j|} - \sum_{p=1}^{N_n}\sum_{i=1}^{N_e}\frac{Z_p}{|\mathbf{R}_p - \mathbf{r}_i|}, \quad (1.11)$$

where the first term and second terms are the kinetic energies of both nuclei and electrons respectively. The last three terms are the nucleus-nucleus, electron-electron, and nucleus-electron Coulomb interactions respectively. M_p is the nuclear mass, and Z is the atomic number.

The direct analytical solution of the Hamiltonian described in Eq. 1.11 for systems with multiple particles is near impossible to obtain. To tackle this challenge posed by many-particle systems, various approximations and theorems have been developed to simplify the wave function and, consequently, the Hamiltonian. The primary approximations and theorems employed include: (i) the Born-Oppenheimer approximation, which separates the motion of nuclei from that of electrons, justified by the significant difference in mass between nuclei and electrons, and (ii) the Hohenberg and Kohn theorems, which form the fundamental basis of the Density Functional Theory (DFT) method. These theorems establish that the ground state energy of the electronic subsystem can be expressed as a functional of the electronic density of the ground state. In other words, a given density, denoted as $n(\mathbf{r})$, can be the ground state density of the electron subsystem for a specific external potential. This determination fully defines the Hamiltonian and, consequently, the ground state energy. Building upon these theorems, Kohn and Sham proposed a simpler formulation by introducing an equivalent system of non-interacting electrons that is assumed to have the same electron density, $n(\mathbf{r})$, in its ground state as the actual system of interacting electrons. This non-interacting electron gas is described by a set of single-electron wave functions, denoted as ϕ_i. These advancements have enabled the reformulation of the search for the electronic ground state energy as the minimization of the density functional:

$$E[n(\mathbf{r})] = -\sum_i \int \phi_i^*(\mathbf{r})\frac{\nabla^2}{2}\phi_i(\mathbf{r})d\mathbf{r} + \int d\mathbf{r} v_{ext}(r)n(\mathbf{r}) + \frac{1}{2}\iint d\mathbf{r}d\mathbf{r}'\frac{n(\mathbf{r})n(\mathbf{r}')}{|\mathbf{r}-\mathbf{r}'|} + E_{XC}[n(\mathbf{r})], \quad (1.12)$$

where $v_{ext}(\mathbf{r})$ is the external potential formed by the nuclei-electrons and nuclei-nuclei interactions, $\phi_i(\mathbf{r})$ is the Kohn-Sham single-electron wave function related to $n(\mathbf{r})$ by $n(\mathbf{r}) = \sum_{i=1}^{N_e}|\phi_i(\mathbf{r})|^2$. The last term $E_{XC}[n(\mathbf{r})]$ is known as the exchange-correlation functional, it plays a big role in DFT since the accuracy of DFT results depends on the description of this functional. In terms of $n(\mathbf{r})$, there is no analytical expression; consequently, it needs to be approximated.

The minimization of the energy functional, with respect to the density, leads to a set of one-electron equations, known as the "Kohn-Sham" equation and written as follows:

$$\underbrace{\left[-\frac{1}{2}\nabla^2 + v_{eff}[n(\mathbf{r})]\right]}_{\hat{H}_{KS}[n(\mathbf{r})]}\phi_i(\mathbf{r}) = \epsilon_i\phi_i(\mathbf{r}), \quad (1.13)$$

where v_{eff} is the effective potential given by:

$$v_{eff}[n(\mathbf{r})] = v_{ext}[n(\mathbf{r})] + \int d(\mathbf{r})\frac{n(\mathbf{r}')}{|\mathbf{r}-\mathbf{r}'|} + \frac{\delta E_{XC}[n(\mathbf{r})]}{\delta[n(\mathbf{r})]}. \quad (1.14)$$

$E_{XC}[n(\mathbf{r})]$ is described using the Local Density Approximation (LDA) or the Generalized Gradient Approximation (GGA). GGA is naturally beyond LDA including the gradient of the electronic density.

GGA corrects the overestimation of binding energies of molecules and cohesion energies of solids that are otherwise obtained with LDA. Thus, GGA improvement leads to more accurate description of structural properties. For most of the calculations done in this thesis, we have used the Perdew-Burke-Ernzerhof (PBE) functional [69], which falls within the framework of GGA.

However, GGA is not a perfect approximation. With semiconductors the inherent self-interaction error (SIE) present in the approximation arises from the incorrect treatment of electron-electron interactions within the GGA framework. In semiconductors, the SIE can lead to the delocalization of charge and a spurious mixing of the valence and conduction bands, effectively reducing the predicted band gap. Here, hybrid functionals can play an important role.

Hybrid functionals

Hybrid functionals are designed to enhance the localization of correlated electrons through a combination of the Hartree-Fock exact non-local exchange functional and the standard exchange functional of DFT, such as GGA or LDA. By blending these functionals in a linear fashion, hybrid functionals aim to strike a balance between accurate electron correlation treatment and computational efficiency. This approach improves the description of electronic interactions and properties, allowing for a more realistic representation of electron localization and exchange effects in electronic structure calculations. One very well known hybrid functional and used in this work is the HSE06 [70]. Below we put the expression of the exchange correlation given by the HSE06 functional:

$$E_{xc}^{HSE} = \alpha E_x^{(HF,SR)}(\mu) + (1-\alpha)E_x^{(DFT,SR)}(\mu) + E_x^{(DFT,LR)}(\mu) + E_c^{DFT}, \tag{1.15}$$

where E_x^{HF} is the exact non-local exchange term of Hartree-Fock, E_x^{DFT} is the local exchange term as used in the PBE functional, and α is a parameter expressing the proportion of DFT functional replaced by the Hartree-Fock functional.

Representation of the wave functions

After formulating the Kohn-Sham single-electron equation (Eq. 1.12), the next challenge is finding a suitable representation for the electron wave functions and selecting an appropriate basis set to describe them effectively. In the region between atoms, the Kohn-Sham single-electron wave functions $\phi_i(\mathbf{r})$ have a relatively smooth form. At the same time, they exhibit rapid oscillations near the atomic nucleus due to the orthogonalization with respect to the core electrons. Two common approaches are used to represent the single-electron Kohn-Sham wave functions. The first approach involves decomposing the wave function using a localized orbital basis, effectively capturing the strong oscillations near the nucleus. However, this basis depends on the atomic positions, and need readjustment whenever the atom positions change. The second approach, decomposition using a plane-wave basis, offers significant advantages. The simplicity of this basis simplifies calculations of forces acting on the atoms. Moreover, increasing the number of plane waves utilized can easily control truncation errors associated with the basis.

Plane wave representation In a crystal, the Kohn-Sham wave functions are assumedly imposed by Bloch's theorem. In Eq. 1.13, the quantum number i becomes a wave vector, that can be restricted to the First Brillouin Zone, $\mathbf{k}$, and with a band index n. Then $\phi_{n\mathbf{k}}$ is the product of a plane wave $e^{i\mathbf{k}.\mathbf{r}}$ and a function $u_{n\mathbf{k}}$ with periodicity of the lattice:

$$\phi_{n\mathbf{k}}(\mathbf{r}) = u_{n\mathbf{k}}(\mathbf{r}) \exp[\mathbf{ik} \cdot \mathbf{r}]. \tag{1.16}$$

Because of the periodicity of $u_{n\mathbf{k}}$, it is possible to expand it as a series of plane waves $e^{i\mathbf{G}.\mathbf{r}}$, where $\mathbf{G}$ is a wave vector in the reciprocal lattice, therefore:

$$u_{n\mathbf{k}}(\mathbf{r}) = \Omega^{-1/2} \sum_{\mathbf{G}} C_{\mathbf{nk}}(\mathbf{G}) \exp[i\mathbf{G} \cdot \mathbf{r}], \tag{1.17}$$

where Ω is the unit cell volume, and $C_{n\mathbf{k}}(\mathbf{G})$ represents the expansion coefficients in the plane wave basis. Finally by replacing Eq. 1.17 in Eq. 1.16 we obtain the final form of the Kohn-Sham wave function in plane wave representation.

In practice, a truncation in the expansion is required, so we need to impose a cut-off energy E_{cut} to the wave function. Therefore $\mathbf{G}$ vectors need to satisfy the following criterion:

$$\frac{\hbar^2(\mathbf{G}+\mathbf{k})^2}{2m} \leq E_{\text{cut}} \ . \tag{1.18}$$

E_{cut} is chosen through convergence tests such that it satisfies the required accuracy criterion on the properties of interest. We remark that throughout this work we have used an $E_{\text{cut}} = 750$ eV which we found to be accurate enough for all the calculations performed. For instance, for Li and Si the recommended values are 555 eV and 245 eV, respectively. Nonetheless, it is still difficult to use plane waves to reproduce wave function near the nuclei due to the high oscillations in the region. The strong oscillations of the wave function will require a very large number of plane waves. To overcomes this problem there are two methods usually used in DFT: the very efficient pseudopotential method, which has a drawback due to its non-transferability; and the Projector Augmented Wave (PAW) method used in the VASP code that we use in this work for our DFT calculations.

Projector Augmented Wave method This formalism is an efficient and accurate method for the description of complex phases that require an atomic relaxation [71, 72]. It consists of dividing the wave function into two complementary parts: (i) a partial wave expansion within an atom-centered sphere called PAW sphere -in the sphere, the wave function oscillates rapidly; (ii) an envelope function outside the PAW sphere where the wave function is smooth, and where the former is expanded onto a plane wave basis set (as presented previously).

Note that within the pseudopotential method, the PAW formalism, considers the core electron as frozen, since their charge density is assumedly not affected by a variation of the chemical environment. That is why for the Li pseudopotential used in this work we have decided to use the one that includes the core electrons as valance as well (called "Li sv"), since we think they play an important role (i.e. reproducing the physics). However, for Si we have used the only one available which considers only the 4 last electrons as valence ones.

DFT energies and thermodynamics

The energies we obtain from DFT are the internal energies U of the systems. Moreover, in static DFT calculations the equilibrium volume corresponds to a zero pressure and temperature (thermal vibrations are not taken into account). Therefore, these calculations give us the Gibbs free energy of the system or the enthalpy at 0 K (please see Sec. 1.3.1). In order to include the effect of thermal vibrations in the energies we have used DFT paired with PHONOPY.

1.3.3 PHONOPY

In this work, we used PHONOPY [73] to calculate the vibrational contribution to the Gibbs free energies of our Li-Si compounds. Note that the calculations of forces are performed with DFT. For this section, we will just explain the formalism behind PHONOPY and how from the forces we can obtain all thermodynamic properties at finite temperatures.

Harmonic approximation

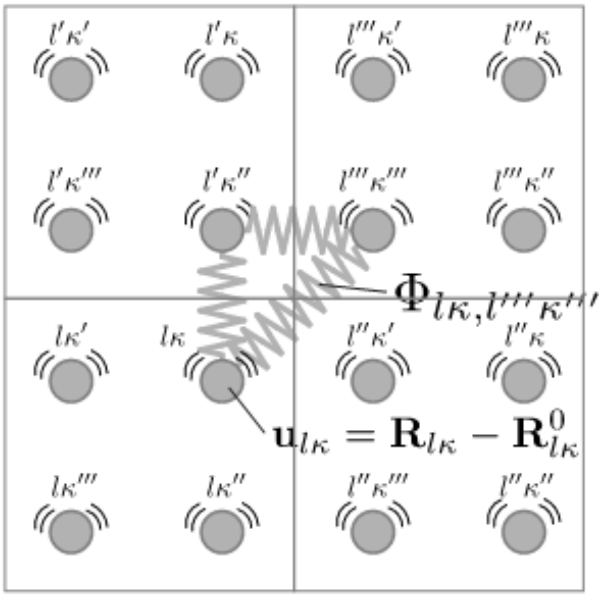

Figure 1.9: Crystal structure model and interacting atoms. The atoms are vibrating in the vicinity of their equilibrium positions R^0_{lk} towards R_{lk} (described by the displacement u_{lk}). In the Taylor series expansion of the crystal potential the spring constants are denoted by Φ. Image taken from [73].

It is presumed that atoms move around their equilibrium positions R^0_{lk} with displacements u_{lk} towards a position R_{lk} (as shown in Fig. 1.9), where l and k denote the unit cell and the corresponding atom, respectively. Crystal potential energy Φ is also presumed to be an analytic function of the displacements of the atoms, and reads as:

$$\begin{aligned}\Phi =& \Phi_0 + \sum_{lk}\sum_{\alpha}\Phi_\alpha(lk)u_\alpha(lk) \\ &+ \frac{1}{2}\sum_{ll'kk'}\sum_{\alpha\beta}\Phi_{\alpha\beta}(lk,l'k')u_\alpha(lk)u_\beta(l'k') \\ &+ \frac{1}{3!}\sum_{ll'l''kk'k''}\sum_{\alpha\beta\gamma}\Phi_{\alpha\beta\gamma}(lk,l'k',l''k'')u_\alpha(lk)u_\beta(l'k')u_\gamma(l''k'') + ...,\end{aligned} \tag{1.19}$$

where α, β, ... are the Cartesian indices. The coefficients of the series expansion Φ_0, Φ_α, $\Phi_{\alpha\beta}$... are the zeroth, first, second ... order force constants, respectively. With small displacements at a constant volume (harmonic approximation), this problem is solved only with the second order terms. The first order term is 0 at equilibrium and the third order and higher order higher order terms are treated by perturbation theory and usually neglected.

The force elements of the first ($F_\alpha(lk)$) and second-order ($F_\beta(l'k')$) force constants are obtained from 1.19 by:

$$F_\alpha(lk) = -\frac{\partial \Phi}{\partial u_\alpha(lk)} \tag{1.20}$$

$$\frac{\partial F_\beta(l'k')}{\partial u_\alpha(lk)} = -\frac{\partial^2 \Phi}{\partial u_\alpha(lk)\partial u_\beta(l'k')}. \tag{1.21}$$

The use of crystal symmetry is important to improve numerical accuracy of the force constants and to reduce computational cost. With the atomic forces and small displacements, the harmonic force constants can be calculated. This is known as the finite-displacement supercell approach very well described in [73].

As already explained in text books [74, 75, 76, 77], dynamical property of atoms in the harmonic approximation is obtained by computing eigenvalue problem of dynamical matrix $D(q)$,

$$\sum_{\beta k'} D^{\alpha\beta}_{kk'}(q) e^{\beta k'}_{qj} = \omega^2_{qj} e^{\alpha k}_{qj}, \tag{1.22}$$

with

$$D^{\alpha\beta}_{kk'}(q) = \sum_{l'} \frac{\Phi_{\alpha\beta}(0k, l'k')}{\sqrt{m_k m'_k}} e^{iq[R^0_{l'k'} - R^0_{0k}]}, \tag{1.23}$$

where m_k is the mass of the atom k, q is the wave vector, and j is the band index. ω_{qj} and e_{qj} are the phonon frequency and polarization vector of the phonon mode labeled by a set q, j, respectively. The eigenvalues ω^2_{qj} of $D(q)$ are real since, the latter is a Hermitian matrix. $D(q)$ is arranged to be a $3n_a \times 3n_a$ matrix [77], where the number 3 stands for the freedom of the crystal Cartesian indices and n_a is the number of atoms in the unit cell. Then e_{qj} is a complex vector with $3n_a$ elements and normalized to be 1 (i.e $\sum_{\alpha k} |e^{\alpha k}_{qj}|^2 = 1$). To better understand e_{qj} which contains information of collective motion of atoms, we write the set of atomic displacement vectors:

$$[u(l1), ..., u(lk)] = \left[\frac{A}{\sqrt{m_1}} e^1_{qj} e^{iqR_{l1}}, ..., \frac{A}{\sqrt{m_{n_a}}} e^{n_a}_{qj} e^{iqR_{lk}}\right], \tag{1.24}$$

where A is the complex constant undetermined by Eq. 1.22, and $e^k_{qj} = \left(e^{xk}_{qj}, e^{yk}_{qj}, e^{zk}_{qj}\right)$.

The phonon density of states, is an entity we compute in this work and show in Chapter 2, it is defined as:

$$g(\omega) = \frac{1}{N} \sum_{qj} \delta(\omega - \omega_{qj}), \tag{1.25}$$

where δ here stands for the Dirac delta function and N is the number of unit cells in crystal. Therefore, $g(w)$ is normalized over the number of unit cells and the integral over frequency becomes $3n_a$. Atom specific phonon DOS projected along a unit direction vector $\vec{n}$ is defined as:

$$g_k(\omega, \vec{n}) = \frac{1}{N} \sum_{qj} \delta(\omega - \omega_{qj}) |\vec{n} e^k_{qj}|^2. \tag{1.26}$$

Once phonon frequencies over Brillouin zone are known, we can calculate the energy E of phonons in the system, from the canonical distribution in statistical mechanics, under the harmonic approximation:

$$E = \sum_{qj} \hbar\omega_{qj} \left[\frac{1}{2} + \frac{1}{\exp\left(\hbar\omega_{qj}/k_B T\right) - 1}\right], \tag{1.27}$$

where T, k_B and $\hbar$ are the absolute temperature, the Boltzmann constant, and the reduced Planck constant, respectively. Using the thermodynamic relations [77], we give the isochoric heat capacity (C_v), the partition function (Z), the contribution to the Helmholtz free energy (F), and the isochoric entropy (S_v) at finite temperature as:

$$C_v = \sum_{qj} C_{qj} = \frac{dE}{dT} = \sum_{qj} k_B \left(\frac{\hbar\omega_{qj}}{k_B T}\right)^2 \frac{\exp\left(\hbar\omega_{qj}/k_B T\right)}{\left[\exp\left(\hbar\omega_{qj}/k_B T\right) - 1\right]^2}, \tag{1.28}$$

$$Z = \exp(-\Phi_0/k_B T) \prod_{qj} \frac{\exp(-\hbar\omega_{qj}/2k_B T)}{1 - \exp(-\hbar\omega_{qj}/k_B T)} \tag{1.29}$$

$$F = -k_B T \ln Z = \Phi_0 + \frac{1}{2}\sum_{qj} \hbar\omega_{qj} + k_B T \sum_{qj} \ln\left[1 - \exp\left(-\hbar\omega_{qj}/k_B T\right)\right], \tag{1.30}$$

and

$$\begin{aligned} S_v = -\frac{\partial F}{\partial T} =& \frac{1}{2T}\sum_{qj} \hbar\omega_{qj} \coth\left[\hbar\omega_{qj}/2k_B T\right] \\ &- k_B \sum_{qj} \ln\left[2\sinh\left(\hbar\omega_{qj}/2k_B T\right)\right]. \end{aligned} \tag{1.31}$$

We remark that the second term of F is the so-called zero point energy (ZPE).

Quasi-harmonic approximation

Understanding the temperature dependence of lattice parameters is essential for accurately characterizing and predicting the behavior of materials. One commonly used approach is the quasi-harmonic approximation (QHA), which assumes that lattice vibrations are harmonic and the lattice can be treated as an elastic continuum. The QHA accounts for the influence of temperature on lattice parameters by incorporating the vibrational contributions to the lattice energy. Phonon properties change as a function of the volume since the crystal potential is an anharmonic function of volume.

The QHA very simply consists in computing the harmonic properties at several fixed volumes for a particular crystal. Due to the quasi anhamonicity, the Helmholtz free-energy in Eq. 1.30 is dependent on unit-cell volume an temperature. Thus, for each temperature, we will have a group of Helmholtz free energies at different volumes for the same crystal. By making a fit of Birch-Murnaghan equation of state at each temperature, we can obtain the minima at each temperature. These minima are the Gibbs free energies at the corresponding temperatures. In Fig. 1.10 we show a schematic representation of the aforementioned explanation.

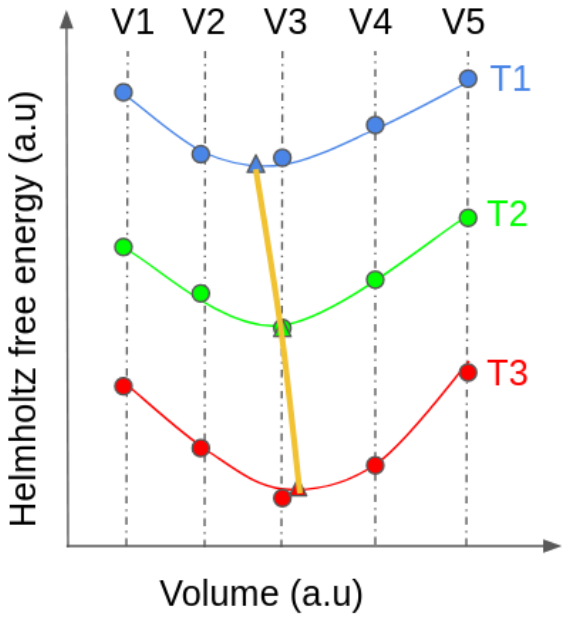

Figure 1.10: Example of plot of the Helmholtz free energies at 5 fixed volumes V1, V2, ..., V5 at temperatures T1 < T2 < T3. The yellow line represents the Gibbs free energies since it connects the minima of the fit of Birch-Murnaghan equation of state at each temperature.

Once we have the Gibbs free energy, we can proceed to calculate the isobaric heat capacity, entropy and enthalpies using the equations presented in Sec. 1.3.1.

1.3.4 Statistical physics approximations

The Low-Temperature Expansion (LTE) method [78, 79, 80, 81] offers several advantages over Cluster-Variation Method (CVM) [82], Monte Carlo (MC) simulations, and Bragg-Williams approximation [78]. The LTE allows for semi-analytical and precise calculations of local geometric configurations of interacting solute atoms within a pure solvent matrix, making it particularly well-suited for studying dilute solid solutions. Furthermore, with the LTE there is no need for an on-lattice interaction model since it is directly linked to the energies obtained by DFT. In contrast, CVM becomes increasingly challenging with larger clusters and extended interactions, while MC simulations face limitations in complex systems or at low temperatures as Kohan et al. showed [83]. Furthermore, Bragg-Williams mean field approximation neglects the local environment of atoms in computing the average site occupancy and configurational entropy. Thus, LTE stands out with its accuracy, especially in systems with low solute concentrations and complex energy landscapes, making it a valuable tool for investigating the behavior of solute atoms in materials. For this study we will be using the LTE when the concentration of point defects is significantly small and the Bragg William mean field approximation when the point defect concentration is high.

Low Temperature Expansion

The LTE formalism allows us to extract the chemical potentials of species as a function of composition in dilute solid solutions and in the off-stoichiometry regime of ordered compounds at low temperature.

In order to work at fixed chemical potentials we introduce the grand potential, $\mathcal{A}$, which is related to the Gibbs free energy G by the following Legendre transformation:

$$\mathcal{A} = G - \sum_{\alpha} N_{\alpha}\mu_{\alpha}, \tag{1.32}$$

where N_α and μ_α are the number of atoms and chemical potential of α species. In a system consisting of $\alpha = \mathrm{Li}, \mathrm{Si}$ elements (for the purpose of Li-Si compounds) the grand potential is related to the grand-canonical partition function (Z) by the following relation:

$$\begin{aligned} \mathcal{A} &= -k_B T \ln Z \\ &= -k_B T \ln \left[\sum_i M_i \exp\left(\frac{E_i - \sum_\alpha N_\alpha^i \mu_\alpha}{k_B T} \right) \right] \end{aligned} \tag{1.33}$$

where k_B is the Boltzmann constant, T the absolute temperature and the summation term runs over microstates i with energy E_i and containing N_α^i atoms of α species. M_i corresponds to the degeneracy of microstate i, and μ_α corresponds to the chemical potential of α species.

We can take a reference configuration (e.g. $i = 0$) such that all the other configurations are considered as "excitations" to this reference. These excitations consist in adding solute point defect clusters to the reference state at fixed values of the chemical potentials. If we take the grand potential of the reference $\mathcal{A}_0 = E_0 - \sum_\alpha N_\alpha^0 \mu_\alpha$, we can then write Eq. 1.33 as:

$$\mathcal{A} = \mathcal{A}_0 - k_B T \ln \left(1 + \sum_{i \neq 0} M_i \exp\left(\frac{E_c^i + \sum_\alpha \Delta N_\alpha^i \mu_\alpha}{k_B T} \right) \right), \tag{1.34}$$

where E_c^i is the i^{th} configuration energy difference given with respect to the reference state $E_c^i = E_0 - E_i$, and $\Delta N_\alpha^i = N_\alpha^i - N_\alpha^0$ is the change in number of atoms of α species in configuration $i \neq 0$ with respect to $i = 0$. The logarithmic term is then Taylor expanded to infinite order and the linked cluster theorem shows that all non linear terms cancel out [78], Eq. 1.34 becomes:

$$\mathcal{A} = \mathcal{A}_0 - k_B T \sum_{i \neq 0} M_i \exp\left(\frac{E_c^i + \sum_\alpha \Delta N_\alpha^i \mu_\alpha}{k_B T} \right). \tag{1.35}$$

We can obtain the concentration of α species per number of sites of Si atom (arbitrary choice) in the reference state (N_{Si}^0) as a function of their chemical potential with Eq.1.36:

$$x_\alpha = -\frac{1}{N_{\mathrm{Si}}^0} \frac{\partial \mathcal{A}}{\partial \mu_\alpha} = x_\alpha^0 + \sum_i \Delta N_\alpha^i m_i \exp\left(\frac{E_c^i}{k_B T} \right) \prod_\alpha \exp\left(\frac{\Delta N_\alpha^i \mu_\alpha}{k_B T} \right), \tag{1.36}$$

where $x_\alpha = N_\alpha / N_A^0$, $x_\alpha^0 = N_\alpha^0 / N_A^0$, and $m_i = M_i / N_A^0$. Either the concentration is known and we solve for the chemical potential of species or vice-versa.

Counter terms

Counter terms refer to additional terms introduced in the expression for the free energy to account for the spatial frustration effects resulting from the number of lattice sites already occupied by solute/point defect clusters. These counter terms are necessary to capture the energetic effects related to system frustration. For a detailed explanation of counter terms we refer to the appendix B of the work of Schuler et al. [79]. Note that for the scope of this work, we decide to neglect counter terms because we assume the concentrations of point defects introduced in our systems is very low.

1.3.5 Phase diagram

Phase diagrams are important tools in materials science and engineering as they provide a graphical representation of the composition-temperature-pressure domains of stability of phases.

Once we obtain the Gibbs free energies using a combination of previously described methods, we proceed to construct the temperature-composition phase diagram at zero pressure. We first explain how to construct the phase diagram in the case we have line compounds with the convex hull of stability and then we explain how to construct it in the case we have off-stoichiometry compounds with the common tangent construction.

Convex hull of stability

In the case we do not consider the off-stoichiometry of phases and work with line compounds only, we can use the convex hull of stability to construct the phase diagram (similar to what they do in the work of Chevrier et al. [41]).

From a thermodynamic point of view, the formation energy of a compound refers to the energy change associated with the formation of that compound from its constituent elements in their standard states. It quantifies the thermodynamic stability of the compound and provides insight into the energetics of its formation. Under the assumption that we have Si and Li reservoirs we calculate the formation energies at 0 K (E_f) per atom of Li-Si phases from DFT 0 K energies (E) as follows:

$$E_f(\mathrm{Li_xSi_{1-x}}) = E(\mathrm{Li_xSi_{1-x}}) - \mathrm{x}E(\mathrm{Li}) - (1-\mathrm{x})E(\mathrm{Si}). \tag{1.37}$$

To consider the finite temperature effects in the formation energies we can include the contributions then we need to replace E by temperature dependent $E^T = E + E^T_{vib}$. Notice that here we do not name E^T because configurational entropy is not accounted for yet.

The convex hull of stability, in the context of thermodynamics, refers to the graphical representation of the stable phases or compositions of a system under specific thermodynamic conditions. It is a fundamental concept used to understand and analyze the stability of different phases or compositions in a given thermodynamic system. In a multi-component system, the stability of different phases is influenced by factors such as temperature, pressure, and composition. The convex hull represents the thermodynamically stable regions in the temperature-composition space generally at zero pressure. Hence, it is a great and facile tool to build phase diagrams of line compounds.

By plotting the formation energy per atom of compounds against their composition we can construct the convex hull of stability [46, 44, 41]. We connect the stable phases by lines, thus stable phases are represented by the points lying on the edges or vertices of the convex hull. These points correspond to the equilibrium states of the system at the given thermodynamic conditions. Phases or compositions lying within (above) the convex hull are not thermodynamically stable under those conditions.

There are different algorithms that can be used to construct the convex hull, such as the Graham's scan algorithm. Here, we will provide an overview of the steps involved in the Graham's scan algorithm, which is commonly used for constructing the convex hull:

1. Select the point with the lowest y-coordinate (or the leftmost point in case of a tie) as the starting point of the convex hull
2. Sort the remaining points in counterclockwise order with respect to the starting point. This can be done by calculating the polar angle of each point with respect to the starting point
3. Initialize an empty stack and push the starting point onto the stack
4. Iterate over the sorted points. For each point, check if it makes a left turn or a right turn with the top two points on the stack. If it makes a left turn, push the point onto the stack. If it makes a

right turn, pop points from the stack until a left turn is formed or the stack is empty, and then push the current point onto the stack

5. Once all the points have been processed, the stack contains the points on the convex hull in counterclockwise order.

6. Connect the points on the convex hull to form the edges or vertices

This algorithm ensures that the points connected form a convex polygon that encloses all the stable phases or compositions. It eliminates any concave sections and connects the outermost points to create the convex hull.

Common tangent construction

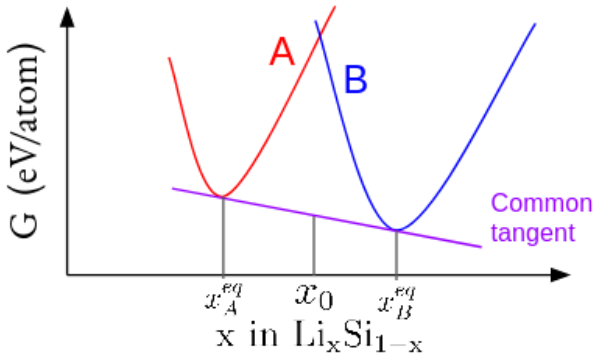

Figure 1.11: Schematic representation of the off-stoichiometry Gibbs free energies of two phases (A and B) and their common tangent. The equation of the common tangent is $y_t = (\mu_{\mathrm{Li}} - \mu_{\mathrm{Si}})x + \mu_{\mathrm{Si}}$.

At equilibrium, we easily show from the differential dG that chemical potential of every species must be equal in every phase in equilibrium. The common tangent construction is a graphical method used to determine the composition and proportion of phases present in a binary system at a given temperature. It yields the equilibrium composition of phases and the boundary limits of a two-phase-equilibrium. The phase diagram of solid phases typically consists of a temperature axis and a composition axis because pressure has generally negligible effects on the boundary limits. The common tangent construction gives the composition of each phase and their proportions (lever rule) at a specific temperature within the two-phase region.

Let phase $\alpha \equiv \mathrm{Li}_{x_\alpha}\mathrm{Si}_{1-x_\alpha}$, where x_α is the number of Li atoms divided by the total number of atoms and x_α belongs in the domain of off-stoichiometry of phase α; after equation 1.3, the Gibbs free energy of α per atom is written as $G(\alpha) = x_\alpha\mu_{\mathrm{Li}} + (1 - x_\alpha)\mu_{\mathrm{Si}}$. Fig. 1.11 depicts how from the off-stoichiometry Gibbs free energies per atom of phases A and B, at fixed temperature, we can construct the common tangent. From the common tangent we can obtain the off-stoichiometry compositions at which phase A is in a two-phase-equilibrium with phase B as well as the chemical potentials at which we have this two-phase-equilibrium. The points of intersection of the tangents with $G(A)$ and $G(B)$ give us the equilibrium compositions (denoted x_A^{eq} and x_B^{eq} in Fig. 1.11) corresponding to the boundaries of the two-phase-equilibrium. At a nominal composition x_0 between x_A^{eq} and x_B^{eq}, the minimum of Gibbs free energy will correspond to a mixture of both A and B phases. To calculate the proportion of each phase, we apply the lever rule (explained later in this section). The slope of the common tangent line $(\mu_{\mathrm{Li}} - \mu_{\mathrm{Si}})$ gives us the alloy chemical potentials at equilibrium.

To be able to construct the phase diagram between the region of A and B phases as a function of temperature and composition, we must construct the common tangent (whenever possible) at all temperatures.

Lever rule

With the help of Fig. 1.11 we write the proportions of phases A (p_A) and B (p_B) at chosen atomic fraction x_0 (in the two-phase-equilibrium) and at a particular temperature:

$$p_A = \frac{x_B^{eq} - x_0}{x_B^{eq} - x_A^{eq}},$$
$$p_B = \frac{x_0 - x_A^{eq}}{x_B^{eq} - x_A^{eq}}.$$

1.3.6 CALPHAD

As shown previously, one of the most popular methods used for constructing phase diagram is CALPHAD (Calculation of Phase Diagrams) [42, 53]. It is a computational approach and methodology used to model and predict phase diagrams of multicomponent materials. It combines thermodynamic data, experimental measurements, and mathematical modeling to calculate the Gibbs free energy.

In CALPHAD, the Gibbs energy of the pure element i (e.g. Li or Si) in phase ϕ may be expressed as

$$\begin{aligned} G_i^{\phi}(T) =& G_i^{\phi}(T) - H_{\mathrm{i}}^{\mathrm{SER}} \\ =& A + BT + CT\ln T + DT^2 + ET^3 + FT^{-1} + GT^7 + HT^{-9} + IT^4 + J\ln T \end{aligned} \tag{1.38}$$

where H_i^{SER} is the molar enthalpy of the element i at 298.15 K and 1 bar in its standard element reference (SER) state. T is the absolute temperature. $G_i^{\phi}(T)$ is Gibbs energy function (e.g. for Li and Si) above 298 K and could be taken from the Scientific Group Thermodata Europe (SGTE) [84].

For the Li-Si system with a phase $\mathrm{Li_mSi_n}$, the Gibbs free energy in terms of temperature would read as:

$$G(\mathrm{Li_mSi_n}, T) = A^* + BT + CT\ln T + DT^2 + ET^3 + FT^{-1} + GT^7 + HT^{-9} + IT^4 + J\ln T, \tag{1.39}$$

where

$$A^* = A + \mathrm{m}G_{\mathrm{Li}}^{\mathrm{BCC}}(298.15\ \mathrm{K}) + \mathrm{n}G_{\mathrm{Si}}^{\mathrm{diamond}}(298.15\ \mathrm{K}) \tag{1.40}$$

Coefficients C, D, E, F, G, H, I and J are determined from the temperature dependence of the heat capacity, C_p, for each individual compound:

$$C_p = -C - 2DT - 6ET^2 - 2FT^{-2} - 42GT^6 - 90HT^{-10} - 12IT^3 + JT^{-1} \tag{1.41}$$

The Gibbs free energies of pure elements at 298.15 K in Eq. 1.40 correspond to the SER reference state from Eq. 1.38. Coefficients A^* and B from Eq. 1.39 for the temperature range $T > 298$ K are optimized for all stoichiometric phases considering the critically assessed experimental thermodynamic data.

The Gibbs energy functions of all solid phases for the temperature ranges below 298 K are subsequently determined in a similar procedure. From Eq. 1.41, validated by direct experimental C_p data, for that

phase and temperature range, the coefficients C, D, E, F, G, H, I, and J are determined. Coefficients A^* and B in Eq. 1.39 are then determined from a continuity constraint for enthalpy and entropy and, thus, also for $G = H - TS$, at the top end temperature, T°, of that range.

Previously reported Li-Si phase diagrams [42, 37, 38, 53] have assessed their solid state data from: the chemical potential for the solid phase equilibria (at high temperatures) determined by Wen and Huggins [35] and Sharma and Seefurth [34], the heat capacity data for the compounds from Thomas et al. [43], and equilibrium compositions on highly lithiated phases given by Zeilinger and coworkers [51, 52, 50, 49]. The solid-liquid boundary limits have been also assessed from various experimental equilibrium compositions (see the dots of Fig. 1.5a).

Even though CALPHAD has been used to investigate non-stoichiometric metallic systems (e.g. Fe-O in [85]), for Li-Si systems it has not been the case yet, to the best of our knowledge. It is understandable given the difficulties of characterizing and modeling non-stoichiometric phases such as complex atomic arrangements, including defects, and Li ordering. Describing these structural complexities accurately within CALPHAD models is challenging, as they require advanced techniques beyond the scope of traditional CALPHAD approaches. Moreover, as previously shown, Li ordering is not easily detectable with XRD making the experimental assessment of CALPHAD with non-stoichiometric Li-Si systems even more difficult.

1.3.7 Open circuit voltage

Voltage is equal to the electric potential difference between two points in an electric circuit and it is measured in Volts (V). The difference in electric potential between two electrodes is actually the potential difference arising from the difference in Gibbs free energy of the chemical reactions. In a system where the electrochemically active species is Li, capable of giving its valence electron (e^-), the redox chemical formula reads:

$$\mathrm{Li} \rightleftharpoons \mathrm{Li^+} + \mathrm{e^-} \tag{1.42}$$

The electrochemical potential is a thermodynamic measure of chemical potential that includes the energy contribution of electrostatics. The electrochemical potential of Li is in fact the chemical potential of Li^+, it may be divided into two terms: first term containing the chemical potential of Li, and a second term containing the local electrostatic potential Φ. In any electrode, according to the Nernst equation, it would read as :

$$\mu_{\mathrm{Li^+}}^{electrode} = \underbrace{\mu_{\mathrm{Li}}^{o} + k_B T \ln a_{\mathrm{Li}}}_{\mu_{\mathrm{Li}}^{electrode}} + e\Phi, \tag{1.43}$$

where μ_{Li}^{o}, k_B, T, a_{Li}, e are the reference chemical potential of Li, Boltzmann constant, the absolute temperature, the activity of Li, and the charge of an electron, respectively. The electrode can be the anode or the cathode.

In the case we have equilibrium state, a battery has no current flow and it means that the electrochemically active species does not have a flux. This means that the chemical potential of Li^+ is the same in both electrodes ($\mu_{\mathrm{Li^+}}^{anode} = \mu_{\mathrm{Li^+}}^{cathode}$). Therefore, we can obtain the electrostatic potential difference $\Delta\Phi = \Phi^{anode} - \Phi^{cathode}$ as a function of the chemical potential difference of Li:

$$\Delta\Phi = \frac{\mu_{\mathrm{Li}}^{cathode} - \mu_{\mathrm{Li}}^{anode}}{e}. \tag{1.44}$$

During discharge or charge, current continues to flow; hence, the system is not at equilibrium. However, in the case we are at a constant OCV, the system is at equilibrium and therefore Eq. 1.44 can be used for steady state OCV. From a thermodynamic point of view, voltage measurements gives us access

to thermodynamic variables as shown in Fig. 1.12. In the case we have a Li_xSi compound the chemical potential of Li is related to its Gibbs free energy per Si $G(Li_xSi)$ by the following relation:

$$\mu_{Li} = \frac{\partial G(Li_xSi)}{\partial x}. \tag{1.45}$$

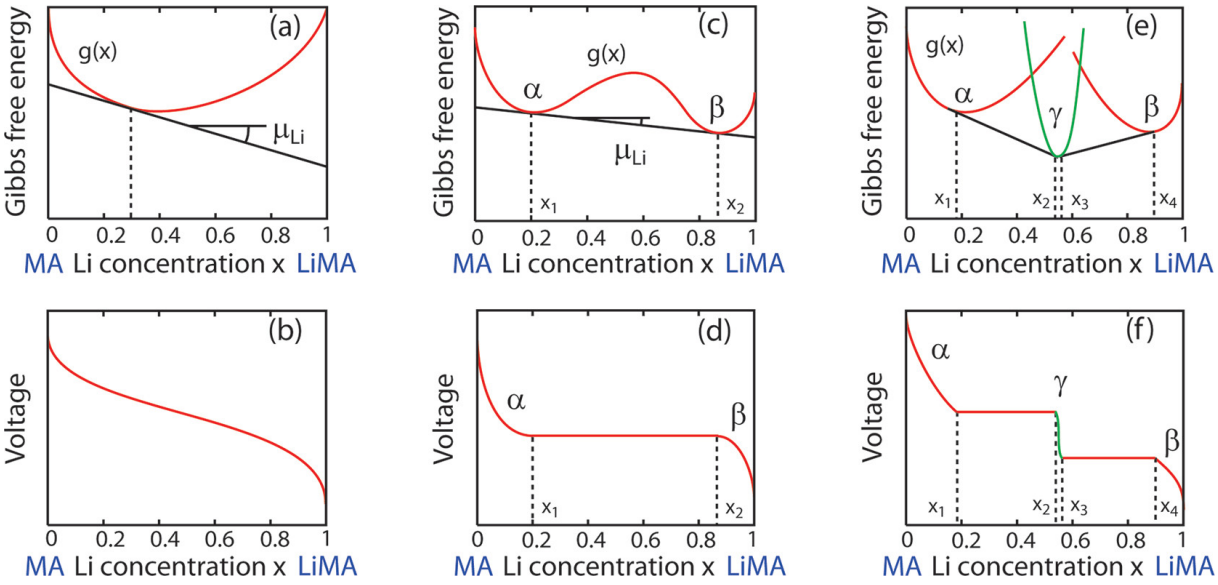

Figure 1.12: Plots showing how voltages are linearly related to the slopes of the Gibbs free energies. Image taken from the work of Van der Ven et al. [86].

The OCV is an important observable related to Li batteries because the experimentally reported electric profiles show the OCV of a battery as a function of the anode Li content [35]. And the OCV can be measured in various scenarios as shown in Fig. 1.12, for example: in the case of a two-phase-equilibrium like shown with α and β phases in sub plots (c) and (d); or in the case of single phase domain like what with happens with γ phase in sub plots (e) and (f).

Many works have calculated the average cell potential, disregarding the off-stoichiometry of phases (shown to be of importance with the γ phase in Fig. 1.12), from a two-stoichiometric-phase reaction from reactant to product (Li_xSi + (y-x)Li $\rightarrow$ Li_ySi) [46, 87, 45] at 0 K as follows:

$$OCV = -\left[\frac{G(Li_ySi) - G(Li_xSi)}{y - x} - G(Li)\right], \tag{1.46}$$

where $G(Li)$ stands for the Gibbs free energy per Li of Li and is the reference chemical potential of Li. The aforementioned works, assume that the drops during single phase equilibrium are sharp (like shown in Fig. 1.13). As a first step in this study, we will rely on the same assumption but also including finite temperature effects from vibrational entropy contribution in Chapter 2 (where we do line compound studies) for comparison.

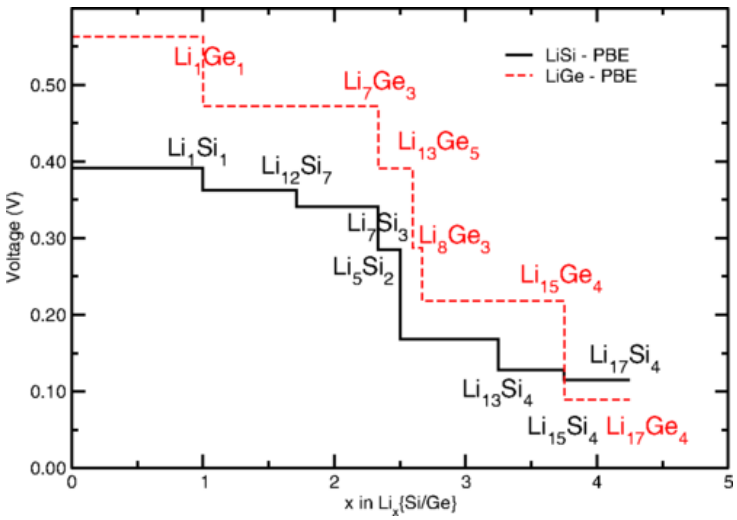

Figure 1.13: Example plot of OCV profile where the off-stoichiometry is disregarded and the drops from OCV plateau to another OCV plateau are sharp. Image taken from [45].

1.3.8 Galvanostatic intermittent titration technique

The Galvanostatic intermittent titration technique (GITT) is an electrochemical technique that applies a small constant current (i.e. galvanostatic) pulse for a short duration on a galvanic cell followed by a rest period (i.e. interminent). The GITT allows us to quantify the amount of ion content being inserted in the anode from the cathode (i.e. titration) and to measure the corresponding voltage. Weppner and Huggins first developed the GITT method in 1977 for kinetic parameter investigation in Li-Sb compounds [88].

For GITT, the designed cell comprises a pure compound of the mobile species (i.e. Li), an electrolyte, and a hosting electrode (i.e. Si) as portrayed in Fig. 1.14. The GITT is based on the idea that the number of ions entering/exiting the hosting electrode (through the electrolyte) can be calculated from the current [88]. In other words, for each electron that goes through the external circuit, one Li atom is being removed or inserted in the Si electrode depending on the current direction due to the electroneutrality condition (i.e. to keep the system neutral). It is worth remarking that this is an approximation that can lead to inaccuracies on Li nominal composition in the Si electrode, as previously mentioned in the experimental limitations.

One example of galvanostatic titration step during lithiation or delithiation is illustrated in Fig. 1.15. When a constant current pulse $|I_{applied}|$ is allowed at time t_0 for a period τ Li ions are being inserted/removed from the Si host electrode. Imposing a constant current corresponds to imposing a constant flux of the Li mobile species, thereby a constant gradient of chemical potential of Li. If we assume Li is the only mobile species, $\nabla\mu_{\mathrm{Li}}$ can be reduced to gradient of Li concentration, and we can use the Fick's law. To maintain charge neutrality of the electron and Li^+ species in the redox reaction (Eq. 1.42) of the electrode $|I_{applied}|$ can be expressed as following using Fick's first law [88]:

$$I_{applied} = \left(-\tilde{D}\left.\frac{\partial c_{\mathrm{Li}}}{\partial x}\right|_{x=0}\right) S z_{\mathrm{Li}}|e| = j_{\mathrm{Li}} S Z_{\mathrm{Li}}|e|, \tag{1.47}$$

where $\tilde{D}$ is the chemical diffusion coefficient of Li (to be explained more later with the thermodynamic factor), c_{Li} is the concentration of Li, x is the distance coordinate (portrayed in Fig. 1.14), S is the surface area of the electrode in contact with the electrolyte, $z_{\mathrm{Li}} = 1$ is the charge number (i.e. the amount of electrons that Li donates/receives during redox), and e is the charge of an electron. Note that

the parenthesis enclosed term is the flux of Li species at x=0 (j_{Li}). It can be expressed as a function of the electrochemical potential of Li (Eq. 1.43). In the case of an isothermal and adiabatic system where the Onsager's cross-coefficients are negligible the flux reads as [88]:

$$j_{\mathrm{Li}} = -\frac{\sigma_{\mathrm{Li}}}{z_{\mathrm{Li}}^2|e|^2}\left.\frac{\partial \mu_{\mathrm{Li}}}{\partial x}\right|_{x=0}, \tag{1.48}$$

where σ_{Li} is the partial electrical conductivity due to the transport of Li. It may also be expressed as:

$$\sigma_{\mathrm{Li}} = z_{\mathrm{Li}}|e|c_{\mathrm{Li}}u_{\mathrm{Li}}, \tag{1.49}$$

where u_{Li} is electrical mobility and it refers to the ability of charged particles (such as electrons or ions) to move in response to an electric field. It is a measure of how easily and quickly the charged particles can move through a medium or material. It is expressed in units of square meters per volt-second ($\mathrm{m^2/Vs}$).

In Fig. 1.15, we show that at the same time the constant current is applied, a drop/increase in voltage happens reaching E_{meas}. During the relaxation period (i.e. the circuit is not longer under applied current) the Li will diffuse and accommodate in the Si electrode to reach an equilibrium that is observed in voltage as E_{eq}. From this E_{eq} another galvanostatic step can occur and so on. In the case we have a two-phase-equilibrium in the system, the same E_eq should be reached for several consecutive galvanostatic steps. Whereas if we have a single phase domain, the E_eq would vary between consecutive galvanostatic steps.

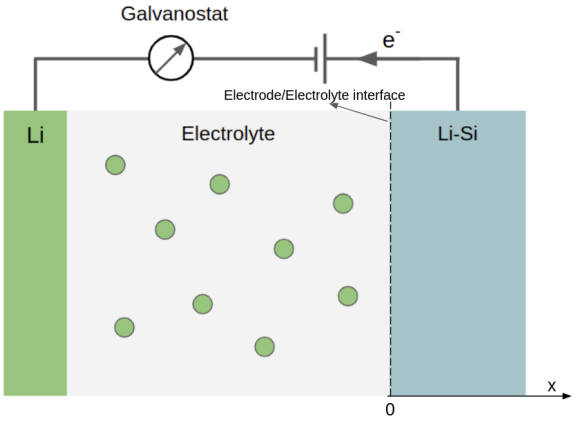

Figure 1.14: Schematic representation of galvanic cell used for GITT. The galvanostat keeps the current constant.

As mentioned above, the GITT is a method for measuring voltage at both transient (during current supply) and equilibrium (during OCV) states. With this in mind, thermodynamics can be retrieved and used to analyze de material properties as a function of Li nominal composition. It is actually the OCV states that provide key information on the thermodynamic properties of the cell (see Sec. 1.3.7). It is actually worth remarking that due to the slow kinetics at room temperature the GITT measurements of a whole voltage profile cycle can take a lot of time to be performed. For instance, some GITT works have shown that long waiting times up to two months may be required to reach an equilibrium (E_{eq}) in some electrodes [89, 90].

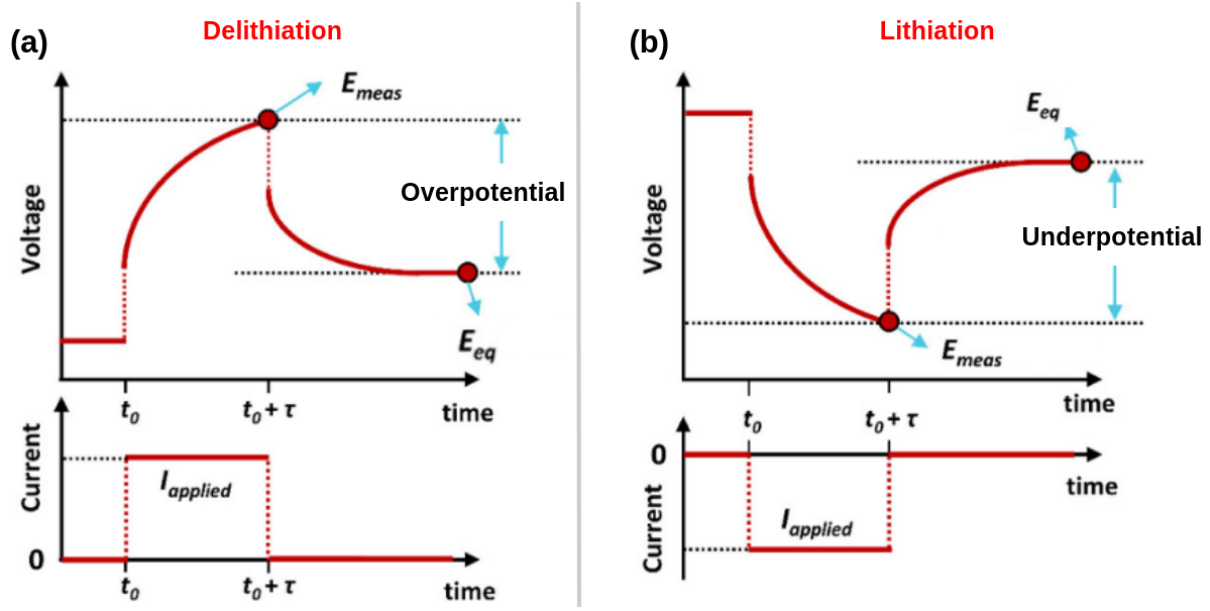

Figure 1.15: Plot of the voltages and currents during of one galvanostatic step of (a) delithiation and (b) lithiation.

Because GITT also provides time-dependent voltage, we can also calculate other important information such as the overpotential/ underpotential during delithiation/lithiation (shown in Fig. 1.15). These come from the aftermath of a sequence of reaction steps such as adsorption, mass transfer, charge transfer processes from a kinetic point of view, and internal resistance [90]. Each of the aforementioned phenomena is a contribution to the over/underpotential and what we are able to observe with the GITT is the total. We can also have an estimate of the internal resistance (R) which comes from the sudden drop/increase observed during applied current regimes (proportional to $I_{applied} \times R$). The underpotential and overpotential absolute values (η) read as:

$$\eta = |E_{meas} - E_{eq}|. \tag{1.50}$$

In other terms, η is the value of the difference of the chemical potential of Li between closed circuit voltage resulting from imposed current and equilibrium OCV. As we will show later in Chapter 4, it is tightly related to the selection of the precipitating secondary phases.

Thermodynamic enhancement factor

By adding Eq. 1.43 and Eq. 1.49 to Eq. 1.48, the flux density reads:

$$j_{\mathrm{Li}} = -\frac{k_B T u_{\mathrm{Li}}}{z_{\mathrm{Li}}|e|}\left[\frac{\partial \ln a_{\mathrm{Li}}}{\partial \ln c_{\mathrm{Li}}}\frac{\partial c_{\mathrm{Li}}}{\partial x} + \frac{z_{\mathrm{Li}} q c_{\mathrm{Li}}}{kT}\frac{\partial \Phi}{\partial x}\right]. \tag{1.51}$$

The factor in front of the bracket has the dimensions of a diffusion coefficient and it corresponds to the diffusion coefficient D of Li as a component. In the electrode, the inner electrostatic potential is constant and therefore $\partial\Phi/\partial x = 0$. Therefore, Eq. 1.51 becomes:

$$j_{\mathrm{Li}} = -D\left[\frac{\partial \ln a_{\mathrm{Li}}}{\partial \ln c_{\mathrm{Li}}}\right]\frac{\partial c_{\mathrm{Li}}}{\partial x}. \tag{1.52}$$

The term inside the brackets is known as the thermodynamic enhancement factor (ϕ) [35, 88]. The thermodynamic enhancement factor enhances the chemical diffusion coefficient of the diffusive species. The chemical diffusion coefficient, $\tilde{D}$ (as shown in Eq. 1.47), is related to the diffusion coefficient D from the following relation:

$$\tilde{D} = \phi D. \tag{1.53}$$

The enhancement factor, as previously mentioned by Weppner and Huggins, can be determined from the local slope of the coulometric titration curve at any composition [88, 35]:

$$\phi = \frac{d\ln a_{\mathrm{Li}}}{d\ln(\mathrm{p})} = -\frac{F}{RT}(\mathrm{p})\frac{dE}{d\mathrm{p}}, \tag{1.54}$$

where p, F, R, T, and E, are the Li concentration in $\mathrm{Li_pSi_m}$, the Faraday constant , the gas constant, the absolute temperature, and the voltage, respectively.

The work of Wen and Huggins calculate this property at 690 K during the single phase domains to observe where in composition the maximum of the thermodynamic factor occurs which they associate to the perfect stoichiometry of the phase [35]. But might not necessarily be the case, since experimental errors might appear if the electrochemically active species are not exclusively used to change the stoichiometry of the sample during the titration [88] (e.g. silicon defects could change the stoichiometry and they are not the electrochemically active species).

1.3.9 Classical nucleation theory and beyond

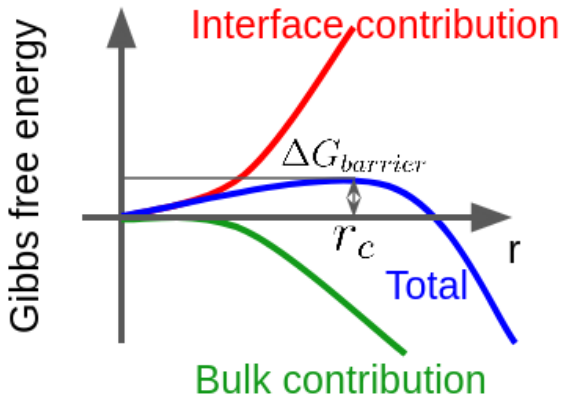

Figure 1.16: Plot of the Gibbs free energy of the system as a function of secondary phase nucleus radius (r). The critical radius, r_c, denotes the radius size at which the nucleus has the greatest Gibbs free energy. The nucleation barrier is denoted as $\Delta G_{barrier}$.

In the following section we will describe the thermodynamic aspect of the classical nucleation theory.

Precipitation of a secondary phase may occur when the initial parent phase is place into the region of the phase diagram where the parent phase should coexist with the secondary phase. Before the decomposition starts, in the case of (de)lithiation the parent phase is a non-equilibrium system under/supersaturated in Li. Note that in these systems, under/supersaturation is directly related to the excess of point defects. The parent phase, being excited, would rather evolve towards a more stable state in order to reach equilibrium. As the parent phase is stable, the continuous creation of point defects in

the whole phase is not possible. Such perturbations would increase the free energy, and they can actually appear (e.g. during de/lithiation or because of thermal fluctuations). However, once these perturbations appear the natural reaction of the system is to relax towards its equilibrium state. The system, therefore, has to overcome an energy barrier to reach its equilibrium to be able to form new clusters of the new phase directly. This is the process known as nucleation.

The Gibbs free energy of the secondary-phase nucleus is ruled mainly by two contributions. The first one is a bulk contribution proportional to the volume of the secondary phase. This contribution is in fact decreasing the Gibbs free energy. When calculated per atom, it is proportional to the nucleation driving force Δg. The second contribution is the surface contribution. This contribution contrary to the bulk one increases the Gibbs free energy of the nucleus because there is a cost that comes from the interface between the parent phase and the new phase. In the simplest treatment, the Gibbs free energy barrier, $\Delta G_{barrier}$, is obtained at the maximum value of the Gibbs free energy as a function of radius size. The radius size giving the maximum of the Gibbs free energy is also known as the critical radius (r_c). At this radius, the probabilities on the nucleus to reduce or increase in size are equal.

Both the interface energy and bulk energy (the nucleation driving force) contributions are essential for calculating both the Gibbs free energy barrier and as a result the nucleation rate (this part corresponds to the kinetics of nucleation) [91].

The thermodynamic nucleation driving force is thus essential for the analysis of phase transformation in materials. So for the scope of this work, we are mainly concerned with studying the magnitude of the nucleation driving force which can explain why some phases can nucleate over others. Let us imagine the formation of a new Li-Si phase β from a parent Li-Si phase α. The driving force for nucleation can be quantified from the Gibbs free energy from dN molecules of supersaturated α phase transfered to the precipitate β phase.

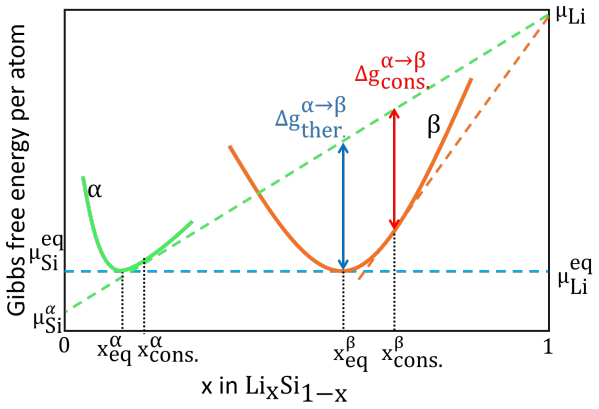

Figure 1.17: Plot of the Gibbs free energies of α and β phase as a function of composition. We portray both the driving force under thermodynamic conditions and constrained chemical potential of Li.

The nucleation driving forces from parent α phase to precipitate β phase, $\Delta g^{\alpha\to\beta}_{therm.}$ and $\Delta g^{\alpha\to\beta}_{cons.}$, are schematically represented in Fig. 1.17. The nominal composition x^i_{eq} such that $i = \alpha, \beta$, represents the nominal composition at which α and β phases are at thermodynamic equilibrium. If the parent phase α is put supersaturated with nominal composition $x^{\alpha}_{cons.}$ and chemical potential μ_{Li} , that means that it has the ability to nucleate the β phase as explained previously. On the one hand, it can nucleate the β phase at thermal conditions with $\Delta g^{\alpha\to\beta}_{ther.}$ nucleation driving force and thermodynamic equilibrium chemical potentials. On the other hand, if we consider Si are immobile, the resulting two-phase state is not an equilibrium state because Si atoms have not the same chemical potential in both phases.

In that case the parent phase α can nucleate into secondary phase β under constrained μ_{Li} (chemical potential of the excited parent phase) with $\Delta g_{cons.}^{\alpha \to \beta}$ nucleation driving force. This constrained nucleation thermodynamic modeling has already been worked in the Li-Sb system by Chang et al. [92] to explain how some thermodynamically stable phases can be skipped during delithiation. Such study requires the computation of variation of chemical potentials of Li and Si with the Li supersaturation. We will tackle it with much greater detail later in Chapter 4 for Li-Si systems.

1.4 Conclusion

In this chapter, we provided a brief overview of the working principle of Li-ion batteries and examined the various components involved. We then explored the potential benefits of using silicon as a negative electrode. Although significant advancements have been made in enhancing the performance of silicon-based electrodes, there are still obstacles to overcome before commercializing Li-ion batteries with these electrodes.

We have also provided enough evidence as to why understanding the Li-Si alloying process is important as part of enhancing these systems. It is important to recall that unlike in other anodes like graphite where we have (de)intercalation of Li, the Si based anode undergoes a volume expansion/shrinkage due to phase transformations during lithiation/delithiation. Major problems happen due to these volume changes like: the constant breaking and build up of solid electrolyte and the delamination of Si particles from the electrode. Both of which cause a major drop in capacity during voltage cycling. We have emphasized from the literature that the formation of certain phases like crystalline $Li_{15}Si_4$ can be problematic for cycling, so understanding its formation over other crystalline phases can be key in enhancing the cyclability of Si based anodes.

We have pinpointed the disagreement between different studies (e.g. between experimental ones or between experimental and theoretical ones) on the stability of phases (i.e. phase diagrams). We remark that even the latest assessed phase diagrams in Li-Si systems do not consider the off-stoichiometry of Li-Si phases which we showed are important to consider for the kinetics of phase transition.

We also presented in this chapter the methodology needed in the scope of this work. We emphasized on the relationship between theoretical methods and those from the experiment (GITT).

We noticed that assessment of the Si-Li thermodynamic model on the measured off-stoichiometric variation of OCV [35] is missing and the off-stoichiometric contribution in current Li-Si phase diagrams [53, 42] is absent. This is why for this work, we have decided to take on the challenge of including the off-stoichiometry modeling of Li-Si phases in order to have a better understanding and perhaps provide an insight in the ongoing disagreement in the literature and partially answer the open questions on the selection o phases in Si-Li upon (de)lithiation.

Chapter 2

Perfectly ordered Li-Si line compounds

In this chapter we present a detailed study of finite temperature effects in ordered phases. Our attempt here is to predict the stability of phases at their perfect stoichiometric composition, to understand the contribution of the vibrational entropy in these phases, and to assess our finite temperature prediction of thermodynamic quantities. We aim at obtaining our own results of all the data that is not available as presented in table 1.1.

First, we start by the calculation of the convex hull of stability at 0 K without zero point energy (ZPE) where we present newly discovered phases of this work. Second, we present section by section the compounds for which we performed the harmonic (HA) and quasi-harmonic (QHA) phonon calculations to add vibrational contribution to the entropy at isochoric (S_v) and isobaric (S_p) conditions, as well as, to the enthalpy. Third, we construct again the convex hull of stability at finite temperatures. Fourth, we study the atomic volume expansion as a function of temperature and composition. Finally, we present the open circuit voltage (OCV) coming from the study of perfect ordered phases at finite temperatures.

We analyse the phonon density of states (PDOS) of each compound because the presence of imaginary (represented as negative in the plots to come) frequencies can tell us if the phase in question is a stable one or if the parameters of the HA/QHA calculations are not converged. We also compare our calculated thermodynamic quantities such as the G, S and heat capacity (C) with previously theoretical and experimental published results for further validation.

Before diving into this chapter, we refer the reader: to the section on thermodynamics in Chapter 1 (1.3.1) for basic, yet important definitions; to the publication of the PHONOPY code [73] or section 1.3.3 for a resume of what is needed to understand from it; and last but not least, to section 1.3.6 for a detailed description of the CALPHAD model that we used to compare our results with in this chapter.

2.1 Table of previously reported compounds in this work

We list in table 2.1 some crystallographic data of the phases shown in the Si-Li phase diagram [42, 53, 55]. In addition to these phases, we add the phases that have a crystallographic relationship with Li_7Si_3 (i.e. Li_5Si_2). The Li_7Si_3 is a vacancy superstructure of the Li_5Si_2 phase, as reported by [44] (see Fig. 2.3 for more information). Similarly, $Li_{21}Si_5$ and $Li_{17}Si_4$ are vacancy superstructures of $Li_{22}Si_5$ therefore they are related and we describe this later in Sec. 3.5. Other phases such as Li_3Si_2, Li_2Si, Li_3Si, Li_7Si_2 and Li_4Si are metastable phases at 0 K reported by [46] (for more crystallographic information on them we refer to the article). The complete structures are reported in the CIF file format in appendix C.

Phase	**x in Li_xSi_{1-x}**	**x in Li_xSi**	**Space group**	**Lattice parameter (Å)**	**Volume (Å^3)**	**Number of atoms**	**Number of Wyckoff sites**	**Ref.**
Si	0	0	$Fd\bar{3}m$	a=5.43	160.103	8	1	[93]
LiSi	0.5	1	$I4_1/a$	a=9.3545(5) c=5.7374(5)	502.06	32	2	[94]
$Li_{12}Si_7$	0.631	1.714	$Pnma$	a=8.600 b=19.755 c=14.33	2434.57	152	22	[95]
Li_9Si_4	0.692	2.25	$C12/m1$	a=12.283 b=4.38 c=7.534	396.7157	26	7	[46]
Li_7Si_3	0.7	2.33	$P3_212$	a=8.886 c=18.134	1240.043	60	11	[96]
Li_5Si_2	0.714	2.5	$R\bar{3}m$	a=4.387 c=17.862	297.7852	7	4	[46]
$Li_{13}Si_4$	0.7647	3.25	$Pbam$	a=7.9488 b=15.1248 c=4.4661	536.9324	34	9	[97]
$Li_{15}Si_4$	0.789	3.75	$I\bar{4}3d$	a=10.6322	1201.90	76	3	[48]
$Li_{21}Si_5$	0.8077	4.2	$F\bar{4}3m$	a=18.71	6549.67	416	16	[98]
$Li_{17}Si_4$	0.8095	4.25	$F\bar{4}3m$	a=18.7259	6566.41	420	17	[49]
$Li_{22}Si_5$	0.814	4.4	$cF432$	a=18.750	6591.797	432	20	[99]
Li	1	1	$Im\bar{3}m$	a=3.5	42.875	1	1	[100]

Table 2.1: Previously reported Li-Si phases that are considered for this work.

2.2 Discovered compounds

In this section we construct the convex hull of stability at 0 K without ZPE using PBE and HSE06 functional using all previously reported-in-literature phases. We also put some phases of our own $Li_{43}Si_{18}$ and $Li_{44}Si_{18}$ that we discovered to be stable perfect ordered compounds at 0 K. Before going into this section the reader must refer to Chapter 1 section on convex hull (Sec. 1.3.5) for more information.

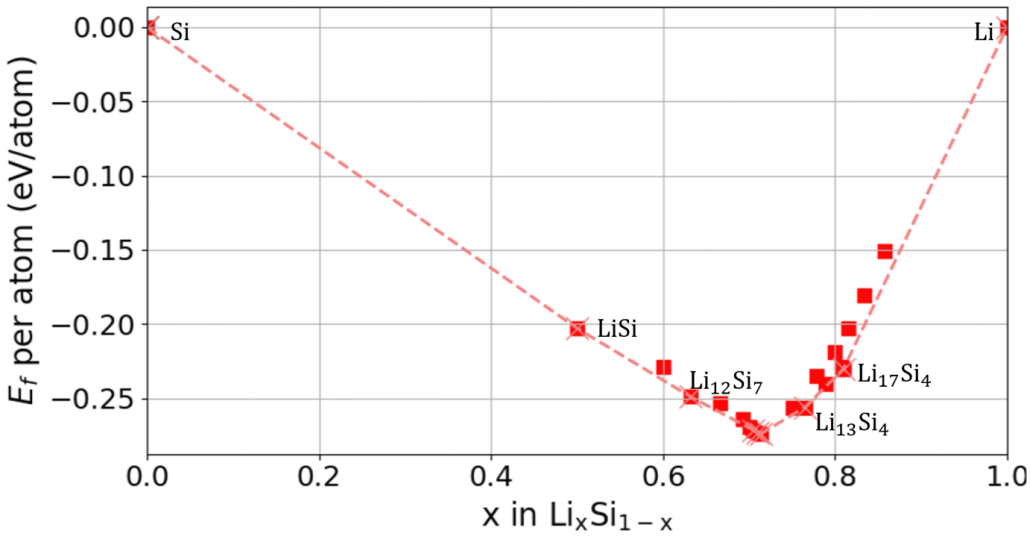

(a) $0 < x < 1$

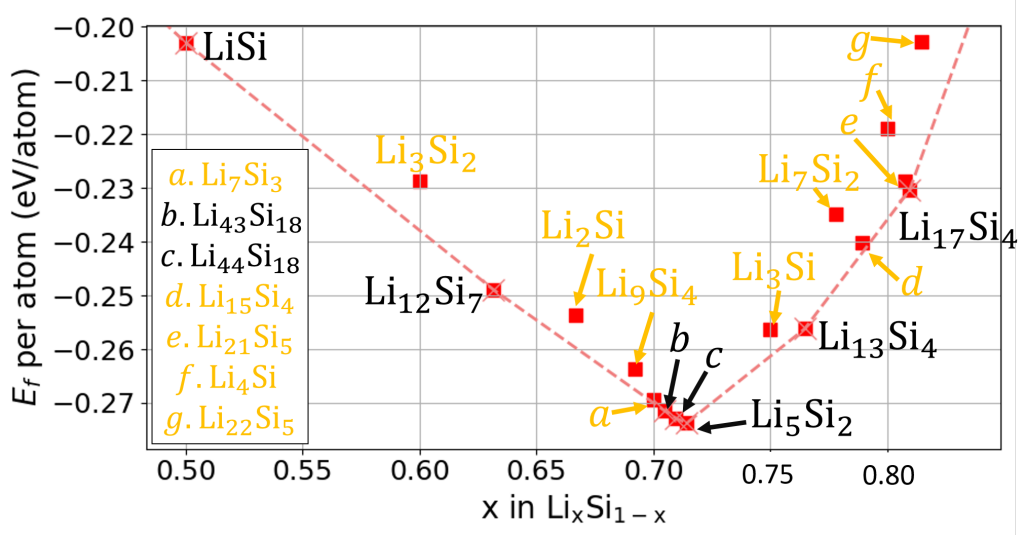

(b) $0.49 < x < 0.85$

Figure 2.1: The formation energies of compounds at 0 K (without zero point energy) using PBE functional vs composition. The red dashed line represents the convex hull of stability joining all the stable phases (from this work) labelled in black. All the other phases above this convex hull are labelled in yellow and are metastable by definition. In (b) the plot is zoomed in the area of interest.

2.2.1 Convex hull of stability at 0 K

From the DFT energies of Li, Si, and Li-Si compounds we can calculate the formation energies (E_f) of Li-Si compounds with metallic Li and diamond Si as energy references at 0 K. Consequently, we construct the convex hull of stability with reference chemical potential of Li and Si reservoirs in Fig. 2.1.

In agreement with [44, 45, 46], we observe in Fig. 2.1 that Li_5Si_2 is a stable phase. Li_7Si_3 is slightly above the convex hull, thereby not stable at 0 K. Our results are in agreement with [53] on $Li_{17}Si_4$ being a stable phase rather than $Li_{21}Si_5$ or $Li_{22}Si_5$ [41, 35] for the fully lithiated phase at 0 K; and last, we are in accord with [41, 46, 45] and the experimental results at 690 K [35] on $Li_{12}Si_7$ and $Li_{13}Si_4$ being stable phases.

The presence of LiSi as a stable phase using PBE functional may arise from the fact that LiSi is metallic with the PBE functional when in reality it is a narrow gap semiconductor (experimental band gap value of 0.057 eV [39]). A previously published work by Paier et al. has shown that atomization energies in solids may vary depending on the functional used [101]. So it is rather important to use the right functional when the material is a semiconductor. Moreover, the work of Stearns et al. shows that this is a high pressure synthesized phase [39], and the work of Wen and Huggins does not mention the existence of this phase at 690 K [35]. To check if the result is an artifact from the PBE functional we redo the calculations at 0 K using the HSE06 functional which is also better at reproducing band gaps of semiconductors. We plot the convex hull of stability again in Fig. 2.2 using the HSE06 functional. We obtain the same stability and metastability as with PBE (Fig. 2.1) except for the LiSi phase that becomes metastable using the HSE06 functional. This result can shed some additional insight in the LiSi inclusion in phase diagrams. For instance, we agree with [42] excluding LiSi and, therefore, disagree with [53]. We know that starting from $Li_{12}Si_7$ included, all phases are metallic; consequently, the computationally cheaper PBE functional can be conveniently used for all phases while ignoring the LiSi phase. Since one of our main interest is to reproduce the off-stoichiometry 690 K results and there is no experimental evidence of LiSi formation at room temperature we may disregard this phase from the sections to come.

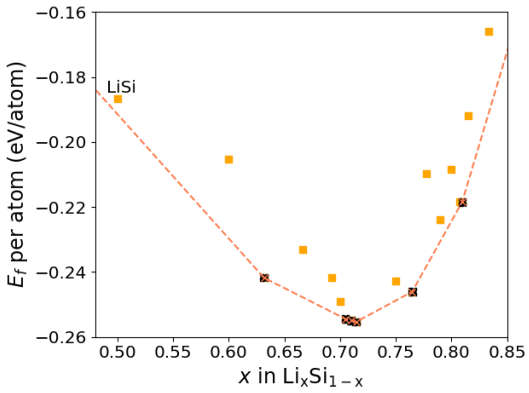

Figure 2.2: The formation energies of compounds at 0 K using HSE06 functional vs composition. The plot is zoomed in the area of interest, at x=0 and x=1 we have Si and Li respectively with $E_f = 0$. The (meta)stability of phases remains the same as in Fig. 2.1 except for LiSi.

Crystallographic studies

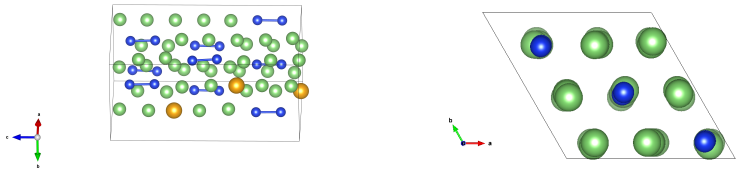

(a) [110] (b) [001]

Figure 2.3: The unit cell ((a) [110] direction, (b) [001] direction) of the generally used and most stable Li_7Si_3 consisting of 9 columns containing 1 Si dumbbell each. Yellow spheres here are used to represent the vacancy sites that Li can potentially fill -they are the 3rd Li site in 3 nearest neighbor columns. If 1, 2, or 3 sites are filled, we have the $Li_{43}Si_{18}$, $Li_{44}Si_{18}$, or the Li_5Si_2 phases, respectively.

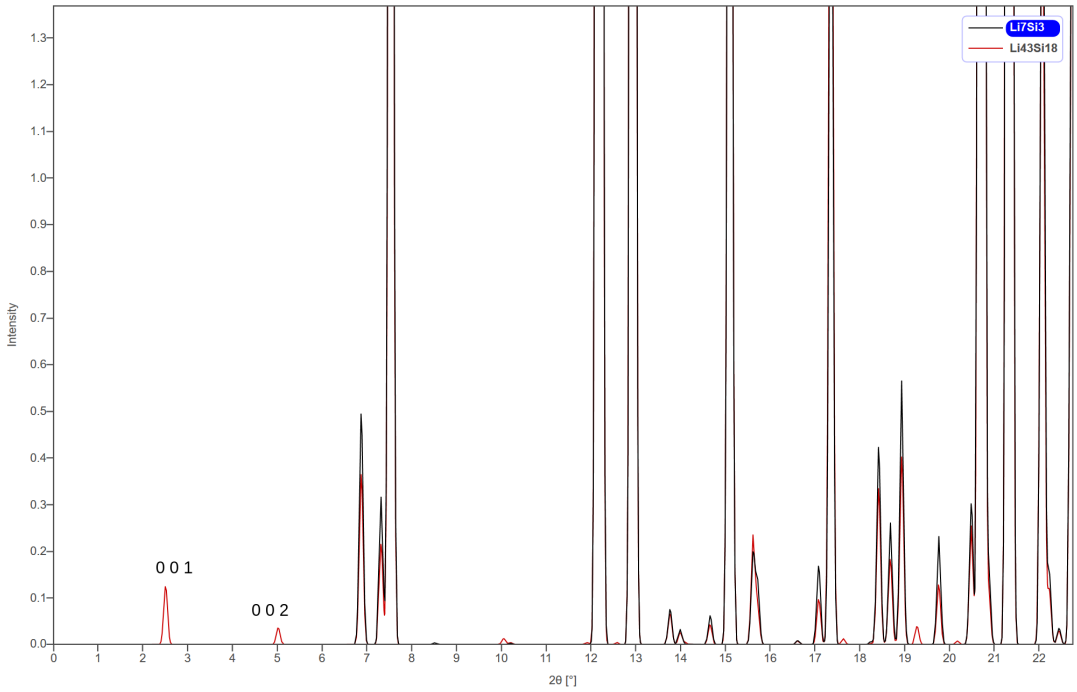

Figure 2.4: Simulated X-ray diffraction pattern (CrystalDiffract©) of Li_7Si_3 (in black) and $Li_{43}Si_{18}$ (in red). Labels of $Li_{43}Si_{18}$ peaks (in hkl index) match the electron scattering labeled spots (Fig. 2.5).

The $Li_{43}Si_{18}$ and $Li_{44}Si_{18}$ phases are, to the best of our knowledge, newly discovered stable phases from this work. They have the same Si sub-lattice as Li_9Si_4, Li_7Si_3 and Li_5Si_2 phases. The Li_7Si_3 structure may be represented as a supercell of Li in which lithium atoms have been removed from certain lattice sites [102]. By choosing different combinations of lithium sites in the supercell, models of Li_7Si_3 can be produced with symmetries. The latter, labeled "#2" by Chevrier et al. [41], is the one used in this

work. We also remark how the metastable Li_9Si_4 (reported by [46]) has been left unnoticed, and the literature lacks how Li_9Si_4 is related to the Li_7Si_3/Li_5Si_2 phase. Li_9Si_4 has the same Si sublattice as both Li_7Si_3 and Li_5Si_2 phases but requires a different Li vacancy sublattice to be formed. $Li_{43}Si_{18}$ and $Li_{44}Si_{18}$ consist of removing 2 and 1 Li, respectively, from the same Li sublattice. In other words, we can say that $6Li_7Si_3 + Li \longrightarrow Li_{43}Si_{18}$ and $Li_{43}Si_{18} + Li \longrightarrow Li_{44}Si_{18}$ -for clarification, we invite the reader to see Fig. 2.3.

We have calculated the theoretical X-ray powder diffraction (using CrystalDiffract© with a Cu K-α radiation) and electron scattering patterns (using SingleCrystal© with 100KeV electrons) in the [110] direction of $Li_{43}Si_{18}$ and compared them to the Li_7Si_3 ones in Fig. 2.4 and 2.5 respectively. We have fixed the lattice parameter of $Li_{43}Si_{18}$ to match the one of Li_7Si_3 since DFT lattice parameters accuracy is already within the differences of these phases. The XRD patterns of both $Li_{43}Si_{18}$ and Li_7Si_3 are almost identical but there are extra peaks around $2\Theta = 2.5°$, $5°$ that correspond to unique peaks of $Li_{43}Si_{18}$ that thanks to the electron scattering we can observe in the form of extra spots that happen in the hkl index of 001 and 002. The intensity of the aforementioned peaks is so small compared to the other peaks that it might not be easily observed experimentally. For instance, Thomas et al. do not compare the peaks below certain intensity; for example, they have a peak with a very small intensity value ($10 < 2\theta < 15$) that they do not compare to the reference pattern of Li_7Si_3 [43].

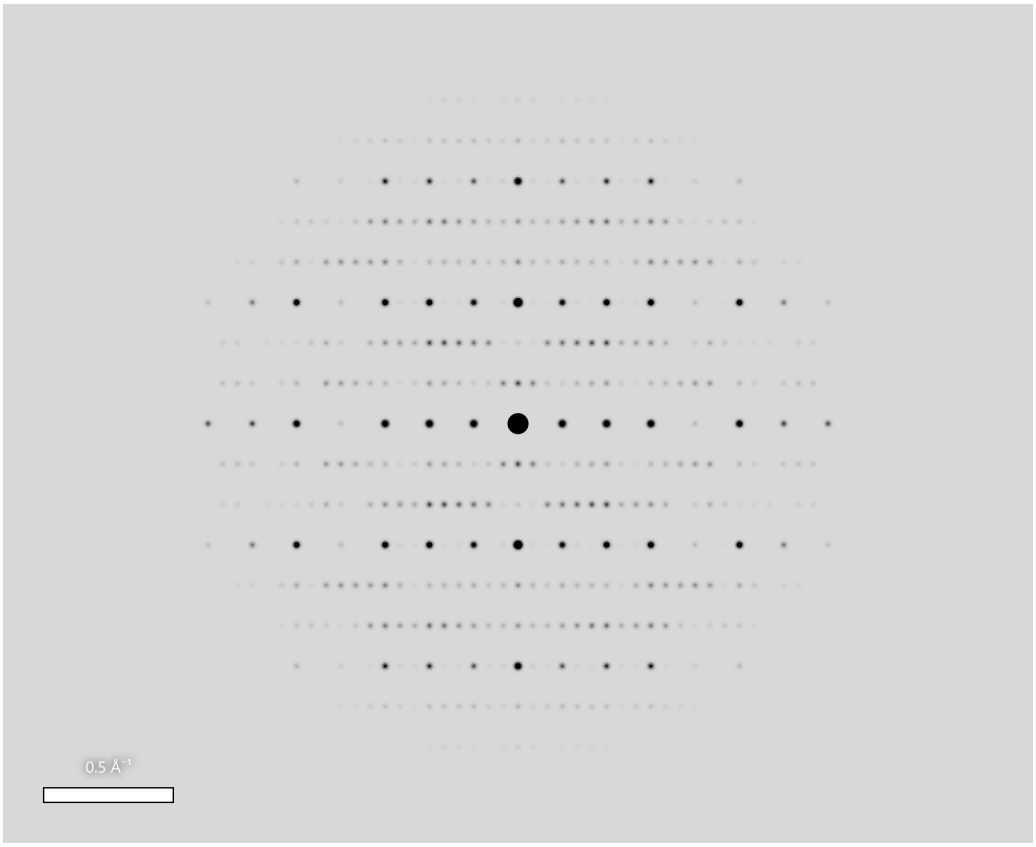

(a) Li_7Si_3

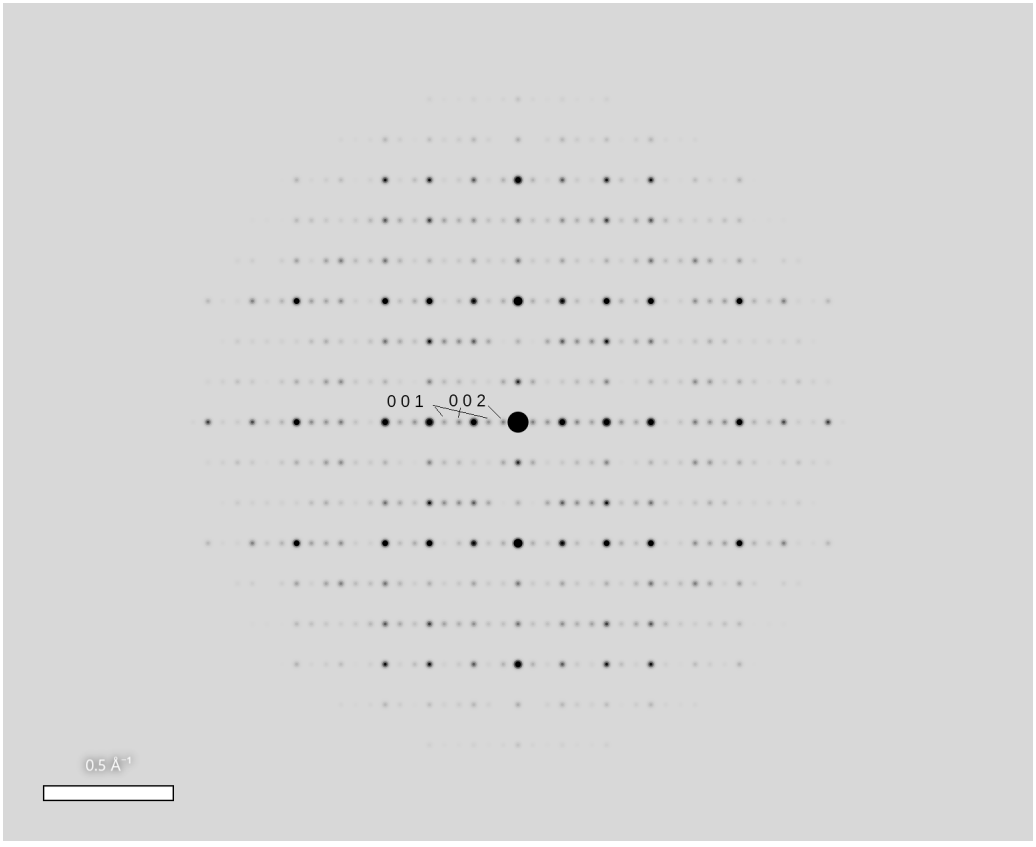

(b) $Li_{43}Si_{18}$

Figure 2.5: Simulated electron scattering pattern (SingleCrystal©). (b) We have labeled (in hkl index) the spots of $Li_{43}Si_{18}$ matching the XRD labeled peaks (Fig. 2.4).

2.3 Vibrational contributions to thermodynamic properties

In this section we calculate the vibrational contribution to thermodynamic properties of Li-Si compounds.

2.3.1 Methodology

Quasi Harmonic Calculations

For the QHA calculations, we perform the HA calculations at least at five different volumes. We do this by multiplying the dimensions of the unit cell parameters by a scaling factor "a". The set of input parameters for VASP code consists of an energy convergence criterion for the self-consistent field (SCF) cycle, an energy cutoff of 750 eV for the plane-wave basis set, a Gamma-centered k-point mesh for Brillouin zone sampling, and a super-cell size ensuring at least 10 Å between the periodicity of displacements. We list all the parameters in table 2.2 for the phases studied in the next subsections. All the unit cells used here are obtained from [103], except Li_9Si_4, Li_5Si_2 (taken from [46]) and $Li_{17}Si_4$ (taken from [49]).

Phase	**Scaling factors (a)**	**K point sampling (Gamma centered)**	**SCF convergence energy (eV)**	**Supercell size**
Li (1)	0.95, 1, ..., 1.15	$2 \times 2 \times 2$	10^{-5}	$4 \times 4 \times 4$
Li (2)	0.95, 1, ..., 1.15	$4 \times 4 \times 4$	10^{-5}	$5 \times 5 \times 5$
Si	0.95, 1, ..., 1.15	$2 \times 2 \times 2$	10^{-5}	$3 \times 3 \times 3$
$Li_{12}Si_7$	0.975, 1, ..., 1.075	$2 \times 2 \times 2$	10^{-4}	$2 \times 1 \times 1$
Li_9Si_4	0.985, 1, ..., 1.06	$6 \times 6 \times 6$	10^{-5}	$1 \times 3 \times 2$
Li_7Si_3	0.975, 1, ..., 1.075	$4 \times 4 \times 4$	10^{-6}	$2 \times 2 \times 1$
$Li_{43}Si_{18}$	0.975, 1, ..., 1.075	$4 \times 4 \times 4$	10^{-4}	$2 \times 2 \times 1$
Li_5Si_2	0.997, 1, ..., 1.015, 1.0325, 1.05, 1.1	$2 \times 2 \times 2$	10^{-5}	$4 \times 4 \times 1$
$Li_{13}Si_4$	0.985, 1, ..., 1.045	$4 \times 4 \times 4$	10^{-6}	$2 \times 2 \times 1$
$Li_{17}Si_4$	0.985, 1, ..., 1.045	$2 \times 2 \times 2$	10^{-6}	$1 \times 1 \times 1$

Table 2.2: Parameters of calculation for the phases of this section.

Note that the parameters are chosen in a way to balance both accuracy and computational cost. For instance, Li_7Si_3 and $Li_{43}Si_{18}$ have almost the same number of atoms and supercell dimensions but $Li_{43}Si_{18}$ has no crystal symmetry. Hence, Li_7Si_3 and $Li_{43}Si_{18}$ QHA calculations cost approximately 2×10^5 and 1.25×10^6 CPU hours respectively. This is the reason why we reduced the SCF convergence energy for $Li_{43}Si_{18}$ despite being similar to Li_7Si_3. Moreover, we have performed Li QHA calculations with two different sets of parameters (denoted 1 and 2 which correspond to a less and a more accurate set respectively) to investigate the effect that imaginary frequencies may have on the calculation of thermodynamic of thermodynamic properties (in the appendix A).

Calculation of thermodynamic properties

We remind the reader that information on how CALPHAD builds the Gibbs free energy fits can be found in Sec. 1.3.6. By definition, at room temperature, CALPHAD's enthalpies are 0 for the pure elements (Li and Si in this case). For Li-Si compounds, the enthalpies are equivalent to the corresponding stoichiometric sum of Li and Si at room temperature, therefore equal to 0 as well. With this in mind, we set the references of enthalpies of all compounds from CALPHAD to match ours at room temperature.

All information necessary for the calculation of thermodynamic properties can be found in Sec. 1.3.1. A detailed explanation on how to obtain entropy, enthalpy and heat capacity can be found there.

We also refer the reader to Sec. 1.3.3 for more information on how to obtain the Free energy and Gibbs free energies from the HA and QHA calculations respectively using PHONOPY [73], we refer to them as G_v and G_p respectively for simplicity since we calculate the thermodynamic properties at constant volume and pressure.

2.3.2 Li

In this subsection we investigate the thermal properties of Li using the more accurate set of parameters Li (2) of table 2.2.

Phonon Density of State

The phonon density of state of Li at 0 K and fully relaxed volume can be found in figure 2.6. We use the two sets of inputs as discussed in the methodology, and we observe that the less accurate set yields negative frequencies. Negative frequencies can be proof of mechanical instability of the phase [104] but can also be artifacts from the calculations, given that we do not use sufficiently accurate input parameters for the calculations. For the purpose of this study we are concerned with the more accurate result. Hence we will just use the Li (2) results in this section. To see the effect that the negative frequencies have in the thermal properties, the reader is invited to the appendix A for a comparison of Li (1) and Li (2) thermodynamic properties properties.

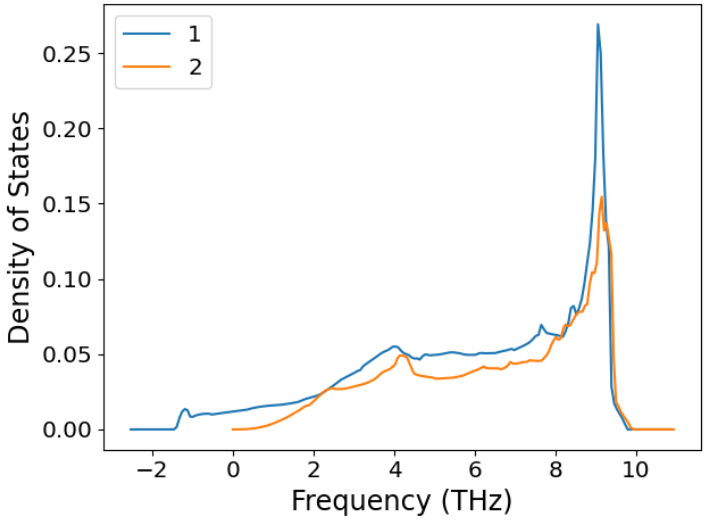

Figure 2.6: Li phonon density of states at the equilibrium volume (a=0) at 0 K. 1 is using the first set of input parameters Li (1), 2 is using the second (more accurate) set of input parameters Li (2) from table 2.2.

Gibbs free energy

The evolution of the free energy as a function of volume at various temperatures can be seen in Fig. 2.7. Taking the minimum of G_v at each temperature with respect to volume gives us the G_p that we can directly compare with CALPHAD Li BCC. We plot the Li G_p against temperature in Fig. 2.8.

This work's G_p and CALPHAD results are very much alike, especially at low T. It is reassuring and surprising at the same time. Li becomes liquid at T=453.7 K, and CALPHAD method accounts for this

in their fit (although they only work with Li BCC) of G_p (by reproducing the experimental C_p as shown in Fig. 2.11), whereas we do not; this can explain why below 450 K our results are virtually the same as CALPHAD and after 450 K we start to observe differences. Nonetheless, it is true that our G_p is closer to CALPHAD's than our G_v it can be credited to the fact that in QHA calculations we account for the volume expansion. While it is also true that we do not represent the phase transformation in anyway, we cannot completely disregard how similar and close our result is to that of CALPHAD (which reproduces the experimental heat capacity, see Fig. 2.11). At a temperature of 690 K, for example, the difference between our predicted G_p and CALPHAD's is approximately 7.9 meV (Fig. 2.9). We will be using our calculated G_p when calculating the OCV since we need a reference (recall section 1.3.7) and at a temperature of 690 K the difference is small and a room temperature even smaller.

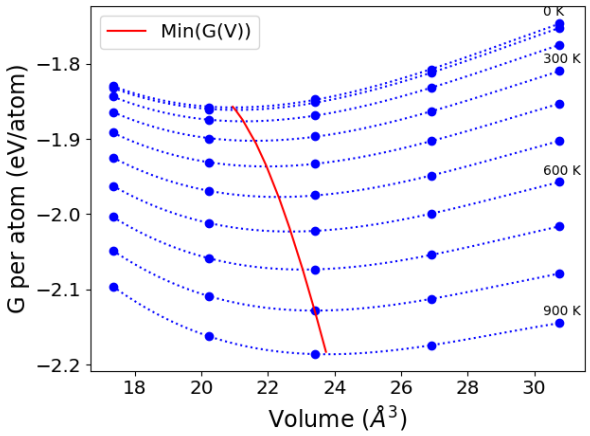

Figure 2.7: Plot of the Li Gibbs free energy vs volume of the unit cell (1 Li atom) at steps of 100 K (from 0 to 900 K). The blue dotted line represents the Birch-Murnaghan equation of state. The red line represents the minimum of G with respect to volume at each temperature.

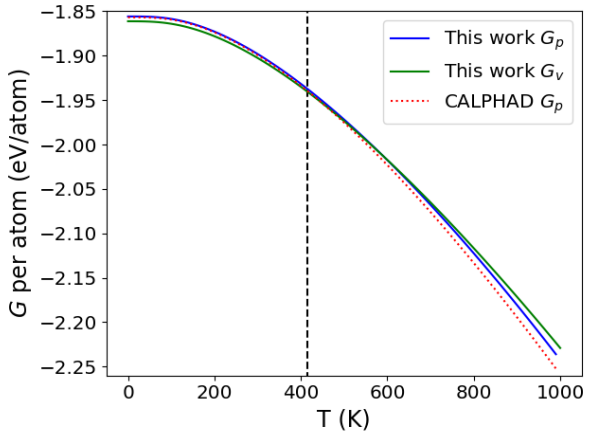

Figure 2.8: Plot of the Li G_p and G_v vs temperature. Comparison with CALPHAD [42]. The analytical fit of our G_p (2) with respect to T can be found in the appendix B. Dashed black line indicates the experimental phase transisition between solid and liquid.

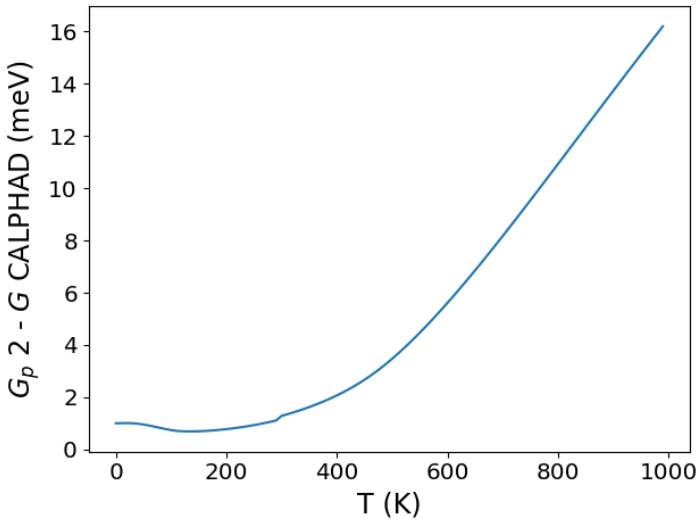

Figure 2.9: Plot of the difference between our Li 2 G_p and that of CALPHAD [42] vs temperature.

Entropy

We calculate the entropy at constant pressure and volume from G_p and G_v respectively. The plot of the isobaric and isochoric entropies (S_p and S_v) against temperature are in Fig. 2.10. Here we can clearly see the effect of ignoring the thermal expansion at temperatures higher than 400 K. S_v leads to a greater underestimation of the vibrational entropy where as S_p gets closer to the measured entropy. However, discrepancy of S_p increases with temperature, from 3.3% at T = 450 K to 4.3% at T = 1000 K.

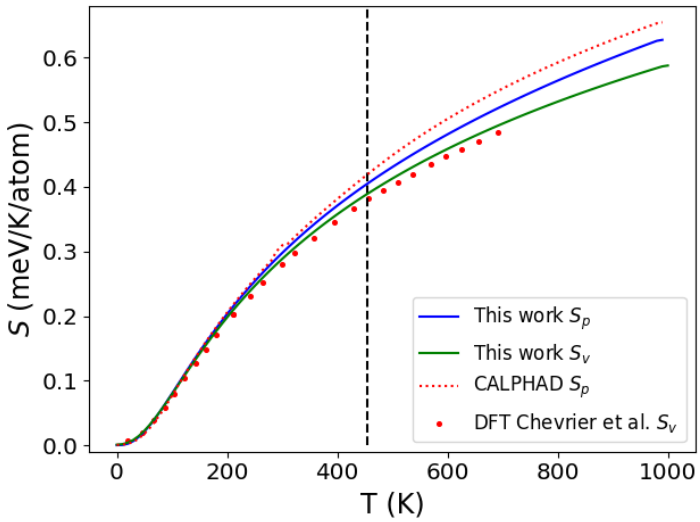

Figure 2.10: Plot of the Li entropy vs temperature. Comparison with CALPHAD [42] and DFT HA by Chevrier et al [41]. Dashed black line indicates the experimental phase transisition between solid and liquid.

Heat Capacity

We can also calculate the heat capacity at constant pressure and volume (C_p and C_v). We compare our results with the literature for theoretical [41, 56] and experimental [105, 42] validation in Fig. 2.11. Our C_p agrees with previously published DFT C_p results; however, both our result and that of Schwalbe et al. [56] do not reproduce the C_p peak which is a signal of the solid-to-liquid first order phase transition. To reproduce this peak, both solid and liquid phases of Li should be treated by DFT. It is worth remarking that the CALPHAD approach cited here does not account for the liquid transition, but still manage to reproduce the experimental C_p meaning that their Gibbs free energy reproduces that of the liquid one.

Our results agree with previously published theoretical results, and below the transition temperature (up to 350 K) our differences with the experimental Gibbs free energy are negligible. Despite having maximum discrepancy of 12% with respect to experiment in C_p at phase transition temperature, in terms of Gibbs free energy it is only a matter of 2.5 meV which is well below the DFT accuracy anyway. This is a reminder to the reader that we can observe greater discrepancies in entropy and heat capacity because they are proportional to the first and second order derivatives with respect to temperature of the Gibbs free energy (Sec. 1.3.1) and also because the scale is in meV instead of eV.

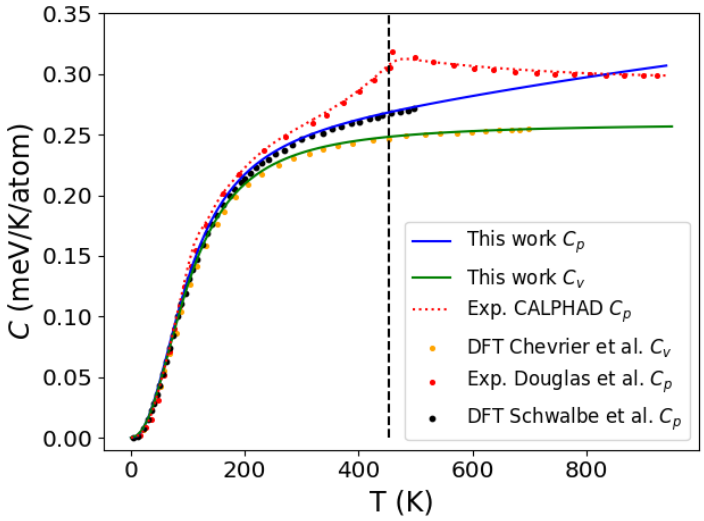

Figure 2.11: Plot of the Li heat capacity vs temperature. Comparison with CALPHAD [42], DFT HA by Chevrier et al. [41], experiment by Douglas et al. [105], and DFT QHA by Schwalbe et al. [56]. Dashed black line indicates the experimental phase transisition between solid and liquid.

Recap of Li section our predicted Li Gibbs free energy can be used as a reference for the upcoming theoretical open circuit voltage calculations or finite temperature convex hull of stability.

2.3.3 Si

Phonon Density of State

The 0 K and fully relaxed Si PDOS has no imaginary frequencies (Fig. 2.12), this means that both our accuracy parameters were optimal for this calculation and the Si structure under the study is mechanically stable.

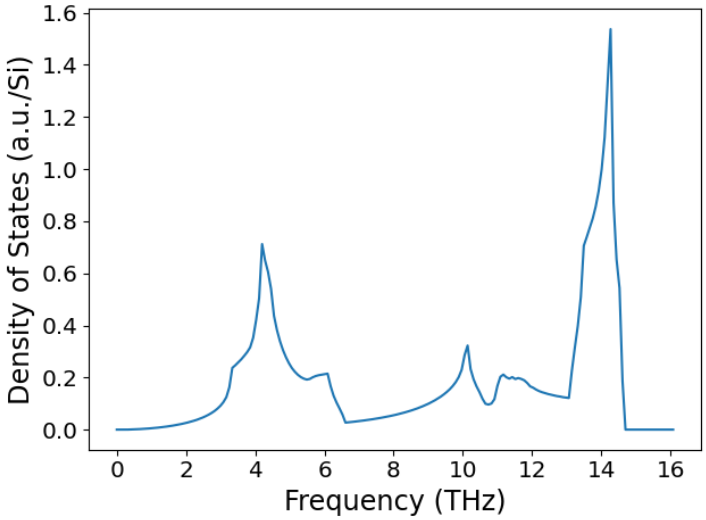

Figure 2.12: Si phonon density of states at the equilibrium volume (a=0) at 0 K.

Gibbs free energy

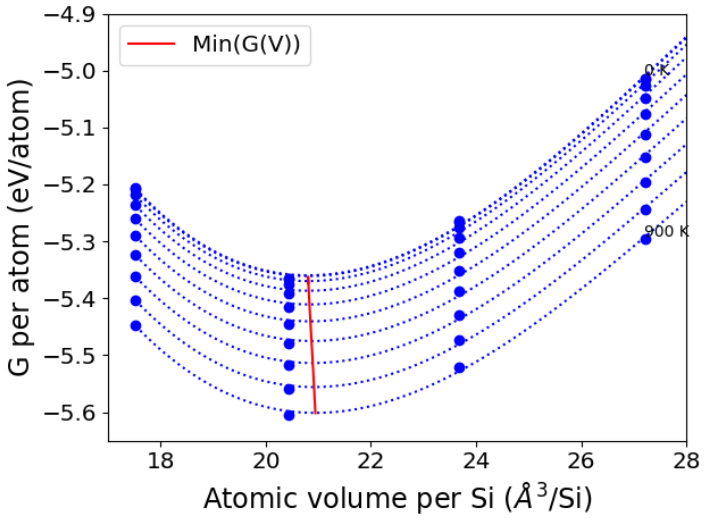

Figure 2.13: Plot of the Si Gibbs free energy vs atomic volume per Si at steps of 100 K (from 0 to 900 K). The blue dotted line represents the Birch-Murnaghan equation of state. The red line represents the minimum of G with respect to volume at each temperature.

The evolution of the Si free energy as a function of volume at various temperatures can be seen in Fig. 2.13. Taking the minimum of G_v at each temperature with respect to volume gives us the G_p that we can directly compare with CALPHAD. We plot the Si G_p against temperature in Fig. 2.14.

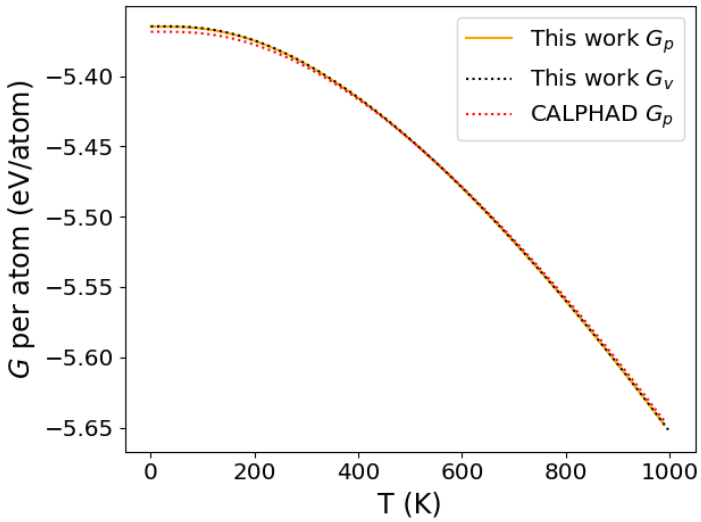

Figure 2.14: Plot of Si G_p and G_v vs temperature. Comparison with CALPHAD [42]. The analytical fit of our G_p with respect to T can be found in the appendix B.

We can also observe in Fig. 2.14 that G_p and G_v are almost the same. This means that the effects that come from the volume expansion, unlike in Li, in Si are negligible from 0 to 1000 K. It is not a surprise comparing the melting temperature of Si with Li (1683 K vs 453.7 K).

Entropy

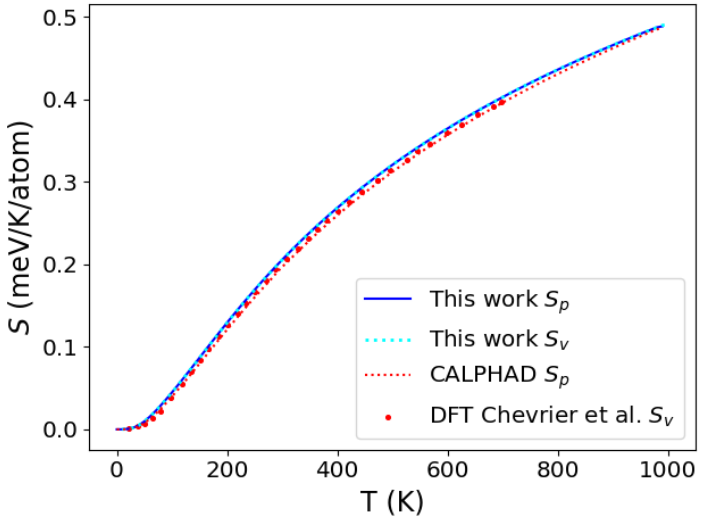

Figure 2.15: Plot of the Si entropy vs temperature. Comparison with CALPHAD [42] and DFT HA by Chevrier et al [41].

The entropy at isobaric and isochoric conditions is very similar to the experimental results and previously published DFT results (Fig. 2.15). It is almost virtually impossible to find the differences between S_v and S_p which is expected given the tiny differences between the G_v and G_p.

Heat capacity

We plot our isobaric and isochoric heat capacities of Si in Fig. 2.16. The agreement between our C_v and that of [41] and similar results from our C_p and that of [56] indicate that our calculations for Si are trustworthy. The differences between theoretical heat capacities and experimental ones can be neglected and should not be of great concern given the similarities in Gibbs free energy.

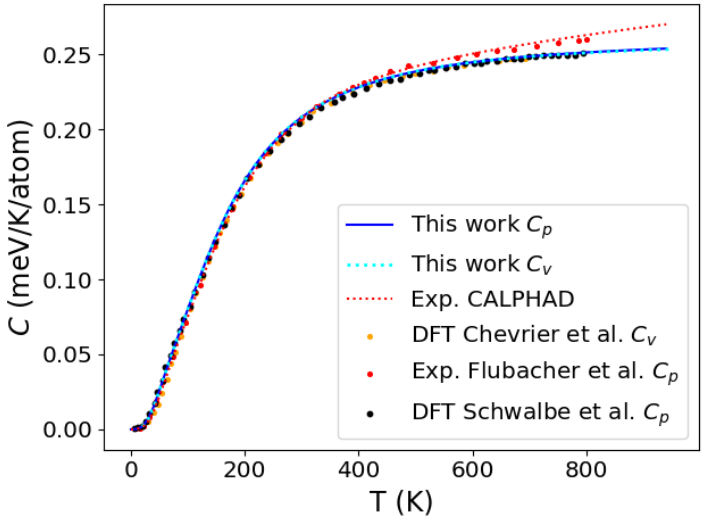

Figure 2.16: Plot of the Si heat capacity vs temperature. Comparison with CALPHAD [42], DFT HA by Chevrier et al. [41], experiment by Flubacher et al. [106], and DFT QHA by Schwalbe et al. [56].

Recap of Si section our predicted Si Gibbs free energy can be used as a reference for the upcoming finite temperature convex hull.

2.3.4 $Li_{12}Si_7$

Phonon Density of State

The phonon density of state of $Li_{12}Si_7$ at 0 K and fully relaxed volume can be found in figure 2.17. From our calculations, we can see the presence of negative frequencies. These can either be an artifact from the calculations (the need for better accuracy parameters) or be physical proof of a mechanically unstable phase [104]. However, this phase has been proven to be stable and to have a phonon density of state with no negative frequencies by the work of Chevrier et al. [41]. Going beyond in accuracy parameters would increment the computational cost tremendously since this is a phase with a 152 atoms unit cell. This might not be deemed worthy since we have proven that we can still reproduce with great agreement previously published DFT thermodynamic properties by ignoring the negative frequencies (see appendix A).

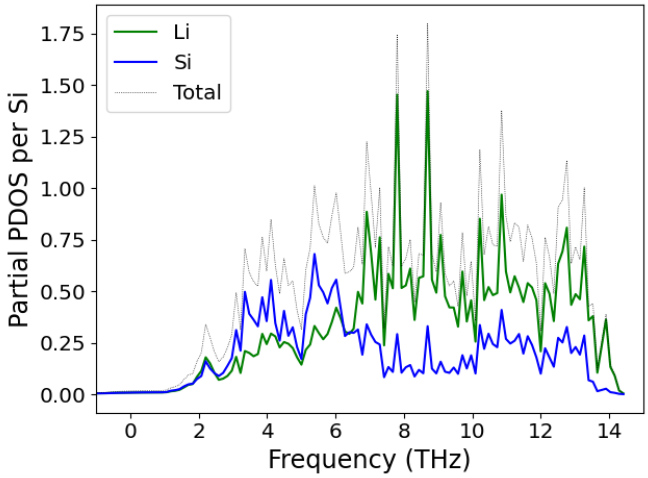

Figure 2.17: $Li_{12}Si_7$ projected phonon density of states at the equilibrium volume (a=0) at 0 K.

The projected phonon density of states shows that both species contribute through all the frequencies. Nevertheless, we can clearly see that high frequency regime has a PDOS of 1:4 ratio for Si against 3:4 ratio for Li and viceversa for the low frequency regime.

Gibbs free energy

The plot of the G vs volume, at each temperature, can be seen in Fig. 2.18. Also, the plot of the G vs temperature is in Fig. 2.19. Our predicted G_p is in virtually excellent agreement with CALPHAD [42].

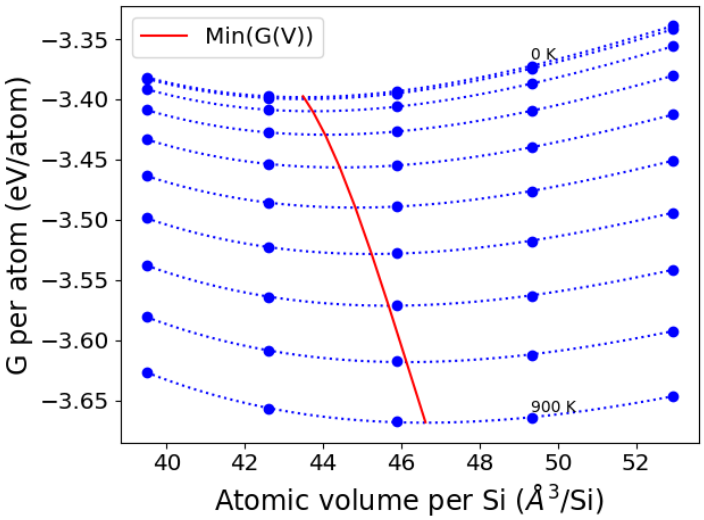

Figure 2.18: Plot of the $Li_{12}Si_7$ Gibbs free energy vs atomic volume per Si at steps of 100 K (from 0 to 900 K). The blue dotted line represents the Birch-Murnaghan equation of state. The red line represents the minimum of G with respect to volume at each temperature.

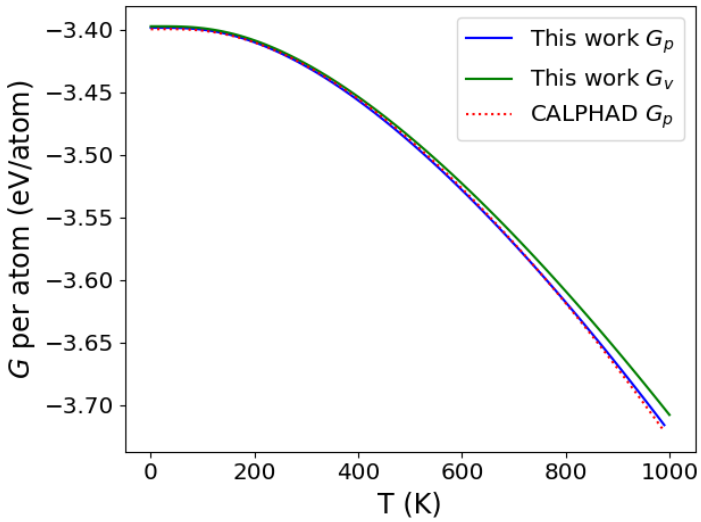

Figure 2.19: Plot of the $Li_{12}Si_7$ G_p and G_v vs temperature. Comparison with CALPHAD [42]. The fit of our G_p can be found in the appendix B.

Entropy

We calculate S_v and S_p from the corresponding G and proceed to plot them against T (Fig. 2.20). Despite having a virtually excellent agreement in G with CALPHAD we can see a little discrepancy of the order of 10^{-1} meV/K especially at high T.

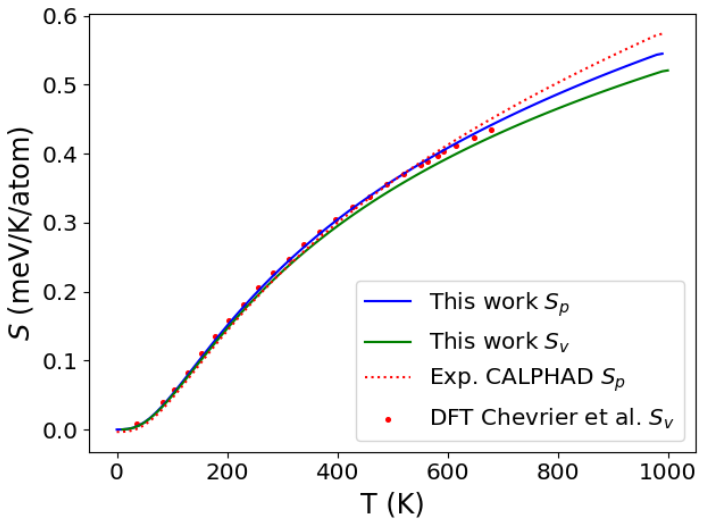

Figure 2.20: Plot of the $Li_{12}Si_7$ entropy vs temperature. Comparison with CALPHAD [42], and DFT HA by Chevrier et al [41].

Our predicted S_v can not exactly reproduce the one of [41]. However, we know that this is due to

the negative frequencies thanks to the study on Li in the appendix A. We observe that we can not also reproduce the isochoric DFT thermal properties with the presence of negative frequencies in the phonon DOS. Nonetheless, we choose to rely on these results since the difference is not significant. Besides, the present entropy accounting for the volume expansion is in very good agreement with the CALPHAD one directly extracted from calorimetric experiments.

Heat capacity

The plot of our heat capacities and the comparison with previously published results can be seen in Fig. 2.21. One possible reason for the discrepancy between our predicted C_p and experimental one could be the impact of anharmonic vibrational effects which occur at higher temperatures and can result in a distinct behaviour of the volume expansion. As already explained in the work of Schwalbe et al. [56], even at high temperature Si_5 ring maintains its bonds, making it easier for the structure to slide the Li atoms inside the Si rings, potentially making its crystalline structure transform into another one or an amorphous one.

Whether or not the discrepancy can affect the phase diagram is a question that can be answered by constructing the convex hull of stability at finite temperatures and observing how the stability of $Li_{12}Si_7$ evolves concerning the other compounds (to be tackled later in this chapter in Sec. 2.5). Reproducing the heat capacity means we are adding more sources of entropy, hence stabilizing the structure even more. According to our calculations, the $Li_{12}Si_7$ phase remains stable from 0 K up to 1000 K. Adding more entropy will keep it just the same. For the scope of this work, this information is valuable.

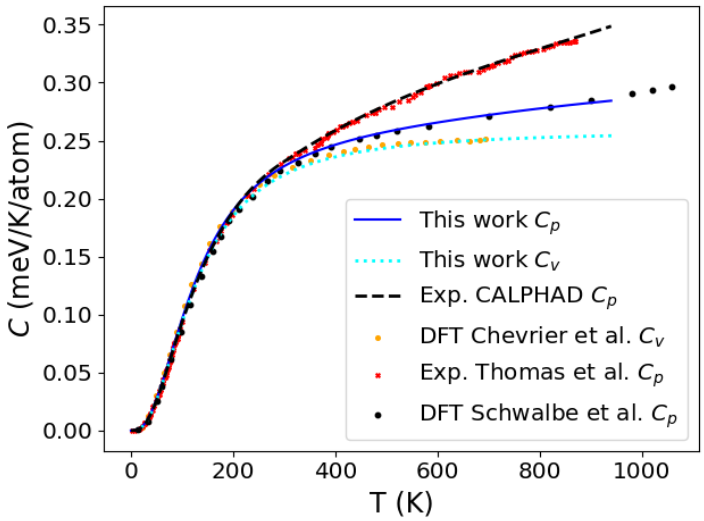

Figure 2.21: Plot of the $Li_{12}Si_7$ heat capacity vs temperature. Comparison with CALPHAD [42], DFT HA by Chevrier et al. [41], experiment by Thomas et al. [43], and DFT QHA by Schwalbe et al. [56].

2.3.5 Line compounds nearby Li_7Si_3

Before we dive into this section, we should explain why all the phases are going to be under the same study. We recall from section 2.2.1 the crystallography structures of the Li_9Si_4, Li_7Si_3, $Li_{43}Si_{18}$, $Li_{44}Si_{18}$, and Li_5Si_2 respectively.

As discussed previously in section 1.1.3, the literature has yet to have a consensus on which phase

is truly the one that happens around Li_7Si_3 composition. To solve this question, we first look at the thermodynamic quantities of all the phases around this composition in an attempt to solve this mystery.

The $Li_{43}Si_{18}$ and $Li_{44}Si_{18}$ phonon calculations are very expensive to perform due to their lack of crystal symmetry operations. Hence for this work we have decided to perform the QHA phonon study of the $Li_{43}Si_{18}$ phase only. For the $Li_{44}Si_{18}$ phase we consider that an extrapolation from a Li composition based fit -taking into account the phases Li_9Si_4, Li_7Si_3, $Li_{43}Si_{18}$ and Li_5Si_2- would be enough given the similarities in crystal structure and Li composition.

Phonon density of states

We plot the phonon density of states of fully relaxed unit cells per Si at 0 K in Fig. 2.22. The PDOS shows that Li_9Si_4, Li_7Si_3, and Li_5Si_2 are stable phases from the absence of negative frequencies. However we do obtain some negative frequencies for $Li_{43}Si_{18}$ which can be a subject of lack accuracy or physical instability. Recall in table 2.2 the SCF convergence energy of $Li_{43}Si_{18}$, it is lower than the other phases'. We are certain that the negative frequencies of $Li_{43}Si_{18}$ are artifacts from our calculation.

We can notice the presence of 2 blocks separated by a pseudo gap around 7.5 THz. The work of Chevrier et al. [41] shows the projected PDOS of Li_7Si_3 on the atom coordinate vectors they show that the low-frequency regime is due to the vibration of Si atoms while the high frequency block mainly results from the vibrations of Li atoms. The projected density of state of the other phases from this section (in Sec. 2.23) have the same low and high frequency blocks, separated by the pseudo-gap. In comparison with $Li_{12}Si_7$ PDOS we can see that the ratio of Si contribution at high frequencies is decreasing.

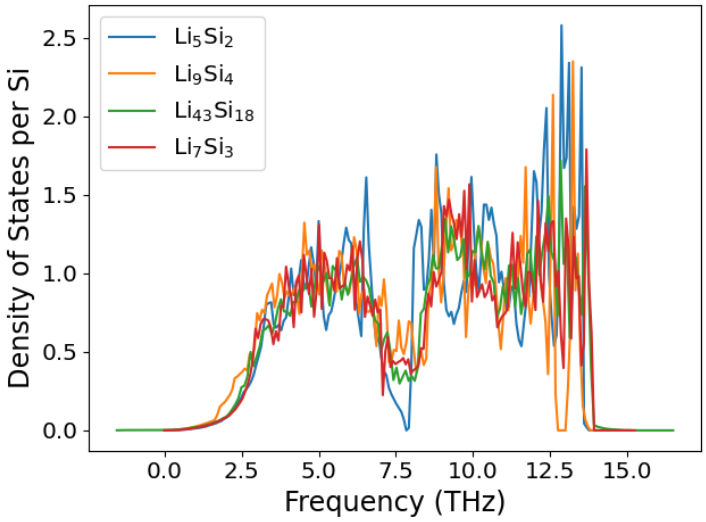

Figure 2.22: Plot of the phonon density of states.

Notice how the magnitude of the pseudo-gap drop is proportional to the Li concentration. For instance, the drop is larger with Li_5Si_2 and smaller with Li_9Si_4. The frequencies around 7.5 THz certainly correspond to the Li vibrations around the Li vacancy thanks to the projected DOS in Fig. 2.23. As Li fills the vacancies from Li_9Si_4 to form Li_5Si_2, the number of Li vacancy neighbors gets smaller and associated vibrational entropy is decreasing. Vibration of the neighboring Li reduces, and hence the drop around 7.5 THz happens.

Nonetheless, the Li_5Si_2 Li PDOS increases in the high-frequency regime, opposite to what happens

to Li_9Si_4. In other words, as we increase Li content, the Li high-frequency PDOS contribution increases whereas the vibrational contribution of the vacancy Li-neighbors decreases around 7.5 THz.

Something to notice as well is the evolution of the Si projected PDOS at high frequencies. At lower concentrations of Li (Li_9Si_4) we have higher PDOS for Si and as concentration increases this PDOS decreases (e.g. Li_5Si_2). This shows how as Li vacancies are formed the Si will compensate for the electroneutrality loss and vibrate towards the columns that have a Li vacancy as there is also more room for the Si atoms (not just the Li atoms). This along with charge badder analysis [107] hints at the existence of strong polar covalent bonds as stated by Kim et al. [108]. The Li-Si bonds will always try to keep the electroneutrality condition at all costs.

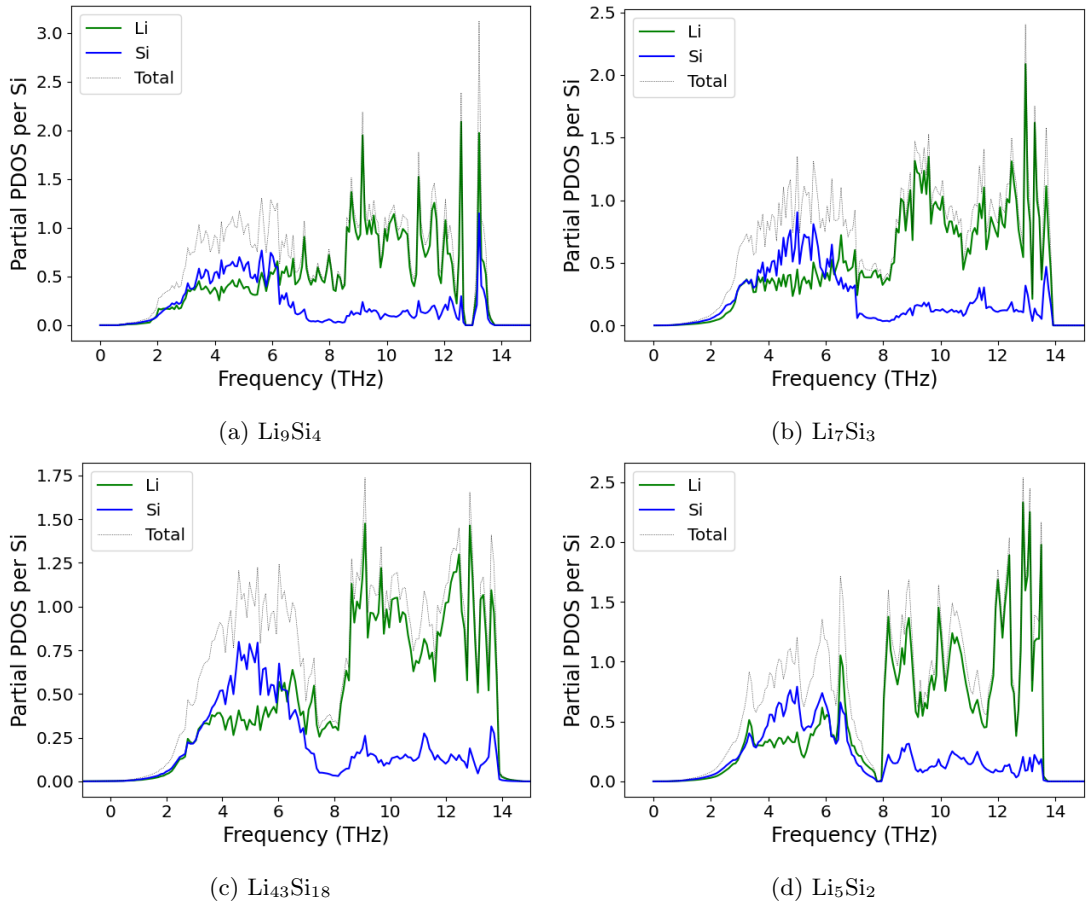

(a) Li_9Si_4 (b) Li_7Si_3

(c) $Li_{43}Si_{18}$ (d) Li_5Si_2

Figure 2.23: Projected PDOS.

Gibbs Free energy

The Gibbs free energy vs volume and vs temperature can be found in Fig. 2.24 and Fig.2.25 respectively. From CALPHAD we have the Li_7Si_3 Gibbs free energy and we fit it such that we get the Li_7Si_3 at room temperature (in accordance to the CALPHAD method, please check 1.3.6). In spite of having different compositions, we can observe, since the differences in Li contents are not big, that the atomic volume expansion is barely affected.

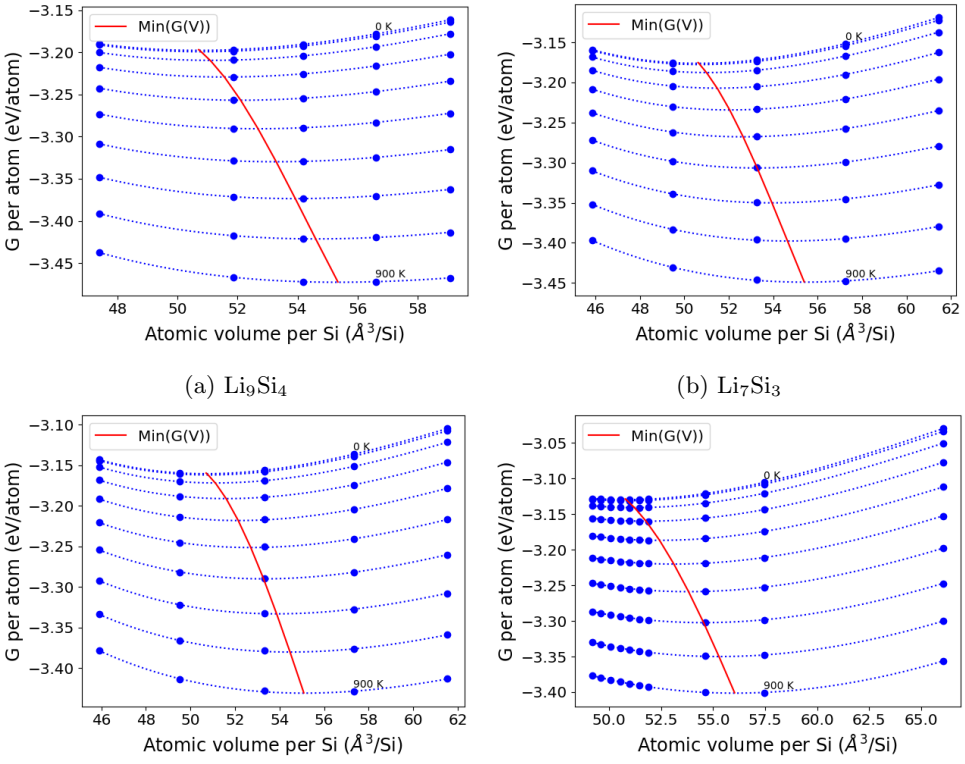

(a) Li_9Si_4 (b) Li_7Si_3

(c) $Li_{43}Si_{18}$ (d) Li_5Si_2

Figure 2.24: Plots of the Gibbs free energy vs atomic volume per Si at steps of 100 K (from 0 to 900 K). The blue dotted line represents the Birch-Murnaghan equation of state. The red line represents the minimum of G with respect to volume at each temperature.

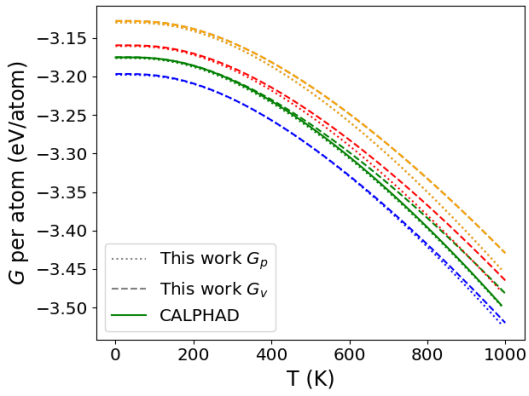

Figure 2.25: Plot of the Li_9Si_4 (blue), Li_7Si_3 (green), $Li_{43}Si_{18}$ (red), and Li_5Si_2 (yellow) Gibbs free energies vs temperature. Comparison with CALPHAD [42]. The fit of our G_p's can be found in the appendix B.

Entropy

We calculate S_v and S_p from G_v and G_p and plot them against temperature in Fig. 2.26. The major differences are observed between isobaric and isochoric conditions. We can not really rely on the entropy to discriminate the phase under the question here because all the phases have similar S.

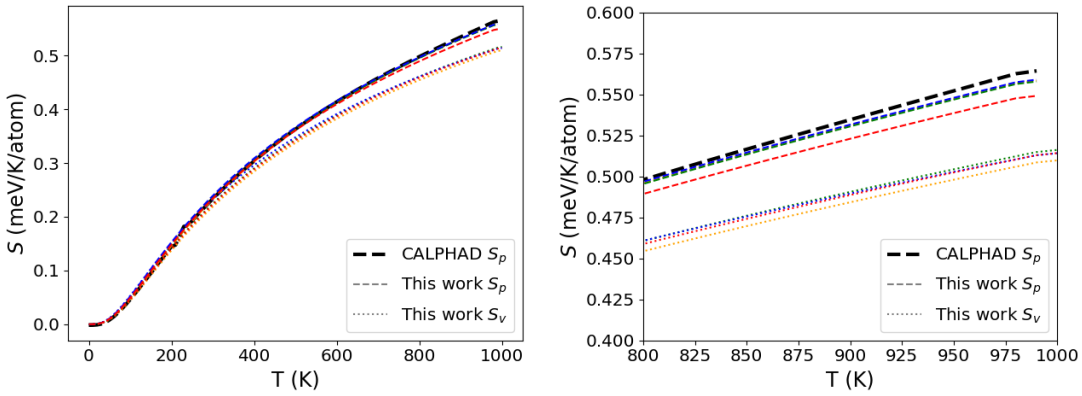

(a) Zoomed out (b) Zoomed in

Figure 2.26: Plot of the Li_9Si_4 (blue), Li_7Si_3 (green), $Li_{43}Si_{18}$ (red), and Li_5Si_2 (yellow) entropy vs temperature. Comparison with CALPHAD [42].

Heat capacity

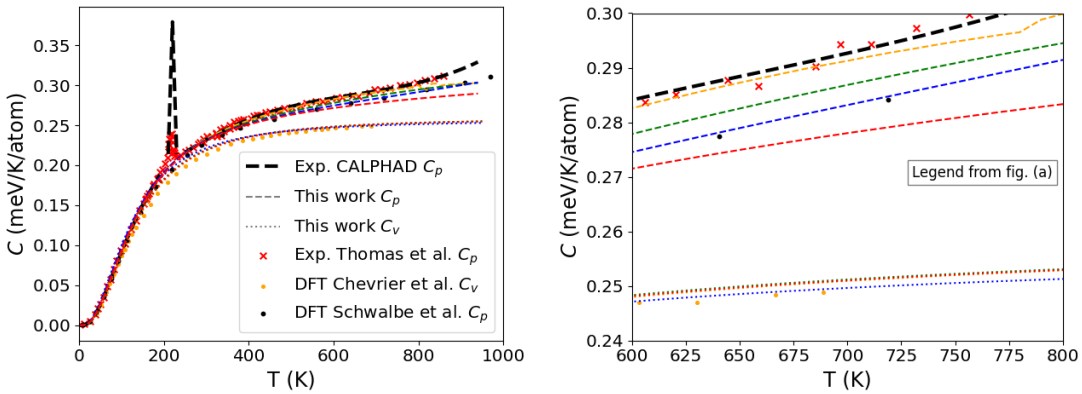

(a) Zoomed out (b) Zoomed in

Figure 2.27: Plot of the Li_9Si_4 (blue), Li_7Si_3 (green), $Li_{43}Si_{18}$ (red), and Li_5Si_2 (yellow) heat capacities vs temperature. Comparison with CALPHAD [42], DFT HA by Chevrier et al. [41], experiment by Thomas et al. [43], and DFT QHA by Schwalbe et al. [56].

The heat capacity is usually the thermodynamic entity that we can rely on for discriminating the phases; for instance, Thomas et al. have used their DFT calculation of the heat capacity and its comparison with their experimental one to identify the Li_7Si_3 phase [43]. We plot our predicted C_v and C_p to compare

with previously published experimental and DFT results in Fig. 2.27. We also observe with DFT QHA a very good agreement with the experimental C_p using Li_7Si_3 but the agreement is even better for the Li_5Si_2.

If we were to follow the logic behind heat capacity comparison for determining a phase, then our predicted phase would be the Li_5Si_2 phase. Notice how it reproduces very well the experimental result of [43], and hence CALPHAD [42], especially at high temperatures (Fig. 2.27b). Anyway, no matter which phase we use, from DFT QHA calculations alone, we cannot reproduce the peak at 210 K, a signal of a first-order phase transition (refer to 1.1.3 for more information on this). We need to study the potential two-phase equilibria to reproduce a temperature-induced phase transformation at a fixed composition -this will be addressed in the next chapter.

Recap of line compounds near Li_7Si_3 The thermodynamic properties alone do not discriminate the phase in question and the heat capacity peak is not reproduced when considering a single line compound. Further investigation of the two-phase equilibrium is needed.

2.3.6 $Li_{13}Si_4$

Phonon density of states

We plot the phonon density of states of the fully relaxed volume in Fig. 2.28a. Despite having one of the best set of accuracy parameters among all the studied phases, we observe the presence of negative frequencies. Chevrier et al. have already mentioned the presence of imaginary frequencies -despite having excellent accuracy parameters- as well [41] but did not address the problem.

In the work of Gruber et al. [109] they report this phase to be a stable one. In fact, the work of Gruber et al. explores the reason behind negative frequencies in the PDOS of fully relaxed volume of $Li_{13}Si_4$ and found out that by increasing the volume 5% isotropically gets rid of the negative frequencies. We plot the PDOS of the 4.5% and 9.2% larger in volume cell from our calculations in 2.28b. We observe how at 4.5% more volume we have less imaginary frequencies and at 9.2% more volume we have 0 imaginary frequencies. For more information on this phase's PDOS we refer to [109]. It seems that this phase could be mechanically stabilized by a thermal volume expansion.

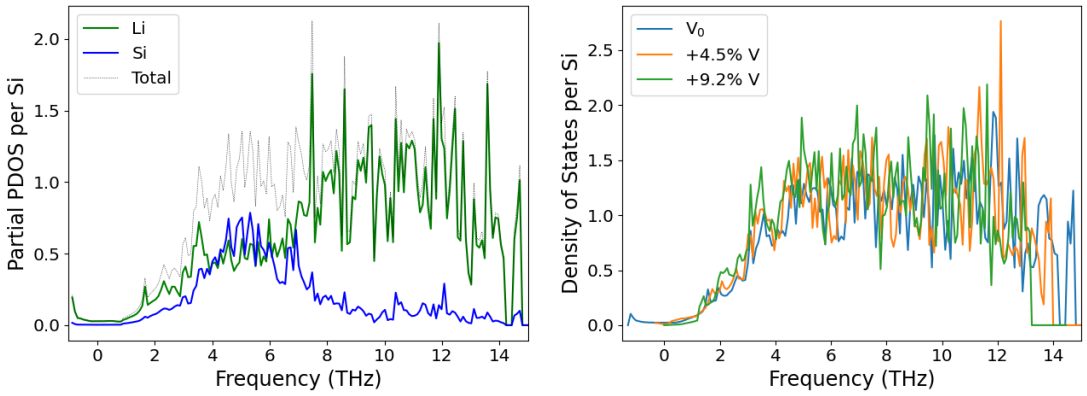

(a) Partial DOS

(b) Total DOS

Figure 2.28: $Li_{13}Si_4$ phonon density of states. (a) is partial DOS of fully relaxed volume; (b) is total DOS of the structure at fully relaxed volume and increased fixed volumes.

In comparison with the previous phases, we can see that we have less contribution of Si at the high frequency block. As we increase the Li content the vibrations of Si decrease in the high frequency block.

Gibbs free energy

The Gibbs free energy vs volume and vs temperature plots are in figures 2.29 and 2.30 respectively.

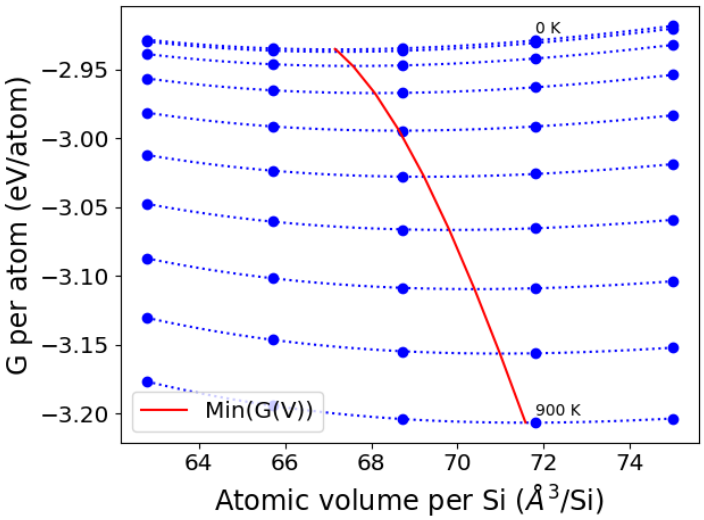

Figure 2.29: Plot of the $Li_{13}Si_4$ Gibbs free energy vs Volume at steps of 100 K (from 0 to 900 K). The blue dotted line represents the Birch-Murnaghan equation of state. The red line represents the minimum of G with respect to volume at each temperature.

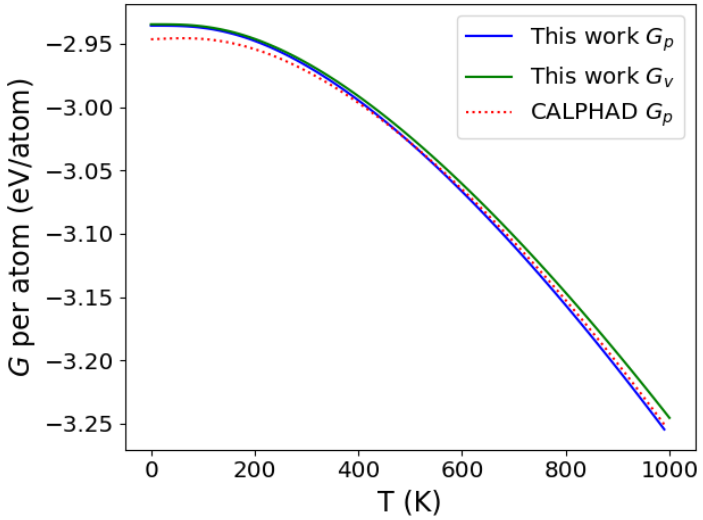

Figure 2.30: Plot of the $Li_{13}Si_4$ G_p and G_v vs temperature. Comparison with CALPHAD [42]. The fit of our G_p can be found in the appendix B.

Entropy

We calculate S_v and S_p from G and plot them against temperature in Fig. 2.31. Something that can be observed is how we obtain negative entropy values at low temperature from CALPHAD [42] which can actually explain the high discrepancy at low T in the G. Entropy is a measure of the disorder or randomness of a system, and it is positive by definition [110]. This means that the CALPHAD low temperature fit of the Gibbs free energy is not well parameterized for the entropy.

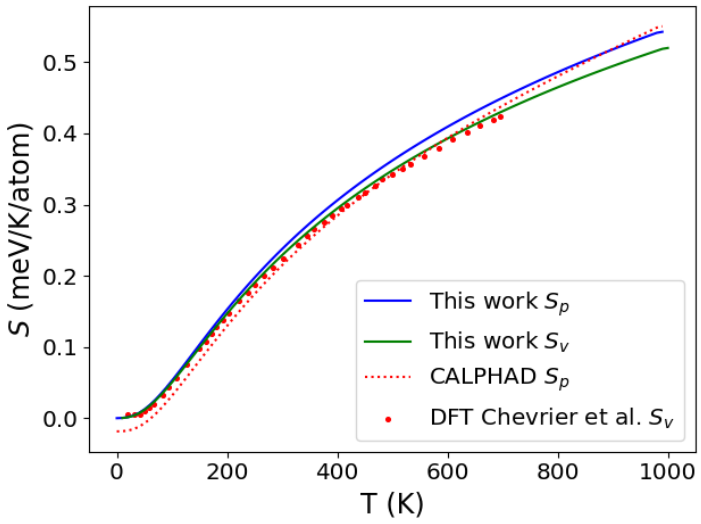

Figure 2.31: Plot of the $Li_{13}Si_4$ entropy vs temperature. Comparison with CALPHAD [42], and DFT HA by Chevrier et al [41].

Heat capacity

The plot of our heat capacities and the comparison with previously published results can be seen in Fig. 2.32. We have discrepancies in C_p compared to [56], which is different from what happened with the previous Li-Si compounds. On the one hand, this is because they use the structure found by the evolution algorithm EVO [111] by Gruber et al. [109] for their C_p calculation. On the other hand, we use the $Li_{13}Si_4$ structure reported by Schnering et al. [112], also found in the identified inorganic crystal structures database (ICSD). Despite the discrepancies between the DFT C_p's, both do not compare to experiment at high temperatures and they should not differ one from another in terms of Gibbs free energy.

The work of Schwalbe et al. [56] mentions that the discrepancy at high temperatures between their C_p and experiment is due to anharmonic effects becoming important and the QHA not being able to produce the right thermal expansion. Moreover, similar to what happens with $Li_{12}Si_7$, Schwalbe et al. claim that there is a crystallographic change around 1200 K: the first nearest neighbors peak in the Si radial pair distribution function increases significantly, which indicates structural changes concerning the Si atoms with increasing temperature. We do not find it so obvious, mainly because there is no C_p data available at 1200 K so we cannot know if there is a change in slope which would be the signature of a second order phase transition.

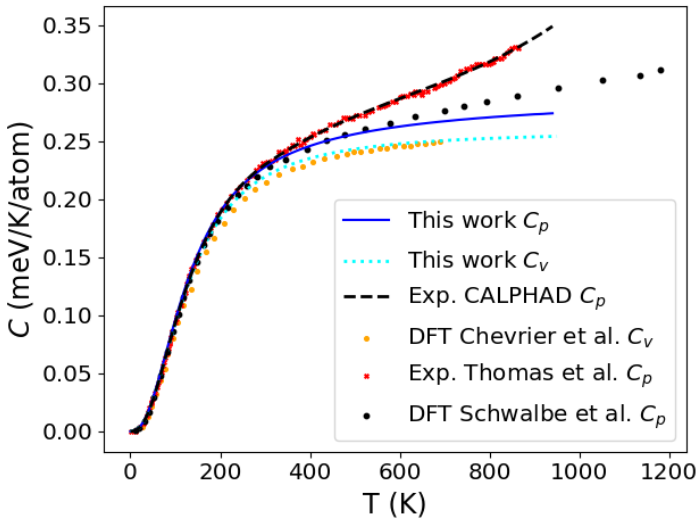

Figure 2.32: C vs temperature. Comparison with CALPHAD [42], DFT HA by Chevrier et al. [41], experiment by Thomas et al. [43], and DFT QHA by Schwalbe et al. [56].

2.3.7 $Li_{17}Si_4$

As mentioned previously in Chapter 1 (Sec. 1.1.3) and like with the Li_7Si_3 phase, there is currently no general agreement in the last crystalline lithiated phase [53]. It is often debated that it is indeed the $Li_{21}Si_5$ phase and recently it has been cleared out that $Li_{22}Si_5$ structure is out of the question [41, 53]. But like Li_7Si_3 and the compounds near it, $Li_{22}Si_5$, $Li_{17}Si_4$ and $Li_{21}Si_5$ differ by Li vacancies. We have decided to study the $Li_{17}Si_4$ phase because it has been proven with first principle calculations by Braga et al. to be a stable phase up to 600 K followed by $Li_{21}Si_5$ phase after 600 K [53]; moreover, an experimental work by Zeilenger and coworkers has found $Li_{17}Si_4$ to be stable up to 761 K [49]. The differences in CALPHAD entropy (S_p) contribution by the work of aforementioned authors hints that it is not worth it to run quasi-harmonic calculations for each of the phases. For this work at least, we calculate both the $Li_{17}Si_4$ isobaric and isochoric thermodynamic properties per atom and assume that they are the same for $Li_{21}Si_5$ or $Li_{22}Si_5$.

Phonon density of states

The 0 K and fully relaxed $Li_{17}Si_4$ PDOS has no imaginary frequencies (Fig. 2.33), this means that both our accuracy parameters were optimal for this calculation and the $Li_{17}Si_4$ structure under the study is mechanically stable.

The calculation of the projected DOS was impossible to do due to the massive amount of memory needed for the matrix. But referencing Chevrier et al. who have done it for $Li_{21}Si_5$ [41], we can say that the low frequency block is controlled by both species but the high frequency block is controlled by Li only. This tells us that the vibrational entropy is coming largely from the Li vibrations.

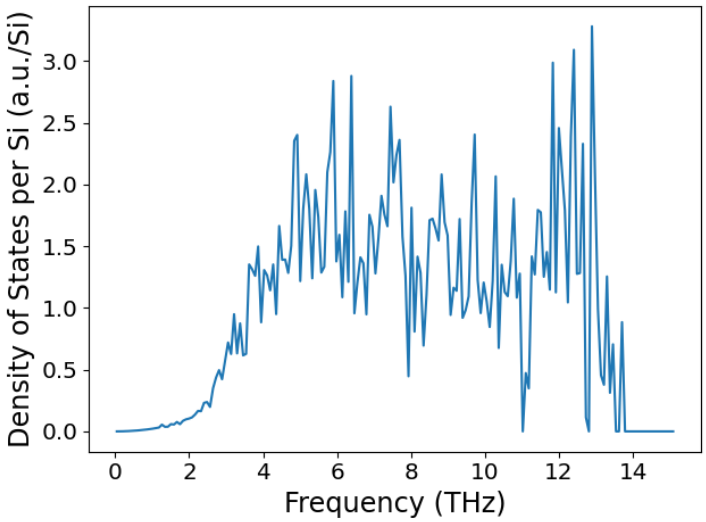

Figure 2.33: $Li_{17}Si_4$ projected phonon density of states at the equilibrium volume (a=0) at 0 K.

Gibbs free energy

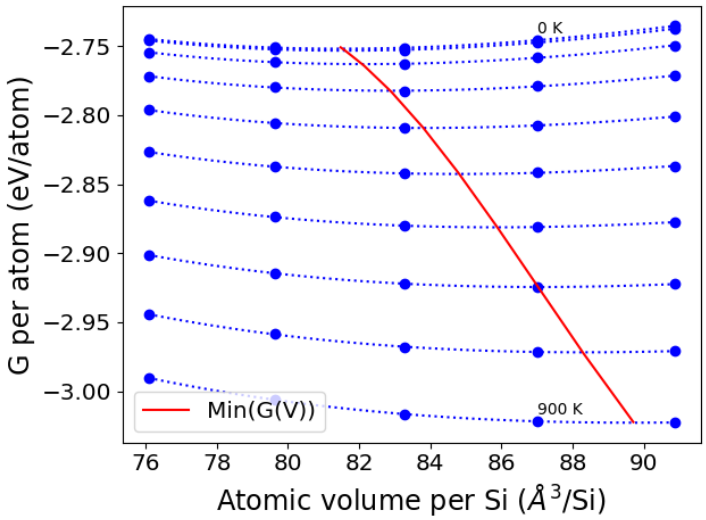

Figure 2.34: Plot of the $Li_{17}Si_4$ Gibbs free energy vs volume at steps of 100 K (from 0 to 900 K). The blue dotted line represents the Birch-Murnaghan equation of state. The red line represents the minimum of G with respect to volume at each temperature.

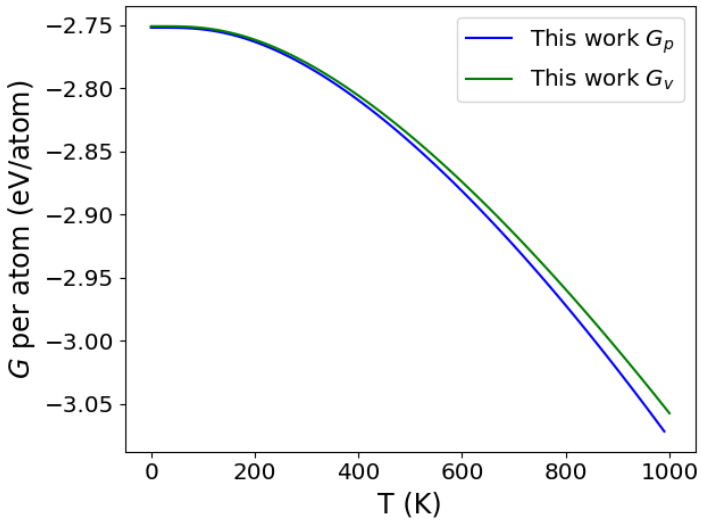

Figure 2.35: Plot of the $Li_{17}Si_4$ G_p and G_v vs temperature. The fit of our G_p can be found in the appendix B.

The Gibbs free energy vs volume and vs temperature plots are in figures 2.34 and 2.35 respectively. The Gibbs free energy plot vs volume shows that this phase has the biggest, relatively speaking, volume expansion with respect to temperature.

Entropy

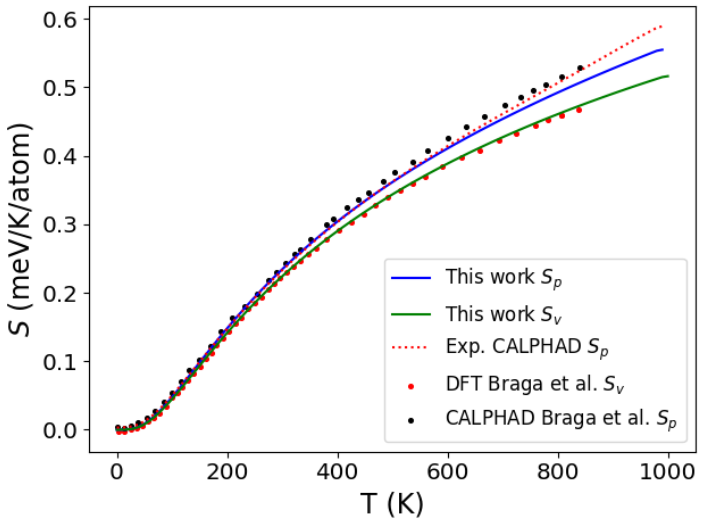

Figure 2.36: Plot of the $Li_{17}Si_4$ entropy vs temperature. Comparison with work of Braga et al. [53] DFT and experimental (CALPHAD).

We calculate S_v and S_p from the corresponding G and proceed to plot them against T (Fig. 2.36). This time we compare with the work of Braga et al. [53]. We have excellent agreement concerning S_v and small discrepancies, especially at high temperatures, with S_p.

Heat Capacity

The plot of our heat capacities and the comparison with previously published results can be seen in Fig. 2.37. We can observe that up to 400 K, we reproduce excellently the experimental result. After 400 K, the experiment seems to diverge, contrary to what happens with other phases. This is a strong change in slope that could either end up in a first order transition (by building a peak, but data after 850 K is needed) or stay like that meaning that there is a second order phase transition.

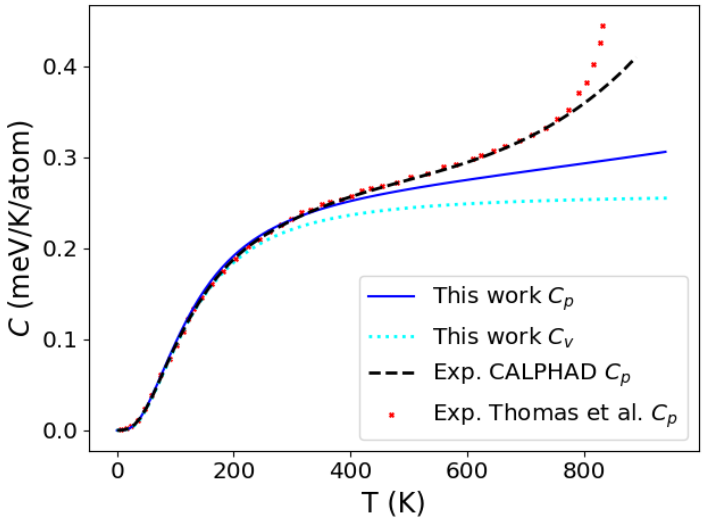

Figure 2.37: $Li_{17}Si_4$ heat capacity vs temperature. Comparison with CALPHAD [42], and experiment by Thomas et al. [43] of "$Li_{21}Si_5$/$Li_{22}Si_5$".

2.4 Volume expansion

In this section we discuss the effect of both concentration and temperature on the volume expansion. We start by comparing the lattice parameters at room temperature in table 2.3. We find that most of our results are in good agreement with previously published experimental results. One notable result is the comparison of Li_7Si_3 with its experimental counter part, we can see that the other two phases Li_5Si_2 and $Li_{43}Si_{18}$ also have the same values. In fact, our $Li_{43}Si_{18}$ has the closest values to the experimental ones.

	Experiment vs this work room temperature						
Phase	a (Å)	b (Å)	c (Å)	α	β	γ	Ref.
Li	3.5 vs 3.4964			90			[100]
Si	5.431074(2) vs 5.47			90			[93]
$Li_{12}Si_7$	8.61(2) vs 8.615	14.341(4) vs 14.429	19.738(4) vs 19.798	90			[112]
Li_7Si_3	7.69 vs 7.664		18.13 vs 18.177	90		120	[113]
$Li_{43}Si_{18}$	N/A vs 7.680	N/A vs 7.680	N/A vs 18.145	90		120	N/A
Li_5Si_2	N/A vs 7.69	N/A vs 7.69	N/A vs 18.069	90		120	N/A
$Li_{13}Si_4$	7.99(2) vs 7.990	15.21(3) vs 15.273	4.43(1) vs 4.459	90			[97]
$Li_{17}Si_4$	18.6563(2) vs 18.7825	18.6563(2) vs 18.7825	18.6563(2) vs 18.7825	90			[49]

Table 2.3: Lattice parameter of our work comparison with experiments (Experiment vs Our work).

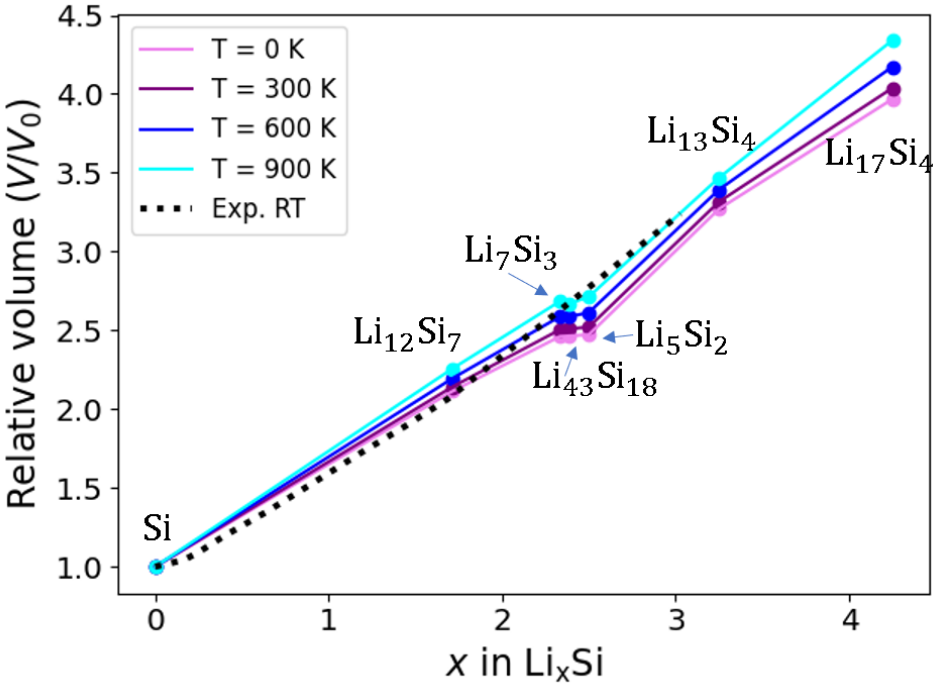

Figure 2.38: Plot of the relative volume with respect to Si (V_0 is the volume of Si at the corresponding temperature) as a function of concentration and temperature. A comparison with experiment done on amorphous Si electrode at room temperature by Schmidt et al. [24].

From our results we can also give the evolution of volume as a function of both the temperature and concentration (Fig. 2.38). The temperature seems to virtually change the rate of expansion with respect to temperature but by negligible amounts (the slopes are not that different). The comparison with amorphous Si electrode experiment suggests that at low concentrations the crystalline structures occupy more volume than the amorphous counterparts and at concentration $x > 1.8$ the structures occupy less volume if they are crystalline. Despite the discrepancies at room temperature between our results and the experiment, the predicted results suggest that both the crystalline and amorphous structures follow a volume expansion that is very similar in both.

Fig. 2.39 shows the relative volume thermal expansion of Li-Si phases with respect to their volume at 0 K. We can observe that, generally, the relative thermal expansion increases from pure Si having the lowest thermal expansion (less than 2% at 900 K) up to pure Li having the greatest thermal expansion (more than 14% at 900 K). This implies that the greatest contribution to the thermal expansion of Li-Si compounds is due to the Li rather than the Si.

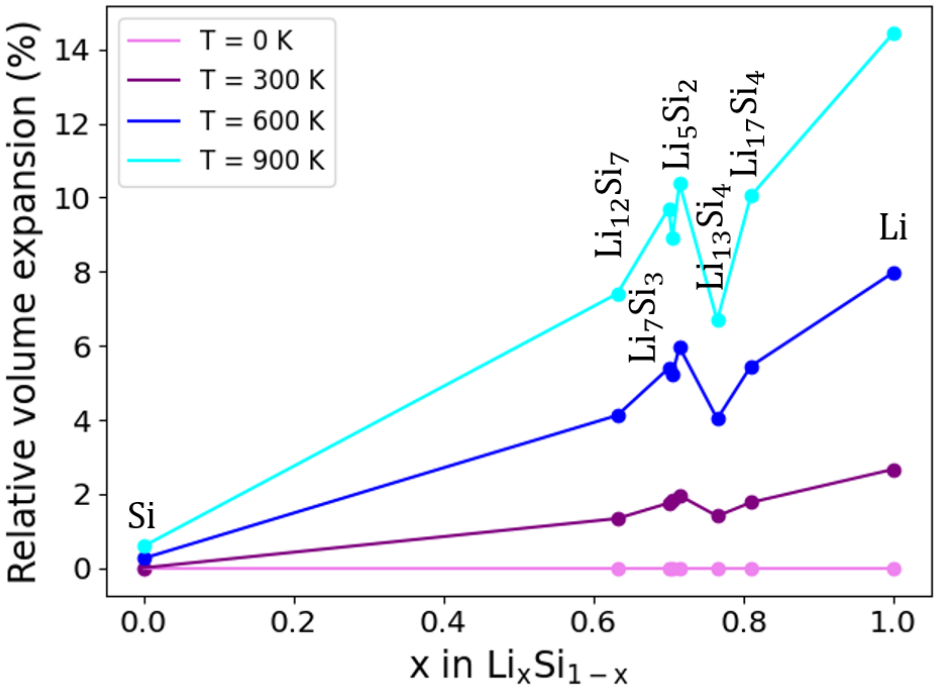

Figure 2.39: Plot of the relative volume expansion of Li-Si phases given in percentage with respect to their volume at 0 K. The atomic volume of the phases Si, $Li_{12}Si_7$, Li_7Si_3, $Li_{43}Si_{18}$, Li_5Si_2, $Li_{13}Si_4$, $Li_{17}Si_4$, and Li at 0 K are the following: 20.53 $\mathring{A}^3$/atom, 15.99 $\mathring{A}^3$/atom, 15.16 $\mathring{A}^3$/atom, 14.93 $\mathring{A}^3$/atom, 14.5 $\mathring{A}^3$/atom, 15.8 $\mathring{A}^3$/atom, 15.52 $\mathring{A}^3$/atom, and 20.85 $\mathring{A}^3$/atom, respectively.

2.5 Convex hull of stability at finite temperatures

After obtaining all the Li-Si compound Gibbs free energies of interest at finite temperatures from HA and QHA phonon calculations, we can proceed to construct the convex hull of stability in isochoric or isobaric conditions at finite temperatures (Fig. 2.40). We use the Li and Si energies at finite temperatures, from the studies done in the previous section, for the energy reference.

In common between HA and QHA convex hulls, we have that Li_5Si_2, $Li_{12}Si_7$, $Li_{13}Si_4$, and $Li_{17}Si_4$ are stable at all temperatures while Li_9Si_4 remains unstable. Not to be neglected, the global stability of Li_9Si_4 increases (i.e. distance with respect to the hull decreases) as we increase the temperature.

Neglecting the volume expansion in HA phonon calculations leads to the stability of both Li_7Si_3 and $Li_{43}Si_{18}$ above 300 K. But if we consider the volume expansion, notice how the $Li_{43}Si_{18}$ loses stability after 500 K against Li_7Si_3. We may say that at low temperatures the creation of Li vacancies is not that favorable and as we increase the temperature the creation of vacancies is favorable. This has already been discussed and proved in the work of Tipton et al. [44] concerning the Li_5Si_2 Li-vacancy formation energy. At high temperature what favours the formation of vacancy is, indeed, the vibrational entropy. As a matter of facts, we should consider the configurational entropy as well in order to understand better what happens around here.

We expect from this analysis that at a given temperature a disordered solid solution will be more stable than a series of ordered phases. This solid solution is one of concentrated Li vacancies around Li_7Si_3 that goes all the way in composition until somewhere around Li_5Si_2. The work of Wen and Huggins already shows Li_7Si_3 to have the biggest single solid solubility domain, besides no hysteresis while lithiating or delithiating the phase [35]. This hypothesis is further studied in the next chapter with off-stoichiometry studies of ordered phases and the calculation of two-phase equilibria.

2.5.1 Enthalpies of formation at 300 K

In Fig. 2.41, we compare the present quasi-harmonic estimation of the enthalpy of formation with the reported CALPHAD and experimental enthalpies at 300 K. Liang et al. [55] claim that the calorimetry data measured by Debski et al. [114, 115] can not be reconciled with the entity of other phase equilibria and thermodynamic properties data. Moreover, none of the previous CALPHAD assessments by Liang et al. [55] or Braga et al. [53] can fit these calorimetry data. The appropiate comparison should be done with the previous CALPHAD publications or DFT results. Fig. 2.41 shows an excellent agreement between our results and CALPHAD (i.e. especially with the results of Braga et al. who have used DFT as well [53]).

2.6 Open circuit voltage from two ordered-phase equilibrium

The electric potential profile is a crucial aspect to observe in lithium batteries. Experimental reports display the open circuit voltage of the battery concerning the amount of lithium in the anode. Assuming a two-phase reaction from reactant to product, the average cell potential can be computed (Sec. 1.3.7). Nominal composition in between two ordered phases leads to a two-phase equilibrium. Hence the convex hull of stability of this section gives us the stable ordered phases (disregarding the off-stoichiometry), thus the two-phase-equilibria that we consider for OCV calculation and the Li reference is chosen according to the temperature. Recall from Sec. 1.3.1, that during a two-phase-equilibrium the chemical potential of elements is constant and the only thing that changes with composition is the proportion of phases. We plot the 0 K OCV regarding the 0 K convex hull (Fig. 2.1) of stability and the finite temperature OCV in accordance to the QHA convex hull (Fig. 2.40b) in Fig. 2.42. It is worth reminding the reader that we have not done finite temperature studies of all 0 K stable phases; for instance, this explains the differences between the two 0 K results.

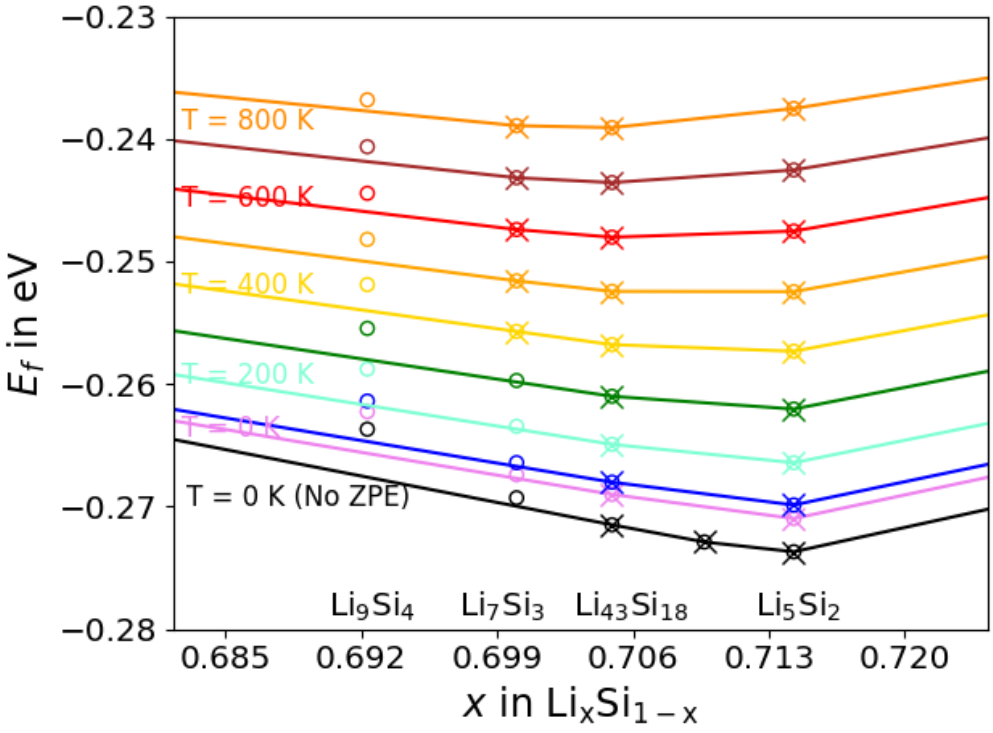

(a) HA

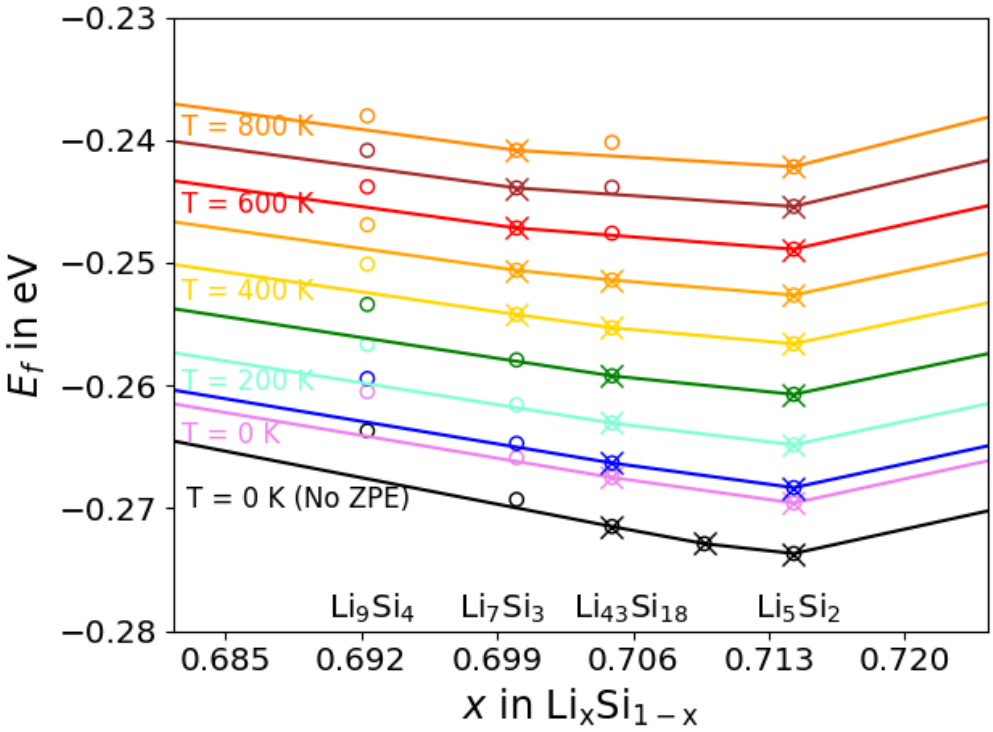

(b) QHA

Figure 2.40: Plot of the formation energies of compounds at steps of 100 K vs composition. The plot is zoomed in such that we portray the phases between Li_9Si_4 and Li_5Si_2 included. The stable phases are marked by '×'.

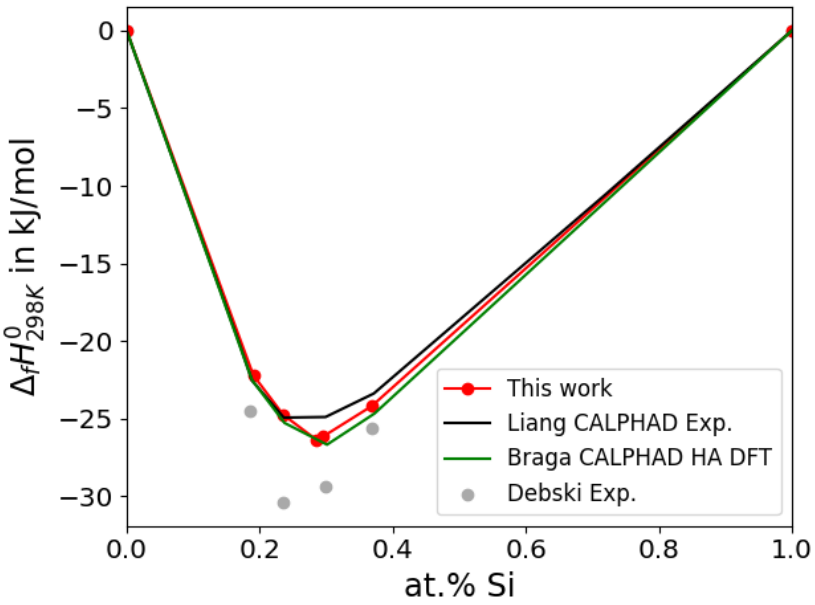

Figure 2.41: Plot of our enthalpies of formation at 300 K vs composition. We plot the enthalpies of formation of CALPHAD assessed from DFT by Braga et al. [53] and assessed from experiment by Liang et al. [55]. We also plot the enthalpies of formation from experiment by Debski et al. [114, 115].

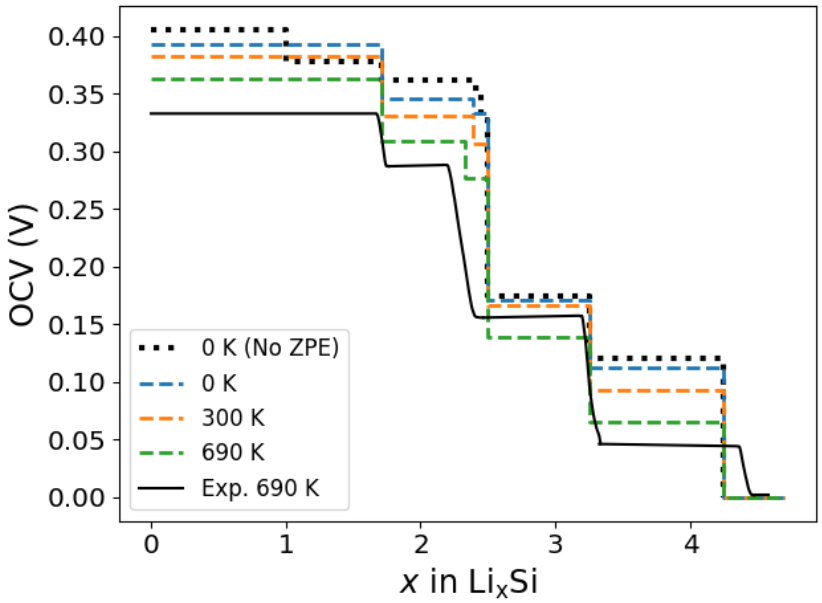

Figure 2.42: Plot of the open circuit voltage vs composition. A comparison of our predicted OCV from 0 K with no zero point energy and at finite temperature with the experiment of Wen and Huggins at 690 K [35].

2.7 Conclusion

We conclude this chapter by listing the things that are important to keep in mind from this chapter.

We have discovered 2 new phases that to the best of our knowledge have not been previously mentioned in the literature, the $Li_{43}Si_{18}$ and $Li_{44}Si_{18}$ phase. They are very difficult to distinguish from previously known Li_7Si_3 and Li_5Si_2 phases as they all share the same Si sublattice and only differ by Li vacancies in a sublattice.

We found that the LiSi phase is not stable against the Li-$Li_{12}Si_7$ two-phase-equilibrium using the HSE06 hybrid functional at 0 K. This result played an important role in deciding to ignore this phase for the rest of this work.

We deduced from the comparison with CALPHAD that our predicted Li G_p can be used as the reference for future OCV studies despite neglecting the phase transformation from solid to liquid at 453 K.

We have seen the effect of including thermal volume expansion in our calculation of thermodynamic properties for Li-Si compounds. It is important for phases containing Li and not that important for pure Si. This gives us an idea that the thermal volume expansion from temperature is mainly due to Li. Another important thing to remark is that the thermal volume expansion seems to be important to consider after 350 K. We have almost reproduced the experimental lattice parameters at room temperature. And we have also reproduced quite well the concentration driven volume expansion of experiment despite being amorphous Si-Li compounds. Studying crystalline structures can give quantitatively an idea of the volume expansion.

Despite having improved the predicted OCV at 690 K relative to the experimental one (Fig. 2.42), the vibrational entropy contribution of ordered phases is not enough to reproduce the experimental one. We still fail to reproduce the stability of phases, specially around Li_7Si_3 composition. This was the motivation behind our work in off-stoichiometry studies (next chapter), we believe that they can help answer many questions that currently exist in the literature such as the stability/metastability of Li_7Si_3 or Li_5Si_2 phase.

Chapter 3

Non-stoichiometric and stoichiometric defects of Li-Si compounds

The previous chapter focused on investigating the thermodynamic properties, at finite temperatures, of Li-Si compounds under perfect stoichiometric conditions. So when it comes to comparing some of our results with experiments we find discrepancies from ignoring the off-stoichiometry of compounds.

To further expand our understanding of these materials, it becomes essential to transition from perfect stoichiometry to off-stoichiometry compounds. By deliberately introducing point defects and exploring non-stoichiometric compositions, we can delve into the complexities of Li-Si compounds.

Point defects do not only give us the off-stoichiometry of compounds but also give us important information about the ordered phases themselves. The presence of point defects can significantly affect the crystal structure and phase stability of Li-Si compounds. They lead to changes in the phase composition, phase transition temperatures, and thermodynamic stability. On another note, point defects can alter the lithium diffusion kinetics within Li-Si compounds which can play a critical role in the charge and discharge processes.

Since we have the formation energies of the point defects, we can use the low temperature expansion of the grand potential (LTE). By using the LTE, we can extract off-stoichiometry chemical potentials of Li and Si. These alone allow us to obtain off-stoichiometry properties (e.g. open circuit voltage) that can be compared directly with experimental off-stoichiometry results [35]. We invite the reader to refer to the section on GITT in Chapter 1 (Sec. 1.3.8) for more information on how the off-stoichiometry OCV is extracted experimentally.

Pairing our off-stoichiometry modeling with that of the experimental results allows us to validate/refute the (meta)stability of phases. For instance, the off-stoichiometry modeling of properties can tell us about the validity of phases with very close values in nominal composition (e.g. Li_5Si_2 vs Li_7Si_3 or $Li_{22}Si_5$ vs $Li_{17}Si_4$) by comparing to the experiment. We can also extract formation energies of point defects from experiments, and more specifically deduce the contribution from finite temperature effects on them.

We first start by presenting the model of the LTE as it is used in this work. We then do off-stoichiometry studies of many of the known Li-Si compounds including finite temperature contributions to the Gibbs free energy (that we present in the previous chapter). These studies contain a detailed presentation of the studied point defects and their formation energies. They also consist of comparisons with experimental data such as OCV, thermodynamic enhancement factor, and formation energies of point defects at 690 K [35].

3.1 Low temperature expansion of the grand potential

In this section we derive from LTE, the chemical potential as a function of formation energies of point defects and Li nominal composition. We also present how to include the vibrational entropy contribution in the LTE. We then present an analytical model of the LTE based on single interstitial/vacancy of Li and the derivation of all off-stoichiometry properties, a model that can be generalized when off-stoichiometry defects are single vacancy and interstitial of only one species.

The degree of off-stoichiometry of an A-B compound containing N_α atoms of species $\alpha = A, B$, with respect to a reference state containing N_α^0 atoms (by convenience, the pristine configuration), is evaluated as the change in number of species α:

$$\delta_\alpha = N_\alpha - N_\alpha^0. \tag{3.1}$$

Using the relationship between N_α and its chemical potential (μ_α) presented in Sec. 1.3.4, we compute δ_α:

$$\delta_\alpha = \sum_i \Delta N_\alpha^i M_i \exp\left(\frac{E_c^i}{k_B T}\right) \exp\left(\frac{\Delta N_\alpha^i \mu_\alpha}{k_B T}\right), \tag{3.2}$$

where the sum over i runs over configurations containing defects of type α (i.e. vacancies, interstitials, dimers, etc...). ΔN_α^i corresponds to the change of number of α species between configuration i and the reference state, M_i corresponds to the multiplicity of configuration i, and $E_c^i = E_0 - E_i$ is the configuration energy given by the difference in energy between configuration i (E_i) and the reference state (E_0).

We then easily relate the compound formulation $A_{a+\delta_A}B_{b+\delta_B}$ to the previous formulation $A_aB_{b+\delta}$ which is how Wen and Huggins studied the variation of OCV vs Li composition [35] (with $A \equiv$Si and $B \equiv$Li). The relation, therefore, between δ and δ_A, δ_B is:

$$\delta = \frac{a(b+\delta_B)}{a+\delta_A} - b. \tag{3.3}$$

Eq. 3.3 allows us to study the impact of all species defects on the unique off-stoichiometry parameter δ in a multi-element compound. However, we also need another equation that gives us the relationship between the chemical potential of the species, and for that we consider the grand potential $\mathcal{A}$ (recall Sec. 1.3.4, Eq. 1.33). At equilibrium $\mathcal{A} = 0$, therefore:

$$\mathcal{A}^0 - k_B T \sum_i M_i \exp\left(\frac{E_c^i + \Delta N_A^i \mu_A + \Delta N_B^i \mu_B}{k_B T}\right) = 0, \tag{3.4}$$

where $\mathcal{A}_0$ is the grand potential of the reference state and reads as:

$$\mathcal{A}^0 = E_0(A_{N_A^0}B_{N_B^0}) - N_A^0\mu_A - N_B^0\mu_B. \tag{3.5}$$

We use equations 3.4 and 3.5 to find the relationship between the chemical potentials of species in the compound. We then use Eq. 3.2 to find the relationship between the Li chemical potential and the nominal composition.

3.1.1 Including finite temperature effect from vibrational entropy in LTE

To account for the effect of vibrational contribution we replace the energy of the reference (E_0) in Eq. 3.5 by E_0^T (the energy of the reference including vibrational entropy contribution). We do not include the vibrational entropy of point defect formation because the computational cost of vibrational energy of a supercell with point defect is tremendously high. Consequently, as a first approximation, we assume that the formation energy of point defects is independent of temperature.

3.1.2 Formation energies of point defects from E_c

We can calculate the formation energy of the i^{th} point defect using Eq. 3.6 given that we know the chemical potential of the corresponding elements that concern the point defect of the configuration:

$$E_f^i = -E_c^i - \sum_{\alpha=A,B} \Delta N_\alpha^i \mu_\alpha, \tag{3.6}$$

where ΔN_α^i is positive or negative in case we have α interstitial or vacancy respectively.

Point defect concentration and effective formation energies

Once we have extracted the chemical potential from the LTE, we can proceed to calculate the α species point defect concentration C_γ^α (Eq. 3.7) and its corresponding effective formation energy $E_{ef,\gamma}^\alpha$ (Eq. 3.8) given that we have the set of non-symmetrical equivalent configurations ϕ that create the γ defect type associated with the species α (e.g. interstitial or vacancy of α):

$$C_\gamma^\alpha = \sum_{i\in\phi} |\Delta N_\alpha^i| \frac{M_i}{N_A^0} \exp\left(\frac{E_c^i}{k_B T}\right) \exp\left(\frac{\Delta N_\alpha^i \mu_\alpha}{k_B T}\right), \tag{3.7}$$

$$E_{ef,\gamma}^\alpha = -\, k_B T \ln C_\gamma^\alpha. \tag{3.8}$$

It is worth remarking that the point defect effective formation energy depends as well on the multiplicity of the defect (M_i) and the stoichiometry of the phase in question, these remarks will be proved later in the up-coming sections.

Binding energy of point defects

We can also extract the binding energy (E_b) of any two point defects with configurations $i = 1$ and $i = 2$ from their corresponding formation energies E_f^i and the formation energy containing the two defects together ($E_f^{1,2}$):

$$E_b^{1,2} = E_f^1 + E_f^2 - E_f^{1,2}, \tag{3.9}$$

such that if $E_b > 0$ the two point defects are attractive to each other, and otherwise repulsive when $E_b < 0$.

Frenkel Pair formation energy

To calculate the AA-Frenkel pair formation energy (E_f^{FP}) we can very simply sum the formation energies of interstitials (E_f^{int}) and vacancies of species A E_f^{vac}:

$$E_f^{FP} = E_f^{int} + E_f^{vac} \tag{3.10}$$

3.1.3 Point defects and off-stoichiometry

Before heading into the next sections it would of great help for the reader to understand how δ is related to point defect fractions. Going back to Eq. 3.3 with compound $A_a B_{b+\delta}$, we assume that A is Si and B is Li. Notice how interstitials and vacancies of Li will directly affect δ accordingly; vacancies of Li will make δ go towards lower values and interstitials of Li will make δ go towards higher values. For Si it will be the other way around, vacancies of Si will make Li content relatively higher and Si interstitials

will make Li content relatively lower; hence making the δ shift accordingly. A graphical representation is given resuming the behaviour of δ with respect to defects population in Fig. 3.1. Off stoichiometry point defects are those that make the δ change, in this work we only work with single interstitials or vacancies of Si or Li. Stoichiometry defects (AA-Frenkel pairs comprising vacancy and self interstitial of the same species A or Schottky) are those that keep the stoichiometry intact, in other words $\delta = 0$; in this work we do not make any specific calculations for those but they are naturally taken into account for $\delta = 0$ (e.g. when Li interstitial concentration is equal to Li vacancy concentration for AA-Frenkel pairs).

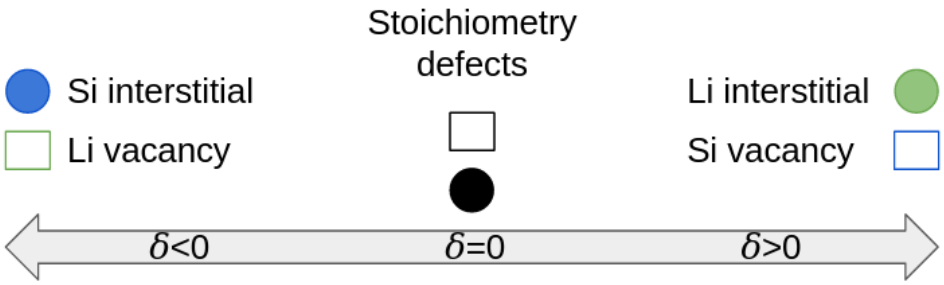

Figure 3.1: Graphical interpretation of δ with respect to point defects.

Interstitial sites

To investigate the possible interstitial configurations, we introduce a very fine 3D grid ($\approx 100\times100\times100$). For every site of the 3D grid we compute the distance between the site and the closest atoms. If the smallest distance calculated is greater than the threshold values of 1.2 Å then we include the site in the list of interstitial positions to be investigated.

Multiplicity

The multiplicity of a point defect is the number of symmetry equivalent sites in which the defect can be sitting, meaning that their corresponding configurations have the same formation energy. To calculate the multiplicity we count the symmetry equivalent sites in the unit cell. Note that, the number of equivalent sites can be found in the given multiplicities of Wyckoff sites in CIF files of the structures (given in the appendix C of this work).

3.1.4 Analytical calculation of off-stoichiometry properties: when point defects are interstitials and vacancies of the same species

Chemical potential

When the off-stoichiometry is governed by single defects of only one species (such as Li single vacancies and interstitials in the case of $Li_{12}Si_7$) we can obtain μ_{Li} as a function of composition from Eq. 3.2 only:

$$\delta = \sum_{i=\text{int}} (+1) M_i \exp\left(\frac{E_c^i}{k_B T}\right) \exp\left(\frac{(+1)\mu_{\text{Li}}}{k_B T}\right) + \sum_{i=\text{vac}} (-1) M_i \exp\left(\frac{E_c^i}{k_B T}\right) \exp\left(\frac{(-1)\mu_{\text{Li}}}{k_B T}\right) \tag{3.11}$$

$$= X_1 \exp\left(\frac{\mu_{\text{Li}}}{k_B T}\right) - X_2 \exp\left(\frac{-\mu_{\text{Li}}}{k_B T}\right), \tag{3.12}$$

where X_1 and X_2 correspond to the summation terms of the single interstitials and vacancies respectively. Therefore we can solve for μ_{Li} as a function of the other terms by replacing $e^{\mu_{\mathrm{Li}}/k_BT}$ by q and solving for the quadratic equation:

$$\delta = X_1 q - X_2 q^{-1} \implies X_1 q^2 + \delta q - X_2 = 0, \tag{3.13}$$

q is positive and non zero, hence we can only have one root and it gives us the value of μ_{Li} which reads as in Eq. 3.14:

$$\mu_{\mathrm{Li}} = k_B T \ln\left(\frac{\delta_n + \sqrt{\delta_n^2 + 4X_1X_2}}{2X_1}\right) \tag{3.14}$$

Open circuit voltage

After predicting the off-stoichiometry μ_{Li} at 690 K, we can calculate the OCV (refer to Sec. 1.3.7). We choose as the reference BCC Li G_p at 690 K (previous chapter). Note that at 690 K Li is liquid; however, in the previous chapter, we showed from the comparison of the Gibbs free energy of experimental values from CALPHAD [42] that the BCC Li is very similar and can be used as a reference. Hence the open circuit voltage (in V, since e is the charge of an electron) reads:

$$OCV = \frac{G_p(\mathrm{Li}) - \mu_{\mathrm{Li}}}{e}. \tag{3.15}$$

Effective formation energies

We calculate E_{eff}^{int} and E_{eff}^{vac}, the effective formation energies of interstitials and vacancies respectively from X_1, X_2 and μ_{Li} given by Eq. 3.14:

$$E_{eff}^{\mathrm{int}} = -k_B T \ln\left[\frac{X_1}{N_A^0}\exp\left(\frac{\mu_{\mathrm{Li}}}{k_B T}\right)\right], \tag{3.16}$$

$$E_{eff}^{\mathrm{vac}} = -k_B T \ln\left[\frac{X_2}{N_A^0}\exp\left(-\frac{\mu_{\mathrm{Li}}}{k_B T}\right)\right]. \tag{3.17}$$

Thermodynamic enhancement factor

Another property that has been studied by Wen and Huggins is the thermodynamic enhancement factor (ϕ) [35]. They define ϕ as a function of δ in $\mathrm{Li_{a+\delta}Si_b}$ as:

$$\phi(\delta) = \frac{1}{k_B T}(a+\delta)\frac{d(OCV)}{d(\delta)} = \frac{1}{e k_B T}(a+\delta)\frac{d(-\mu_{\mathrm{Li}})}{d(\delta)}, \tag{3.18}$$

where OCV stands for the open circuit voltage. Using Eq. 3.14 to replace μ_{Li} gives:

$$\phi(\delta) = (a+\delta)\frac{\sqrt{\delta^2 + 4X_1X_2} + \delta}{\delta\sqrt{\delta^2 + 4X_1X_2} + \delta^2 + 4X_1X_2}, \tag{3.19}$$

let $4X_1X_2 = X$, the derivative with respect to δ yields:

$$\frac{d\phi}{d\delta} = \frac{\left[\sqrt{\delta^2+X} + \delta + (a+\delta)\left(\frac{\delta}{\sqrt{\delta^2+X}} + 1\right)\right]\left[\delta\sqrt{\delta^2+x} + \delta^2 + X\right] - \left[\sqrt{\delta^2+X} + \frac{\delta^2}{\sqrt{\delta^2+X}} + 2\delta\right]\left[(a+\delta)\left(\sqrt{\delta^2+X} + \delta\right)\right]}{\left(\delta\sqrt{\delta^2+X} + \delta^2 + X\right)^2}, \tag{3.20}$$

when $\delta = \delta_{max} = X/a$ we obtain the maximum ($\frac{d\phi}{d\delta} = 0$). If we replace this δ_{max} back in Eq. 3.19 we obtain:

$$\phi(\delta_{max}) = (a + \frac{X}{a})\frac{\sqrt{\frac{X}{a}^2 + X} + \frac{X}{a}}{\frac{X}{a}\sqrt{\frac{X}{a}^2 + X} + \frac{X}{a}^2 + X}. \tag{3.21}$$

Notice that X is actually inversely proportional to the exponential of formation energy of Frenkel pairs (E_f^{FP}) because the formation energy of a single interstitial or vacancy of Li as a function of $E_c^i = E_0 - E_i$ is given by Eq. 3.6 hence:

$$E_f^{\text{int}} = -E_c^{\text{int}} - \mu_{\text{Li}},$$
$$E_f^{\text{vac}} = -E_c^{\text{vac}} + \mu_{\text{Li}}.$$

The formation energy of the Frenkel pair (FP) is in fact the summation of the formation energy of interstitial and vacancy:

$$E_f^{\text{FP}} = -E_c^{\text{int}} - E_c^{\text{vac}}. \tag{3.22}$$

We assume only the cheapest vacancy and interstitial , then $X = 4X_1X_2$ is written as:

$$X = 4m_{\text{int}}m_{\text{vac}} \exp\left(\frac{E_c^{\text{int}}}{k_BT}\right) \exp\left(\frac{E_c^{\text{vac}}}{k_BT}\right) = 4m_{\text{int}}m_{\text{vac}} \exp\left(\frac{E_c^{\text{int}} + E_c^{\text{vac}}}{k_BT}\right) = \frac{4m_{\text{int}}m_{\text{vac}}}{\exp\left(E_f^{\text{FP}}/k_BT\right)}. \tag{3.23}$$

For instance, in the case of Li-Si compounds $X \ll 1$. We can then simplify Eq. 3.21:

$$\phi(\delta_{max}) \approx \frac{a}{\sqrt{X}} \approx \frac{a}{2} \exp\left(\frac{E_f^{FP}}{2k_BT}\right) \tag{3.24}$$

this equation shows that ϕ increases as Frenkel pair formation energy increases.

From the demonstration above, we prove that, contrary to what Wen and Huggins suggest [35], the maximum of ϕ is not necessarily at $\delta = 0$ but rather very close to 0 ($\delta = \exp(-E_f^{FP}/k_BT)/a$). In other words, the higher the cost of Frenkel pair, the smaller X is, and therefore the closer the maximum will be to $\delta = 0$.

3.1.5 Methodology

The E_c^i of Eq. 3.2 are calculated from the difference in DFT energies between the pristine and defective structures using the PBE functional. The set of input parameters for VASP code consists of an energy convergence criterion for the self-consistent field (SCF) cycle of 0.1 meV, an energy cutoff of 750 eV for the plane-wave basis set, a maximum force on each atom is constrained to 0.03 eV/Å, a $2 \times 2 \times 2$ mesh for Brillouin zone is sampled using Monkhorst-Pack, and a super-cell size ensuring at least 10 Å between the periodicity of defects in all directions. We list all the supercell sizes in table 3.1 for the phases studied in the next sections.

Phase	Super cell size
$Li_{12}Si_7$	$2 \times 1 \times 1$
Li_7Si_3 $Li_{43}Si_{18}$	$2 \times 2 \times 1$
$Li_{13}Si_4$	$2 \times 1 \times 3$
$Li_{17}Si_4$ $Li_{21}Si_5$ $Li_{22}Si_5$	$1 \times 1 \times 1$

Table 3.1: Super cell sizes of pristine and defective structures for the calculations of E_c^i.

3.2 Off-stoichiometry studies of $Li_{12}Si_7$

In this section we calculate the point defect formation energies of $Li_{12}Si_7$ and from it the variation of OCV with the off-stoichiometry of $Li_{12}Si_7$. We also compute effective formation energies and thermodynamic enhancement factor of $Li_{12}Si_7$.

3.2.1 Point defects

Vacancies								
Label	E_f (eV)	m_i	**Label**	E_f (eV)	m_i	**Label**	E_f (eV)	m_i
Li0	0.3754	8/56	**Li8**	0.2699	8/56	**Si15**	1.8231	8/56
Li1	0.3771	8/56	**Li9**	0.2809	8/56	**Si16**	1.5986	8/56
Li2	0.5208	8/56	**Li10**	0.4434	8/56	**Si17**	1.9982	8/56
Li3	0.4485	8/56	**Li11**	0.3507	4/56	**Si18**	1.8145	4/56
Li4	0.8529	8/56	**Li12**	0.78	4/56	**Si19**	1.6687	4/56
Li5	0.5468	8/56	**Li8-Li9**	0.9653	8/56	**Si20**	1.1177	4/56
Li6	0.8375	8/56	**Si13**	1.8684	8/56	**Si21**	1.6476	4/56
Li7	0.5608	8/56	**Si14**	1.6623	8/56			

Interstitials		
Label	E_f (eV)	m_i
Li13	0.3635	4/56
Li14	0.1789	4/56
Li15	0.5282	4/56
Li13-Li13	1.4963	2/56
Si22	1.3210	4/56

Table 3.2: Table of formation energies of point defects in $Li_{12}Si_7$ with their respective multiplicity normalized by the number of Si atoms in the reference $m_i = M_i/N_{\mathrm{Si}}^0$. The Li and Si reference chemical potentials are extracted at $\delta = 0$ from LTE at T = 690 K.

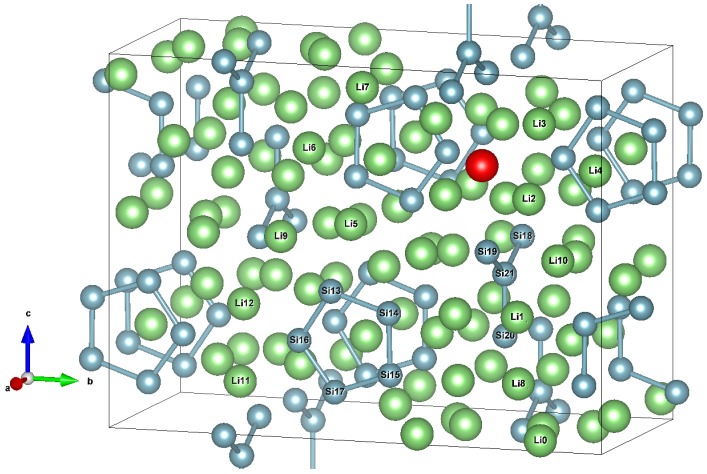

Figure 3.2: $Li_{12}Si_7$ unit cell labeled according to the "symmetric CIF" file found in Materials Project website [103] or appendix C. The red sphere represents the lowest in E_f interstitial site for Li (Li14) and its coordinates are a=0.95, b=0.75 and c=0.75 (in fractions of lattice parameters).

We list, in table 3.2 with the help of Fig. 3.2, the E_f of most $Li_{12}Si_7$ point defects using as a reference the chemical potential of Li and Si at $\delta = 0$ in $Li_{12+\delta}Si_7$ and T = 690 K. The predicted values of point defect E_f suggest that the off-stoichiometry of this phase is driven exclusively by Li defects of both interstitial and vacancy nature, because the E_f of Si defects is really high compared to their Li counterparts. The binding energies of Li8-Li9 vacancies and Li13-Li13 interstitials are -0.415 and -0.770 eV respectively suggesting that the isolated defects are more energetically stable than in pairs. Therefore, in the present study, we choose to neglect all defects other than Li interstitials/vacancies, which can in fact reduce the complexity in extracting the Li chemical potential as a function of composition. The energetically lowest Frenkel pair to create is the one of Li14 interstitial plus Li8 vacancy with a value of 0.452 eV.

3.2.2 Properties of $Li_{12}Si_7$ in single phase domain

The dominant point defects in the off-stoichiometry regime of $Li_{12}Si_7$ are Li vacancies and interstitials. This means that we can use the analytical formulations presented in Sec. 3.1.4 for the calculation of properties.

The plot of the OCV vs composition can be found in Fig. 3.3. Because the point defect properties only depend on the variation of OCV with δ, the importance here is to reproduce the slope of the experimental line between the two plateaus. To reproduce the plateaus we must include the 2-phase-equilibria with the previous and next phase, something that will be tackled in the next chapter. It is also worth noting that changes, in the order of 10 meV, in E_c in Eq. 3.3 can lead to significant changes in the slope. The result obtained here is satisfactory given the DFT accuracy.

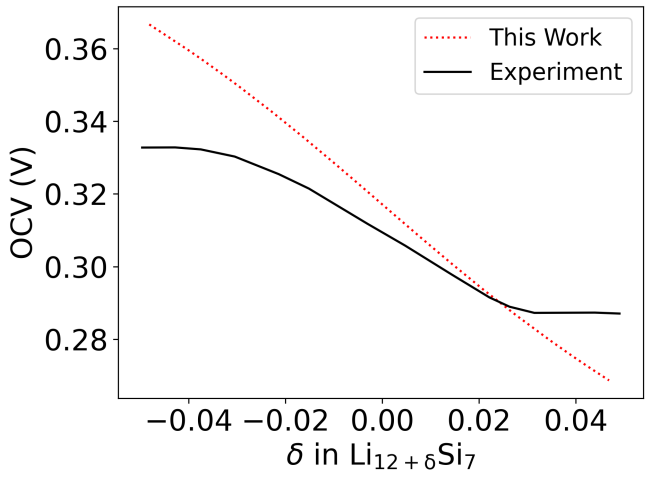

Figure 3.3: Plot of the $Li_{12}Si_7$ OCV vs composition. Comparison with experiment by Wen and Huggins at 690 K [35]; the Li of the counter electrode is liquid at 690 K.

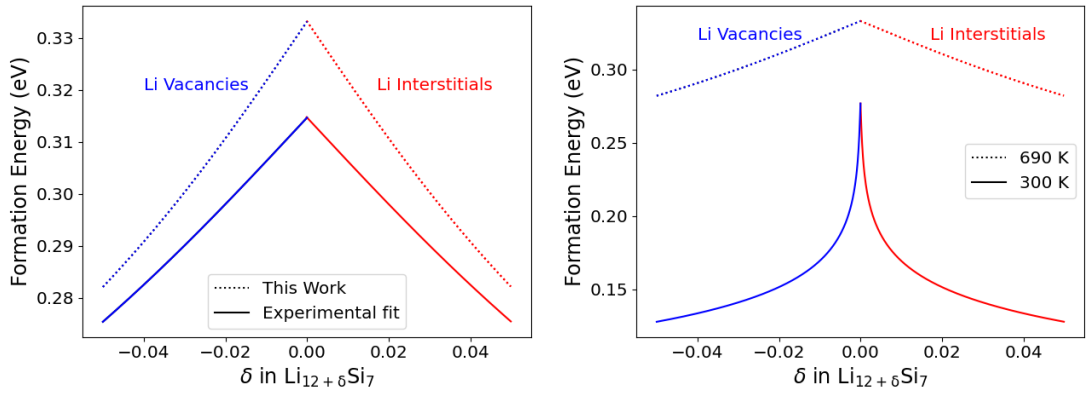

(a) (b)

Figure 3.4: Plot of the $Li_{12}Si_7$ effective formation energies vs composition. (a) Comparison with experiment by Wen and Huggins at 690 K [35]. (b) Our results at temperatures 690 K and 300 K.

To see the level of agreement between the experiment and our predicted values we can also look at the effective formation energy of point defects as shown in Sec. 3.1.2. We calculate the effective formation energies using our predicted values and the values coming from a fit of the experimental OCV based on our LTE model (to obtain X_1 and X_2). We plot the effective formation energies as a function of composition at 690 K and 300 K in Fig. 3.4. We observe a discrepancy of 0.02 eV at most at $\delta = 0$ at 690 K, this discrepancy can be related to DFT inaccuracies or the fact that we did not include the effect of vibrational entropy on E_c for Li.

Our model predicts effective formation energies of Frenkel pairs with values of 0.63 eV and 0.54 eV at 690 K and 300 K respectively at $\delta = 0$. The way we modeled the effective formation energies (in Sec. 3.1.2) implies that the lower the temperature the less significant the contribution of the multiplicity in the effective formation energy ($-k_B T \ln(M_i/N_{\mathrm{Si}}^0)$). In fact, comparing these results to the ones in tab.

3.2, we see that we are converging to the values of the most stable Frenkel pair formation energy as we decrease the temperature (0.45 eV).

We plot our predicted enhancement factor ϕ as a function of composition in Fig. 3.5. The comparison with experiment suggests that we manage to reproduce qualitatively the maximum. For the quantitative comparison, it is important to keep in mind that, we are comparing the exponential of point defect formation energies. We can use Eq. 3.24 to extract the differences in Frenkel pair formation energy between our predicted values and experiment at the maximum of ϕ. The experimental Frenkel pair effective formation energy is predicted to be around 0.63 eV while ours is predicted to be 0.67 eV; the experimental cheapest E_f^{FP} is predicted to be 0.41 eV vs our modeled one predicted to be 0.45 eV (reported above). The differences are of order of 10 meV. Which, again (similar to what happens to the slope of OCV), can be related to the lack of vibrational entropy contribution in Li E_c or DFT accuracy itself. It can also be due to the interaction between the point defects of the Frenkel pair which is ignored in the present study. For instance, a slight attraction between point defects would decrease the Frenkel pair formation energy.

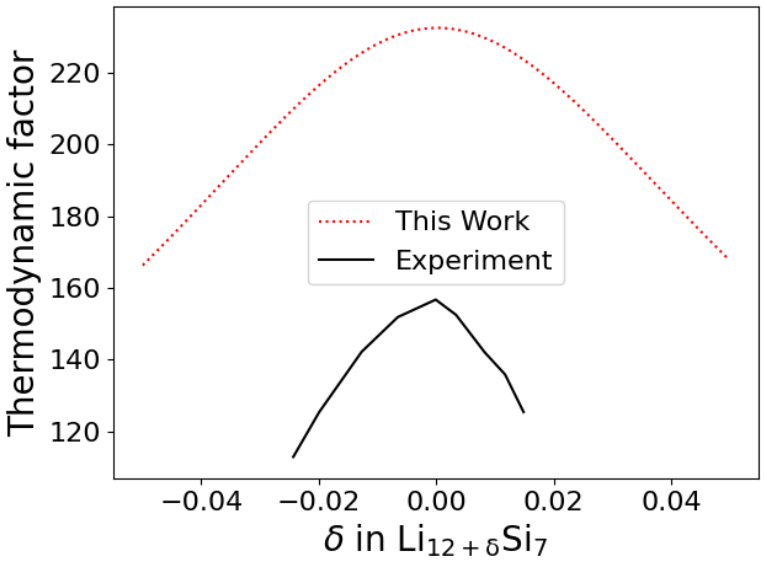

Figure 3.5: Plot of the $Li_{12}Si_7$ thermodynamic enhancement factor vs composition. Comparison with experiment by Wen and Huggins at 690 K [35].

3.3 Off-stoichiometry studies of vacancy superstructures of Li_5Si_2

In this range of composition, we have highlighted a series of line compounds differing by the Li-sublattice. For this section we investigate the phases between Li_7Si_3 and Li_5Si_2. Wen and Huggins report this phase to be the Li_7Si_3 with a composition of $x = 2.367$ in Li_xSi [35], which is closer in composition to $Li_{43}Si_{18}$ ($x = 2.389$) than to the perfect stoichiometric Li_7Si_3 ($x = 2.333$). In this section we calculate formation energy of point defects, and calculate the off-stoichiometry properties of Li_7Si_3, $Li_{43}Si_{18}$, and Li_5Si_2.

To facilitate the understanding of the structures under this chapter we can define some terms. As already shown previously (Sec. 2.2.1), these structures consist of columns each one containing 1 Si dumbbell and at least 4 Li. We define columns of type A as the one with 5 Li and 1 Si dumbbell and type B as the one with 4 Li and 1 Si dumbbell.

3.3.1 Origin of vacancy superstructure ordering

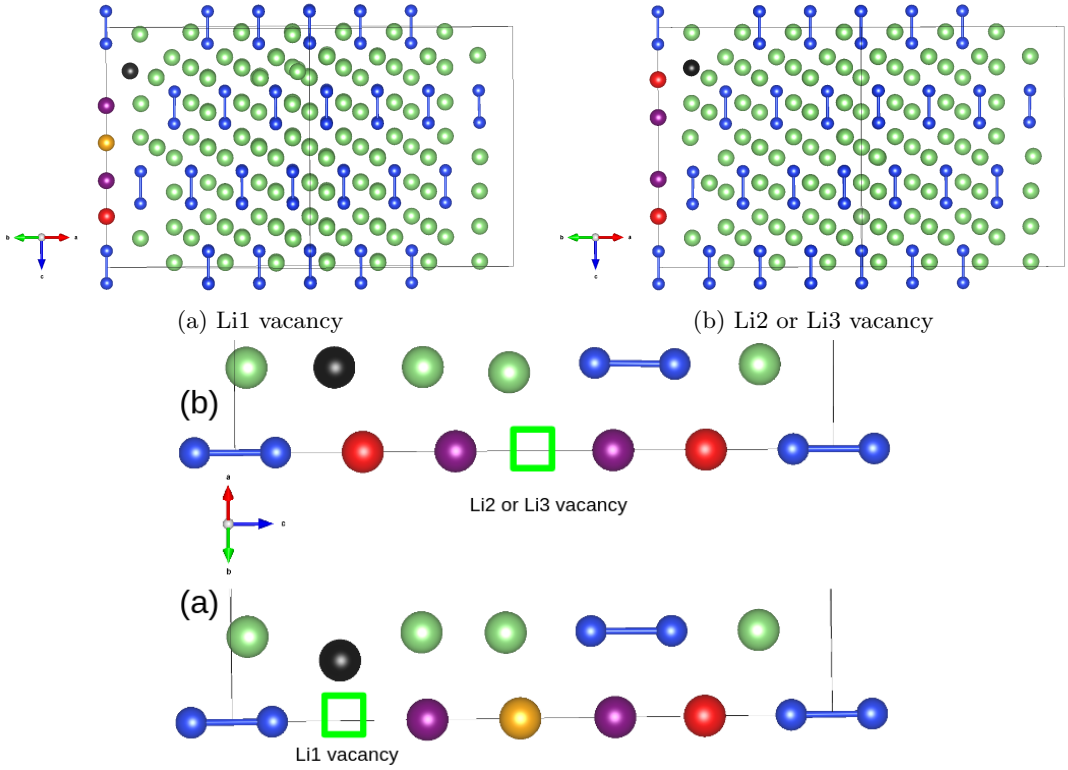

(a) Li1 vacancy

(b) Li2 or Li3 vacancy

(c) Zoomed in

Figure 3.6: Structures of $4 \times 4 \times 1$ Li_5Si_2 super-cell after relaxation including the Li1, Li2 or Li3 vacancy sites. The red, purple, and yellow colored spheres represent the Li1, Li2 and Li3 sites respectively, and the black colored sphere represents the Li3 site of the neighboring column. (c) Represents the zoomed (in the columns containing the vacancy) version of (a) and (b).

The work of Chevrier et al. [116] indicates that both structures the fully ordered Li_5Si_2 and Li_7Si_3, represent the $Li_{2.333}Si$ phase that can be formed experimentally. However, Li_5Si_2 and Li_7Si_3 have different crystallographic symmetries. Li_7Si_3 can be obtained from Li_5Si_2 by placing 3 Li3 vacancies in a super-cell of Li_5Si_2. Therefore, Li_7Si_3 is a vacancy superstructure of Li_5Si_2 and the investigation of vacancy formation energy in Li_5Si_2 should give valuable information.

Tipton et al. [44] report vacancy formation energies valued at 0.049 eV, 0.010 eV, 0.015 eV and 1.11 eV for the Li1, Li2, Li3 and Si (check 3.6 for Li sites) respectively using a cell of 168 atoms ($2 \times 2 \times 2$ super-cell) using the 2-phase-equilibrium $Li_{12}Si_7$-Li_5Si_2 chemical potential of Li and Si at 0 K as reference. We also calculated our own values using a larger supercell of 336 atoms ($4 \times 4 \times 1$ super-cell), in order to ensure at least 16 Å in all directions between images. We report values of 0.0330 eV, 0.0025 eV, 0.0036 eV and 1.4170 eV respectively using our 2-phase-equilibrium $Li_{12}Si_7$-Li_5Si_2 chemical potential of Li and Si as reference as well. The values differ due to supercell size -which can influence the interaction between point defect images- and also due to differences in the parameters of calculation. However, in terms of relative values we are consistent with Tipton et al.: Li3 is the cheapest vacancy to create followed by Li2 and then Li1. Although not mentioned in [44], both Li2 and Li3 vacancies after full relaxation lead to the

same Li3 vacancy site (Fig. 3.6b) despite having different formation energy values. We do not observe any differences in morphology, therefore we believe that this difference is due to accuracy from the DFT calculations.

Creating a Li1 vacancy leads to a stable configuration of a divacancy with a self interstitial. The cost of creating such defect is at least 1 order of magnitude higher than its counterparts Li2 and Li3 vacancies. A Li3 -being the most favorable vacancy to make- would leave its site to become a self-interstitial in between two columns to compensate for the Li1 vacancy in the other column. This can be associated to an attraction between Si and Li. We report a Li1 vacancy to be at least 9 times higher in cost than its Li2 and Li3 counterparts. In other words if we form a column of type B it prefers to have the Li vacancy to be farthest it can from the Si dumbbell. Moreover, both our calculations and [44] report Si vacancies to be extremely expensive when in equilibrium with $Li_{12}Si_7$.

Regardless of which site, the formation energies of Li vacancies in Li_5Si_2 is low compared to k_BT and even negative at specific values of Li chemical potential. Which leads to high amount of Li vacancies. Consequently, it is crucial to consider the way the vacancies interact with each other (or equivalently how the Li3 atoms interact with one another). To make accurate predictions about the vacancy concentrations, a more in-depth analysis that takes into account these interactions is required.

Defect	E_f (eV)	m_i
Li3 vacancy	0.3905	3/6
Si vacancy	0.1404	6/6
Li4 interstitial	1.5113	3/18

Table 3.3: Table of formation energies of point defects in Li_5Si_2 with their respective multiplicity normalized by the number of Si atoms in the reference $m_i = M_i/N^0_{\mathrm{Si}}$. The Li and Si reference chemical potentials are extracted at $\delta = 0$ from LTE at T = 690 K.

We list the formation energies of point defects at perfect stoichiometry at 690 K in table 3.3 with the help of Fig. 3.7. We remark the high formation energy of Li interstitials compared to their Si vacancy counterpart for $\delta > 0$ off stoichiometry. The system would rather create Si vacancies, specially at $\delta = 0$, than to create Li4 interstitials.

A thought on diffusion

We can also suggest how Li3 diffuse from one column to the other. It is all thanks to the Li3 site in the neighboring column that can potentially jump from Li3 site to the Li1 vacancy site. Further investigation (e.g. calculation of energy barrier) is needed here to draw a conclusion.

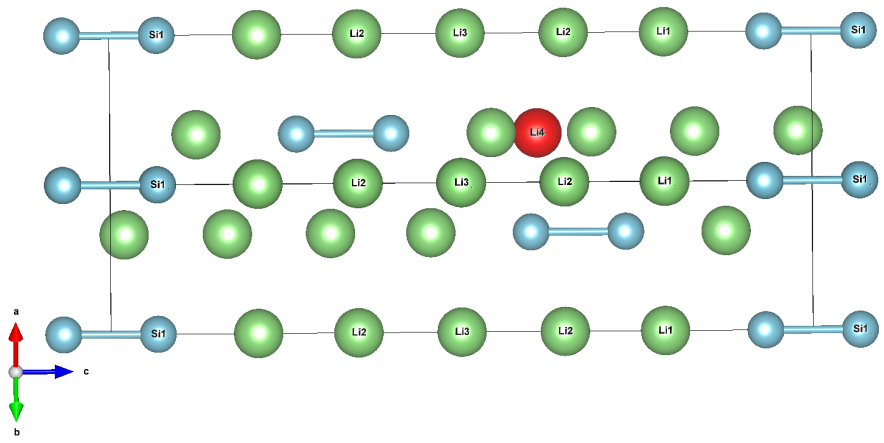

Figure 3.7: Li_5Si_2 unit cell labeled according to the CIF published by Valencia et al. [46]. The red sphere represents Li4 and its coordinates are a=0.3949, b=0.066 and c=0.6098 (in fractions of lattice parameters).

3.3.2 Point defects in Li_7Si_3

We list, in table 3.4 with the help of Fig. 3.8, the E_f of most Li_7Si_3 point defects using as a reference the chemical potential of Li and Si at $\delta = 0$ in $Li_{7+\delta}Si_3$ and at T = 690 K.

Vacancies					
Label	E_f (eV)	m_i	**Label**	E_f (eV)	m_i
Li0	0.2884	6/18	**Li6**	0.1502	3/18
Li1	0.4575	6/18	**Li7**	0.1970	3/18
Li2	0.2295	6/18	**Li6-Li7**	0.7238	6/18
Li3	0.3484	6/18	**Si8**	1.3848	6/18
Li4	0.2872	6/18	**Si9**	1.4495	6/18
Li5	0.2606	6/18			

Interstitials		
Label	E_f (eV)	m_i
Li8	0.1044	3/18
Li8-Li8	0.2774	3/18
Si10	1.1713	3/18

Table 3.4: Table of formation energies of point defects in Li_7Si_3 with their respective multiplicity normalized by the number of Si atoms in the reference $m_i = M_i/N^0_{\mathrm{Si}}$. The Li and Si reference chemical potentials are extracted at $\delta = 0$ from LTE at T = 690 K.

The predicted values of point defect E_f, like for Li_7Si_3, suggest that the off-stoichiometry of this phase is driven exclusively by Li defects of both interstitial and vacancy nature. The binding energy of a pair of Li8 interstitials and Li6-Li7 vacancies are -0.0686 eV and -0.3766 eV respectively meaning that these are less energetically stable than their isolated counterparts. Overall, we can neglect all defects other than Li interstitials/vacancies.

The reader might find it easier to look at Li_7Si_3 as 6 columns of type A and 3 columns of type B (recall the introduction to Sec. 3.3). Notice from tab. 3.4 how expensive it is to create the Li1 and Li3 vacancies compared to the rest, this is because these are vacancies that belong to a column B. Whereas Li6 and Li7 are the cheapest vacancies to create because they are at the centered Li site (furthest separated from the Si dumbbell) of each column A. Generally, we can see that the vacancies prefer not to be in the column B, and if they are in column A they prefer to be the farthest possible from the Si dumbbell -this

behaviour is not any different than the one observed already previously in Li_5Si_2. The Si vacancy, similar to what happens with Li_5Si_2, is so expensive to create because it would require destroying the bond of Si dumbbell. We prove that creating 2 nearest neighbour Li vacancies (Li6-Li7) is high in formation energy (more than 4 times more expensive than Li6 vacancy) they have a binding energy of -0.37 eV meaning it is rather repulsive between them. Due to the repulsive interaction, vacancies prefer to be at a different z coordinates -which explains why Li_7Si_3, for example, has 3 B type columns with different z coordinate for the Li3 vacancy sites in its unit cell. Same can be said about $Li_{43}Si_{18}$ and the 2 B type columns.

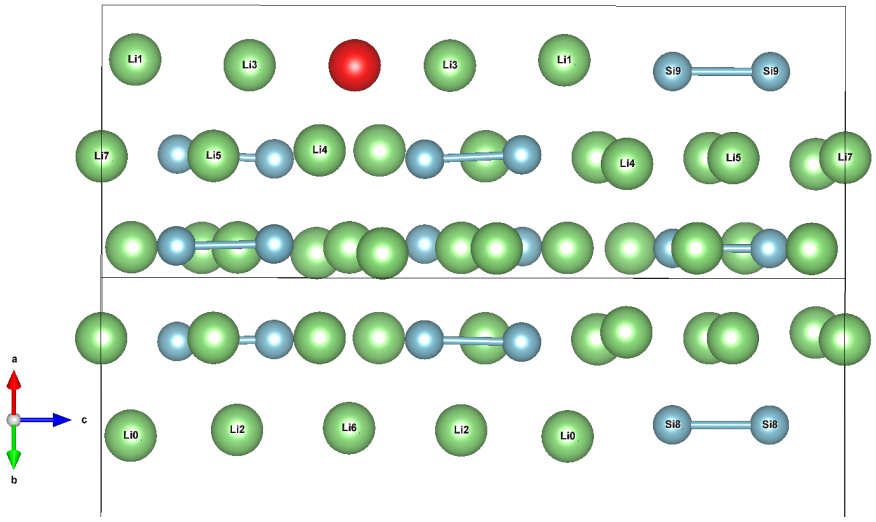

Figure 3.8: Li_7Si_3 unit cell labeled according to the symmetric CIF file found in Materials Project website [103] or in the appendix C. The red sphere represents the interstitial site for Li8 and its coordinates are a=0.22, b=0.77 and c=0.66 (in fractional).

The Li interstitials prefer to be at the "Li3" site of the column A. In fact, adding 1 Li interstitial is the cheapest point defect to be created. This is in line with the stability of our novel $Li_{43}Si_{18}$ phase. It is to be reminded to the reader that this E_f is calculated for a $2 \times 2 \times 1$ super-cell, so adding 4 Li8 interstitials leads to $Li_{43}Si_{18}$, or 12 Li8 interstitials leads to Li_5Si_2. It can be interesting to look at the convex hull between Li_7Si_3 and Li_5Si_2 supercells ($Li_{168}Si_{72}$ and $Li_{180}Si_{72}$ respectively) to study the ordering of vacancies in the superstructure.

3.3.3 Family of Li_5Si_2 vacancy superstructures

To make sure that we have no other intermediary stable phases between Li_7Si_3 and Li_5Si_2, we perform several DFT calculations at different Li concentrations of the farthest Li vacancy from the Si dumbbell (denoted Li3 in Li_5Si_2) varying from Li_7Si_3 to Li_5Si_2. Fig. 3.9 shows the 12 lattice sites that can be filled with Li atoms. We find from the calculations of the formation energies at 0 K in Fig. 3.10 that the transition from Li_7Si_3 to Li_5Si_2 requires Li to completely fill a plane (with no particular order) before being able to fill another plane. Hence, the most energetically (meta-)stable phase for a particular composition are the ones that try to fill a plane (of Li3 lattice sites) before filling another one. For example, the configuration with two filled Li3 sites prefers that these 2 Li belong to the same plane (most stable configuration) than each in two different planes (least stable configurations). The convex hull of stability shows $Li_{43}Si_{18}$ and $Li_{44}Si_{18}$ are stable phases (which require 1 and 2 completely Li filled planes as shown in Fig. 3.9).

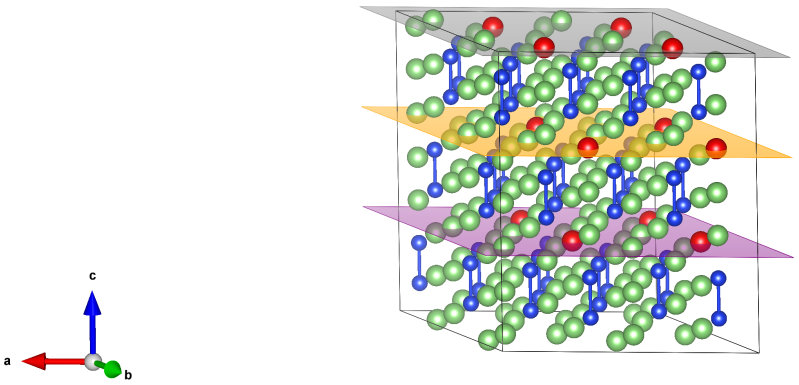

Figure 3.9: Li_7Si_3 $2 \times 2 \times 1$ super-cell where the red spheres denote the places that Li can fill. The grey, yellow, purple planes denote the lattice [001] planes that contain the 12 sites (4 each plane) that Li fills in order to become Li_5Si_2.

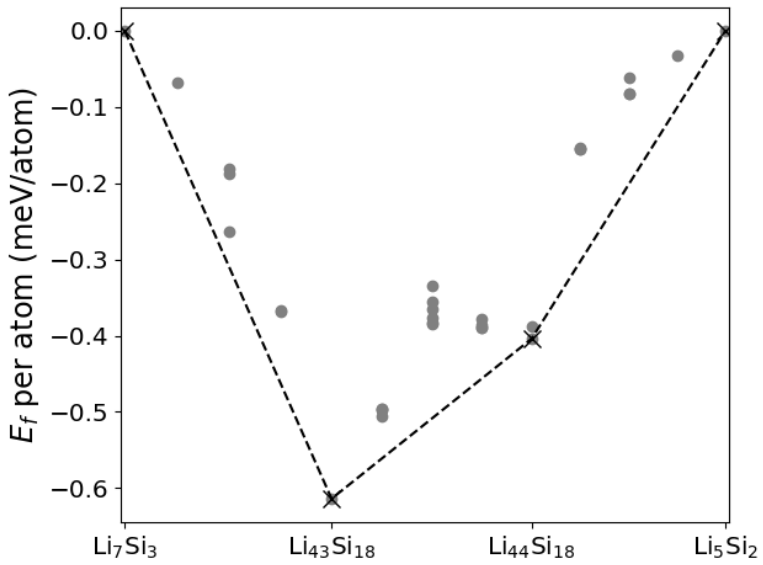

Figure 3.10: Plot of the formation energies of vacancy ordered superstructures of Li_5Si_2. Convex hull of stability (black dashed line) is constructed showing the stable phases marked by '×'. To calculate the $E_f(Li_aSi_b)$ we use the chemical formula $Li_7Si_3 + Li_5Si_2 \longrightarrow Li_aSi_b$

3.3.4 Point defects in $Li_{43}Si_{18}$

We can extract the most stable Li point defect formation energies of $Li_{43}Si_{18}$ from Fig. 3.10. Since we know already from Li_7Si_3 that Li interstitial and vacancies govern the off-stoichiometry, we expect the same to be for $Li_{43}Si_{18}$. We list in table 3.5 the two most stable point defects formation energies at 690 K, and at perfect stoichiometry.

Defect	E_f (eV)	m_i
Li vacancy	0.0719	1/18
Li interstitial	0.1131	2/18

Table 3.5: Table of formation energies of point defects in $Li_{43}Si_{18}$ with their respective multiplicity normalized by the number of Si atoms in the reference $m_i = M_i/N^0_{\mathrm{Si}}$. The Li reference chemical potential is extracted at $\delta = 0$ from LTE at T = 690 K.

3.3.5 Thermodynamic properties of the stable Li_5Si_2 superstructures in their single phase domain

We rely on LTE to compute thermodynamic properties in the single phase domains. For instance, because the off-stoichiometry is governed by Li interstitials and vacancies for the phases Li_7Si_3 and $Li_{43}Si_{18}$ we use the same analytical model as proposed in Sec. 3.1.4 for the calculation of off-stoichiometry properties. Notice that for the comparison between $Li_{43}Si_{18}$ and the experimentally reported Li_7Si_3 we assume that the composition of Li_7Si_3 can be amended.

We plot the predicted OCV of both Li_7Si_3 and $Li_{43}Si_{18}$ (which we may refer to as $Li_{7.17}Si_3$) in Fig. 3.11. We observe the OCV of the Li_7Si_3 compound is significantly above the reported measured OCV around the Li_7Si_3 stoichiometry; where as for the $Li_{43}Si_{18}$ we observe a small underestimation compared to the experiment [35]. Moreover, the slope of $Li_{43}Si_{18}$ is closer to the experimental one than that of the Li_7Si_3 -recall that the slope is related to the formation energies of point defects.

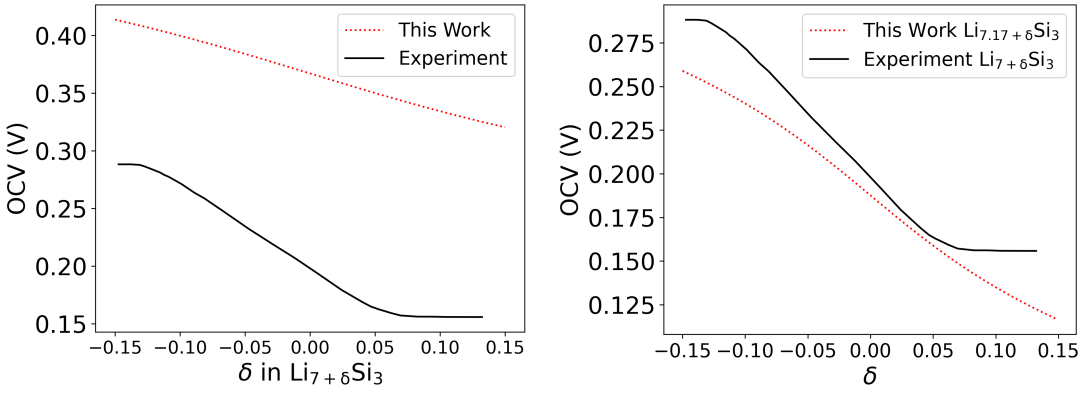

(a) Li_7Si_3 (b) $Li_{43}Si_{18}$

Figure 3.11: Plot of the Li_7Si_3 and $Li_{43}Si_{18}$ OCV at 690 K vs composition. Comparison with experiment by Wen and Huggins at 690 K [35] which uses liquid lithium at 690 K as reference. We remark that for the comparison of $Li_{43}Si_{18}$ and Li_7Si_3 (Fig. b) we assume that the experimental composition could be wrong.

We plot the effective formation energies of both Li_7Si_3 and $Li_{43}Si_{18}$ Li point defects as a function of composition in Fig. 3.12. We extract the effective formation energies from the composition dependent experimental OCV from the experimental values using the LTE function. The discrepancy between our predicted formation energies and experiment goes up to 0.06 eV at $\delta = 0$ which is small in DFT accuracy. However, the differences in values between $Li_{43}Si_{18}$ and experiment (0.02 eV at $\delta = 0$) are at least 3 times less than those of Li_7Si_3 (0.06 eV at $\delta = 0$).

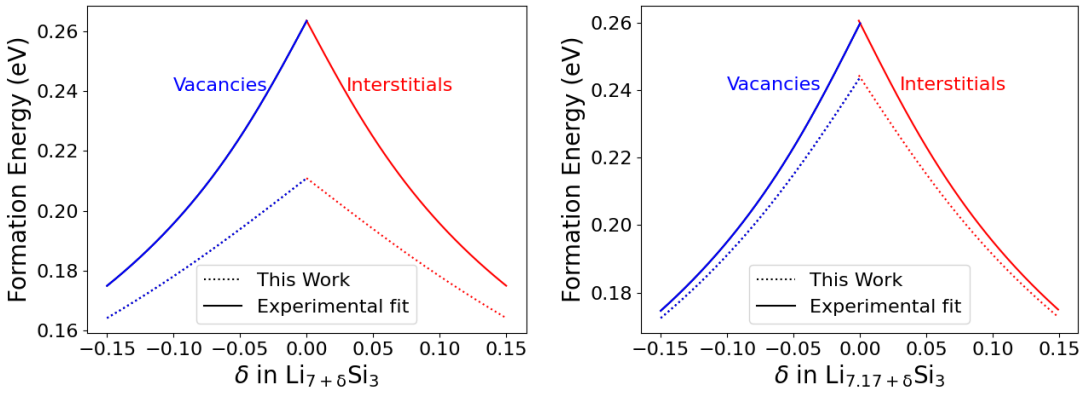

(a) Li_7Si_3 (b) $Li_{43}Si_{18}$

Figure 3.12: Plot of the Li_7Si_3 and $Li_{43}Si_{18}$ effective formation energies of point defects at 690 K vs composition. Comparison with experiment by Wen and Huggins at 690 K [35]. We remark that for the comparison of $Li_{43}Si_{18}$ and Li_7Si_3 (Fig. b) we assume that the experimental composition could be wrong.

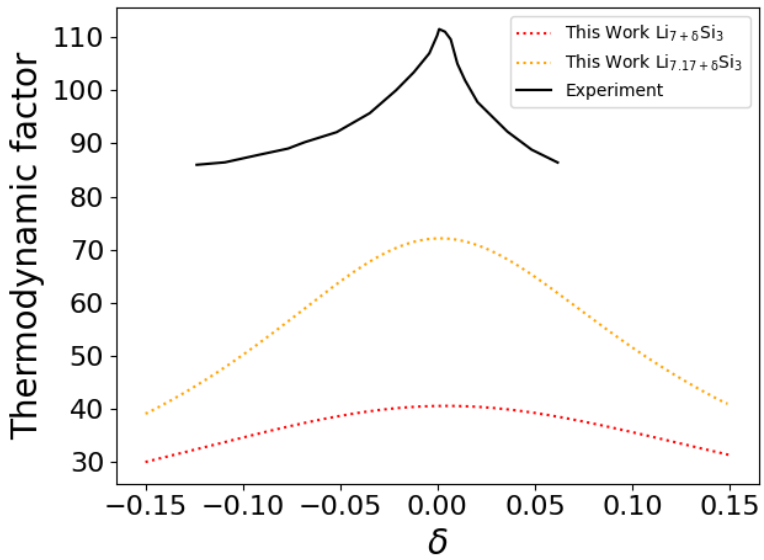

Figure 3.13: Plot of the Li_7Si_3 (in red) and $Li_{43}Si_{18}$ (in yellow) of the thermodynamic enhancement factor vs composition. Comparison with experiment by Wen and Huggins at 690 K [35]. We remark that for the comparison of $Li_{43}Si_{18}$ and Li_7Si_3 we assume that the experimental composition could be wrong.

We calculate the thermodynamic enhancement factor of both Li_7Si_3 and $Li_{43}Si_{18}$ as a function of composition and plot it in Fig. 3.13. Not only we have a good qualitative agreement because we reproduce a maximum at $\delta = 0$ but also lack quantitative agreement because the values are approximately 1.5 times higher (with $Li_{43}Si_{18}$ values) for the experiment. Nonetheless, the thermodynamic enhancement factor deduced from $Li_{43}Si_{18}$ is much closer to the experiment than the one deduced from Li_7Si_3.

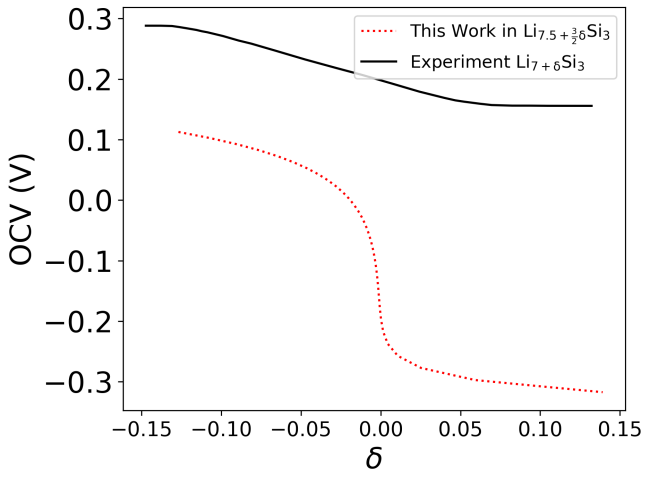

Figure 3.14: Plot of the Li_5Si_2 OCV vs composition. Comparison with experiment (Li_7Si_3) by Wen and Huggins at 690 K [35] which uses liquid lithium at 690 K as reference.

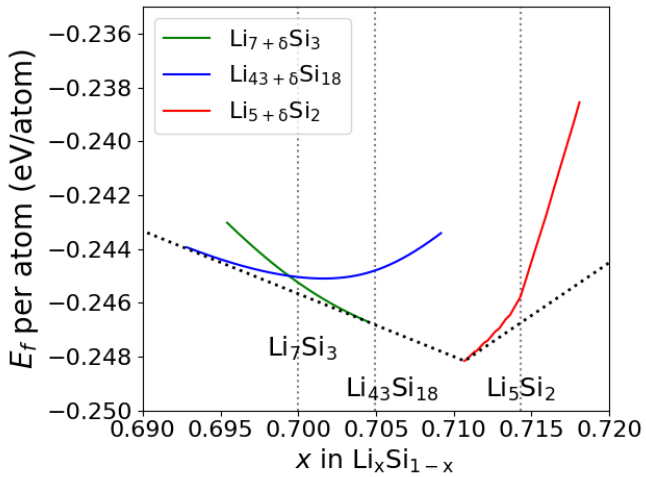

Figure 3.15: Plot of the Li_7Si_3, $Li_{43}Si_{18}$, and Li_5Si_2 off stoichiometry formation energies per atom at 690 K vs composition. The black dotted line represents the convex hull of stability and the grey vertical lines represent the perfect stoichiometry composition of the phases.

We plot our predicted Li_5Si_2 OCV vs composition in Fig. 3.14. We observe a good agreement in the slope for $\delta < 0$ and large discrepancy for $\delta > 0$. For $\delta > 0$, we already know that formation energies of

point defects such as vacancy of Si or Li interstitials is really high. This suggests that around $\delta < 0$ in composition for $Li_{5+\delta}Si_2$, Li_5Si_2 is under-stoichiometric with Li3 vacancies.

The very good agreement between the experiment OCV and the calculated one suggest that $Li_{43}Si_{18}$ is actually the investigated experimental phase at 690 K. However, the QHA finite temperature convex hull presented in Chapter 2 suggested that only Li_7Si_3 is a stable phase at 690 K. Nonetheless, Fig. 3.15 suggests that all 3 phases are stable in the off-stoichiometry regime. For instance, $Li_{7+\delta}Si_3$ is stable when $\delta > 0$ (when it has interstitials of Li), $Li_{43+\delta}Si_{18}$ is stable when $\delta < 0$ (when it has vacancies of Li), and $Li_{5+\delta}Si_2$ is stable when $\delta < 0$ (when it has vacancies of Li). At high temperature, far from perfect stoichiometry, ordered or disordered phases with partially filled Li-sublattices might be more stable than ordered phases with a few point defects. Nonetheless, the good agreement observed between the OCV of $Li_{43}Si_{18}$ and the experimental one tends to show that $Li_{43}Si_{18}$ phase is the one that has been experimentally characterized at 690 K [35].

A comparison with the stability of a vacancy disordered solid solution should be done. The composition domain of such a vacancy-disordered solid solution would cover the Li_7Si_3-Li_5Si_2 composition interval.

3.4 Off-stoichiometry studies of $Li_{13}Si_4$

In this section we calculate the point defect formation energies of $Li_{13}Si_4$ and extract the off-stoichiometry OCV, effective formation energies and thermodynamic enhancement factor of $Li_{13}Si_4$. We also introduce a model for extracting vibrational contribution to the Si point defect formation energies.

3.4.1 Point defects

We list, in table 3.6 with the help of Fig. 3.16, the E_f of most $Li_{13}Si_4$ point defects using as a reference the chemical potential of Li and Si at $\delta = 0$ in $Li_{13+\delta}Si_4$ and T = 690 K. Unlike the phases discussed above, $Li_{13}Si_4$ has relatively lower Li dimer formation energy, and higher Si interstitial formation energy. The binding energy of the Li8 dimer is positive and equal to 0.60 eV at $\delta = 0$ and 690 K, which means that this point defect strongly prefers to be in pairs rather than alone.

Despite being lower in cost than Si interstitials, Li vacancies are not the point defect that govern the $\delta < 0$ regime of $Li_{13+\delta}Si_4$ at 690 K. At this temperature, we cannot ignore the contribution of the point defect multiplicity to the equilibrium concentration of point defects. As we discuss in Sec. 3.2, the effective formation energies of Frenkel pairs strongly depends on the multiplicity at 690 K. The case here, however, is a bit more complicated than just the intrinsic multiplicity of the defect. We need to take into account the stoichiometry of the phase in question. Including one Si interstitial is equivalent to removing 3.25 Li (by stoichiometry) in the case of $Li_{13}Si_4$. We could say that if the formation energy of a point defect (e.g. Si interstitial in $Li_{13}Si_4$) is not significantly larger and yet it contributes stoichiometry-and-multiplicity-wise more times than the cost ratio with respect to another point defect (e.g. Li vacancy in $Li_{13}Si_4$) we should not neglect the former point defect. We show in Fig. 3.19 that the Si interstitial effective formation energy is lower than the one of Li vacancies.

Vacancies					
Label	E_f (eV)	m_i	**Label**	E_f (eV)	m_i
Li0	0.7373	4/8	**Li5**	0.7437	4/8
Li1	0.7011	4/8	**Li6**	0.5248	2/8
Li2	0.6744	4/8	**Si7**	1.3288	4/8
Li3	0.4575	4/8	**Si8**	1.5612	4/8
Li4	0.6779	4/8			

Interstitials		
Label	E_f (eV)	m_i
Li8	0.5393	4/8
Li8-Li8	0.4720	2/8
3-Li8	0.9504	4/8
4-Li8	1.2811	1/8
Si10	0.7052	4/8

Table 3.6: Table of formation energies of point defects in $Li_{13}Si_4$ with their respective multiplicity normalized by the number of Si atoms in the reference $m_i = M_i/N^0_{Si}$. The Li and Si reference chemical potentials are extracted at $\delta = 0$ from LTE at T = 690 K.

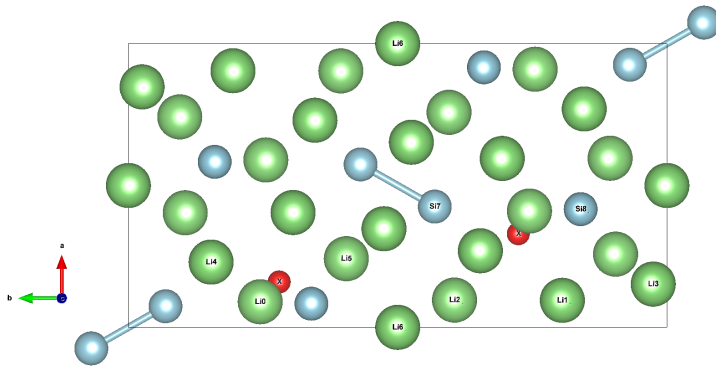

Figure 3.16: $Li_{13}Si_4$ unit cell labeled according to the "symmetric CIF" file found in Materials Project website [103] or in the appendix C. The red spheres represent the cheapest in E_f di-interstitial sites for Li and their coordinates, in fractions with respect to lattice parameters, are (0.16, 0.72, 0.16) and (0.33, 0.276, 0.16). The red spheres are symmetrically equivalent and also represent the Si10 site.

A thought on diffusion

The high point defect formation energy at perfect stoichiometry (compared to all phases) suggests that this phase has a lower diffusion coefficient relative to all other phases since the activation energy of diffusion mediated by point defects is the sum of the point defect formation energy and migration barrier [117]. Besides, the variation of E_f with δ is also high, which could explain the observed significant variation of the Li experimental diffusion in [35]. Indeed, Wen and Huggins measure a diffusion coefficient that depends on the composition of Li unlike the others, lowest at $\delta = 0$ and higher at $|\delta| > 0$ in $Li_{13+\delta}Si_4$ [35]. At $\delta = 0$ Wen and Huggins report this phase to have the lowest diffusion coefficient valued at 2.88×10^{-7} cm^2/s.

Another work by Bernard et al. has shown by impedance measurement the resistance of solid electrolyte interface (SEI) to increase starting from $Li_{2.5}Si$ [65]; resistance in SEI is inversely proportional to ionic transport coefficient, hence, the diffusion coefficient of Li [118]. What happens around this phase can be more complex than just a slowing down of diffusion of Li. As shown in Fig. 3.19 Si interstitial is the defect that governs off-stoichiometry for $\delta < 0$. Si interstitials have to be formed rather than Li vacancies which can be the explanation for lower Li diffusion coefficient than the other phases' ones. Si interstitials do not mediate Li diffusion, unless a complex diffusion mechanism operates. The small concentration of Li-vacancy might explain the slowing down of Li diffusion.

The Si interstitial defect

As already mentioned above, the Si interstitial plays a crucial role in the $\delta < 0$ domain of $Li_{13+\delta}Si_4$. For that, we take a particular look in the fully relaxed structure before and after introducing the Si10 defect in Fig. 3.17. We observe that after the insertion of the Si10 interstitial 2 bonds with Si8 sites are created. Such bond creation can have a significant effect on the vibrational entropy contribution of the Si defect.

Also we know, that half of the low frequency phonons are contributions from the Si (please see previous chapter). The low frequency phonons are the ones that mainly contribute to the Gibbs free energy (recall Sec. 1.3.3). On top of the bond creation, the addition of Si can have an impact on the vibrational entropy contribution of the Si defect.

In the next section, we quantify the effect that the vibrational entropy has on this Si defect.

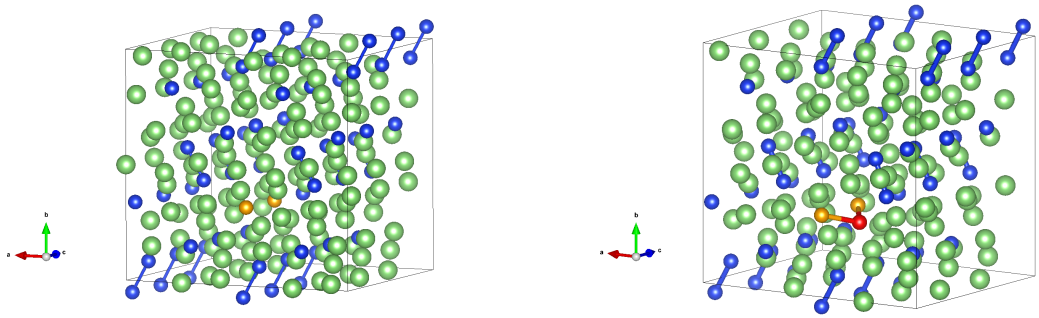

(a) Pristine (b) With Si10

Figure 3.17: $Li_{13}Si_4$ $2 \times 1 \times 3$ supercell used for calculation of point defects E_f. (a) Is the pristine structure, (b) is the structure with the Si10 point defect. The yellow spheres denote the Si8 site, the red sphere denotes the Si10 interstitial.

3.4.2 Properties of $Li_{13}Si_4$ in single phase domain

Since the dominant off-stoichiometry point defects are not of the same nature, we cannot extract the values of μ_{Li} as a function of composition analytically (like shown in Sec. 3.1.4). However, we can still numerically solve Eq. 3.4, compute μ_{Si} and μ_{Li} , and deduce δ from Eq. 3.3.

To understand the effect of vibrational entropy contribution on the Si interstitial formation energy we plot the OCV using LTE with 4 conditions in Fig. 3.18:

1. Ignoring Si defects, in particular Si interstitials. We note that accounting for or ignoring Si vacancies has no effect on the off-stoichiometry OCV
2. Omitting vibrational entropy contribution on the Si defect formation energy
3. Neglecting Li8-Li8 dimers
4. Accounting for Si defects (in particular Si interstitials) and adding an approximate vibrational entropy to the Si point defect formation energy

To include the effect of vibrational entropy in the E_f of Si point defect we consider that the vibrational contribution to the reference (E^T_{vib}), in this case the $Li_{13}Si_4$ ordered compound, is exclusively due to Si atoms . We also assume that the vibrational contribution per Si atom ($\chi^T = E^T_{vib}/N_{\mathrm{Si}}$) in the reference and defective structures is the same. Therefore, we replace E^i_c in equations 3.4 and 3.2 by Eq. 3.25:

$$E_c^{(i,T)} = E_0(A_{N_A^0} B_{N_B^0}) + (N_A^0 + N_B^0)\chi^T - [E_0(A_{N_A^i} B_{N_B^i}) + (N_A^i + N_B^i)\chi^T] = E_c^i + (N_A^0 - N_A^i)\chi^T, \quad (3.25)$$

where $A \equiv$Si and $B \equiv$Li.

Fig. 3.18 suggests that adding the vibrational contribution to the Si vacancies formation energies makes no difference -as they are so high in E_f, it does not modify the result. Fig. 3.18 also shows that neglecting Li8 dimers causes a very steep slope around $\delta = 0$ making the $\delta < 0$ domain similar to that of the OCV without Si defects. Both dimers of Li and Si interstitials including vibrational entropy seem to have an effect on the whole $Li_{13}Si_4$ single phase domain. Li vacancies are clearly not contributing to the $\delta < 0$ domain as observed with the results without Si defects. We remark that including or ignoring Si vacancies makes no difference for the $\delta > 0$ domain. Overall, to best reproduce the slope it is important that we consider Li8 dimers and Si interstitials with vibrational entropy contribution on the Si interstitial defect. Therefore, for the purpose of the next studies we consider the results yielded by considering Li8 dimers and interstitials of Si with vibrational entropy contribution on its formation energy.

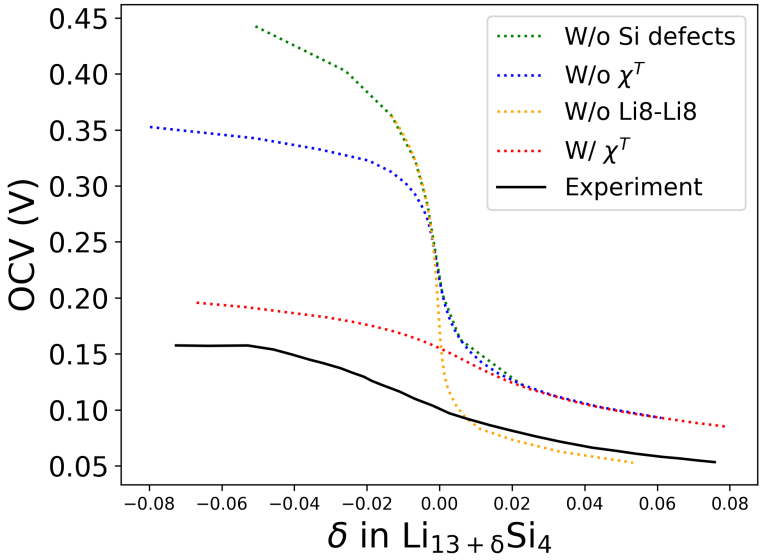

Figure 3.18: Plot of the $Li_{13}Si_4$ OCV vs composition. Comparison with experiment by Wen and Huggins at 690 K [35] which uses liquid lithium at 690 K as reference. The green line represents the OCV in the case we neglect Si defects and account for all the rest; the blue line represents the OCV in case we consider Si defects without adding vibrational entropy contribution per Si (W/o χ^T) to Si defects (recall Eq. 3.25); the yellow line is the outcome of ignoring Li8-Li8 dimers; and the red line represents the results including both Si defects and vibrational entropy contribution (W/ χ^T) in the formation energy of Si defects.

The effective formation energies of point defects as a function of composition can be observed in Fig. 3.19. We show that the off-stoichiometry is controlled by Si interstitial and Li dimers. For $Li_{12}Si_7$ and Li_7Si_3 we may directly extract the energy of Li Frenkel pair formation at $\delta = 0$. In $Li_{13}Si_4$, however, the defect complex that conserves the perfect stoichiometry is a Schottky defect made of 4 Si interstitials and 13 Li interstitials (equivalent to 6.5 Li8 dimers). Notice that at $\delta = 0$ our predicted effective formation energy of a Si interstitial is around 0.45 eV , and our predicted formation energy of a Li dimer is around

0.35 eV; hence the formation energy of our predicted Schottky pair is around $(0.35/2)\times 3.25+0.45 = 1.019$ eV which is almost identical to the experimental one we extracted with a value of 1.029 eV. We note that at $\delta = 0$ the Li contribution in comparison to the Si contribution to the formation energy of the Schottky defect. The Si contribution is greater than that of the Li one.

We plot the thermodynamic enhancement factor of $Li_{13}Si_4$ as a function of composition in Fig. 3.20. These results are in very good quantitative agreement with the reported experimental values. This is also in line with the predicted Schottky defect formation energies being similar to the experimental one. The experimental value of the maximum is at $\delta = 0$ with a value around 310; but our results predict a maximum value of 360 at $\delta \approx 0.01$. Based on the excellent agreement of the Schottky pair defect formation energy between experiment and theory we may state that the experimental estimation of the Li composition is 0.25% off in Li composition. Indeed Wen and Huggins have reported a slow voltage drift and had to calculate the change in composition for each voltage step as the arithmetic mean of charge and discharge that was always compared to a theoretical value [35]. This could have lead to a false prediction of the composition or a slight shift in δ in $Li_{13+\delta}Si_4$ for the maximum of thermodynamic enhancement factor.

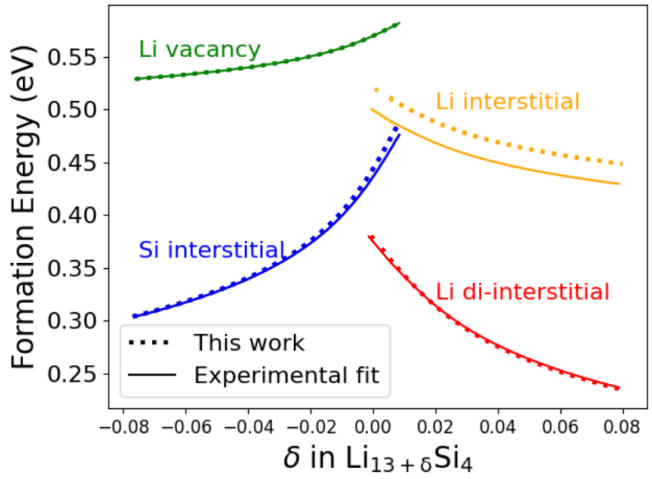

Figure 3.19: Plot of the $Li_{13}Si_4$ effective formation energies vs composition. Comparison with experiment by Wen and Huggins at 690 K [35] .

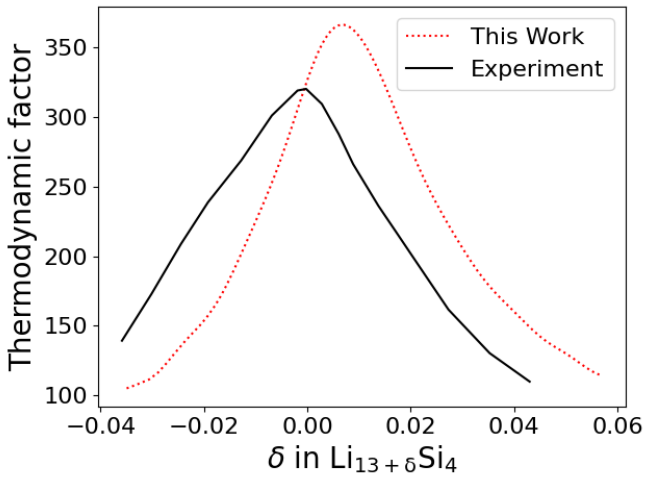

Figure 3.20: Plot of the $Li_{13}Si_4$ thermodynamic enhancement factor vs composition. Comparison with experiment by Wen and Huggins at 690 K [35].

3.5 Off-stoichiometry studies of vacancy superstructures of $Li_{22}Si_5$

Similar to what happens to with Li_5Si_2 and its family of vacancy super-structures, $Li_{22}Si_5$ has a slight differences in composition with $Li_{21}Si_5$ and $Li_{17}Si_4$, while also having the same Si sublattice. In fact, creating 16 and 12 vacancies in a $Li_{22}Si_5$ cell of 352 Li atoms leads to $Li_{21}Si_5$ and $Li_{17}Si_4$ phases respectively. Therefore, $Li_{21}Si_5$ and $Li_{17}Si_4$ are vacancy superstructures of $Li_{22}Si_5$. The work of Zeilinger, Braga, Chevrier, and their collaborators have provided enough evidence that $Li_{22}Si_5$ is not the most highly lithiated phase [41, 53, 49]. Even a work that was done 35 years ago corrected the stoichiometry of $Li_{22}Si_5$ to be $Li_{21}Si_5$ [98]. However, Zeilinger et al. report $Li_{21}Si_5$ to most likely exist but rather as a metastable phase [49]. Whereas Braga et al. claim that both $Li_{17}Si_4$ and $Li_{21}Si_5$ are stable phases but the former being stable at low temperatures while the latter at temperatures higher than 650 K [53]. For the purposes of this section, we investigate the off-stoichiometry of these phases (in particular $Li_{21}Si_5$ and $Li_{17}Si_4$) in an attempt to discriminate the stable highly lithiated phase at 690 K.

We account for the vibrational contribution to the Gibbs free energy of $Li_{17}Si_4$ only (presented in the previous chapter). We assume that the contribution of the vibrational entropy and enthalpy per atom is the same for $Li_{21}Si_5$ and $Li_{22}Si_5$.

3.5.1 Point defects

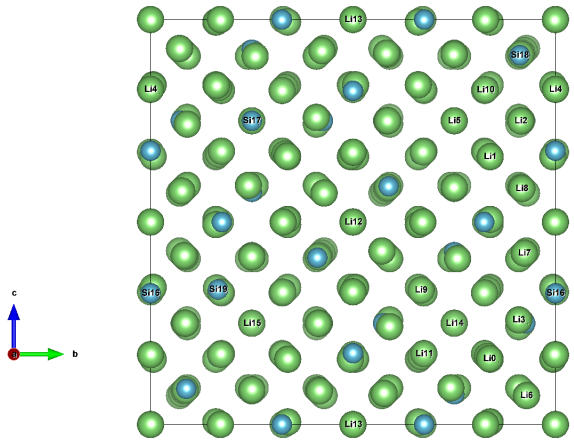

Figure 3.21: $Li_{22}Si_5$ unit cell labeled according to the "symmetric CIF" file found in Materials Project website [103] or in the appendix C. The Li16 interstitial site is given by the fraction coordinates in terms of the lattice parameters (0.10896, 0.10896, 0.65343).

We list, in table 3.7 with the help of Fig. 3.21, the E_f at 690 K of most $Li_{22}Si_5$ point defects using as a reference the chemical potential of Li and Si at $\delta = 0$ for $Li_{22}Si_5$. The presence of Li vacancy highly negative E_f of Li suggests that this phase is unstable like otherwise claimed by Wen and Huggins [35]. Another interesting point is the low cost of Si18 vacancy vs Li16 interstitial potentially suggesting that the Li-Si compounds when highly lithiated prefers to create Si vacancies rather than Li interstitials.

Vacancies								
Label	E_f (eV)	m_i	Label	E_f (eV)	m_i	Label	E_f (eV)	m_i
Li0	-1.0044	48/80	Li8	-0.4084	16/80	Si16	1.1292	24/80
Li1	0.4080	48/80	Li9	-0.9423	16/80	Si17	1.3407	24/80
Li2	0.4130	48/80	Li10	0.5369	16/80	Si18	-0.0587	16/80
Li3	-0.9243	48/80	Li11	-0.9423	16/80	Si19	0.9577	16/80
Li4	0.4461	24/80	Li12	-1.0310	4/80			
Li5	0.5580	24/80	Li13	-0.4247	4/80	**Interstitials**		
Li6	-1.0235	16/80	Li14	0.4265	4/80	Li16	1.2255	48/80
Li7	-0.4113	16/80	Li15	-0.9302	4/80			

Table 3.7: Table of formation energies of point defects in $Li_{22}Si_5$ with their respective multiplicity normalized by the number of Si atoms in the reference $m_i = M_i/N^0_{\mathrm{Si}}$. The Li and Si reference chemical potentials are extracted at $\delta = 0$ from LTE at T = 690 K.

We list the formation energies at 690 K of point defects of the $Li_{21}Si_5$ phase using as a reference the chemical potential of Li and Si at $\delta = 0$ for $Li_{21+\delta}Si_5$ in table 3.8 with the help of Fig. 3.22. We find the Li12 interstitial site to have a negative formation energy meaning that this phase is not stable at $\delta > 0$. We predict $Li_{17}Si_4$ to be stable (see the convex hull at 0 K from previous chapter). To form $Li_{17}Si_4$ from $Li_{21}Si_5$ we create 4 Li12 interstitials per 80 Si atoms. We may say that, if ever formed, $Li_{21}Si_5$ at 690 K prefers to have the Li12 interstitials to potentially form $Li_{17}Si_4$.

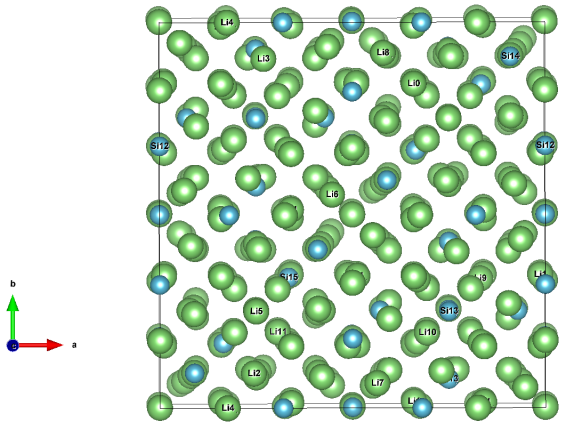

Figure 3.22: $Li_{21}Si_5$ unit cell labeled according to the symmetric CIF file found in Materials Project website [103] or in the appendix C. The Li12, Li13, Li14, and Si16 interstitial site are given by the fractional coordinates (0.04705, 0.9529, 0.8224), (0.751, 0.2502, 0.7512), (0.5, 0.5, 0.5), and (0.11, 0.88, 0.88), with respect to the lattice parameters, respectively.

Vacancies								
Label	E_f (eV)	m_i	**Label**	E_f (eV)	m_i	**Label**	E_f (eV)	m_i
Li0	0.0637	48/80	**Li6**	0.4228	16/80	**Si12**	0.8935	24/80
Li1	0.3061	48/80	**Li7**	0.7127	16/80	**Si13**	1.2648	24/80
Li2	0.3561	48/80	**Li8**	0.0217	16/80	**Si14**	1.0007	16/80
Li3	0.2163	48/80	**Li9**	0.3939	16/80	**Si15**	0.8022	16/80
Li4	0.5654	24/80	**Li10**	0.2701	16/80			
Li5	0.4825	24/80	**Li11**	0.8397	16/80			

Interstitials		
Label	E_f (eV)	m_i
Li12	-0.1511	4/80
Li13	0.6616	4/80
Li14	1.1154	4/80
Si16	1.5724	4/80

Table 3.8: Table of formation energies of point defects in $Li_{21}Si_5$ with their respective multiplicity normalized by the number of Si atoms in the reference $m_i = M_i/N^0_{\mathrm{Si}}$. The Li and Si reference chemical potentials are extracted at $\delta = 0$ from LTE at T = 690 K.

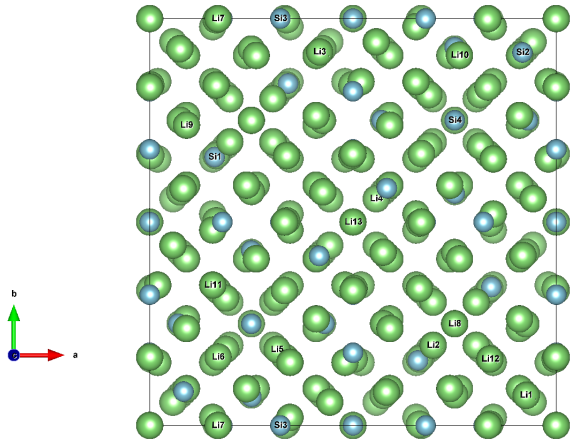

Figure 3.23: $Li_{17}Si_4$ unit cell according to the symmetric CIF file found in the work of Zeilinger et al. [49] and labeled as reported in the appendix C. The Li13 and Si17 are given by the fractional coordinates with respect to the lattice parameters (0.5, 0.5, 0.5).

We list the formation energies of point defects of the $Li_{17}Si_4$ phase using as a reference the chemical potential of Li and Si at $\delta = 0$ for $Li_{17+\delta}Si_4$ in table 3.9 with the help of Fig. 3.23. We predict this phase to be controlled by Li and Si vacancies due to their low cost compared to their Si and Li interstitial respective counterparts. Notice also how this phase contains no negative formation energies of point defects at 690 K. Contrary to $Li_{21}Si_5$ and $Li_{22}Si_5$, we predict $Li_{17}Si_4$ is a stable one at perfect stoichiometry and at 690 K.

Vacancies								
Label	E_f (eV)	m_i	**Label**	E_f (eV)	m_i	**Label**	E_f (eV)	m_i
Li0	0.2322	16/80	**Li7**	0.5338	24/80	**Si14**	0.3182	16/80
Li1	0.5522	16/80	**Li8**	0.3773	48/80	**Si15**	0.7108	24/80
Li2	0.5443	16/80	**Li9**	0.1358	48/80	**Si16**	0.4755	24/80
Li3	0.4829	16/80	**Li10**	0.1838	48/80			
Li4	0.8381	16/80	**Li11**	0.2062	48/80	**Interstitials**		
Li5	0.6296	16/80	**Li12**	0.1364	4/80	**Li13**	1.1926	4/80
Li6	0.4398	24/80	**Si13**	0.6762	16/80	**Si17**	3.3641	4/80

Table 3.9: Table of formation energies of point defects in $Li_{17}Si_4$ with their respective multiplicity normalized by the number of Si atoms in the reference system $m_i = M_i/N_{\mathrm{Si}}^0$.

3.5.2 OCV of $Li_{21}Si_5$, $Li_{17}Si_4$, and $Li_{22}Si_5$ in their single phase domain

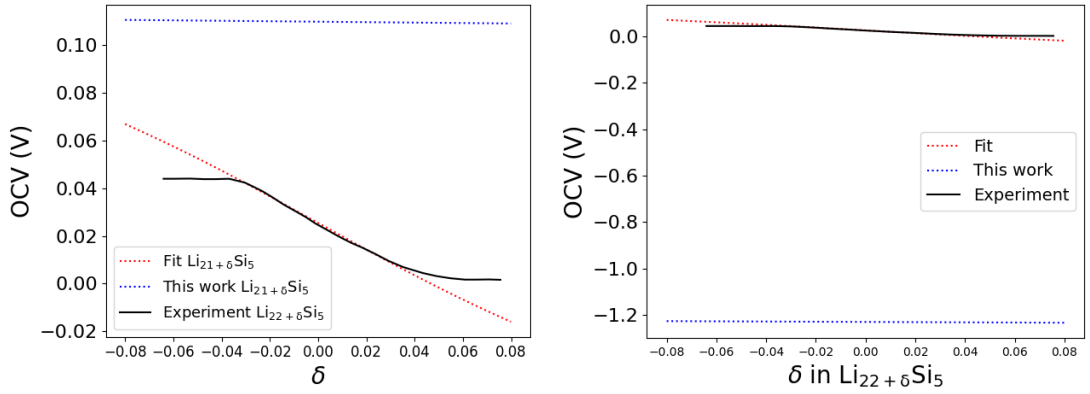

(a) $Li_{21}Si_5$ (b) $Li_{22}Si_5$

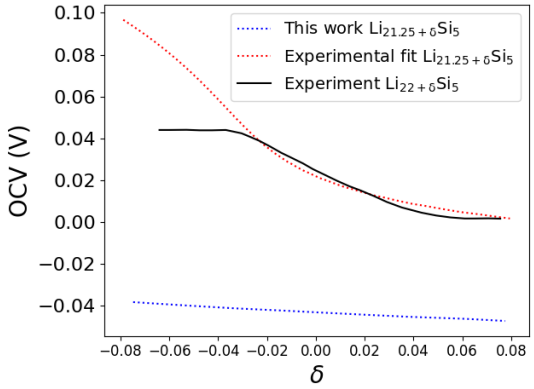

(c) $Li_{17}Si_4$

Figure 3.24: Plot of the $Li_{21}Si_5$, $Li_{22}Si_5$, and $Li_{17}Si_4$ OCV at 690 K vs composition. Comparison with experiment by Wen and Huggins at 690 K [35] which uses liquid lithium at 690 K as counter electrode. The blue lines represent the predicted values with no modifications to the formation energy of point defects, and the red lines represent the corresponding fit by modifying the formation energy of point defects.

Although $Li_{21}Si_5$ and $Li_{22}Si_5$ are unstable according to the point defect studies, we choose to investigate their OCV. We plot, in Fig. 3.24, the predicted OCV of $Li_{21}Si_5$, $Li_{17}Si_4$ (denoted $Li_{21.25}Si_5$) and $Li_{22}Si_5$, and their corresponding experimental fits in order to understand the influence of the cost of point defects on the results. We remark that for the comparison of $Li_{22}Si_5$ with the other two phases $Li_{17}Si_4$ and $Li_{21}Si_5$ we assumed that the experimental one by Wen and Huggins might be wrong in composition.

We extract the experimental $Li_{21}Si_5$ formation energies of Li vacancies and interstitials which turned out to be 0.159 eV and 0.328 eV higher in cost than our reported ones in table 3.8; and for $Li_{22}Si_5$ the difference in E_f between our predicted values and the experiment is 1.418 eV and -1.098 eV for Li vacancies and interstitials respectively (with respect to values in table 3.7). The differences in formation energy between our predicted values and the experimental fit are unreasonably big which tend to show that the experimental phase is not any of these two phases, at least at 690 K.

On the other hand, for the experimental values of $Li_{17}Si_4$, we predict the formation energies of Li vacancies to be higher by 0.19 eV and also the Si vacancy formation energies to be less by 0.15 eV in comparison with the values of table 3.9. The difference in E_f from the fit is more reassuring, in comparison with $Li_{21}Si_5$ and $Li_{22}Si_5$. However, we observe that the slope of the fit is not linear around $\delta = 0$ which is an outcome of taking Si vacancies as defects. Notice that at $\delta < 0$ the variation of OCV is linear for the fit of $Li_{17}Si_4$, this could hint to a phase between $Li_{21}Si_5$ and $Li_{17}Si_4$ knowing that for $\delta > 0$ in $Li_{21+\delta}Si_5$ the dominant off stoichiometry point defect is Li interstitial rather than Si vacancy. This could also hint to a more complicated off-stoichiometry point defect such as substitution of a Si by a Li. Nonetheless, the possibility of a solid solution with $Li_{21}Si_5$ and $Li_{17}Si_4$ as end members cannot be discarded. For instance, the work of Braga et al. shows, with harmonic calculations, how the stability of $Li_{21}Si_5$ vs $Li_{17}Si_4$ is dependent on temperature (at temperatures higher than 600 K $Li_{21}Si_5$ is stable) [53]; therefore, assuming that the same would happen with quasi-harmonic calculations, this is similar to what happens to Li_7Si_3 and $Li_{43}Si_{18}$ with our quasi-harmonic calculations in the convex hull of our work at finite temperatures (see previous chapter).

Vibrational Gibbs free energy of Li defects

As previously mentioned in the last chapter of the $Li_{17}Si_4$ finite temperature studies, Chevrier et al. have showed as the Li content increases that the Si species have less effect on the phonon density of states at high frequency [41]. They have showed that for $Li_{21}Si_5$ only the small frequencies have some of the Si influence but as much as the Li. Unlike any of the previous phases, the $Li_{17}Si_4$ has no Si-Si bonds. So it is as if we are dealing with a network of Li with inserted isolated Si atoms. Thus, we do something similar to what we did before with $Li_{13}Si_4$ Si defects. But now we assume the vibrational contribution to the Gibbs free energy is proportional to the number of Li atoms (χ^T); therefore, the Li defects E_c^i from equations 3.3 and 3.4 is replaced by:

$$E_c^{(i,T)} = E_0(A_{N_A^0}B_{N_B^0}) + (N_A^0 + N_B^0)\chi^T - [E_0(A_{N_A^i}B_{N_B^i}) + (N_A^i + N_B^i)\chi^T] = E_c^i + (N_A^0 - N_A^i)\chi^T, \quad (3.26)$$

where $A \equiv$Li and $B \equiv$Si.

For the purpose of this study we compute the OCV by adding the vibrational entropy contribution per Li of the ordered $Li_{17}Si_4$ phase to E_c^i of Li defects (similar to what was done with Si defects in $Li_{13}Si_4$). We plot this OCV in comparison with previously computed one in Fig. 3.25. We see that adding the finite temperature effect on Li vacancies greatly improves the results. The predicted effect of the vibrational part on the Li vacancy increases its formation energy by 0.19 eV at 690 K (in comparison to the values in table 3.9). This is in line with the previously reported values of Li vacancy formation energies of the $Li_{17}Si_4$ fit. For the purpose of the next studies we consider the $Li_{17}Si_4$ phase with Li and Si vacancies. We also assume that the defects of Li require a very important correction which we believe is associated to the vibrational contribution to the formation energy of Li vacancy.

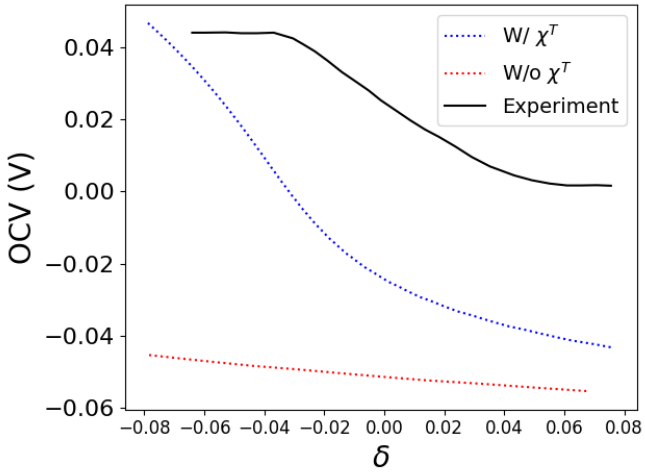

Figure 3.25: Plot of the $Li_{17}Si_4$ OCV vs composition. Comparison with experiment of $Li_{22}Si_5$ by Wen and Huggins at 690 K [35]. The blue dotted line represents the results by including the effect of vibrational entropy per Li in Li defects (specially vacancies) while the red dotted line is without it.

3.5.3 Properties of $Li_{17}Si_4$ in single phase domain

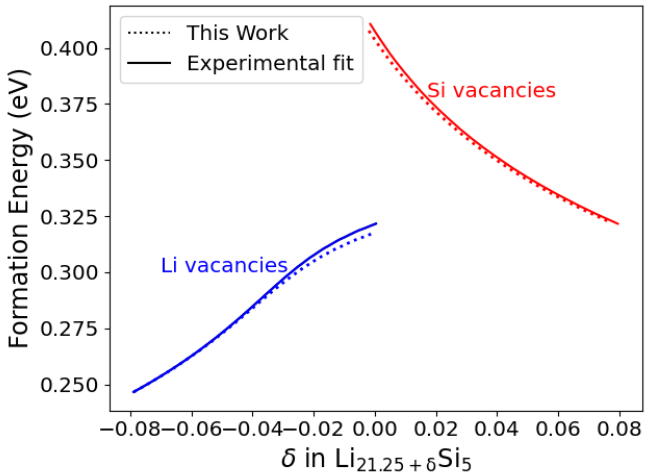

Figure 3.26: Plot of the $Li_{17}Si_4$ effective formation energies vs composition. Comparison with experiment of the supposed $Li_{22}Si_5$ by Wen and Huggins at 690 K [35].

The plot of the effective formation energy of point defects in $Li_{17}Si_4$ can be found in Fig. 3.26. The excellent agreement between our results and the values extracted from experiment suggest that we have captured the right defects.

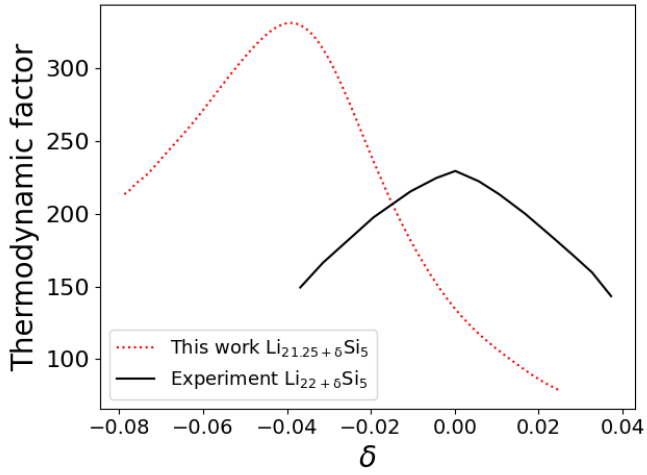

Figure 3.27: Plot of the $Li_{17}Si_4$ thermodynamic enhancement factor vs composition. Comparison with experiment of the supposed $Li_{22}Si_5$ by Wen and Huggins at 690 K [35].

We plot the thermodynamic enhancement factor of both the fit and predicted results from our work in Fig. 3.27. Qualitatively, the same thing that happens with $Li_{13}Si_4$, for not having Frenkel pairs but Schottky defects happens here. We predict that the peak of the thermodynamic enhancement factor is not at $\delta = 0$. By assuming that the maximum of the experimental peak was at $\delta = 0$, Wen and Huggins come to the conclusion that they have a slow voltage drift. We may say this drift was actually resulting from a wrong estimation of the Li-composition. Quantitatively, we observe that we overestimate the thermodynamic enhancement factor by almost 100 units, this however we have proven to be in the order of 10 meV differences in the formation energy of point defects.

Despite $Li_{17}Si_4$ having the best agreement in formation energy of point defects with respect to experiment. We cannot completely discard the possibility of another phase between $Li_{21}Si_5$ and $Li_{17}Si_4$, or the existence of a concentrated vacancy solid solution between the two. More investigation on this matter would be necessary to draw conclusive thoughts.

3.6 Discussion

In this section we give a general discussion of the results presented in the previous sections.

3.6.1 Prediction of Li-Si compounds

To start with, we predict through the comparison of effective formation energies from our models and those extracted from the experiment that the crystalline phases at 690 K are $Li_{12}Si_7$, $Li_{43}Si_{18}$, $Li_{13}Si_4$ and $Li_{17}Si_4$.

The $Li_{12}Si_7$ and $Li_{13}Si_4$ phases have never been a subject of debate in the literature (please see Sec. 1.1.3); moreover, this chapter's results along with the ones presented in the previous chapter (with the convex hull at 0 K) suggest that these two phases remain stable from 0 K all the way up to 690 K.

Our claimed $Li_{43}Si_{18}$ phase, however, is a new entry to the Li-Si compounds with nominal composition around $Li_{2.333}Si$. The $Li_{43}Si_{18}$ belongs, in nominal composition, between the previously debated Li_7Si_3 and Li_5Si_2 phases [44, 46]. Our results suggest via the slope of the OCV that this phase, in contrast to Li_7Si_3 and Li_5Si_2, is the one that happens around this stoichiometry.

As for the highly lithiated crystalline phase, we claim the $Li_{17}Si_4$ is, indeed, the phase. This result is in line with the work of Zeilinger and collaborators [49]. In order to compare with the theoretical work of Braga et al. [53] we should also include the quasi-harmonic vibrational contribution to the Gibbs free energies in the calculations of $Li_{21}Si_5$ to see the effect of isobaric vibrational contribution on the stability of this phase.

3.6.2 Point defects

From our results we notice that the formation energies of point defects depend on the nominal composition of Li. Thus, in Fig. 3.28 we plot the formation energy of both Li and Si vacancies and interstitials with respect to composition. We list below the observations from this plot:

- Li vacancies remain relatively low in formation energy throughout all phases
- Li interstitials formation energy increases as we increase Li nominal composition
- Si vacancies decrease in formation energy as we increase Li nominal composition
- Si interstitials are relatively high in formation energy with respect to all the other point defects except for $Li_{13}Si_4$; after this phase, the formation energy of Si interstitial is even higher

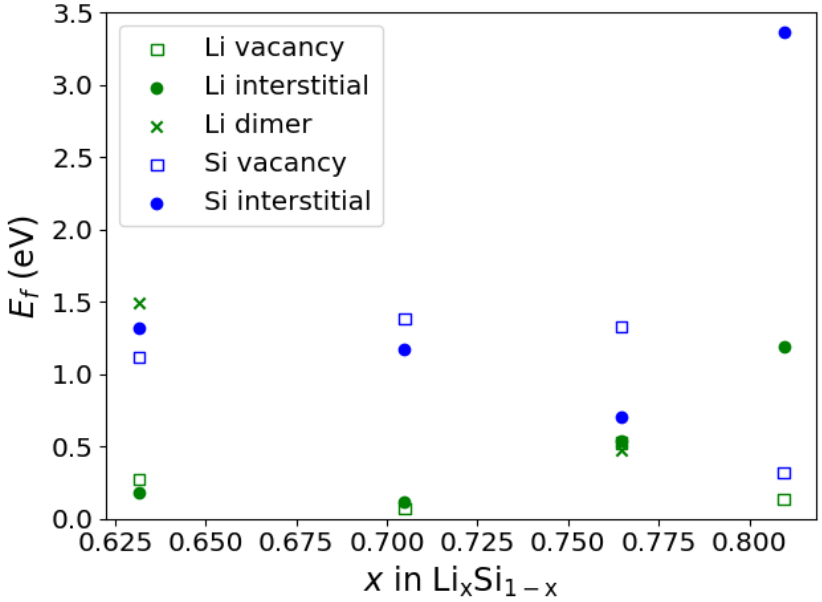

Figure 3.28: Plot of the formation energies of point defects with respect to Li nominal composition of $Li_{12}Si_7$, $Li_{43}Si_{18}$, $Li_{13}Si_4$, $Li_{17}Si_4$ using LTE at perfect stoichiometry ($\delta = 0$) and at 690 K. Note that for the formation energy of Si vacancies and interstitials in $Li_{43}Si_{18}$ we have used the values of Li_7Si_3 (we assume that it does not change much for $Li_{43}Si_{18}$).

Firstly, we notice a dependence on the nature of the species when creating point defects depending on the concentration. For the first two compounds only Li defects govern their off-stoichiometry domains and then for the last two, the Si defects play a role as well. Secondly, we may mention that around

$Li_{13}Si_4$ there is a turning point related to the Si interstitial formation energy. Finally, we note that at the composition of $Li_{17}Si_4$ the system prefers to create vacancies of Si than interstitials of Li. We may say that at high concentrations, the system tends to imitate that of a pure BCC Li system; hence, removing atoms of Si would easier to become higher in Li concentration.

We also observe from the effective formation energies of point defects (see all the effective formation energies plots from previous sections), that point defects formation energies decrease as we tend towards their corresponding off-stoichiometry regime (e.g. Li vacancies for $\delta < 0$).

Vibrational contribution to point defects

We remark that only the two most highly lithiated phases ($Li_{13}Si_4$ and $Li_{17}Si_4$) with dominant Si point defects are the ones that require a correction on the point defect formation energies that we associate to a contribution from the vibrational entropy. We may say that when Si defects are involved, there is a strong contribution from the vibrational entropy on the point defect formation energy that we should take into account. For instance, the extremely expensive calculations of the Gibbs free energies (at finite temperatures) of the Li-Si compounds with their dominant point defects would help us draw a conclusion.

3.6.3 Comparison with experimental values

Thermodynamic enhancement factor

In the previous sections, we show how the thermodynamic enhancement factor is related to the slope of the OCV and therefore the formation energies of point defects. This property is very sensitive to small changes (in the order of 10 meV) in formation energies of point defects. Because of this, we believe that not only the LTE is a good method to validate the existence of phases, but also a good method to calculate the formation energies of point defects from experimental OCV values. Our predicted effective formation energies and the ones extracted from experiment are always within 0.03 eV, which is excellent in terms of DFT accuracy.

We recall that the last two phases $Li_{13}Si_4$ and $Li_{17}Si_4$ thermodynamic enhancement factors have a small shift in composition for their maxima with respect to the experimental ones of Wen and Huggins [35]. Wen and Huggins report a slow voltage drift. A slow voltage drift in GITT means that it can affect the accuracy of state of charge estimation, as the drift can be mistaken for changes in the cell's actual state of charge. We note that a slow voltage drift could mean point defects of Silicon are actually changing the Li nominal composition, hence the reason why the state of charge is not longer accurate. This may actually explain why we have a shift in the maxima of both thermodynamic enhancement factors of $Li_{13}Si_4$ and $Li_{17}Si_4$ which we have proven to be due to silicon defects playing a role. In other words, we can use our LTE model to determine the real nominal composition of the maximum in case a slow voltage drift happens in GITT.

Experimental data in the literature

We make emphasis on the fact that there is only, to the best of our knowledge, the work of Wen and Huggins done at 690 K that investigates the single phase domain of Li-Si compounds [35]. We insist that this kind of experiment should be done at various temperatures by taking into account that kinetics plays a role to keep the crystalline structures (more on this discussion in the next chapter).

3.7 Conclusion

In this chapter, we highlighted the importance of studying off-stoichiometry domains of ordered compounds.

We computed the formation energies of point defects as means to investigate the instability of phases and identify the dominant point defects in each phase. These formation energies were used along in the LTE of the grand potential of Li-Si compounds. We found a correlation between the point defect nature and the composition of the Li-Si phase at 690 K. For instance, we saw that Si point defects become more stable at high Li-Si phase compositions: Si interstitials have a the lowest formation energy around $Li_{13}Si_4$ and very high in all other compositions; and Si vacancies are easy to create at the highest lithiated phase $Li_{17}Si_4$.

We used the LTE to extract the chemical potential of Li and Si as a function of composition around each compound. These allowed us to compare our predicted results with those of the experiment at 690 K. We could compare the OCV, the effective formation energies of point defects, and the thermodynamic factor. Remarkably, we implemented a way for using the LTE to extract effective formation energies of point defects from experimental single phase domain OCV values with an accuracy of 0.03 eV.

We predicted from our comparisons with experiment which are the phases that most likely exist at 690 K. We report $Li_{12}Si_7$, $Li_{43}Si_{18}$, $Li_{13}Si_4$ and $Li_{17}Si_4$ to be the phases based on the similarities with experiment (e.g. OCV, point defects effective formation energies, etc.).

We showed that the maximum of the thermodynamic enhancement factor is proportional to the Frenkel pair formation energy when the dominant point defects are single interstitials and single vacancies of the same species. We also proved that the maximum is not necessarily always at perfect stoichiometry ($\delta = 0$ in $Li_{a+\delta}Si_b$) like otherwise claimed by Wen and Huggins [35]. We proved that in the case we have Li-Li Frenkel pair as dominant stoichiometry point defect, the maximum of thermodynamic enhancement factor is virtually at $\delta = 0$. However, in the case we have Schottky defects as dominant stoichiometry point defect, we showed the maximum of the thermodynamic enhancement factor is not at $\delta = 0$.

The results of this chapter do not consider the off-stoichiometry two-phase-equilibria between phases. However, from the off-stoichiometry Gibbs free energies and chemical potentials that we obtained in this chapter we can, in the next chapter, calculate the two-phase-equilibria between phases that will then include the OCV plateaus that we will be able to compare with the experiment.

Chapter 4

Phase stability

We rely on the formation Gibbs free energies of Li and Si point defects to calculate the Gibbs free energies of the Si-Li solid solutions and ordered compounds (including off-stoichiometry). Using the common tangent construction, we compute the Si-Li phase diagram. We deduce the composition range of single and two-phase-equilibrium domains. We compare our calculations to the experimental results when available: specific heat capacity [54, 43], OCV from GITT [35]. Then, we analyze the precipitation driving forces in constrained (applied voltage) conditions.

Building a phase diagram with deviations from perfect stoichiometry allows to model the variation of OCV in single phase domains and the composition interval of the two-phase OCV plateaus, then compare with experimental OCV like those presented by Wen and Huggins at 690 K [35].

In this chapter, we start with a study of the dilute Si(Li) solid solution. We calculate the solubility limit of Li in Si and compare with experimental results. We also compare our formation energy of Li in Si with the experimental one. We then introduce a mean field model of the Li_7Si_3 solid solution to represent the partially "disordered $Li_{43}Si_{18}$" that is expected to be more stable than the ordered $Li_{43}Si_{18}$ at high temperatures. With this model we are able to extract information such as order-disorder transition temperature that would not otherwise be possible with the previous LTE study of Li_7Si_3 in the infinitely dilute approximation. From this solid solution free energy model and the previous LTE off-stoichiometric Gibbs free energies of the $Li_{12}Si_7$, $Li_{13}Si_4$ and $Li_{17}Si_4$ phases, we construct a phase diagram. Since charging of Si at room temperature involves the precipitation of the iconic and well known $Li_{15}Si_4$ metastable phase, we present a thermodynamic study of this phase. Finally, we take advantage of our thermodynamic study to analyze the precipitation driving forces during lithiation, in particular, the one of $Li_{15}Si_4$. We also use the same model to understand the delithiation process that the Li-Si phases undergo.

4.1 Dilute solid solution of Li in Si

In this section, we calculate the DFT formation energies of neutral or positively charged Li interstitial (Li^0 and Li^+) in the tetrahedral site of bulk Si (which has been proven to be the most favorable configuration [108]). Then, we calculate the solubility limit of Li in Si.

4.1.1 Formation energy of Li interstitial in Si

The formation energy of neutral and charged Li interstitial has been calculated by Kim et al. [108] using a 216-Si-atom supercell. In the present study we use the same supercell size and k-point sampling grid ($2 \times 2 \times 2$ in the scheme of Monkhorst-Pack). However, we use the PBE and the HSE06 functionals (instead of the PW91) and an energy cut off of 750 eV (instead of 300 eV) for the plane-wave basis set. As explained in Chapter 1, it is important to note that the HSE06 is known for giving closer-to-experiment values of band gap compared to the underestimated ones by PBE [119].

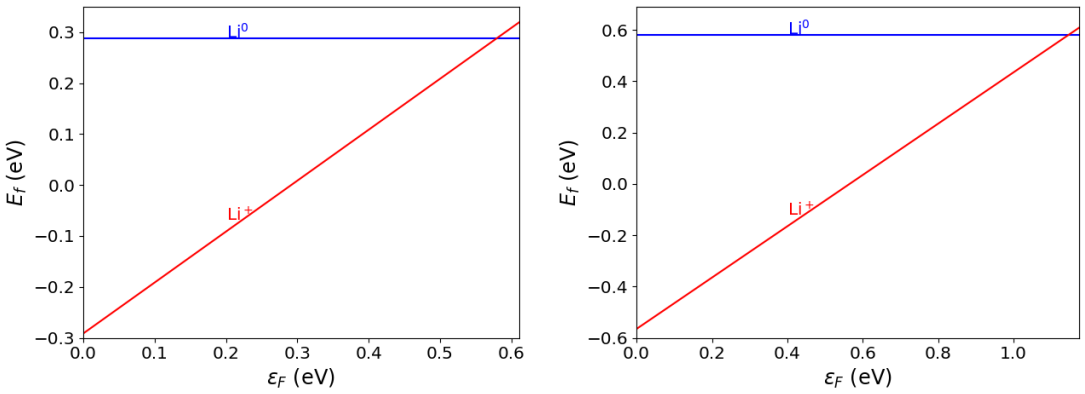

(a) PBE (b) HSE06

Figure 4.1: Variation in formation energy of Li^+ and Li^0 vs Fermi level relative to the valence band maximum of Si band gap using PBE (a) and HSE06 (b) functionals. The chemical potential of Li is the enthalpy of pure metal Li at 0 K.

We plot the formation energies of Li^0 and Li^+ with respect to the Fermi level in Fig. 4.1. Notice that the formation energies of Li^+ can be negative according to the Fermi level which will never happen because in these conditions many Li would be incorporated and the dilute limit approximation is no longer valid. The formation energy of Li^+ ($E_f(Li^+)$) is obtained from the relationship:

$$E_f(\mathrm{Li^+}) = \mathrm{E_0[Si(Li^+)]} - \mathrm{E_0(Si)} + \mu_{\mathrm{Li}} + \mathrm{q(E_v} + \epsilon_{\mathrm{F}}), \tag{4.1}$$

where E_0[Si(Li^+)], and E_0(Si) are the DFT energies of Li^+ in bulk Si (including the Makov Payne monopole correction [120]) and bulk Si, respectively. The chemical potential of Li, μ_{Li} , is the one of pure metal Li at 0 K. ϵ_F is the Fermi level relative to the valance band maximum (E_v). Notice how the domain of the ϵ_F depends on the functional used (0.61 and 1.174 eV for PBE and HSE06 respectively) in Fig. 4.1, the PBE band gap is in agreement with the band gap reported by Song et al. (value of 0.62 eV) [108]. However, the HSE06 band gap is in agreement with experimentally measured value of 1.12 eV. The results with both functionals suggest that charged Li in Si is stable for almost all the Fermi energies within the band gap. Both results also suggest that the predicted first donor (+/0) level is found near the conduction band minimum (E_c). With the HSE06 functional we predict it at $E_c - 0.0252$ eV and with

the PBE functional we predict it at $E_c - 0.031$ eV. Both values are in good agreement with the previously reported one by the PW91 functional at a value of $E_c - 0.02$ eV [108] and with previously experimentally reported values [121] of Li ionization in Si. Moreover, they are in good accordance with [122] that has showed when a Li atom is inserted into c-Si, it stays in an interstitial position with tetrahedral symmetry and exhibits similar behavior to shallow donors in group V. Having the ϵ_F close to the conduction band minimum is in fact a property of n-type semiconductors.

4.1.2 Li solubility limit in Si

From the formation energy of the charged and neutral Li tetrahedral interstitials we calculate the solubility limit of Li in Si.

Gibbs free energy of the solid solution

The present solid solution Si(Li) consists of Si atoms sitting on the lattice sites of the host matrix and solute Li atoms sitting on the tetrahedral (Td) interstitial sites. We know from previous publications that Li-Li interactions in Si are repulsive because the formation energy of Li dimers increases as the distance between 2 Li interstitials decreases [108, 107]. Consequently, as a first approximation, we choose to ignore clusters of Li interstitials (i.e. infinite dilute approximation). Thereby, the occupation of an interstitial site does not depend on the occupation of the other interstitial sites, and the configurational entropy is an ideal one. The Gibbs free energy per atom A of the solid solution is thus equal to:

$$g(ss, x_{\mathrm{Li}}) = g(\mathrm{Si}) + x_{\mathrm{Li}} E_s(\mathrm{Li}) + \frac{N_{Td}}{N_{\mathrm{Si}}} k_B T \left[y_{\mathrm{Li}} \ln y_{\mathrm{Li}} + (1 - y_{\mathrm{Li}}) \ln 1 - y_{\mathrm{Li}} \right], \tag{4.2}$$

where $g(\mathrm{Si})$ is the Gibbs free energy per Si atom of pure Si, x_{Li} is the number of Li atoms divided by the number of Si atoms, y_{Li} is the occupation of Li interstitials in the tetrahedral sub-lattice:

$$y_{\mathrm{Li}} = \frac{N_{\mathrm{Li}}}{N_{Td}} = \frac{N_{\mathrm{Li}}}{N_{\mathrm{Si}}} \frac{N_{\mathrm{Si}}}{N_{Td}}. \tag{4.3}$$

Note that y_{Li} is equal to x_{Li} since the number of tetrahedral sites is equal to the Si sites ($N_{Td} = N_{\mathrm{Si}}$), and $E_s(\mathrm{Li})$ is the solute energy (related to the formation energy of Li in Si by Eq. 4.9). We estimate $E_s(\mathrm{Li})$ by means of DFT 0 K energies (E_0) of the compound containing a single Li Td interstitial in Si matrix ($\mathrm{Si}_{N_{\mathrm{Si}}}\mathrm{Li}$) and the Si host matrix ($\mathrm{Si}_{N_{\mathrm{Si}}}$) as:

$$E_s(\mathrm{Li}) = E_0(\mathrm{Si}_{N_{\mathrm{Si}}}\mathrm{Li}) - E_0(\mathrm{Si}_{N_{\mathrm{Si}}}). \tag{4.4}$$

Note that the bigger the hosting supercell (the bigger N_{Si}), the less energy of (repulsive) interaction the Li interstitials will have from preriodic images. The derivative of $g(ss, x_B)$ with respect to x_{Li} gives us the solute chemical potential:

$$\mu_{\mathrm{Li}} = \frac{\partial g(ss, x_{\mathrm{Li}})}{\partial x_{\mathrm{Li}}} = E_s(\mathrm{Li}) + k_B T \ln \frac{x_{\mathrm{Li}}}{1 - x_{\mathrm{Li}}}, \tag{4.5}$$

Equilibrium between ordered compound and Si(Li)

The Gibbs free energy per atom of Si of any ordered compound $\mathrm{Li_bSi}$ that comes after the Si(Li) solid solution (e.g. $\mathrm{Li_{12}Si_7}$, $\mathrm{Li_7Si_3}$, etc...) is expressed as:

$$g(\mathrm{Li_bSi}) = \mu_{\mathrm{Si}} + b\mu_{\mathrm{Li}}. \tag{4.6}$$

The solid solution can be approximated in DFT calculations by a system with sufficiently large Si host matrix and one Li interstitial. For this work we have used the 216-Si-atom supercell (since going beyond this with hybrid DFT can be computationally expensive). Therefore, the chemical potential of Li (μ_{Li}) can be calculated using the following equation:

$$\mu_{\mathrm{Li}} = \frac{g(\mathrm{Li_bSi}) - g(\mathrm{Si_{216}Li})}{b - (1/216)}. \tag{4.7}$$

We can then find from equations 4.5 and 4.7, the equilibrium fraction of interstitial on its sublattice and therefore its solubility limit (x_{Li}^{lim}):

$$x_{\mathrm{Li}}^{lim} = \exp\left(-E_f(\mathrm{Li})/k_B T\right), \tag{4.8}$$

where $E_f(\mathrm{Li})$ stands for the formation energy of Li in Si and can be written in terms of the solute energy (Eq. 4.4):

$$E_f(\mathrm{Li}) = E_s(\mathrm{Li}) - \mu_{\mathrm{Li}}. \tag{4.9}$$

Solubility limit of Li in Si in equilibrium with $\mathbf{Li_{12}Si_7}$

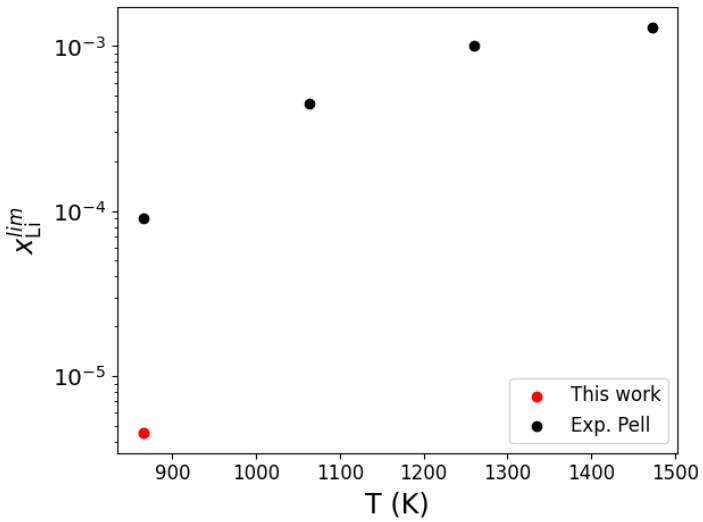

Figure 4.2: Plot of the solubility limit of Li in Si vs temperature in equilibrium with $Li_{12}Si_7$. Comparison with experiment by experimental work by Pell at around 860 K [123].

We calculate the solubility limit of Li in Si in equilibrium with $Li_{12}Si_7$ since it is the first thermodynamically stable phase that Si forms a two-phase-equilibrium with (according to our convex hull of stability in chapter 2). The formation energy of Li in Si in a two-phase-equilibrium with $Li_{12}Si_7$ is 0.917 eV (at 0 K and with the HSE06 functional) and used in Eq. 4.8. We plot our predicted solubility limit of Li^0 in Si as a function of temperature in Fig. 4.2 at around 860 K. For comparison we can use the experiment of Pell which has investigated the solubility limit at high temperatures down to the eutectic temperature (around 860 K) [123]. Besides, we observe in previously published phase diagrams this eutectic point is in fact the three-phase-equilibrium between Si, $Li_{12}Si_7$ and liquid (refer to the Fig. 1.5b). So we can compare the

presented result with the experiment only around 860 K (since we have a two-phase-equilibrium between Si and $Li_{12}Si_7$).

At around 860 K, the experimental work by Pell reports a solubility limit of 9×10^{-5}. We report a value almost two orders of magnitude below of 4.53×10^{-6}. The discrepancy between the results in the presented model and that of experiment could be due to the lack of finite temperature effects in the present calculation of the formation energy of Li interstitial in Si.

We also report a solubility limit of 3.9×10^{-16} with our model at 300 K. These low values of solubility limit (even at higher temperatures) suggest that the chemical potential of Si should not be affected by Li insertion. Also, this means that the Li chemical potential in Si(Li) from an infinitely dilute approximation (Eq. 4.5) is a good approximation.

4.2 Two phase equilibria from LTE

To compute the (meta)stable two-phase-equilibria, we plot the chemical potential of Si vs chemical potential of Li of each of the phases. The chemical potentials of species in a two-phase-equilibrium are equal in both phases. Thus, every intersection point corresponds to a two-phase-equilibrium with chemical potentials of Li and Si respectively given by the x and the y coordinates of the crossing point.

4.2.1 Studies at 690 K

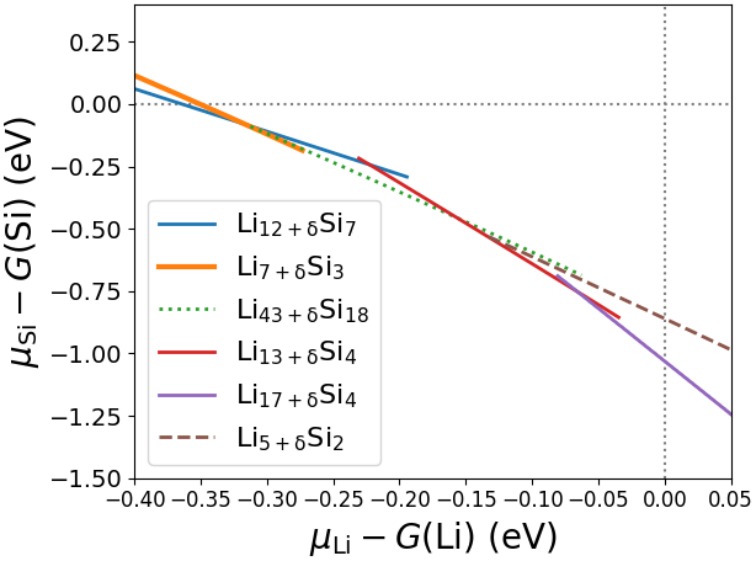

Figure 4.3: Plot of the chemical potential of Si against Li at 690 K (given with respect to the Gibbs free energies per atom of Si and Li respectively as found in Chapter 2) in the single phase domain of the phases we study in the previous sections. Therefore, the x-axis represents the negative of open circuit voltage. The grey horizontal and vertical dotted lines represent the Gibbs free energies per atom (chemical potential) of pure Si and Li respectively.

In Fig. 4.3 we plot the chemical potential of Si as a function of the chemical potential of Li of the phases studied in the previous chapter. The dilute solid solutions Li in Si (Si(Li)) and Si in Li (Li(Si)) are in

equilibrium with $Li_{12}Si_7$ and $Li_{17}Si_4$ respectively, as the latter are the first and last Si-Li compounds of our binary system (at least, this is what we know from our finite temperature convex hull in chapter 2). For instance, if we assume the dilute species Li in Si does not affect the chemical potential of Si, we may set the chemical potential of pure Si to the Gibbs free energy of Si per atom (see the horizontal grey dotted line in Fig. 4.3). Similarly, if we assume the dilute species of Si in Li does not affect the chemical potential of Li, we set the chemical potential of Li to the Gibbs free energy of Li per atom (see the vertical grey dotted line in Fig. 4.3).

Fig. 4.3 then shows that Li_7Si_3 can have a metastable two-phase-equilibrium with Si (i.e. it happens at a higher chemical potential of Li than the Li chemical potential resulting from the two-phase-equilibria between Si and $Li_{12}Si_7$). Then we virtually have a three-phase-equilibrium among $Li_{12}Si_7$-$Li_{43}Si_{18}$-Li_7Si_3 since the corresponding μ_{Si} (μ_{Li}) functions are crossing at the same intersection point. We can then observe a metastable two-phase-equilibrium between $Li_{12}Si_7$ and $Li_{13}Si_4$. After, we see that $Li_{43}Si_{18}$ forms a two-phase-equilibrium with $Li_{13}Si_4$. We also predict that Li_5Si_2 can form a two-phase-equilibrium with $Li_{13}Si_4$ and a metastable one with Li. Finally, we see that $Li_{17}Si_4$ forms two-phase-equilibria, first with $Li_{13}Si_4$, and then with Li.

Plotting the Gibbs free energies against composition allows us to analyze the composition domains of single and two-phase-equilibria and the relative stability of the two-phase-equilibria by comparing their Gibbs free energies. In Fig. 4.4, $Li_{43}Si_{18}$ phase is the only phase able to form two-phase-equilibria with both $Li_{12}Si_7$ and $Li_{13}Si_4$. However, we can also see that the one with $Li_{13}Si_4$ is a metastable one. Moreover, between the understoichiometric ($\delta < 0$) $Li_{43+\delta}Si_{18}$ and the overstoichiometric ($\delta > 0$) $Li_{7+\delta}Si_3$ there is a two-phase-equilibrium happening almost at the same chemical potential with $Li_{12}Si_7$ (i.e. almost the same common tangent between $Li_{43}Si_{18}$ and $Li_{12}Si_7$).

We can also observe in Fig. 4.4, in line with Fig. 4.3, that at 690 K, it is not possible to construct a common tangent between Li_5Si_2 and $Li_{12}Si_7$. The Gibbs free energy should be prolonged and at one point we should observe a negative slope. If it continues down to the composition of $Li_{12}Si_7$ (x=0.6316 in Li_xSi_{1-x}) without a negative slope then it would mean that the two-phase-equilibrium between $Li_{12}Si_7$ and Li_5Si_2 is not an equilibrium state of the system. Besides, we can observe that the LTE Gibbs free energy of Li_5Si_2 is decreasing as more Li vacancies (i.e. the most stable understoichiometric point defect in Li_5Si_2) are created. Even at such high concentrations of point defects of vacancies of Li, the understoichiometric Li_5Si_2 shows no behaviour of increasing its Gibbs free energy. Nonetheless, the underestimated Gibbs free energy values may be the consequence of neglecting interactions between vacancies in our LTE model of Li_5Si_2. We expect that at a composition x=0.7 in Li_xSi_{1-x} (i.e. at stoichiometric Li_7Si_3) we have strong repulsive interactions that would provide a significant increment of the Gibbs free energy and therefore allow us to construct a common tangent, and therefore find a thermodynamically stable two-phase-equilibrium. To have an idea of how much these interactions can affect the understoichiometric Li_5Si_2 stability, although not necessarily the same as Li3-Li3 vacancies in Li_5Si_2, we can look at the interaction from the Li6-Li7 vacancies in Li_7Si_3 which shows a strong repulsive interaction of 0.377 eV (as previously reported in Chapter 3). Nonetheless, this behaviour of the Gibbs free energy of understoichiometric Li_5Si_2 could also hint at the existence of another ordered and stable vacancy superstructure of Li_5Si_2 that could potentially have been missed during this study. This raises the need of a model with high concentration of vacancies for the Li_5Si_2 phase (to be seen later in Sec. 4.3).

In the case we can trust these Gibbs free energies we can then assume that there will be a two-phase-equilibrium between the $Li_{12}Si_7$ and understoichiometric Li_5Si_2, another two-phase-equilibrium between understoichiometric Li_5Si_2 and over stoichiometric Li_7Si_3, and lastly a two-phase-equilibrium between overstoichiometric Li_7Si_3 and $Li_{13}Si_4$.

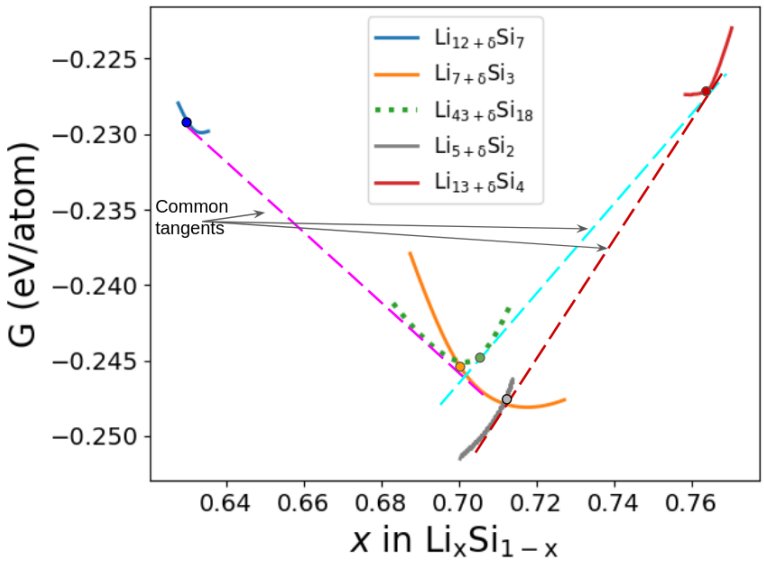

Figure 4.4: Plot of the Gibbs free energies at 690 K of intermediary Li-Si phases as a function of composition. The common tangents denote the two-phase-equilibria. The colored circles correspond to the perfect stoichiometry of the phase.

As mentioned above, the intersection points (in Fig. 4.3) give us the chemical potentials that correspond to the meta(stable) two-phase-equilibria at 690 K. Alternatively, we can also look at the slopes of the common tangents (in Fig. 4.4). This allows us to plot the OCV at 690 K of each phase including the two-phase-equilibria and the composition domains (i.e. the width in composition of the OCV plateaus) in Fig. 4.5. As a first approximation, we may disregard the Li_7Si_3 and the Li_5Si_2 phases, since we cannot obtain a coherent series of two-phase-equilibria among the intermediary phases. Hence, as a first approximation, we choose to work with $Li_{43}Si_{18}$ as the representative phase of the series of ordered phases in this composition range. Overall, as shown in Fig. 4.5, we observe a good agreement with the experimental OCV measured by the work of Wen and Huggins [35] in terms of single phase domain composition ranges (composition between two consecutive plateaus), and also the absolute drop in OCV between two consecutive plateaus at 690 K. Notice that considering Li_7Si_3 and Li_5Si_2 would make a discontinuity in the OCV domain of $Li_{43}Si_{18}$ and would not allow us to have a plateau with the next phase $Li_{13}Si_4$.

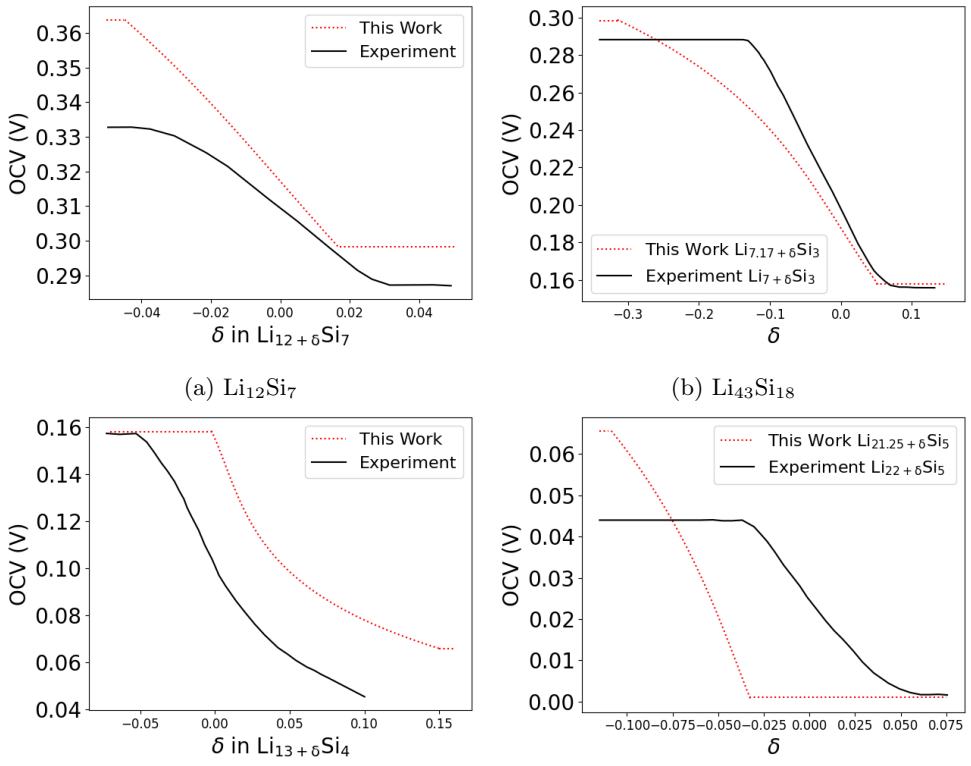

(a) $Li_{12}Si_7$ (b) $Li_{43}Si_{18}$

(c) $Li_{13}Si_4$ (d) $Li_{17}Si_4$

Figure 4.5: Plot of the OCV at 690 K vs composition including the two phase equilibria. Comparison with experiment by Wen and Huggins [35]. Notice that for (b) and (d) the nominal compositions of the experiment do not match ours (as explained previously in Chapter 3).

In Fig. 4.6, we plot the whole OCV from pure Si to $Li_{22}Si_5$ to compare with the experiment at 690 K and our previous results of ordered compounds at 0 K (with no zero point energy) and 690 K. As mentioned previously, for the Si-$Li_{12}Si_7$ equilibrium, the chemical potential of Si is fixed by the Gibbs free energy of pure Si. The resulting Li chemical potential is then very close to the one deduced from the finite temperature convex hull with line compounds as reported in Chapter 2. We show for the composition $x = 2.333$ in Li_xSi we have a single drop in potential that is caused by the $Li_{43}Si_{18}$ single phase domain (that is if we ignore Li_7Si_3 and Li_5Si_2). The off-stoichiometry results reproduce better the experiment than the line compound approximation -which has at least 2 plateaus in between the OCV drop; therefore, we observe a better agreement with experiment concerning the two-phase-equilibria OCV value with the previous phase ($Li_{12}Si_7$) and the one after ($Li_{13}Si_4$). We see that the $Li_{17}Si_4$ phase has a greater shift in composition in comparison with the supposed-to-be $Li_{22}Si_5$ [35] ($x = 4.25$ vs $x = 4.4$ in Li_xSi) . On the other hand, Li_7Si_3 and $Li_{43}Si_{18}$ only have a difference of $x = 0.06$ in Li_xSi. We emphasize that the discrepancy between the present theoretical results and the experimental data is within 0.03 V suggesting an excellent agreement between our model and the experiment -as long as only the metastable two-phase-equilibria with the $Li_{43}Si_{18}$ phase is considered.

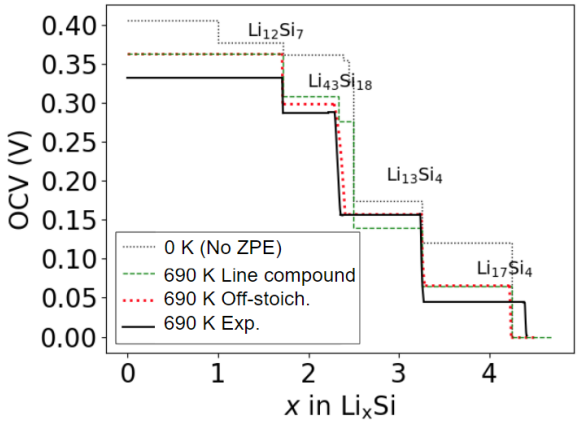

Figure 4.6: Plot of the OCV vs composition. Comparison with our previous line compound OCV at 690 K (vibrational entropy only), with our previous 0 K OCV, and experiment by Wen and Huggins at 690 K [35].

4.2.2 Studies at 300 K

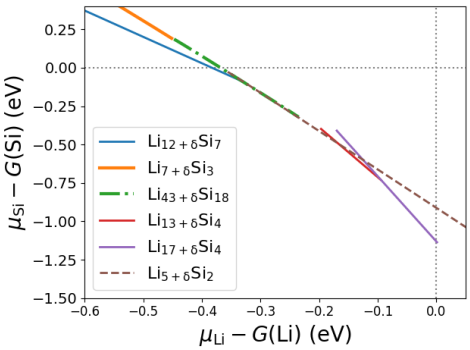

Figure 4.7: Plot of the chemical potential of Si against Li at 300 K (given with respect to the Gibbs free energies per atom of Si and Li respectively as found in Chapter 2) in the single phase domain of the phases we study in the previous sections. Therefore, the x-axis represents the negative of open circuit voltage. The grey horizontal and vertical dotted lines represent the Gibbs free energies per atom (chemical potential) of pure Si and Li respectively.

We perform the same calculation at 300 K, we find the 2-phase-equilibria in the plot of Fig. 4.7. We plot the Gibbs free energies against composition in Fig. 4.8 between $Li_{12}Si_7$ and $Li_{13}Si_4$. We see that we have a two-phase-equilibrium (by common tangent construction) between $Li_{12}Si_7$ and $Li_{43}Si_{18}$, followed by another one between $Li_{43}Si_{18}$ and Li_5Si_2, and then another one between Li_5Si_2 and $Li_{13}Si_4$.

Similar to what happens with understoichiometric Li_5Si_2 at 690 K, we see that the same happens with overstoichiometric Li_7Si_3 at 300 K. The Gibbs free energy should be prolonged and at one point we should observe a positive slope. This would allow us to construct a common tangent with either $Li_{12}Si_7$ or Si. But given that a positive slope would not be observable for compositions higher than $Li_{13}Si_4$ it would also mean that Li_7Si_3-$Li_{13}Si_4$ is not an equilibrium state of the Li-Si system. Moreover,

we observe that the LTE Gibbs free energy of Li_7Si_3 is decreasing as more Li interstitials (i.e. the most stable overstoichiometric point defect in Li_7Si_3) are created. Even at such high concentrations of Li interstitials, the understoichiometric Li_7Si_3 shows no behaviour of increasing its Gibbs free energy. Nonetheless, the underestimated Gibbs free energy values may again be the consequence of neglecting interactions between interstitials in our LTE model of Li_7Si_3. We expect that at a composition x¿0.714 in Li_xSi_{1-x} (i.e. at stoichiometric Li_5Si_2) we have strong repulsive interactions that would provide a significant increment of the Gibbs free energy and therefore allow us to construct a common tangent, and therefore find a thermodynamically stable two-phase-equilibrium. For instance, the interaction from the Li8-Li8 interstitials in Li_7Si_3 is a repulsive interaction of 0.0686 eV (as previously reported in Chapter 3). Nonetheless, in line with Li_5Si_2 at 690 K, the behaviour of the Gibbs free energy of overstoichiometric Li_7Si_3 could also hint at the existence of another ordered and stable vacancy superstructure of Li_5Si_2 that could potentially have been missed during this study. As previously noted, a model with high concentration of vacancies for the Li_5Si_2 phase is needed (to be seen later in Sec. 4.3).

In the case we can trust these Gibbs free energies we can then assume that there will be a two-phase-equilibrium between the $Li_{12}Si_7$ and overstoichiometric Li_7Si_3, another two-phase-equilibrium between overstoichiometric Li_7Si_3 and overstoichiometric $Li_{43}Si_{18}$, and lastly a two-phase-equilibrium between overstoichiometric $Li_{43}Si_{18}$ and $Li_{13}Si_4$.

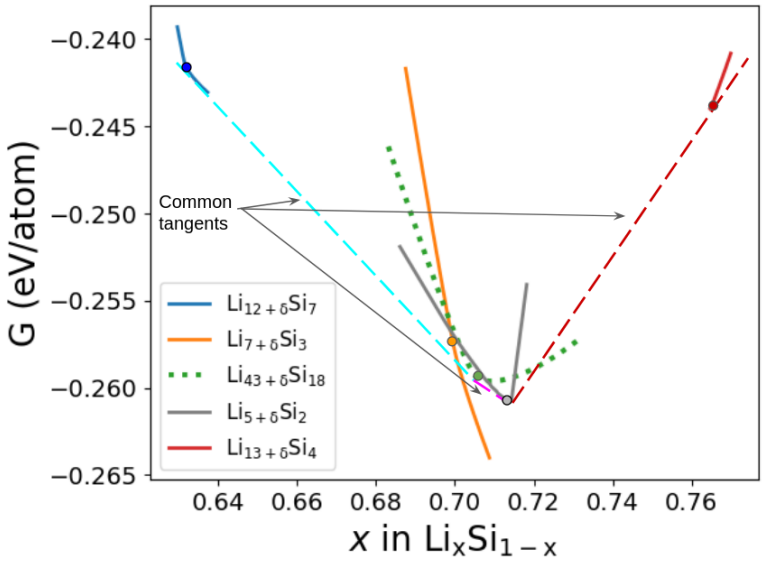

Figure 4.8: Plot of the Gibbs free energies of intermediary Li-Si phases as a function of composition. The common tangents denote the two-phase-equilibria. The colored circles correspond to the perfect stoichiometry of the phase.

In Fig. 4.9, we plot the OCV at 300 K of each phase including the two-phase-equilibria (i.e. the OCV plateaus). In comparison with the results obtained at 690 K, we observe that around perfect stoichiometry ($\delta = 0$) the slope is steeper causing the chemical potential of species to vary drastically and deviations from perfect stoichiometry to be smaller. The ordered phases almost behave like line compounds. As expected, the lower the temperature the closer the OCV to the one resulting from finite temperature line-compound convex hull (reported in Chapter 2).

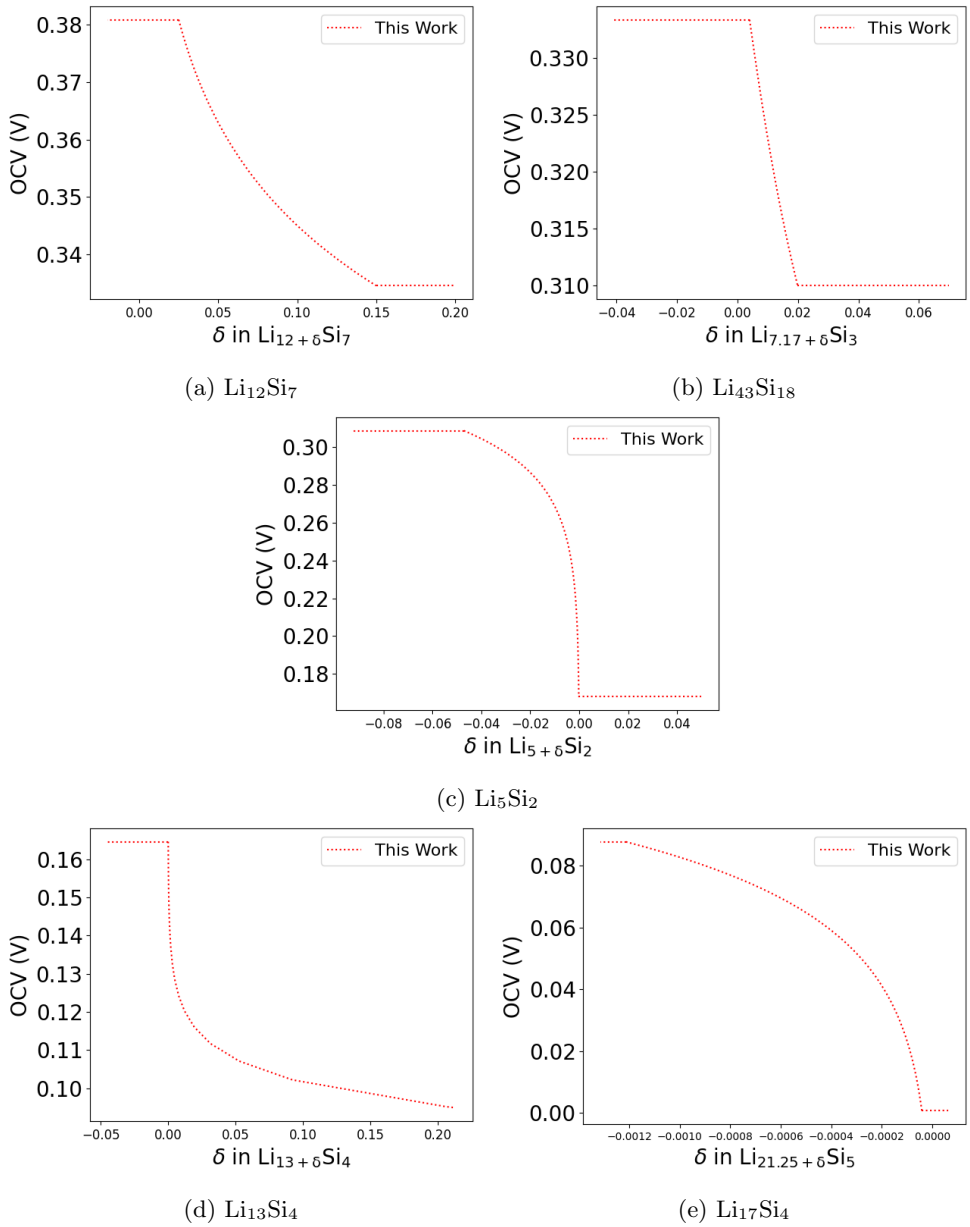

(a) $Li_{12}Si_7$ (b) $Li_{43}Si_{18}$

(c) Li_5Si_2

(d) $Li_{13}Si_4$ (e) $Li_{17}Si_4$

Figure 4.9: Plot of the OCV at 300 K vs composition including the two phase equilibria.

Fig. 4.10 shows that our OCV plot almost follows the one deduced from the line compound convex hull including vibrational entropy. We globally observe the same sequence of two-phase-equilibria at 690 K with absolute values roughly shifted up 0.05 V. For the OCV results at 690 K, we observe that accounting for Li_5Si_2 leads to an underestimation of the plateau while considering the off-stoichiometry of $Li_{43}Si_{18}$ in equilibrium with $Li_{13}Si_4$ yields a more consistent result with respect to the other two-phase-equilibria. We remark that our off-stoichiometry OCV values are in good agreement, except for the plateau between Li_5Si_2 and $Li_{13}Si_4$ (i.e. underestimated by our results), with those of Sharma and Seefurth ones that we extrapolate down to 300 K using their linear fit based on high temperature measurements between 650

K and 750 K [34]. Nonetheless, it is important to remark that it is not surprising that we observe a large discrepancy between the present fourth plateau and the extrapolated experimental third plateau [34]. After all, we predict a change in the two-phase-equilibria between 690 K (given that we had to ignore Li_5Si_2 in the calculation) and at 300 K (where we could consider Li_5Si_2 in the calculation).

We cannot directly compare the present calculations with published experimental room temperature voltage composition profiles [23], because as previously explained in Chapter 1, the lithiation of Si at room temperature alloys amorphous phases and crystalline $Li_{15}Si_4$ when precipitated at the end of the lithiation. However, an unpublished and ongoing work by our collaborator Magali Gauthier potentially shows (Fig. 4.11) that if we delithiate starting from $x = 2.5$ with Galvanostatic Intermittent Titration Technique (recall Sec. 1.3.8) at very slow rates (C/100 for 10 minutes) and with very long open circuit periods (30 hrs) allows for the system to remain crystallized (to be further confirmed with X-ray diffraction pattern results). However, it is important to note that the relaxation of OCV towards its equilibrium value (i.e. GITT during open circuit) is not fully achieved. It was not possible to obtain a value in its final steady state even after 30 hours so we are over/under estimating the experimental OCV for de/lithiation. Increasing the temperature not only enhances the atomic diffusion but also increases the thermal fluctuations which makes it easier to go over second phase nucleation barriers. This is why Wen and Huggins managed to do the GITT with much shorter relaxation time and faster charging rate at 690 K [35].

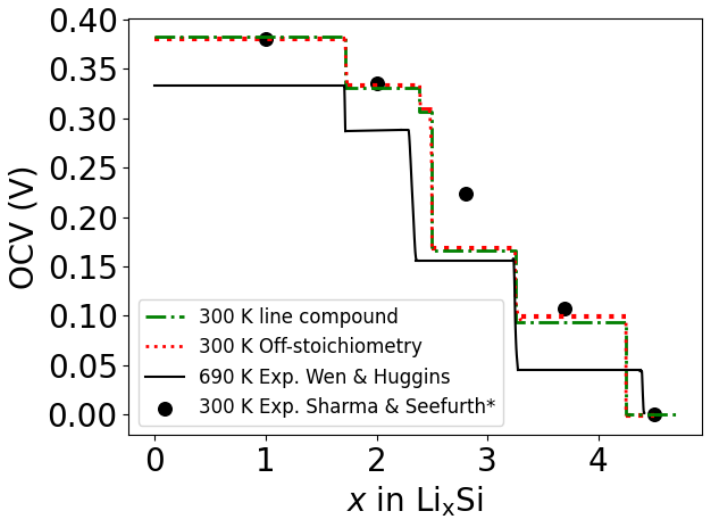

Figure 4.10: Plot of the OCV vs composition of all the phases. Comparison with our previous ordered compound OCV at 300 K (vibrational entropy only), our previous 0 K OCV, and experiment by Wen and Huggins at 690 K [35]. We also compare with *extrapolated 300 K OCV plateau values from experiment at high temperatures by Sharma and Seefurth [34].

The experiments of Magali Gauthier were performed with 2 set ups. One of them was a two-electrode measurement GITT where the starting point was the two-phase-equilibrium between Li_7Si_3 and $Li_{13}Si_4$ (see the XRD 1 Fig. D.2 in the appendix D) and the finishing point was a measured OCV plateau for which we have the XRD patterns (see XRD 2 in Fig. 4.12). The other set up was a three-electrode measurement for which we have no XRD patterns. By using three-electrode set up, the counter and reference electrodes are two different piece of lithium metal. One is electrochemically active (the counter), while the other is supposed to be inactive, thus having a constant potential (e.g. independent of passivation or Li stripping)

that can really serve as a reference electrode.

In Fig. 4.11, both GITT experiments start with an OCV value of approximately 0.45 V greater than the calculated ones whatever the two-phase-equilibrium. Several publications report the same OCV high value during delithiation [124, 65, 48]. We believe that this OCV could be the signature of an equilibrium with Si-Li oxide. In Fig. 4.11 we observe a discontinuity of the OCV first derivative with the Li fraction around 0.33 V with Exp. 1. Notice that the two-phase-equilibrium OCV plateau between $Li_{12}Si_7$ and $Li_{43}Si_{18}$ happens almost at the same OCV value. This might hint at the existence of a two-phase-equilibrium between Li_7Si_3 and $Li_{12}Si_7$; however, XRD measurement at that particular discontinuity is missing to draw a conclusion. It is also worth noting that an OCV plateau in Exp. 1 after the discontinuity could not be reached certainly due to sluggish diffusion and second-phase precipitation.

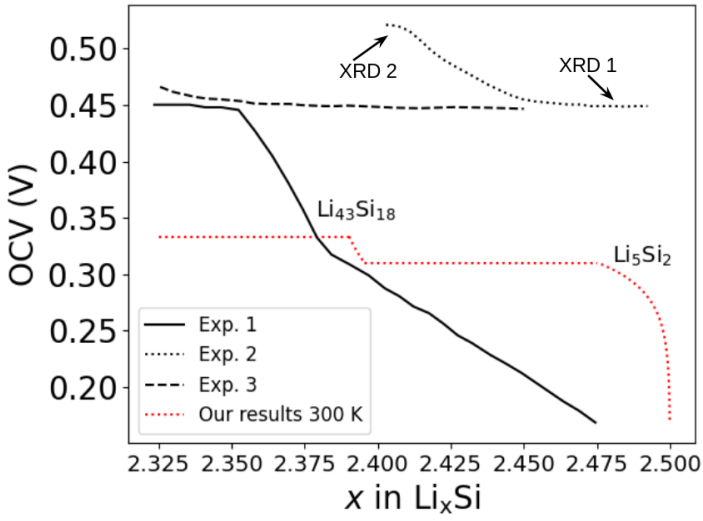

Figure 4.11: Plot of the OCV at 300 K vs composition (around Li_7Si_3). Comparison with 3 experimentally measured OCV [GITT courtesy of Magali Gauthier]: (1) OCV upon lithiation measured with a 3 electrode cell; (2) and (3) are delithiation with 2 and 3 electrode cells respectively. Note that the compositions of the experiments are susceptible to change. We have labeled the composition of Exp. 2 where the XRD were performed.

XRD analysis of the experimental results at 300 K

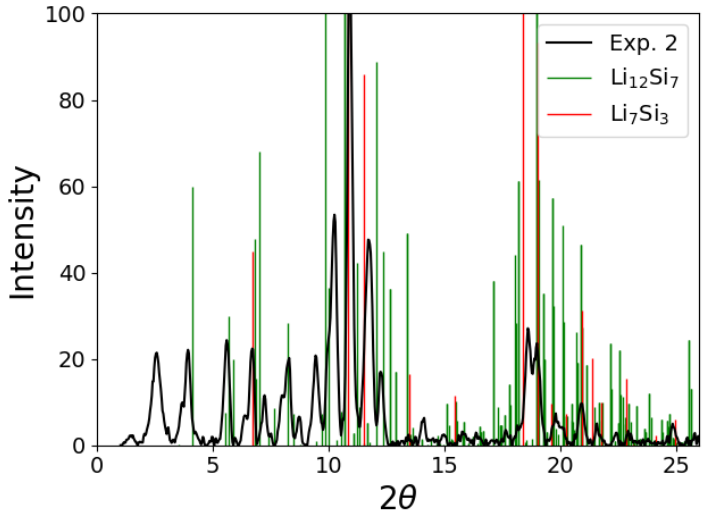

Figure 4.12: The XRD 2 pattern of the Exp. 2 at $x = 2.41$ in Li_xSi as reported in Fig. 4.11. A comparison with the experimental XRD data reported by The International Centre for Diffraction Data of $Li_{12}Si_7$, and Li_7Si_3 [125].

The X-ray diffraction patterns of Exp. 2 by Magali Gauthier can be seen in Fig. 4.12. The XRD is performed at Li composition where the plateau with the previous phase starts to appear (at $x = 2.41$ in Exp. 2, labeled XRD 2 in Fig. 4.11). All the peaks of the experimental sample can be identified and attributed to peaks of either $Li_{12}Si_7$ or Li_7Si_3 from an international database [125] suggesting the existence of these ordered phases even at room temperature. We remind the reader that the peak around $2\theta = 2.5°$ is, indeed, reported by our simulated XRD of $Li_{43}Si_{18}$ in the previous chapter. But the same peak could also be a peak of the kapton tape used to keep the sample from reacting with air. Another sample was synthesized at a composition of $Li_{2.333}Si$ and characterized by XRD without the kapton tape: no peak at $2\theta = 2.5°$ is observed (Fig. D.1 in the appendix D). The difference between Li_7Si_3 and $Li_{43}Si_{18}$ in XRD analysis is very small and only concerns small peaks. If possible, neutron scattering should be done for this phase to draw a definite conclusion.

4.3 Li_7Si_3 as a disordered solid solution of $Li_{43}Si_{18}$

As previously shown, the LTE modeling of the non-stoichiometric Li_7Si_3 is problematic because the stability composition domain of this phase is far from the composition of the perfect stoichiometric phase which is used as the reference state of the LTE calculation. While at temperatures above 500 K we may find Li_7Si_3-$Li_{12}Si_7$ two-phase-equilibria, the corresponding equilibrium composition of Li_7Si_3 is systematically very far which calls into question the basic assumption of the dilute solid solution (SS) in the present LTE calculation. Moreover, above 600 K (like previously shown for 690 K) there is not a consistent way of predicting consecutive two-phase-equilibria (we had to ignore the Li_7Si_3 and the Li_5Si_2 phases). This may be the limitations we have from the LTE at high temperatures when it comes to modeling disordered structures with large concentration of point defects. Nonetheless, the LTE gives consistent results at lower temperatures (such as 300 K) since we were able to consistently build the two-

phase-equilibria in a coherent way without ignoring any phase. The limitations of an LTE calculation above 600 K is not surprising. We expect order-disorder transitions of the Li_xSi compounds. Li_7Si_3 can be seen as a disordered SS of $Li_{43}Si_{18}$ with large deviations from the perfect stoichiometry. This can be understood as a transition from ordered (at lower temperatures) to disordered (at higher temperatures). Thus, the need for an alternative energy model and statistical method capable of modeling the disordering of Li vacancies/interstitials around Li_7Si_3 arises.

In this section, we explain how we model the Li interstitial solid solution around Li_7Si_3. We begin by defining the sub-lattices used in our model, we then discuss the parameters of our model (the interactions), and finally give the Gibbs free energy of this solid solution.

4.3.1 Li Sublattices

As we know from the previous chapter, the Li3 (the farthest Li from the Si dumbbell) is the most stable vacancy to create in the Li_5Si_2. Conveniently, these Li3 vacancies are enough to construct the ordered Li_7Si_3, $Li_{43}Si_{18}$, $Li_{44}Si_{18}$ phases from the Li_5Si_2 phase. The $Li_{43}Si_{18}$ and the $Li_{44}Si_{18}$ phases have the same symmetry but different compositions. To describe the increase of symmetry from these phases to Li_7Si_3 or Li_5Si_2, we need to introduce two sublattices of Li. With these two sub-lattices, we are able to reproduce all the perfectly ordered phases as end members. In Fig. 4.13, we show the sublattices that we pick for the model. Note that with these sublattices, the model cannot reproduce the disordering from Li_7Si_3 to Li_5Si_2. The perfectly stoichiometric Li_5Si_2 phase only appears as an end member of the Li_7Si_3 ordering model. We refer to the vacancy occupancy fraction per site of the i^{th} sublattice as y_i which is equivalent to the number of introduced vacancies divided by the number of sub-lattice sites. The sublattice occupancies are defined as followed:

$$\begin{aligned} y_1 &= y + \beta, \\ y_2 &= y - 0.5\beta, \end{aligned} \tag{4.10}$$

where, β is the long range order parameter (LROP), and y stands for the total occupation of vacancies in the Li sublattices. The prefactors of the LROP are chosen such that the normalization condition $3y = y_1 + 2y_2$ is satisfied. The LROP is such that it minimizes the Gibbs free energy (to be discussed later in this section). Table 4.1 shows that full occupations of the sublattice in Li or vacancy leads to the perfect stoichiometric phases that can be considered as end members of the present ordering model. Notice that whenever the LROP is zero, the Li-sublattices 1 and 2 become equivalent which corresponds to the symmetry of the Li_7Si_3 ordered phase.

Ordered Phase	y_1	y_2
Li_7Si_3	1	1
$Li_{43}Si_{18}$	0	1
$Li_{44}Si_{18}$	1	0
Li_5Si_2	0	0

Table 4.1: Ordered phases and corresponding sub-lattice occupancies.

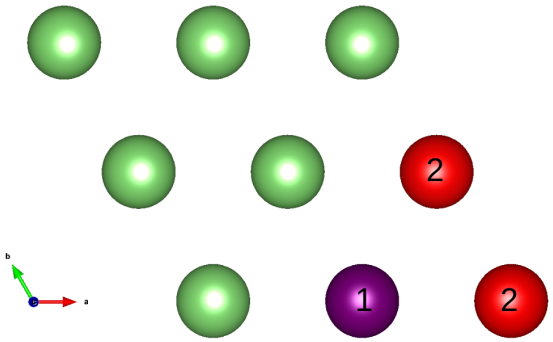

Figure 4.13: [001] projection of the Li_7Si_3 unit cell. For simplicity, the Si dumbbells are not shown. The colored (purple, red) and numbered (1, 2 respectively) sites represent Li3 sites of each column. Columns with number 1 and 2 respectively represent the chosen sublattices. Notice that the number of sites of sublattice 2 is twice the ones of sublattice 1.

4.3.2 Vacancy interaction energy model

We introduce a temperature dependent, ϵ^T_{vv}, between first nearest neighbour Li3 vacancies located on two neighboring columns. In addition, we introduce an on-site temperature-dependent vacancy energy E^T_v. We adjust E^T_v and ϵ^T_{vv} to reproduce the formation energies of the perfectly stoichiometric phases Li_7Si_3, $Li_{43}Si_{18}$, and Li_5Si_2 including their vibrational contribution. We plot ϵ^T_{vv} and E^T_v as a function of temperature in Fig. 4.15. It is important to remark that vacancy-vacancy interactions are a convenient way to model the modification of Li-Li interactions in the presence of vacancy.

The energy ϵ^T_{vv} corresponds to the binding energy of 2 nearest column Li3 vacancies ($E_b^{\text{vv},T}$) because:

$$E_b^{\text{vv},T} = \epsilon^T_{\text{vv}} + \epsilon^T_{\text{LiLi}} - 2\epsilon^T_{\text{vLi}}, \tag{4.11}$$

where ϵ^T_{LiLi} and ϵ^T_{vLi} are the Li-Li, and Li-v interactions respectively. They are set to 0 in our model, hence $E_b^{\text{vv},T} = \epsilon^T_{\text{vv}}$. We predict that from 0 K to 540 K the interaction is a repulsive one and above 540 K it is an attractive one (Fig. 4.15a).

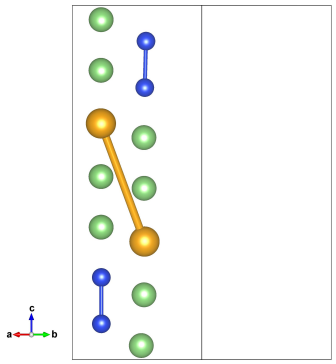

Figure 4.14: Li3 vacancies (denoted as yellow spheres) first nearest column interaction (denoted as a yellow line) projected on [110] plane in the Li_7Si_3 unit cell. For simplicity, we remove all the other columns to just show the 2 columns needed to represent the interaction.

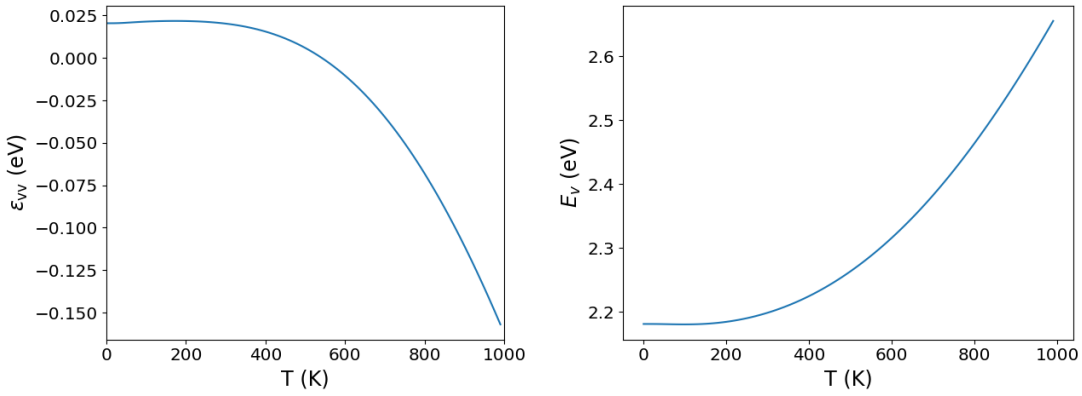

(a) Interaction energy

(b) Onsite energy

Figure 4.15: Plots of the interaction (a) and onsite energies vs temperature.

The number of interactions among the sublattices 1 and 2 (defined in the previous subsection) are listed in table 4.2.

Sublattice	**j=1**	**j=2**
i=1	0	2/18
i=2	2/18	1/18

Table 4.2: Number of first nearest vacancy-vacancy interactions between sublattices i and j (z_{ij}) normalized by the number of Si.

4.3.3 Mean Field Model of the Gibbs Free energy

We rely on the Bragg-Williams mean field approximation to write the Gibbs free energy including the vibrational and ideal configurational entropy. In the mean field model (MFM) the occupation does not depend on the occupation of other sites (regular solution model). Within the mean field approximation, the mean occupation of a pair of sites is equal to the product of mean occupations of the sites of the pair. Consequently, the enthalpy depends on the nominal composition only; so all possible atomic configurations for a particular nominal composition equally contribute to the configurational entropy. Hence, the entropy is given by the logarithm of the number of permutations between atoms (multiplicity) and equal to the ideal configurational entropy. The Gibbs free energy then reads as in Eq. 4.12:

$$\begin{aligned} G &= H - T(S_{vib} + S_{conf}) \\ &= G_0^T + N_\alpha y E_\alpha + \sum_{l\in\Omega}\sum_{i,j\in\Phi} \frac{z_{ij}^l}{2} y_i y_j \epsilon_l^T + N_\alpha k_B T \sum_{i\in\Phi} \lambda_i \left[y_i \ln y_i + (1-y_i)\ln(1-y_i) \right], \end{aligned} \tag{4.12}$$

where $G_0^T = H_0 - TS_{0,vib}$ corresponds to the Gibbs free energy including only vibrational entropy at temperature T of the reference system, N_α is the number of lattice sites in both sublattices, $y = n_\alpha/N_\alpha$ (as defined previously) is the total occupation ($0 \leq y \leq 1$) of the sublattice in α species with respect to the reference, E_α^T is the α species temperature dependent onsite energy, y_i is the occupation in the i^{th} sub-lattice and must respect the normalization condition $y = \sum_{i\in\Phi} \lambda_i y_i$, λ_i is the normalization ratio (i.e. $N_\alpha \lambda_i$ is the number of sites of sublattice i), Φ is the set of chosen sub-lattices in the crystal, ϵ_l denotes

the l^{th} interaction, Ω is the set of interactions, and z_{ij}^{l} is the total number of l interactions between the i^{th} and j^{th} sub-lattices. The last summation term of Eq. 4.12 is in fact the summation of the ideal configurational entropy in each sub-lattice.

We took G_0^T as the $G_p(\text{Li}_5\text{Si}_2)$ normalized per Si given in the appendix A (normalized per atom). We chose E_α^T as the onsite energy of a vacancy given in Fig. 4.15b. The z_{ij}^{l} and ϵ_{vv}^{T} values can be found in table 4.2 and Fig. 4.15 respectively. The λ_i values are 1/3 and 2/3 for sublattices 1 and 2, respectively (taken from the normalization condition $3y = y_1 + 2y_2$).

4.3.4 Li order-disorder transition temperature

The values of sublattices occupations (y_1 and y_2) depend on the LROP β. At each composition and temperature, β is the parameter that minimizes the Gibbs free energy, this is also known as the compound energy formalism proposed by M. Hillert [126]. We plot β and sublattices occupations against composition at several temperatures in Fig. 4.16. We notice that β tends to 0 as temperature increases. At temperatures greater than 60 K β is equal to 0 at all compositions. In terms of sublattice occupancy, when $\beta = 0$ both y_1 and y_2 are equal to y (recall Eq. 4.10). The ordering temperature depends on composition; for example, from 60 K and below, at the composition around $x = 2.44$ in Li_xSi, the solid solution is ordered (i.e. $\beta \neq 0$ at $x = 2.44$). The presented results predict that above 60 K the Li_7Si_3 phase -also called the Li-disordered solid solution (SS)- is more stable than the $\text{Li}_{43}\text{Si}_{18}$ and $\text{Li}_{44}\text{Si}_{18}$ ordered phases.

We plot the Gibbs free energy against composition from 0 K to 70 K in Fig. 4.17. The transition from ordered to disordered is seen, in the Gibbs free energy, by the switch of two-local minima to one minimum. The local minima represent the Gibbs free energies of ordered phases $\text{Li}_{43}\text{Si}_{18}$ and $\text{Li}_{44}\text{Si}_{18}$ around their respective composition. Consequently, there will be a small domain in composition and temperature for which we have a two phase equilibrium between the ordered $\text{Li}_{43}\text{Si}_{18}$ and $\text{Li}_{44}\text{Si}_{18}$. The disordering of the $\text{Li}_{43}\text{Si}_{18}$ and $\text{Li}_{44}\text{Si}_{18}$ phases leads to the so called Li_7Si_3 phase at temperatures greater than 60 K. The disordering of Li_7Si_3 towards Li_5Si_2 cannot be modeled with the current state of our model, since we have no sublattice (therefore, no long range order parameter) that describes the Li_5Si_2 phase.

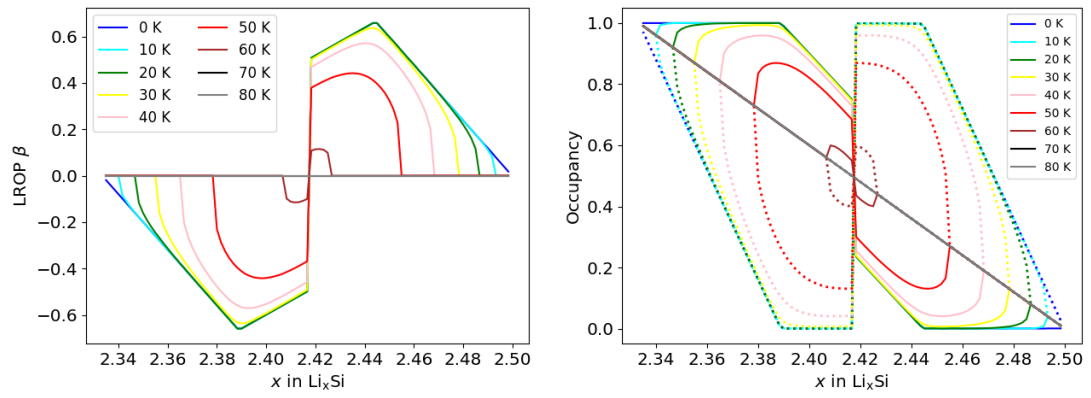

(a) LROP

(b) y_1 (dotted lines) and y_2 (solid lines)

Figure 4.16: (a) Plot of the LROP vs composition at several temperatures. (b) Plot of the sublattice occupation vs composition at several temperatures.

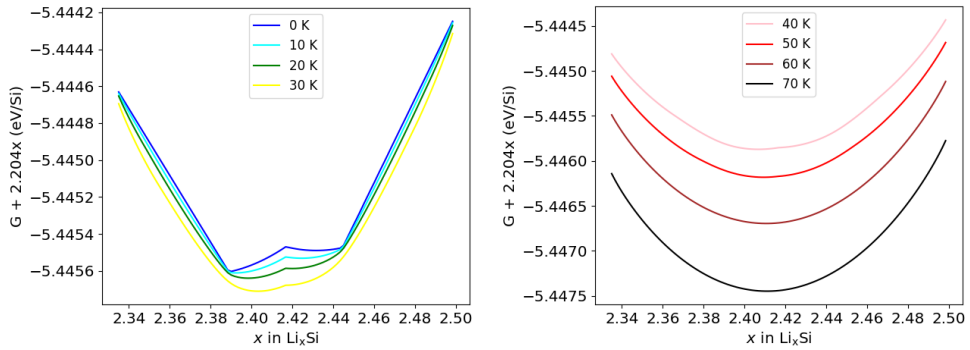

(a) From 0 K to 30 K (b) From 40 K to 70 K

Figure 4.17: Plot of the Gibbs free energy per Si. Note that a linear term ($-2.204x$ eV/Si) is subtracted from G to be able to highlight the transition from ordered to disordered state of the Li-sublattices.

4.3.5 Thermodynamic stability of the Li-disordered solid solution

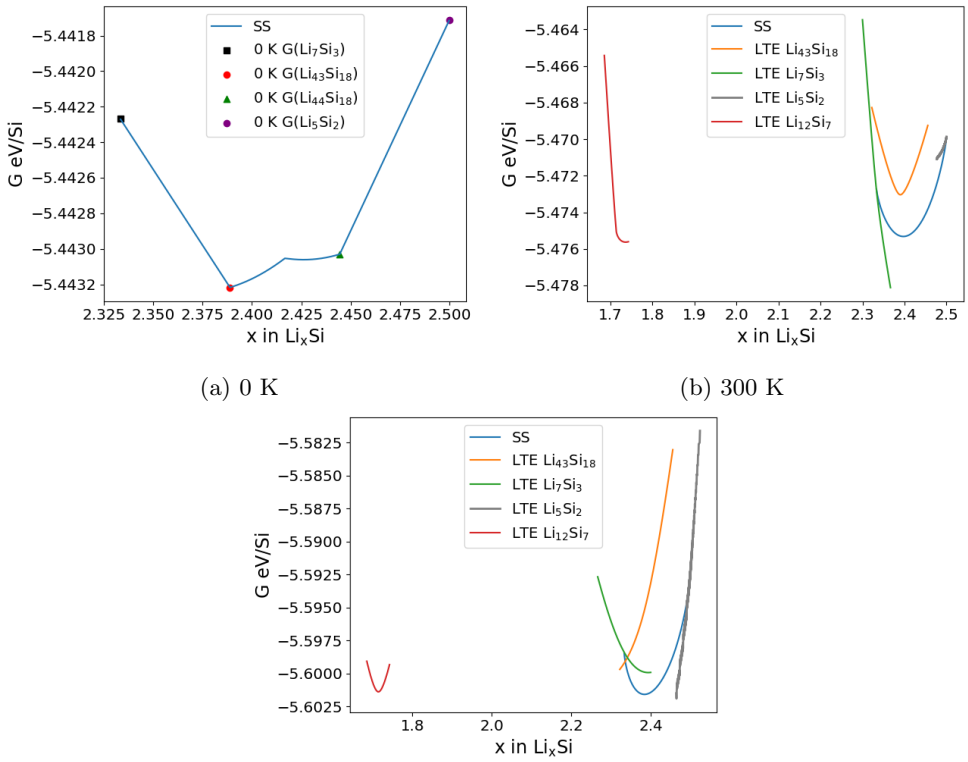

(a) 0 K (b) 300 K

(c) 690 K

Figure 4.18: Plot of the Gibbs free energies at 0 K, 300 K, and 690 K. We remove the common tangent ($G - x\mu_{eq}$ such that $x = N_{\mathrm{Li}}/N_{\mathrm{Si}}$) in each plot in order to align the Gibbs free energy minima of $Li_{12}Si_7$ with that of the SS at equilibrium.

We plot the Gibbs free energies of Li_7Si_3, $Li_{43}Si_{18}$, Li_5Si_2 and the SS in Fig. 4.18 at 0 K, 300 K and 690 K. Our calculations predict that the SS is thermodynamically more stable than $Li_{43}Si_{18}$ and Li_7Si_3 against $Li_{12}Si_7$. Note that at 0 K, the SS model exactly reproduces the 0 K Gibbs free energies of the end members (Li_7Si_3, $Li_{43}Si_{18}$, $Li_{44}Si_{18}$ and Li_5Si_2).

If we compare to the convex hull at finite temperatures (chapter 2), we observe a discrepancy on the relative stability of $Li_{43}Si_{18}$ and Li_7Si_3 which mainly results from the large deviation of Li_7Si_3 from perfect stoichiometry.

4.3.6 Phase Diagram based on the solid solution model

After obtaining the Gibbs free energies as a function of composition for each phase we can proceed to construct the phase diagram using the common tangent construction (explained in Sec. 1.3.5). For this phase diagram (Fig. 4.19) we have taken the Gibbs free energies of $Li_{12}Si_7$, $Li_{13}Si_4$ and $Li_{17}Si_4$ obtained with the LTE and the previously described Gibbs free energy of the SS.

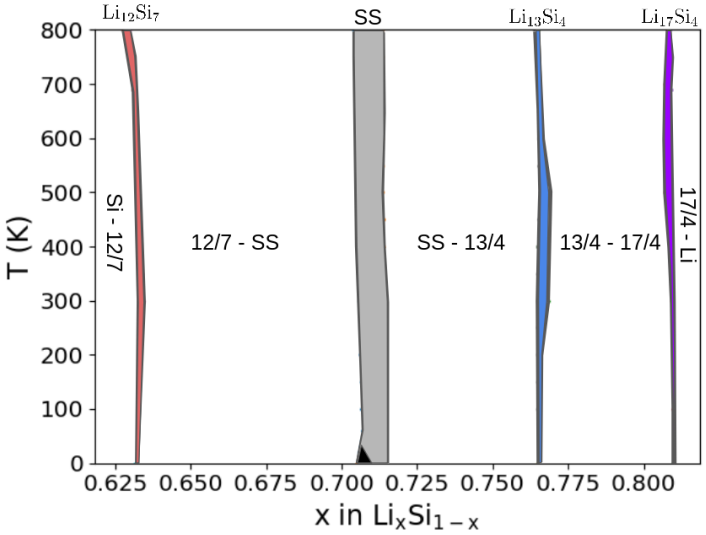

Figure 4.19: Phase diagram of the Li-Si system including the SS. The phase diagram is zoomed in between $Li_{12}Si_7$ and $Li_{17}Si_4$, before and after these two phases we have the pure elements Si and Li, respectively. The colored areas represent the single phase domains of the compounds. To denote the two-phase-equilibrium between A and B compounds we put "A-B" in the plots. We use the notation "n/m" to denote the Li_nSi_m phase. The black area in the solid solution domain is to be further discussed in Fig. 4.20.

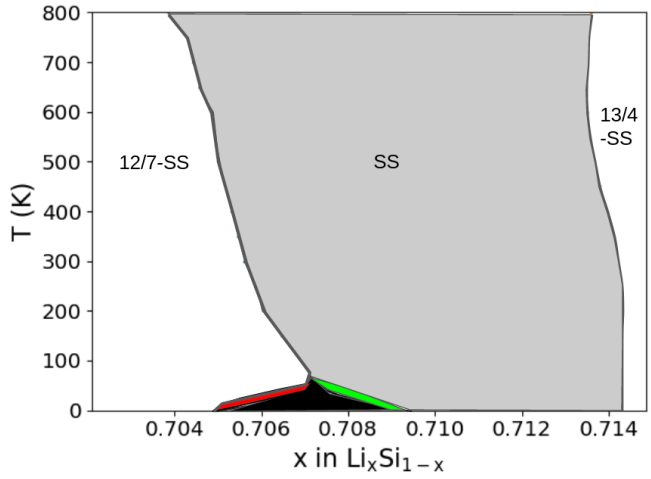

Figure 4.20: Plot of the phase diagram around the solid solution. The black area represents the domain of two phase equilibrium between the ordered phases $Li_{43}Si_{18}$ and $Li_{44}Si_{18}$. The red area represents the domain of the single phase $Li_{43}Si_{18}$. The green area represents the $Li_{44}Si_{18}$ single phase domain. The two phase equilibria domains between the Li_7Si_3 disordered solid solution and the previous ($Li_{12}Si_7$) and next ($Li_{13}Si_4$) phases are labeled "12/7-SS" and "13/4-SS" respectively.

We remark that the presented phase diagram does not contain the liquid transition hence the comparison with previous CALPHAD phase diagrams can only be done for the solid-state temperatures. We list below the comparison of our phase diagram with latest, experimentally assessed, and reported in the literature [42, 53] (previously shown in the bibliography):

- Contrary to [42, 53], the presented phase diagram includes the off-stoichiometry; therefore, it can predict the single phase domain of each of the phases that can be useful for comparison with experiments.

- The presented phase diagram is in agreement with both [42, 53] on $Li_{12}Si_7$ and $Li_{13}Si_4$ being stable phases.

- We do not consider the LiSi as a stable phase unlike [53]. Our DFT using HSE06 hybrid functional 0 K calculations in Chapter 2 demonstrated that this phase is in fact a metastable one. Finite temperature studies should, however, be performed using the HSE06 functional to draw a conclusion on the stability of LiSi.

- Both [42] and [53] report the Li_7Si_3 phase which in our case it comprises the ordered $Li_{43}Si_{18}$, $Li_{44}Si_{18}$, and Li_5Si_2 at temperatures below 60 K and the disordered SS at temperatures greater than 60 K.

- We agree with [53] and disagree with [42] (reporting $Li_{22}Si_5$) on the highly lithiated phase being the $Li_{17}Si_4$ from 0 K to almost 800 K. However, unlike [53], we do not report the $Li_{21}Si_5$ and the $Li_{4.11}Si$ at high temperatures. Finite temperature and LTE studies should be performed with these two phases to understand what happens around 800 K with these phases. It could be something similar to the presented SS.

4.3.7 OCV and thermodynamic enhancement factor

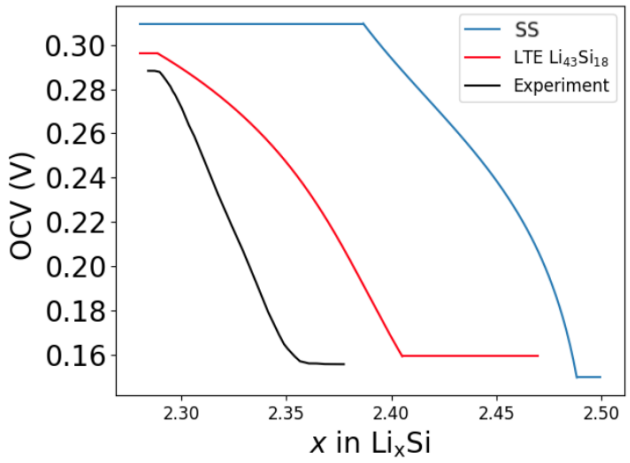

Figure 4.21: Plot of the open circuit voltage at 690 K of SS, LTE $Li_{43}Si_{18}$, and experiment by [35] vs composition.

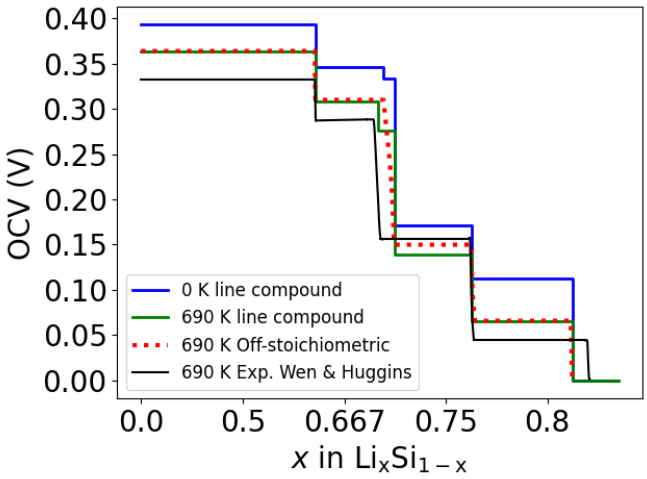

Figure 4.22: Plot of the evolution of OCV using the methods of this work vs composition. From line compound calculations at 0 K and finite temperatures to the inclusion of off-stoichiometry.

The chemical potential of Li can be calculated from the Gibbs free energy (recall Eq. 1.45 in Chapter 1), therefore we can calculate the OCV. We plot, in Fig. 4.21, the OCV at 690 K of the SS from the MFM and compare it to the metastable LTE OCV of $Li_{43}Si_{18}$ and the experiment [35]. In comparison with the previous LTE results of $Li_{43}Si_{18}$ (ignoring Li_5Si_2 and Li_7Si_3), the SS overestimates the range of composition for which we have the single phase domain. However, the slope is very close to the one of the LTE of $Li_{43}Si_{18}$ suggesting that the interaction model correctly reproduces the formation free energy of Li-point defects (recall that the slope of OCV is related to the formation energies of point defects from

the previous chapter).

Fig. 4.22 highlights the calculated finite temperature effects progressively added to the chemical potential of Li and provides a direct comparison with the measured OCV at 690 K. With respect to the line compounds OCV including vibrational finite temperature effects reported in Chapter 2, significant changes in OCV can be observed. First of all, we observe the OCV plateau between Li_7Si_3 and $Li_{13}Si_4$ is shifted towards the right value. Second of all, we obtain a single drop from $Li_{12}Si_7$-Li_7Si_3 plateau to Li_7Si_3-$Li_{13}Si_4$ plateau instead of 2 observed with line compounds. Finally, the resulting slopes of the OCV drops in the single phase domains are in good agreement with the experimental ones.

The thermodynamic enhancement factor ϕ (recall from previous chapter Eq. 3.18) is computed for the SS. Notice how, unlike the thermodynamic enhancement factor of $Li_{43}Si_{18}$ (see Fig. 4.23), we do not obtain a maximum but rather a minimum.

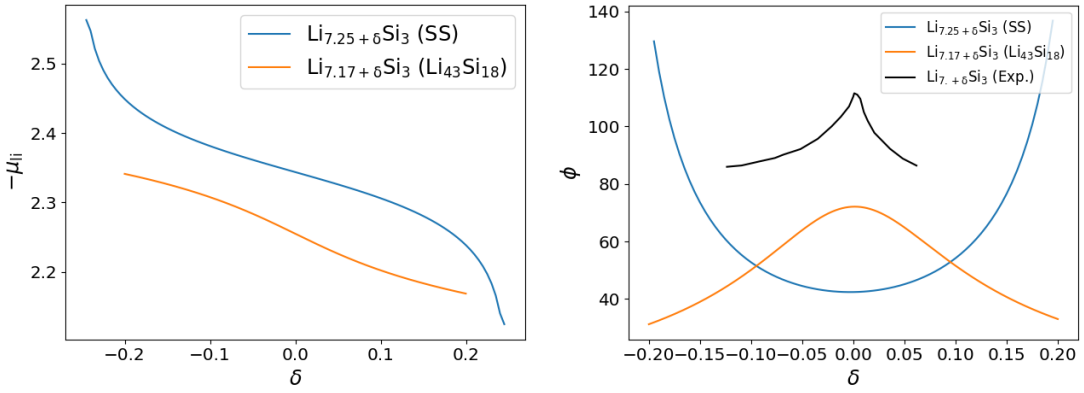

(a) -μ_{Li} ≡ OCV (b) Thermodynamic enhancement factor

Figure 4.23: (a) Chemical potential of Li excluding the two-phase-equilibria, and (b) enhancement thermodynamic factor of the SS and $Li_{43}Si_{18}$ phase at 690 K as a function of composition. We also plot the experimental thermodynamic enhancement factor at 690 K by [35].

To explain why we obtain a minimum instead of a maximum, we can look at the plot of the chemical potential of Li of the solid solution and $Li_{43}Si_{18}$ vs composition (Fig. 4.23a). Both the $Li_{43}Si_{18}$ and the SS lead to roughly pair functions whereas the measured one is not a pair function of δ. However, in the SS forming a Frenkel pair (FP) merely corresponds to adding a Li and removing a Li atom on the same sublattice. Thereby there is no possibility to create a FP in the SS model, or in other words there is no energy cost associated with the formation of the FP. Nonetheless, there is an entropy contribution to the formation of FP which just corresponds to the number of possible permutations, modeled by the ideal configurational entropy. For instance, we can observe this analytically if we do the double derivative of G (Eq. 4.12) with respect to y giving a quantity which is proportional to the thermodynamic factor:

$$\phi \propto \frac{d^2G}{dy^2} = A + B\frac{1}{y - y^2}, \tag{4.13}$$

where A is a constant containing the interaction energy and B is another constant coming from the prefactor of the ideal configurational entropy. Notice how only the ideal configurational entropy term is the only one contributing to the thermodynamic enhancement factor (and giving a minimum since $0 \leq y \leq 1$).

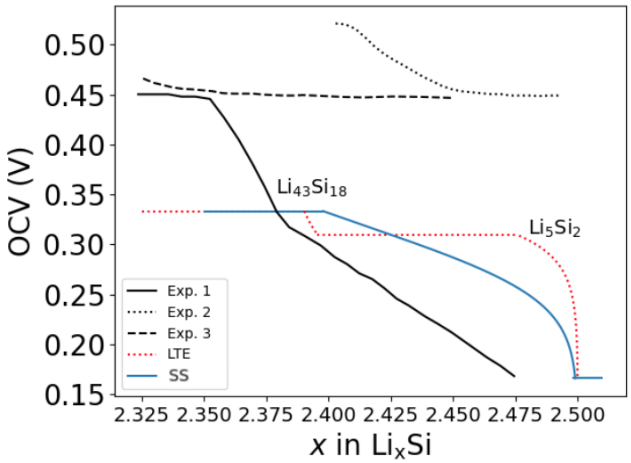

Figure 4.24: Plot of the OCV using our solid solution model and LTE $Li_{43}Si_{18}$ at 300 K vs composition of the $Li_{43}Si_{18}$ phase. Comparison with 3 measure OCV [courtesy of Magali Gauthier]: (1) OCV upon lithiation measured with a 3 electrode cell; (2) and (3) are delithiation with 2 and 3 electrode cells respectively.

We also plot the OCV at 300 K to compare with the previously reported experimental results (as shown previously in Fig. 4.11) and the LTE results of $Li_{43}Si_{18}/Li_5Si_2$ in Fig. 4.24. In comparison with the results at 690 K, we observe that the SS model yields an OCV slope that is closer to the experimental one than that of the $Li_{43}Si_{18}/Li_5Si_2$ LTE leading to an intermediary OCV plateau. This result is in line with the XRD identification of Li_7Si_3 at room temperature (see figures 4.12 and D.1); what we have is the SS which in fact represents the Li_7Si_3 at room temperature (as previously explained).

OCV plateaus as a function of temperature

We plot in Fig. 4.25 the OCV plateau values (including the off-stoichiometry) as a function of temperature and we compare with the linear law proposed by the work of Sharma and Seefurth based on high temperature measured OCV [34] and the values provided by the CALPHAD work of Wang et al. [42]. It is worth noting that we denote them as first, second, third and fourth plateau as the two-phase-equilibria are different in each of the works.

The OCV plateau values presented in this work and CALPHAD show that a linear fit from high temperature values extrapolated down to room temperature is a good approximation, hence we can use the fits of Sharma and Seefurth [34] to extrapolate the OCV of crystalline phases down to room temperature. Even though the CALPHAD values were assessed from heat capacity measurements [42], they differ (i.e. at most ∼50 mV) from the ones reported by the experiment at all temperatures [34].

The third plateau shows the largest discrepancy between experiment and our results, especially at low temperatures. As previously explained, we believe this is due to Li_5Si_2 being an end member in our solid solution model. The OCV values of the two-phase-equilibrium between Li_5Si_2 and $Li_{13}Si_4$ using line compounds at 300 K and 690 K (please see chapter 2 finite temperature OCV values or Fig. 4.10) are similar to the ones predicted by the solid solution model. Although the error might be within the DFT accuracy, there is room for improvement in the solid solution model -especially around the end member Li_5Si_2.

All the other OCV plateau values show a better agreement with the experimental extrapolated values from the fit at 300 K. This hints at the fact that we are missing finite temperature effects in the present

thermodynamic models such as the vibrational contribution on the Li point defect formation energy that might be necessary at high temperatures -recall that we prove in the previous chapter that small changes of the order of 10 meV to the formation energies can drastically change the slope and therefore the two-phase-equilibrium OCV value.

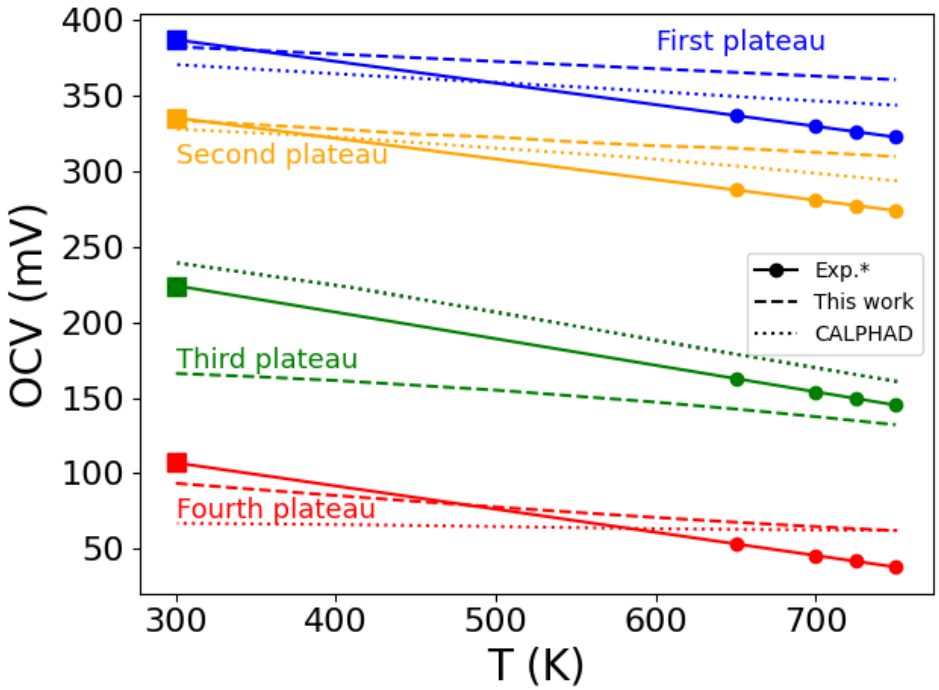

Figure 4.25: Plot of the OCV plateau values as a function of temperature. The order of plateaus from two-phase-equilibria according to our work are as follow: Si-$Li_{12}Si_7$ (blue), $Li_{12}Si_7$-SS (orange), SS-$Li_{13}Si_4$ (green), $Li_{13}Si_4$-$Li_{17}Si_4$ (red). The experimental values are obtained from Sharma and Seefurth [34]. The CALPHAD values are obtained from Wang et al. [42]. *Note that we do an extrapolation down to 300 K (represented by squares) of a linear fit on high temperature values.

4.3.8 Heat Capacity

In Fig. 4.19, we observe the SS has the largest single phase composition domain. It is also around this composition domain that isobaric heat capacity (C_p) shows a cusp at 220K [54, 43]. As previously mentioned in the bibliography, the NMR characterization of Dupke et al. reports in parallel the disappearance of the iconic Si5 ring of $Li_{12}Si_7$ NMR signal around 210 K [54]. If we consider the Li_7Si_3 composition of the experimental studies [54, 43], reported to to be the one of the perfect stoichiometric phase (i.e $x = 0.7$ in Li_xSi_{1-x}), we obtain no phase transformation according to our phase diagram. In order to obtain a phase transformation from a $Li_{12}Si_7$-SS two-phase-equilibrium to a single phase at a solvus temperature of 210 K, our zoomed in solid solution phase diagram (Fig. 4.20) suggests a composition of $x = 0.706$ in Li_xSi_{1-x}. At this nominal composition, however, we observe two other phase transitions occuring at very low temperature, 10 K and 20 K. The 10 K phase transition happens from the $Li_{43}Si_{18}$-$Li_{44}Si_{18}$ two-phase-equilibrium to the $Li_{43}Si_{18}$ single phase domain. Then at 20 K the single phase $Li_{43}Si_{18}$ separates into $Li_{12}Si_7$ and SS. The discontinuities of the second derivative of the free enthalpy with respect

to temperature at $x = 0.706$ will cause 3 cusps to appear as shown in Fig. 4.26. Nonetheless, in the experiments only one cusp is observed at T = 210 K.

Interestingly, the shape of the cusp, in particular its increasing rate with temperature and its height, is related to the proportion of phases forming, hence to the nominal composition and the variation of the solvus temperature with composition in the phase diagram. We observe the predicted increasing rate of the cusp is lower than the experimental one. This discrepancy could be due to an overestimation of the variation of the solvus temperature decrease with Li composition (boundary limit of the SS delimiting the $Li_{12}Si_7$/SS domain).

We doubt that the first predicted cusp from the $Li_{43}Si_{18}$-$Li_{44}Si_{18}$ two-phase-equilibrium to $Li_{43}Si_{18}$ single phase domain would be observable in the experiment. The temperature is too low for atomic diffusion to be effective [127]. We also doubt for the same reasons that the second cusp can be observed since it also happens at very low temperature and at composition very close to the boundary limit (the precipitation driving force and the proportion of $Li_{12}Si_7$ would be small).

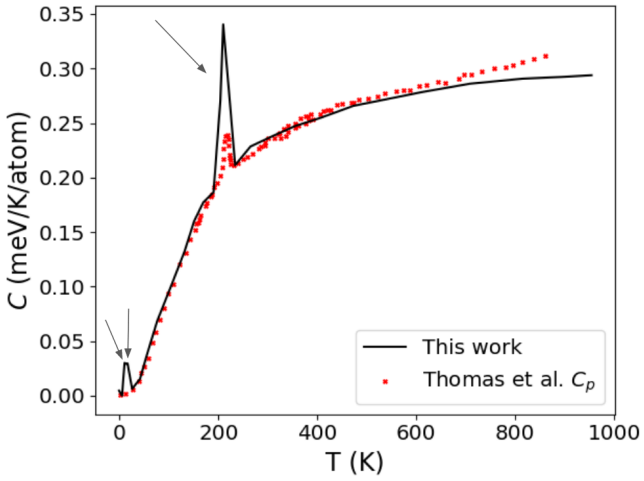

Figure 4.26: Heat capacity vs temperature. Comparison with experiment by Thomas et al. [43]. The peaks are indicated by arrows.

4.4 The metastable $Li_{15}Si_4$ phase

Before heading into the next section where we study constrained nucleation driving forces at 300 K, it is important that we present the finite temperature studies and off-stoichiometry studies for $Li_{15}Si_4$ (like the ones done for all the other phases in chapter 2 and chapter 3).

Unlike the previously done studies for all the other phases, we just use the Harmonic approximation because we are interested in the results at 300 K. Remark that at 300 K the Gibbs free energy (denoted G_p in Chapter 2) and the Helmholtz free energy (denoted G_v in Chapter 2) are very similar (recall all the G_p and G_v vs T plots in Chapter 2).

The set of input parameters for VASP code consists of an energy convergence criterion of 10^{-7} eV for the self-consistent field of cycle, an energy cutoff of 750 eV for the plane-wave basis set, a $4 \times 4 \times 4$ Gamma-centered k-point mesh for Brillouin zone sampling, and a super-cell. We note that the unit cell (taken from [103]) is large enough to have 10 Å between the images for the finite displacement method.

4.4.1 Phonon density of state

The 0 K and fully relaxed $Li_{15}Si_4$ phonon density of states (PDOS) has no imaginary frequencies (Fig. 4.27), this means that both our accuracy parameters were optimal for this calculation and the $Li_{15}Si_4$ structure under the study is mechanically stable.

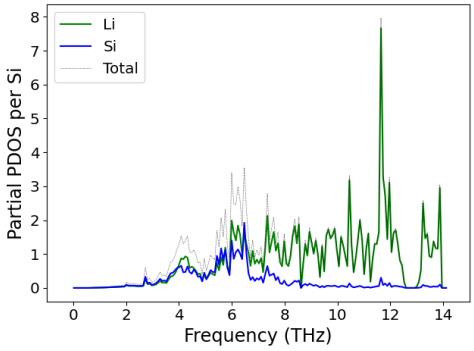

Figure 4.27: $Li_{15}Si_4$ projected phonon density of states at the equilibrium volume (a=0) at 0 K.

The projected PDOS is very similar to the ones of the highly lithiated phase where the low frequency block is dominated by both species and the high frequency block is only dominated by the Li species (recall the projected PDOS of $Li_{13}Si_4$ in chapter 2 and the one reported for $Li_{21}Si_5$ by [41]).

4.4.2 Free energy, Isochoric Entropy, and Isochoric Heat Capacity

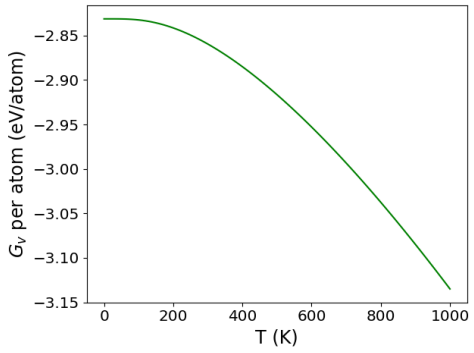

Figure 4.28: Plot of the $Li_{15}Si_4$ G_v vs temperature.

We assume that the Gibbs free energy is almost the same as the Helmholtz free energy up to 300 K. Therefore, for the studies done at 300 K we consider that G_v (Fig. 4.28) is enough and we do not need quasi-harmonic calculation including the effect of volume expansion.

We calculate S_v and C_v from the corresponding G_v and proceed to plot it against T (Fig. 4.29a). We can compare it with previous results of Chevrier et al. using also Harmonic approximation [41]. We see that we have very good agreement with the results of Chevrier et al.

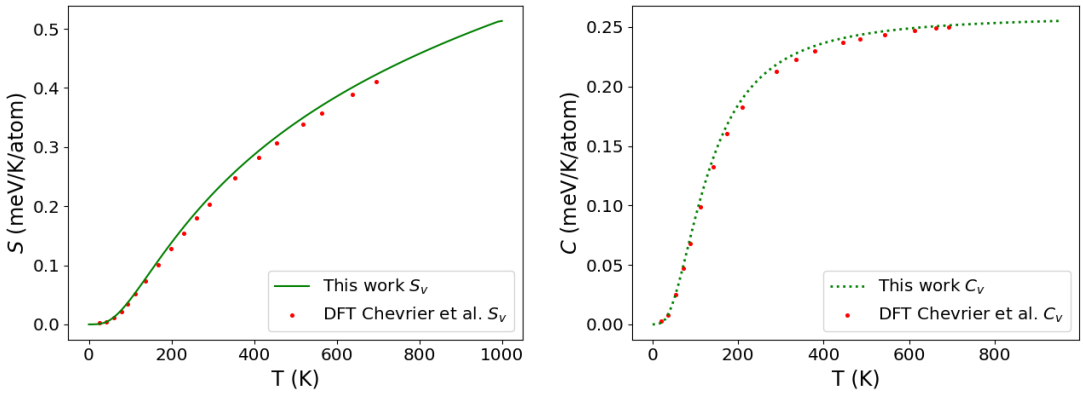

(a) Entropy (b) Heat Capacity

Figure 4.29: Plot of the $Li_{15}Si_4$ isochoric entropy (a) and heat capacity (b) vs temperature. Comparison with DFT HA by Chevrier et al [41].

Thermodynamic stability of $Li_{15}Si_4$

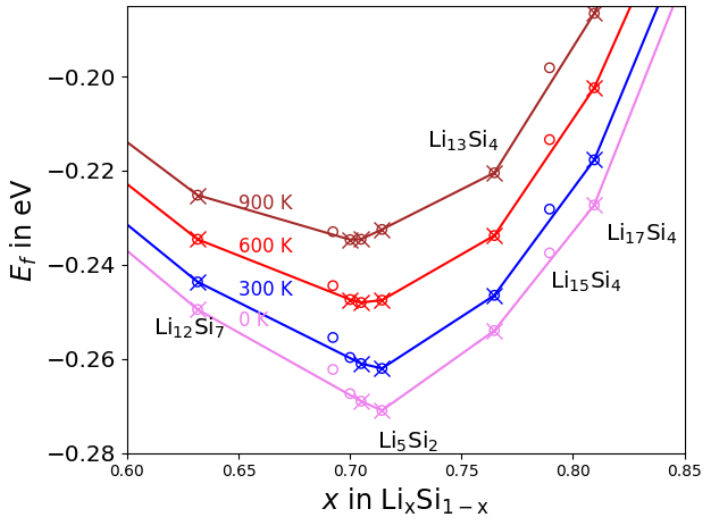

Figure 4.30: Convex hull of the formation free energies (including HA atomic vibrations) of compounds at steps of 300 K vs composition. The plot is zoomed in such that we portray the phases between $Li_{12}Si_7$ and $Li_{17}Si_4$ included. The stable phases are marked by '×'.

We plot the harmonic approximation convex hull at finite temperatures to see the stability of $Li_{15}Si_4$ vs the ones of phases studied in Chapter 2 in Fig. 4.30. In terms of stability, $Li_{15}Si_4$ is not thermodynamically stable against the two-phase-equilibrium of $Li_{13}Si_4$ and $Li_{17}Si_4$. This is in line with previously reported HA finite temperature convex hull by Chevrier et al. [41] and also all the experimental evidence showing that $Li_{15}Si_4$ is metastable phase that dissolves in thermal conditions [62] (refer to Chapter 1 on for more information).

4.4.3 Point defects in $Li_{15}Si_4$

The formation energies of point defects are calculated in a $2 \times 2 \times 2$ supercell, with a self consistent field convergence energy of 10^{-4} eV and with a $2 \times 2 \times 2$ mesh Monkhorst-Pack Brillouin zone. We list, in table 4.3 with the help of Fig. 4.31, the formation energies (E_f) of $Li_{15}Si_4$ point defects using as a reference the chemical potential of Li and Si at $\delta = 0$ in $Li_{15+\delta}Si_4$ and T = 300 K. The formation energy of point defects suggests that the off-stoichiometry of $Li_{15}Si_4$ is governed by interstitials of Li for $\delta > 0$ and interstitials of Si for $\delta < 0$ in $Li_{15+\delta}Si_4$. It is also worth noting that like $Li_{13}Si_4$, the $Li_{15}Si_4$ phase has a Si interstitial low formation energy.

Vacancies			**Interstitials**		
Label	E_f (eV)	m_i	**Label**	E_f (eV)	m_i
Li0	0.9156	48/16	**Li2**	0.4550	26/16
Li1	1.1841	12/16	**Si3**	0.4762	26/16
Si2	0.9550	16/16			

Table 4.3: Table of formation energies of point defects in $Li_{15}Si_4$ with their respective multiplicity normalized by the number of Si atoms in the reference $m_i = M_i/N^0_{\mathrm{Si}}$. The Li and Si reference chemical potential are the ones at $\delta = 0$ in $Li_{15+\delta}Si_4$ from LTE at T = 300 K.

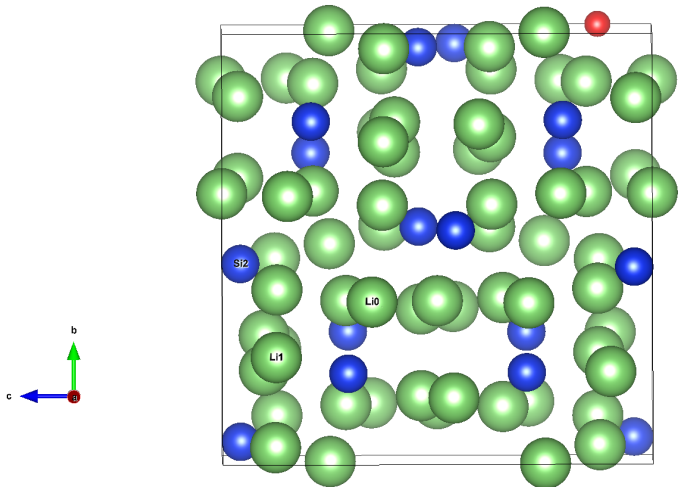

Figure 4.31: $Li_{15}Si_4$ unit cell labeled according to the "symmetric CIF" file found in Materials Project website [103] or the appendix C. The red sphere represents the E_f interstitial site for Li2 and Si3 and their coordinates are (0, 0, 0.125) in fraction of lattice parameter.

4.4.4 Single phase domain properties of $Li_{15}Si_4$

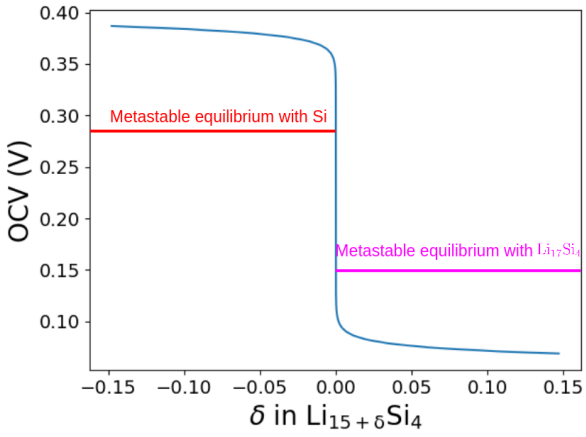

Figure 4.32: Plot of the single $Li_{15}Si_4$ phase domain OCV (in blue) as a function of composition at 300 K. The metastable two-phase-equilibria (OCV plateaus) with Si (in red) and $Li_{17}Si_4$ (in violet) are also portrayed.

Similar to what we do with $Li_{13}Si_4$ in Chapter 3, we can extract the chemical potential of Li and Si as a function of composition using the LTE.

We plot the OCV as a function of composition at 300 K and at the single phase domain of $Li_{15}Si_4$ in Fig. 4.32. We can see that very close to the perfect stoichiometry, the $Li_{15}Si_4$ has access to a wide range of chemical potentials of Li.

4.5 Nucleation driving forces under applied voltage

In the previous sections, we did not account for kinetics and assumed the system was always in thermodynamic equilibrium. When it comes to the reality of charging and discharging galvanic cells (e.g. during the closed circuit period in GITT), we force the chemical potential of Li (μ_{Li}) to take values that would not otherwise take place given the thermodynamics of the system. Recall that we impose the Li charging rate by fixing the current. If the Li-charging rate is too fast when compared to Li diffusion and to the mobility of the reaction fronts, we expect the chemical potentials to be far from their equilibrium values. Actually, imposing the current, in a GITT experiment, does not exactly correspond to imposing uniform chemical potential of Li. Imposing the current is equivalent to fixing the flux of Li, hence the gradient of Li chemical potential at the interphase. Nucleation models under a gradient of chemical potential (or equivalently a gradient of Li concentration) could show that above a threshold value, nucleation of the secondary phase might be delayed or even hindered [128]. In the present study, as a first step, we investigate the constrained nucleation driving forces driven by a non-equilibrium uniform Li chemical potential, whose value depends on the applied charging conditions.

In this section, we discuss the precipitation driving forces of stable or metastable phases starting from different reference states and applied Li-chemical potential, investigate all the possible phase transformation paths that can happen under a fixed non-equilibrium value of μ_{Li} . The analysis is performed at room temperature in order to discuss the possibility of forming the metastable $Li_{15}Si_4$. We apply the same approach, to analyze the phase transformations under de-lithiation and the resulting hysteresis that occurs during the voltage cycling of Li-Si systems. Before heading into this section, the reader is advised

to read the sections on the classical nucleation theory and GITT in Chapter 1 (Sec. 1.3.9, and Sec. 1.3.8) .

4.5.1 Constrained nucleation driving force

In a GITT experiment, we observe the relaxation of the Li chemical potential towards its (meta)stable equilibrium value in open circuit conditions. The resulting drop (resp. increase) of the OCV (which is minus the Li chemical potential) corresponds to the so-called overpotential (under potential). As explained in [88], an overpotential is mainly controlled by the thermally activated reactions of the galvanic cell, or more precisely by the limiting slowest reaction rate of the cell. This limiting reaction might be the diffusion rate of Li injected into the electrode, the nucleation rate of a secondary phase, or the mobility of the secondary phase reaction front. Here, we consider the limiting rate is the secondary phase nucleation rate. We assume that during (de)lithiation the Si atoms are immobile, and that Li diffuses fast enough to homogenize its chemical potential between phases. However, if the nucleation and growth of the secondary phase is too slow, the chemical potential of Si atoms in this phase will not be the equilibrium one.

In order to work at a fixed chemical potential of Li and different Li compositions between the parent and the secondary phase, we introduce the grand potential Φ:

$$\Phi = g - z\mu_{\mathrm{Li}}, \tag{4.14}$$

where g is the Gibbs free energy per Si, and z is the number of Li atoms divided by the number of Si atoms. Note that, Φ corresponds to the chemical potential of Si in the system. The grand canonical free energies of α, β and γ phases are schematically represented in Fig. 4.33. We choose not to represent them with respect to μ_{Li} but with respect to -μ_{Li} which directly corresponds to the voltage. We note that α, β and γ can, for example, be Si, $Li_{12}Si_7$ and the SS. It is important to recall from the μ_{Si} vs voltage plots (see Fig. 4.6), that the crossing points refer to the thermal equilibrium chemical potentials of the two-phase equilibrium states.

To measure the deviation from the chosen reference equilibrium state, we define the over- or under-potential as the difference of Li chemical potentials between its equilibrium and applied non-equilibrium values. When this difference is positive (resp. negative), we call it over-potential (resp. under-potential). Recall from Sec. 1.3.8 that when Li is being inserted in Si electrode, we need to apply an underpotential (UP). Otherwise, when Li is being removed, we need to apply an overpotential (OP). First we define a reference equilibrium state and then we define UP or OP with respect to this reference equilibrium state. Note that, the higher the Li removal/insertion rate (i.e. current at which we (de)lithiate the Si), the higher the values of overpotential/underpotential.

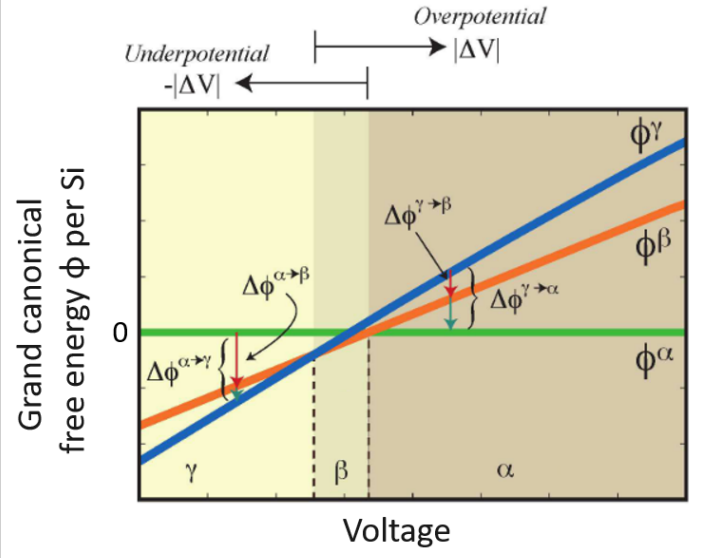

Figure 4.33: Plot of the grand canonical free energies of α, β and γ phases vs voltage. The phases thermodynamic stability are determined by the lowest grand canonical free energy, hence the areas are labeled accordingly. This image has been adapted from [92].

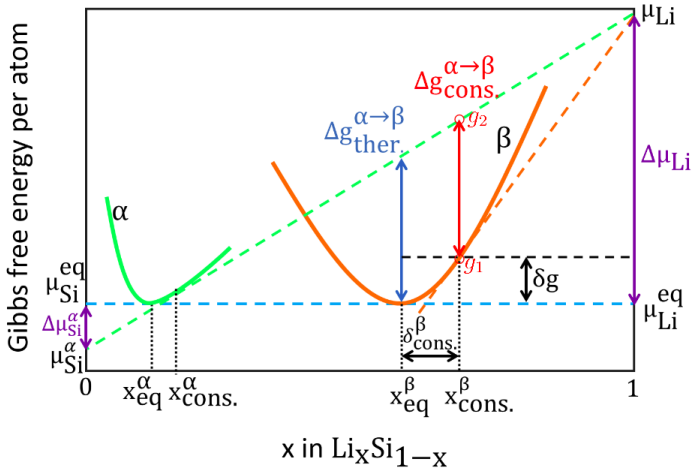

Figure 4.34: Plot of the Gibbs free energy per atom vs atomic fraction per atom. The equation of the tangents are of the form $y_t = (\mu_{\mathrm{Li}} - \mu_{\mathrm{Si}})x + \mu_{\mathrm{Si}}$ at fixed chemical potentials. $|\Delta\mu_{\mathrm{Li}}|$ gives us the absolute value of the overpotential or underpotential. $\delta^{\beta}_{\mathrm{cons.}}$ is the relative constrained nucleation atomic fraction with respect to x^{β}_{eq}. $\Delta g^{\alpha\to\beta}_{\mathrm{ther.}}$ and $\Delta g^{\alpha\to\beta}_{\mathrm{cons.}}$ stand for the thermal and constrained nucleation driving forces per atom, respectively. It is important to note that to make the schematic representation easier we have aligned the minimum of the Gibbs free energies of α and β.

As we previously mentioned, Si in these systems, in comparison to Li, do not move which means that

we do not necessarily have the same Si chemical potential in the parent and second phases. The release of this constraint can lead to a multi-phase constrained equilibrium, that does not obey the thermodynamic phase rule. Besides, the selection of phases from a parent phase can lead to other phases rather than the next thermodynamically stable one.

In Fig. 4.33, at a given OP (relative to the α-β thermal two-phase-equilibrium), we show the constrained nucleation driving force to transform an inclusion of α into β phase is defined here as $\Delta\phi^{\alpha\rightarrow\beta}(V) = \phi^{\beta}(V) - \phi^{\alpha}(V)$. As long as Li interface energy between α and β are assumed to be not too different between phases, the higher $\Delta\phi^{\alpha\rightarrow\beta}(V)$, the more likely the β phase is to form from α phase. In Fig. 4.34, we represent the Gibbs free energy vs Li atomic fraction (x) the thermal and constrained nucleation driving forces ($\Delta g^{\alpha\rightarrow\beta}_{\text{ther.}}$ and $\Delta g^{\alpha\rightarrow\beta}_{\text{cons.}}$, respectively). We define $x^{\beta}_{\text{cons.}}$ as the composition for which the nucleation of β phase happens from α phase in conditions of constrained chemical potential. It is worth remarking that the voltage constraint may drive the composition of the parent phase and new phase very far from their thermal equilibrium values, or lead to very high excess Gibbs free energies. These effects strongly depend on the composition range and Gibbs free energy curvature of both phases. We hence expect significant effects of the applied current or voltage on the precipitation driving forces and the selection of phases. We also need to consider the possibility of precipitating metastable phases.

Notice that in Fig. 4.34, g_1 and g_2 are the Gibbs free energy of β phase at $x^{\beta}_{\text{cons.}}$ and the value of the tangent line to α phase in $x^{\alpha}_{\text{cons.}}$ evaluated at $x^{\beta}_{\text{cons.}}$. They read as follow:

$$g_1 = \mu_{\text{Li}} x^{\beta}_{\text{cons.}} + (1 - x^{\beta}_{\text{cons.}})\mu^{\beta}_{\text{Si}}, \tag{4.15}$$

$$g_2 = (\mu_{\text{Li}} - \mu^{\alpha}_{\text{Si}})x^{\beta}_{\text{cons.}} + \mu^{\alpha}_{\text{Si}}, \tag{4.16}$$

where μ^{α}_{Si} and μ^{β}_{Si} are the constrained chemical potential of Si of α and β phase respectively. Therefore $\Delta g^{\alpha\rightarrow\beta}_{\text{cons.}}$ at constrained μ_{Li} is equal to $\Delta\phi^{\alpha\rightarrow\beta}(V \equiv -\mu_{\text{Li}})$ at corresponding constrained voltage since:

$$\Delta g^{\alpha\rightarrow\beta}_{\text{cons.}} = g_2 - g_1 = \mu^{\alpha}_{\text{Si}} - \mu^{\beta}_{\text{Si}} = \Delta\phi^{\alpha\rightarrow\beta}(\mu_{\text{Li}}) \tag{4.17}$$

4.5.2 Lithiation of Si

We plot, in Fig. 4.35, the grand canonical free energies of all the previously studied phases at 300 K, including the metastable $Li_{15}Si_4$ phase (which was not included in the previous thermodynamically stable phase diagram), as a function of the chemical potential of Li (i.e. equal to minus the voltage). We arbitrarily decide that a maximum of 0.1 Li point defect fractions per Si can be created; like that we are allowing the limits to be almost 3 times that of the limits observed in the single phase domain at 690 K by the experiment of Wen and Huggins [35]. Thus, for all $Li_{b+\delta}Si_a$ phases we have $-0.1a < \delta < 0.1a$. For the solid solution, on the other hand, the end-members Li_7Si_3 and Li_5Si_2 are chosen to be the limits in composition.

Notice that starting from pure Si, we can have one stable ($Li_{12}Si_7$-Si) and several constrained ($Li_{43}Si_{18}$-Si, $Li_{13}Si_4$-Si) two-phase-equilibria. To decide a realistic value of UP, during lithium insertion, we can take a look at the GITT results at room temperature at relatively fast charging rate in Fig. 4.36 [Courtesy of Magali Gauthier]. The underpotential is related to the voltage drop with respect to the OCV regime during the GITT (please refer to Sec. 1.3.8 for more information). We can see from the first 2 drops, that the underpotential can reach high values (higher than 0.5 V). Such strong underpotential allows for the precipitation of several secondary phases. Therefore, several α to β nucleation driving forces appear such that $\alpha \equiv$Si and β is any of the other phases capable of forming (meta)stable equilibrium with Si. The underpotential in this case can be given with respect to the OCV value of the two-phase-equilibrium between $Li_{12}Si_7$ and Si.

We plot the nucleation driving forces as a function of the chosen underpotential in Fig. 4.37. At low values of underpotential the biggest driving force is held by the $Li_{12}Si_7$ phase. Meaning that at a very low charging rate we would be able to observe the expected Si-$Li_{12}Si_7$ OCV plateau. At high charging rates, on the other hand, such that we have values above 0.18 V in underpotential the nucleation driving forces from Si to $Li_{43}Si_{18}$, $Li_{13}Si_4$ and $Li_{15}Si_4$ are not negligible and do not differ much from one another. Nonetheless, what differs from one another is the Li atomic fraction in every phase β and in the inclusion of phase α to be transformed in phase β. We define $x^{\beta}_{\text{cons.}}$ as the composition of phase β for which the Li chemical potentials are equal in α and β phases relative to the atomic fraction at which meta(stable) two-phase-equilibria happen x_{eq}. Please note that this fraction of Li is per atom and not per Si. In order to observe how far in composition each phase nucleates from the thermodynamic two-phase-equilibria compositions, we define $\delta^{\beta}_{\text{cons.}} = x^{\beta}_{\text{cons.}} - x^{\beta}_{eq}$ (schematically represented in Fig. 4.34 for phase β). We plot the values of $\delta^{\beta}_{\text{cons.}}$ as a function of the under potential in Fig. 4.38.

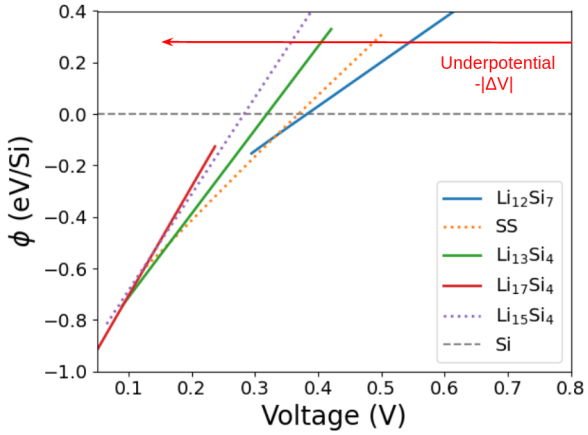

Figure 4.35: Plot of the grand canonical free energies (Eq. 4.14) vs voltage (-μ_{Li}). Here the underpotential is null at the two-phase-equilibrium between $Li_{12}Si_7$ and Si.

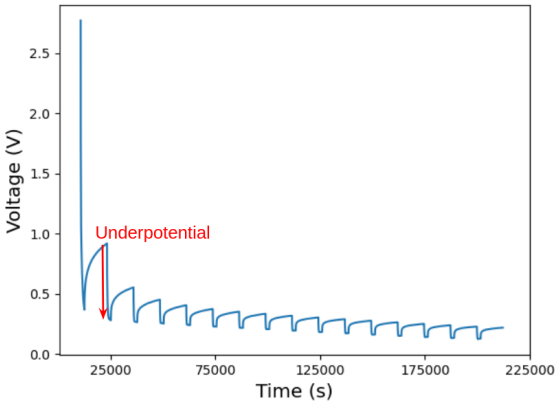

Figure 4.36: GITT plot starting from pure unlithiated Si [Courtesy of Magali Gautier]. The charging rate is C/20, the OCV regime is 3 hours followed by 30 minutes of closed circuit voltage.

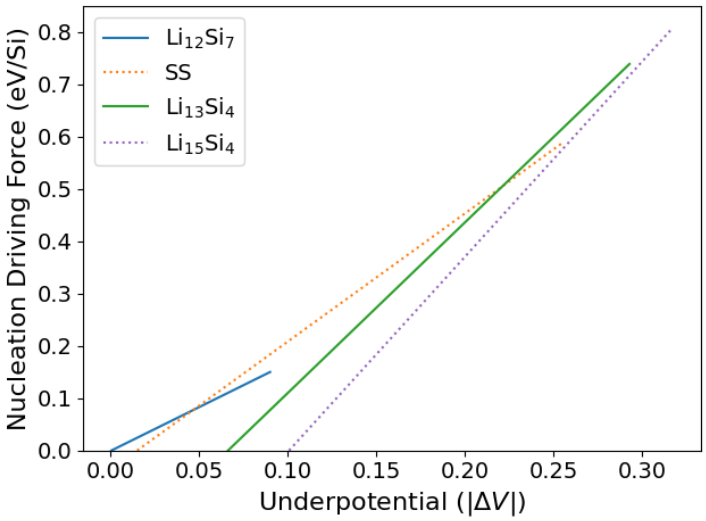

Figure 4.37: Plot of the nucleation driving forces from Si to all the other phases it can have a two-phase-equilibrium with.

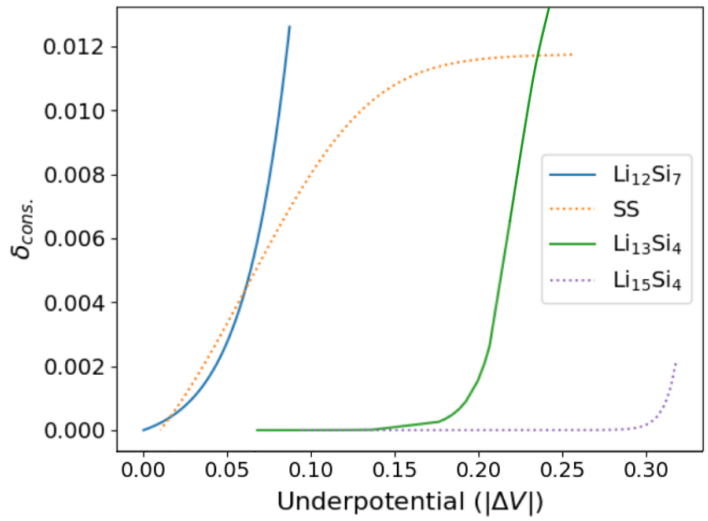

Figure 4.38: Plot of the atomic fraction where nucleation occurs relative to the atomic fraction where a two-phase-equilibrium with Si happens.

When a constrained two-phase-equilibrium is formed, it may relax towards its (meta)stable two-phase-equilibrium. To evaluate this relaxation driving force, we may compute the excess energy associated with the constrained two-phase equilibrium with respect to its (meta)stable equilibrium state. We believe as a first assumption the lower the relaxation driving force the more likely it could promote the growth of the corresponding phase on the expense of the other possible phases. It corresponds to the difference in Gibbs free energies of the α and β phases at the constrained compositions ($x^{\alpha}_{\text{cons.}}$ and $x^{\beta}_{\text{cons.}}$ Li atomic

fractions, respectively) with respect to the (meta)stable equilibrium ones (x^{α}_{eq} and x^{β}_{eq}, respectively). The difference in the Gibbs free energy of a system comprising a parent phase α nucleating phase β, $\Delta G_{cons.}$ at constrained μ_{Li} , is given by:

$$\Delta G_{cons.} = p_{\alpha}(G^{\alpha}_{cons.} - G^{\alpha}_{Eq.}) + (1 - p_{\alpha})(G^{\beta}_{cons.} - G^{\beta}_{Eq.}), \tag{4.18}$$

where p_{α} is the proportion of phase α, and $G^{\alpha}_{cons.}$ and $G^{\alpha}_{Eq.}$ are the Gibbs free energies of α phase at $x^{\alpha}_{\mathrm{cons.}}$ and x^{α}_{eq}, respectively.

Given that we are interested in comparing the relaxation driving forces, δg (see Fig. 4.34), of various second phases β in constrained equilibrium with the same parent phase α, we can very simply study the excess Gibbs free energies at a given value of the constrained Li chemical potential.

For a given nominal composition, the proportion of phases will be the result of this nominal composition and the constrained compositions of the parent and secondary phases. We hence expect that the Li-richest phase will have the smallest proportion $(1 - p_{\alpha})$. As a first step, we choose the parent phase to be Si, we assume the proportion of the secondary phase is a constant. Thereby, the comparison of the excess energies reduces to the comparison of the second phase excess energies per atom, $\delta g = G^{\beta}_{cons.} - G^{\beta}_{Eq.}$ (see Fig. 4.34). To calculate δg we can do a Taylor expansion to second order of the Gibbs free energy (per atom) of phase β, $G(x) = x\mu_{\mathrm{Li}} - (1 - x)\mu_{\mathrm{Si}}$, around x^{β}_{eq}:

$$G(x) = G(x^{\beta}_{eq}) + (x - x^{\beta}_{eq})G^{(1)}(x^{\beta}_{eq}) + \frac{1}{2}(x - x^{\beta}_{eq})^2 G^{(2)}(x^{\beta}_{eq}), \tag{4.19}$$

where $G^{(n)}(x^{\beta}_{eq})$ stands for the n$^{\mathrm{th}}$ derivative of $G(x)$ with respect to x evaluated at $x = x^{\beta}_{eq}$. Therefore, we obtain:

$$G^{(1)}(x^{\beta}_{eq}) = \mu^{eq}_{\mathrm{Li}} - \mu^{eq}_{\mathrm{Si}}, \tag{4.20}$$

and

$$G^{(2)}(x^{\beta}_{eq}) = \left.\frac{d(\mu_{\mathrm{Li}} - \mu_{\mathrm{Si}})}{dx}\right|_{x=x^{\beta}_{eq}} \approx \frac{\mu_{\mathrm{Li}} - \mu^{eq}_{\mathrm{Li}} - \mu_{\mathrm{Si}} + \mu^{eq}_{\mathrm{Si}}}{x - x^{\beta}_{eq}}. \tag{4.21}$$

We then obtain, by replacing the two previous equations in Eq. 4.19, $\delta g = G(x) - G(x^{\beta}_{eq})$ at the constrained equilibrium ($x = x^{\beta}_{\mathrm{cons.}}$) reads as:

$$\delta g = \frac{1}{2}\delta^{\beta}_{\mathrm{cons.}}(\mu_{\mathrm{Li}} + \mu^{eq}_{\mathrm{Li}} - \mu_{\mathrm{Si}} - \mu^{eq}_{\mathrm{Si}}). \tag{4.22}$$

In Fig. 4.39 we plot the δg of all phases that can possibly nucleate from Si. The $Li_{15}Si_4$ has the smallest δg for all the underpotential values above 0.13 V (i.e. high lithiation rate). Which could explain its nucleation against other crystalline phases (e.g. $Li_{13}Si_4$) despite having slightly smaller constrained precipitation driving force (Fig. 4.37). For underpotentials below 0.13 V (i.e slow lithiation rate) the δg of phases other than $Li_{15}Si_4$ are also small. We predict that for a small domain of the underpotential (between 0.06 V and 0.13 V) the $Li_{13}Si_4$ can potentially nucleate. We also predict that for underpotentials below 0.06 V, there could be a competition between the formation of the SS and $Li_{12}Si_7$ phase for which $Li_{12}Si_7$ seems to win over the SS for a larger domain.

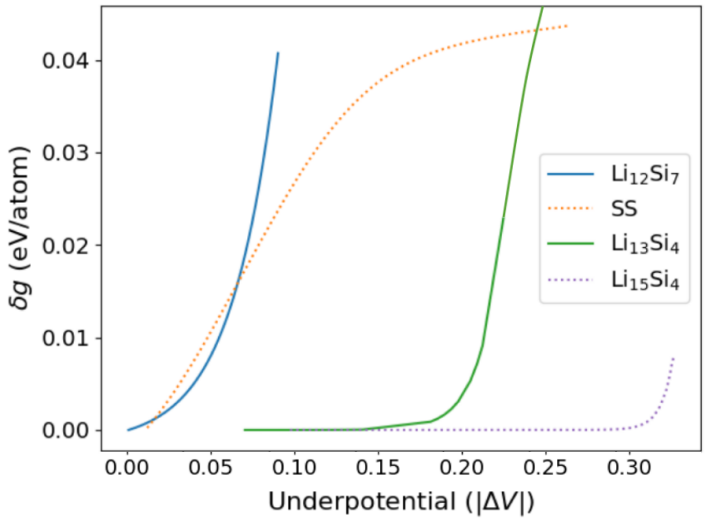

Figure 4.39: Plot of relative difference in Gibbs free energy between the thermodynamic equilibrium and the constrained equilibrium with Si as a function of the underpotential.

After fast lithiation of Si (i.e. with high underpotential values), the $Li_{15}Si_4$ may precipitate. The corresponding OCV value of the metastable two-phase-equilibrium Si-$Li_{15}Si_4$ is predicted to be equal to 0.28 V at room temperature, which happens to be very close to the measured OCV in Fig. 4.36 (at lithiation time greater than 125000 seconds). This suggests that the system after circuit opening could be relaxing towards a Si-$Li_{15}Si_4$ two-phase-metastable equilibrium.

From the nucleation driving forces vs underpotential plots we can also say that there is the possibility of a pair of constrained three-phase-equilibria. One is the $Li_{12}Si_7$-SS-Si and the other is $Li_{13}Si_4$-$Li_{15}Si_4$-Si. Notice how depending on the underpotential, the nucleation driving forces can become very close to each others. The system may then form constrained three-phase-equilibria with Si.

4.5.3 (De)Lithiation starting from intermediary Li-Si compounds

Lithiation

We can also extract information from this model given that we start from already synthesized Li-Si compounds at 300 K. In this case, the reference two-phase equilibrium is the synthesized Li-Si compound in equilibrium with the investigated second phase. our model predicts that we will only be able to precipitate into the next closest phase with respect to Li composition. Indeed, we observe in Fig. 4.35 the ϕ-V segments of every phase are too short (even by allowing 0.1 Li interstitials per Si) to cross multiple other segments and thus produce metastable two-phase-equilibria with phases beyond the next Li-richer phase. Also, even if the crossing points were to happen at very far values from perfect stoichiometry, we can see that the nucleation driving force will always favour the first next phase over any of other of the next phases for a large overpotential domain. In Fig. 4.35, for example, take $Li_{12}Si_7$ and the SS, their crossing point means that we have a thermodynamic two-phase-equilibrium; however, even if we were to extend the line of $Li_{12}Si_7$ to meet the one of $Li_{13}Si_4$ (i.e it would be a metastable two-phase-equilibrium in this case) the nucleation driving force to form the SS only increases favoring the nucleation of SS even more than that of the $Li_{13}Si_4$ phase.

Delithiation

In the case we start delithiation from a Li-Si compound the situation is different. We observe that all phases have 2 two-phase-equilibria (one of them being a metastable one). For the purpose of this study we divide the overpotential regimes (i.e potentials at which we remove Li) into three regimes OP 1, OP 2 and OP 3, starting from 3 stable two-phase-equilibria, that are shown in Fig. 4.40.

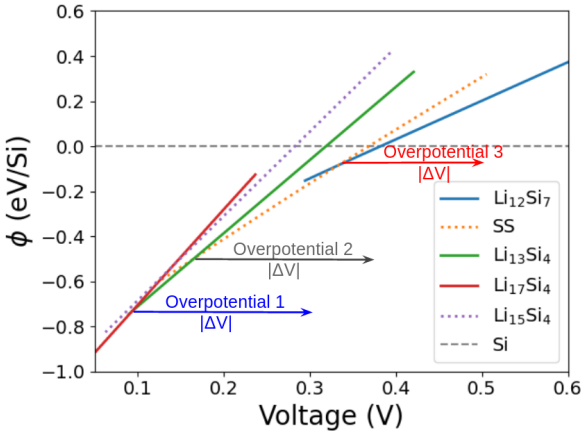

Figure 4.40: Plot of the grand canonical free energies vs voltage. OP 1 (in blue) is null at $Li_{17}Si_4$-$Li_{13}Si_4$ two-phase-equilibrium, OP 2 (in grey) is null at $Li_{13}Si_4$-SS two-phase-equilibrium, and OP 3 (in red) is null at SS-$Li_{12}Si_7$ two-phase-equilibrium

Fig. 4.40 shows how depending on the OP 1 $Li_{17}Si_4$ can choose to have a constrained two-phase-equilibrium between $Li_{15}Si_4$ and $Li_{13}Si_4$ or both (three-phase-equilibrium). The nucleation driving force seems to always favour $Li_{13}Si_4$ (Fig. 4.41). We see in the δg vs overpotential plot that μ_{Li} -constrained $Li_{15}Si_4$ is a less excited phase μ_{Li} -constrained than $Li_{13}Si_4$: its corresponding relaxation driving force δg is smaller in absolute value than the one of $Li_{13}Si_4$. This could possibly favour the stability and growth of $Li_{15}Si_4$ at the expense of $Li_{13}Si_4$ during the delithiation of $Li_{17}Si_4$.

We predict that delithiating from $Li_{13}Si_4$ can yield 2 two-phase-equilibria with the SS and pure Si (Fig. 4.40) or the three phase Si-$Li_{13}Si_4$-SS constrained equilibrium. But depending on the OP 2 value we can have nucleation driving forces that can favour Si over SS (Fig. 4.42). We see that starting at an overpotential of 0.17 V the nucleation driving force for Si is bigger than that for the SS. We can also see the δg for Si is smaller than that for SS. This suggests that the nucleation and growth of Si over SS from $Li_{13}Si_4$ may be favored.

In Fig. 4.40 we notice that SS can be in a two-phase-equilibrium with $Li_{12}Si_7$ and Si (metastable one) or three-phase-equilibrium with the latter. We can also observe that, depending on the values of OP 3, the nucleation driving force for Si is greater than that for $Li_{12}Si_7$ (Fig. 4.43). We can also see the δg for Si is smaller. This suggests that the nucleation and growth of Si over $Li_{12}Si_7$ from SS may be favored.

Our results suggest that if we ever started from the metastable $Li_{15}Si_4$, a large overpotential will promote the precipitation of Si without proceeding through the precipitation of other intermediary Si-Li crystalline compounds. Moreover, $Li_{12}Si_7$ has no alternative other than directly nucleating Si while delithiating.

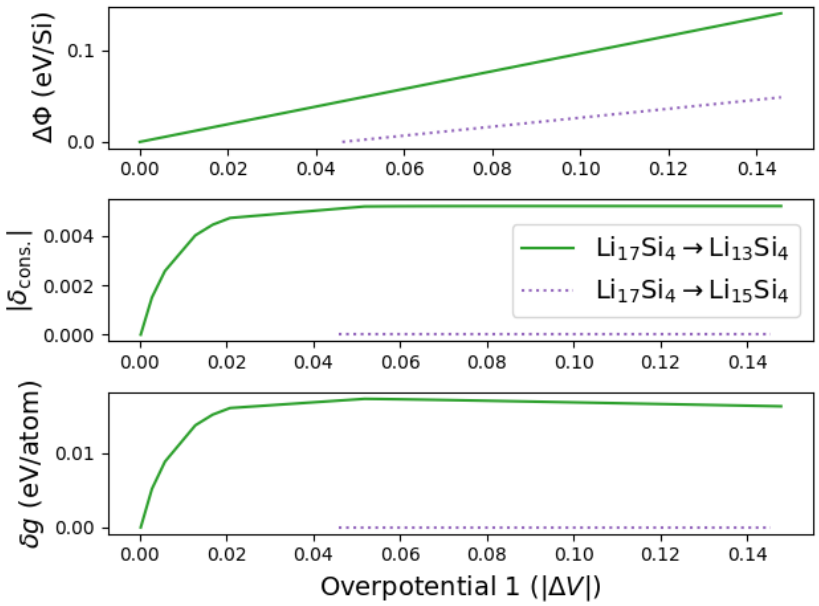

Figure 4.41: Plots of the Nucleation driving forces from $Li_{17}Si_4$ to $Li_{13}Si_4$ and $Li_{15}Si_4$, the relative constrained nucleation atomic fraction, and the relative difference in constrained Gibbs free energy with respect to equilibrium Gibbs free energy as a function of overpotential 1.

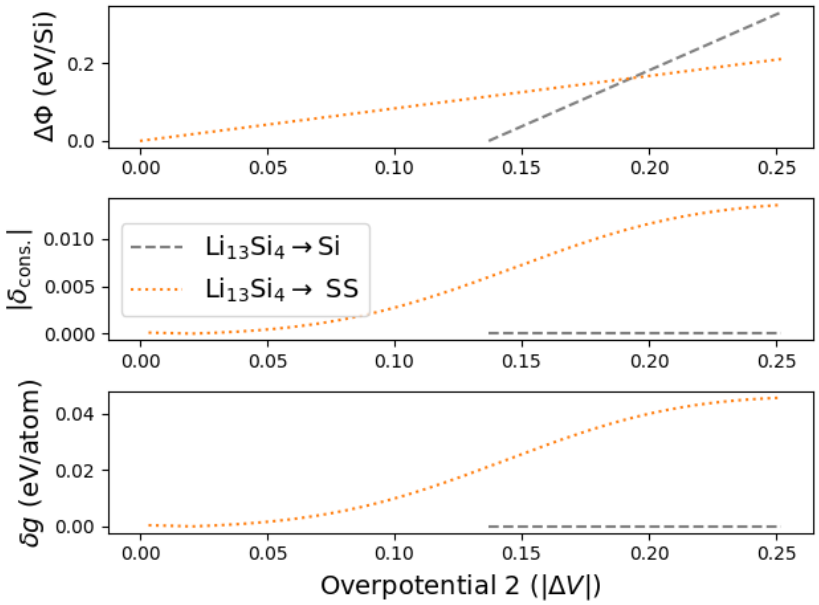

Figure 4.42: Plots of the Nucleation driving forces from $Li_{13}Si_4$ to SS and Si, the relative constrained nucleation atomic fraction, and the relative difference in constrained Gibbs free energy with respect to equilibrium Gibbs free energy as a function of overpotential 2.

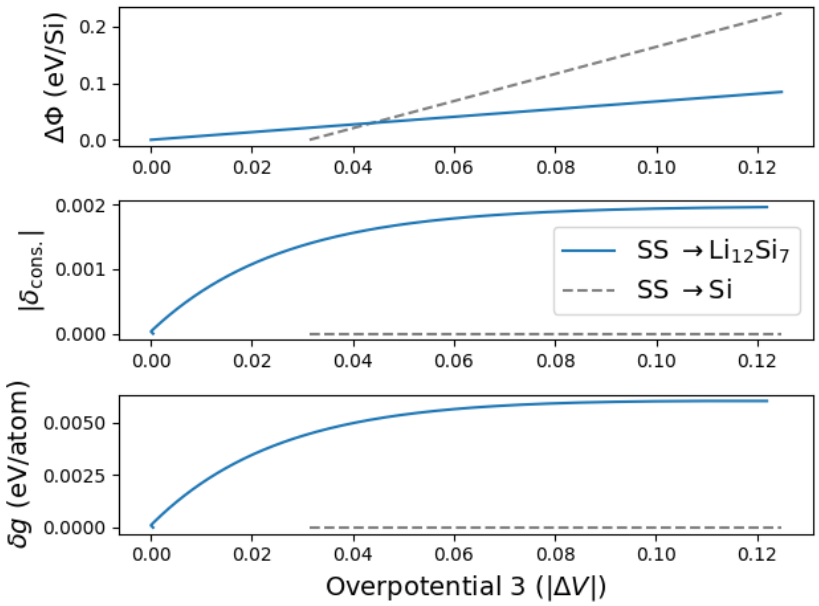

Figure 4.43: Plots of the Nucleation driving forces from SS to $Li_{12}Si_7$ and Si, the relative constrained nucleation atomic fraction, and the relative difference in constrained Gibbs free energy with respect to equilibrium Gibbs free energy as a function of overpotential 3.

Comparison with experiment

The thesis of Magali Gauthier [124] has some results of delithiation starting from several crystalline compounds (Fig. 4.44). We can see that depending on the initial parent phase, we can observe an OCV plateau during the first delithiation. For Li_7Si_3, we see a small plateau at 0.56 V, for "$Li_{15}Si_4$" a larger plateau at 0.48 V and for "$Li_{22}Si_5$" we have an even larger plateau at 0.4 V. For the second delithiation all the first 3 Li-Si compounds reach a plateau around 0.45 V. In order to compare with our results we assume that "Li_7Si_3" is our studied SS, "$Li_{15}Si_4$" is our studied $Li_{13}Si_4$, and "$Li_{22}Si_5$" is actually $Li_{17}Si_4$.

The values of such plateaus are higher than any of the thermodynamic equilibrium ones extrapolated from high-temperature experiments [34, 35] or even the ones computed here. The comparison with our previous analysis could suggest that Si is directly precipitating whatever the composition of the parent phase due to a high overpotential. Moreover, as previously mentioned, there could be a three-phase-equilibrium with Si-Li oxide at the interface playing a role for such high voltage.

Our previous results suggest that Si nucleation will be always favored (under delithiation, i.e. under an applied voltage). The results we present here are in line with other systems such as Li-Sb compounds [92]. For instance, when undergoing delithiation, Li_3Sb skips the Li_2Sb (observed during lithiation) to directly nucleate into Sb.

In Fig. 4.44 with $Li_{12}Si_7$, "Li_7Si_3" and "$Li_{15}Si_4$" we observe during the second delithiation that a plateau fixed at 0.45 V is reached. This is also what happens when "$Li_{15}Si_4$" undergoes its first delithiation. We may say that if the starting composition is at "$Li_{15}Si_4$" or before it we will always reach this 0.45 V plateau during delithiation. But if the starting composition is after "$Li_{15}Si_4$" (e.g. $Li_{17}Si_4$ or "$Li_{22}Si_5$") we do not obtain this plateau during delithiation. According to our results, $Li_{17}Si_4$ cannot form a two-phase-equilibrium with Si; by analogy, we may say that forming a plateau at 0.45 V is a signature of direct Si nucleation during delithiation whenever delithiation starts from $Li_{15}Si_4$.

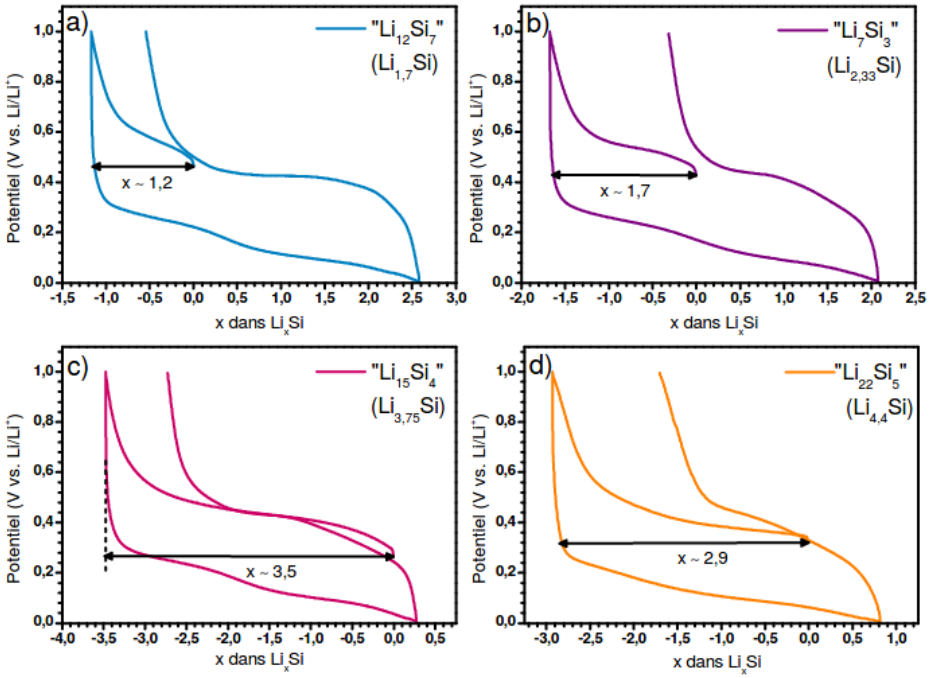

Figure 4.44: Evolution of the Voltage as a function of x in Li_xSi. x is normalized in a way that when the voltage is 0 V, x is 3.75. The samples a)$Li_{12}Si_7$, b)"Li_7Si_3", c)"$Li_{15}Si_4$" and d)"$Li_{22}Si_5$" start from delithiation until reaching 1 V, then they undergo lithiation until 0 V and then undergo delithiation again until 1 V. Figure is taken from the thesis of Magali Gauthier [124].

4.5.4 Confined-volume constrained nucleation

In reality, there is also a confined volume constraint that can play a role in the selection of phases. For instance, the precipitation of a Li-rich oversized phase could be partially accommodated with the transformation of Si atoms into self interstitial atoms (SIA). Indeed, although the volume of formation of SIA is positive, it is generally smaller than an atomic volume per silicon, thereby the transformation of an atom sitting on its lattice site into a self-interstitial, decreases the volume of the precipitating phase. This mechanism may happen only if the formation free energy of SIA is not too high. We plot the formation energies of the most stable point defects of all phases at 300 K and perfect stoichiometry in Fig. 4.45. Notice how the lowest E_f of Si interstitials goes for $Li_{15}Si_4$ phase and then increases tremendously for $Li_{17}Si_4$. Therefore, in $Li_{17}Si_4$ there is no easy accommodation mechanism of a compressive stress; whereas in $Li_{15}Si_4$ this mechanism may be favored.

Note that a Si-rich phase may also transform into an undersized amorphous phase as shown in Fig. 2.38. This is a concurrent accommodation mechanism as long as there is a possibility of forming amorphous phases denser than the corresponding crystalline secondary phase. We hence expect amorphization transitions at low content of Li.

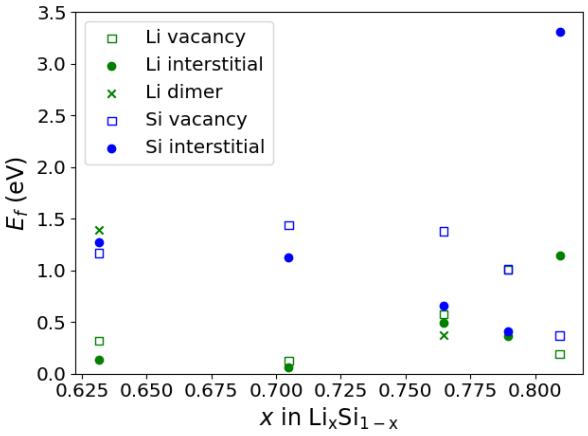

Figure 4.45: Plot of the formation energies of point defects with respect to Li nominal composition of $Li_{12}Si_7$, $Li_{43}Si_{18}$, $Li_{13}Si_4$, $Li_{15}Si_4$, $Li_{17}Si_4$ using LTE at perfect stoichiometry ($\delta = 0$) and at 300 K. Note that for the formation energy of Si vacancies and interstitials in $Li_{43}Si_{18}$ we have used the values of Li_7Si_3 (we assume that it does not change much for $Li_{43}Si_{18}$).

4.6 Conclusion

In this chapter we have investigated the alloying process of Li-Si systems from a thermodynamic and constrained voltage thermodynamic point of view. Below we list the things that we find important to keep in mind.

We calculated the solubility limir using our model of the dilute solid solution Si(Li) in equilibrium with $Li_{12}Si_7$ and showed that the solubility limit is also very low at room temperature. We inferred from these very low values of the solubility limit that the chemical potential of Si is not affected by the Li insertion in Si(Li).

We attempted to construct the phase diagram by using first the LTE modeling of the off-stoichiometric ordered compounds including the equilibrium concentration of their lattice point defects. We realized that LTE dilute approximations could not provide a consistent sequence of the Li_7Si_3-$Li_{43}Si_{18}$-Li_5Si_2 phase equilibria. This lead to the development of a mean field model of the concentrated solid solution Li_7Si_3. From this model we were able to extract an order-disorder transition temperature of $Li_{43}Si_{18}$ and $Li_{44}Si_{18}$ and found out that at temperatures below 70 K the stable ordered phase is in fact the $Li_{43}Si_{18}$ and above 70 K it is the Li_7Si_3 solid solution.

From the Gibbs free energy of the concentrated solid solution and off-stoichiometry ordered phases, we constructed the first reported phase diagram including off-stoichiometry. Our phase diagram contains information about the ordering-disordering transition around the Li_7Si_3 composition. It excludes the LiSi phase since our hybrid DFT calculations in Chapter 2 predicted this phase to not be stable at 0 K. The presented phase diagram reports the $Li_{17}Si_4$ as the highly lithiated phase. It also includes the $Li_{12}Si_7$ and the $Li_{13}Si_4$ phases which have been previously reported in all phase diagrams with no disagreement.

We were then able to predict the OCV including off-stoichiometry. The calculated composition intervals and values of the OCV plateaus are in good agreement with with reported experimental values at 690 K [35]. We found that in order to match the experimentally reported 210 K peak of Li_7Si_3 [43, 54] (a signature of a first order phase transition) we need to slightly overestimate the Li nominal composition (by almost 0.9% percent with respect to the one reported experimentally). In line with reported NMR experiments[54], we suggest that the first order phase transition is from a two-phase-equilibrium between

Li_7Si_3 and $Li_{12}Si_7$ to the single phase Li_7Si_3.

We studied the constrained nucleation driving forces. We inferred that in order to model the selection of precipitating phases under an applied uniform Li chemical potential, it is useful to introduce the concept of constrained nucleation driving force ($\Delta\Phi$) and the relaxation driving force (δg) of the constrained equilibrium towards its equilibrium state. We showed that the nucleation and growth of $Li_{15}Si_4$ could be favored, despite having slightly lower nucleation driving force $\Delta\Phi$ than its counterparts (e.g. SS or $Li_{13}Si_4$). We believe as a first assumption that its low relaxation driving force δg for most of the underpotential values could promote its growth at the expense of the other nucleated phases. Our results suggested that if $Li_{15}Si_4$ is formed, it may either decompose into stable phases or establish a metastable equilibrium with Si. Similarly, the direct nucleation of Si could be possible if we delithiate directly from a Li-Si compound. We concluded that the experimentally observed 0.45 V plateau during delithiation at room temperature, might be a signature of direct Si nucleation from Li-Si intermediary phases.

General conclusion

The main objective of this study was to investigate the thermodynamic properties of the Si-Li system including finite temperature and deviation-from-perfect-stoichiometry effects. In the Si-Li compounds, the Gibbs free energies of lattice point defect formation determine the deviations from perfect stoichiometry.

From this study, we were able to deduce specific heat capacities, the Si-Li phase diagram, the equilibrium concentration of lattice point defects, the variation of the open circuit voltage in function of composition, and eventually voltage-constrained precipitation driving forces. Below, we provide our conclusions by chapter that we believe are worth keeping in mind. Finally, we propose some perspectives for further research based on our work.

Results overview

In this study, using 0 K DFT calculations, we identified two previously unknown stable phases: the $Li_{43}Si_{18}$ and the $Li_{44}Si_{18}$ phases that have the same group symmetry. These phases are particularly difficult to distinguish from previously known Li_7Si_3 and Li_5Si_2 phases as they all share the same Si sublattice and only differ by Li vacancy ordering. These discovered phases gave us an insight of what could possibly be happening around the Li_7Si_3 composition, and the reason why there is no consensus in the literature between experiment and DFT concerning the stability of phases. The discovery of these phases with large unit cells, is the living proof that DFT-based phase discovery methods can be inefficient (because of their computational cost) at identifying stable phases with large unit cells (which could be the case in Li-Si systems). We also showed the LiSi phase is not stable at 0 K using the HSE06 functional. Thereby, we expect this phase is not a thermodynamically stable phase, at least at low temperature.

We saw the effect of including thermal volume expansion in our calculation of thermodynamic properties for Li-Si compounds (with the quasi-harmonic approximation). From the comparisons of thermodynamic properties using the quasi-harmonic and harmonic approximations (QHA and HA, respectively), we conclude that we should not ignore anharmonic contributions to the thermal volume expansion above 350 K, with an exception to pure Si. For instance, the formation free energies at finite temperatures using the quasi-harmonic or harmonic approximations shows how the stability or relative stability of phases can change according to the method used. Using the QHA we saw that the Li_7Si_3 and $Li_{43}Si_{18}$ stabilities depend on temperature, whereas using the HA we saw that the $Li_{43}Si_{18}$ is stable at all temperatures. We showed that the Li composition mainly determines the volume expansion of phases. Indeed, the calculated equilibrium volumes of the ordered phases happen to be very close to the experimentally measured volume of the amorphous phases at room temperature (within 10% percent). In addition, we show that the volume of the amorphous phase up to $x = 2$ in Li_xSi is smaller than the one of crystalline phase at the same Li composition.

We showed that LTE is an efficient tool to extract from the DFT formation energies, the chemical potential of Li and Si as a function of composition around each phase and provide variation laws of OCV in function of lattice point defect formation free energies. These analytical laws allowed us to compare our

predicted results with those of the experiment at 690 K [35]. Among the things that we could compare are the OCV, the effective formation free energies of point defects, and the thermodynamic enhancement factor. Eventually, we have introduced a simple procedure to use the LTE to extract effective formation free energies of point defects from the variation of OCV with composition in the single phase domains.

We showed that the maximum of the thermodynamic enhancement factor is proportional to the Frenkel pair formation free energy when the dominant point defects are single interstitials and single vacancies of the same species. We also proved that the maximum is not necessarily always at perfect stoichiometry ($\delta = 0$ in $Li_{a+\delta}Si_b$) in contradiction to Wen and Huggins [35]. Only when single vacancies and single interstitials of the same species are the most dominant point defects, the maximum of thermodynamic enhancement factor is virtually at $\delta = 0$. However, in the case we have Schottky defects as dominant stoichiometry point defect, the maximum of the thermodynamic enhancement factor is not necessarily at $\delta = 0$. The study of defect stability as a function of phase composition has enabled us to identify that the relative stability of Si point defects increases with Li composition in particular. Si interstitials exhibit the lowest formation energy near the compositions of $Li_{15}Si_4$ and $Li_{13}Si_4$, while they have significantly higher formation energy in all other compositions. Similarly, the creation of Si vacancies is promoted in the highly lithiated phase $Li_{17}Si_4$ only.

By comparing the calculated variation of OCV with composition in the single phase domains of the ordered non-stoichiometric compounds with the measured ones at 690 K, we were able to confirm the predicted relative stability of phases. The OCV modeling of the non-stoichiometric ordered compounds $Li_{17}Si_4$, $Li_{21}Si_5$, and $Li_{22}Si_5$ and their comparison with experiment showed that the stable phase is in fact the $Li_{17}Si_4$. The good agreement between the calculated OCVs of $Li_{12}Si_7$ and $Li_{13}Si_4$ with their experimental counterparts at 690 K, suggests that these compounds are indeed the stable phases.

Even though we demonstrated in Chapter 3 that the $Li_{43}Si_{18}$ had the least discrepancy vs Li_7Si_3 and Li_5Si_2 in comparison with the experimental "Li_7Si_3" phase. By relying on a mean field model of the concentrated Li-vacancy solid solution Li_7Si_3, we showed in Chapter 4 that the order-transition temperature between the $Li_{43}Si_{18}$ and $Li_{44}Si_{18}$ phases and the partially disordered Li_7Si_3 phase is significantly below room temperature (around 70 K). However, the mean field model of the concentrated solid solution 'Li_7Si_3 could be improved to take proper account of the energy cost of forming a Frenkel pair in the perfectly stoichiometric Li_7Si_3.

From the obtained off-stoichiometry Gibbs free energies, we were then able to construct the phase diagram, From this phase diagram, we have deduced the single phase composition domains of the ordered phases. At 690 K, these composition domains turned out to be in good agreement with the experimental ones [35]. We showed the first-order transition peak of the heat capacity observed in experiments [54, 43] around the nominal composition of Li_7Si_3 at 210 K, could be related to the increasing deviation from perfect stoichiometry of Li_7Si_3 with temperature. By relying on the heat capacity peak and NMR characterizations emphasizing the abrupt change of Si short range order at 210 K from the ones of $Li_{12}Si_7$ and Li_7Si_3 to the single one of Li_7Si_3[54], we suggest the initial nominal composition of the experimental sample is not exactly $x = 0.7$ but $x = 0.706$ in Li_xSi_{1-x}(which is still within the experimental confidence interval of composition) and the first order phase transition would be from a $Li_{12}Si_7$-"Li_7Si_3" two-phase-equilibrium to a "Li_7Si_3" single phase domain above 210 K. These findings underline the importance of incorporating non-stoichiometric lattice point defect contributions to the phase diagrams, as the previous line compound phase diagrams fail to reproduce these results.

For a first investigation of the selection of phases upon (de)lithiation of the Si electrode, we have computed metastable two-phase equilibria, in particular the ones involving the metastable phase $Li_{15}Si_4$ (e.g. Si-$Li_{15}Si_4$). We observed that at room temperature $Li_{15}Si_4$ could be in metastable equilibrium with Si only, which could partially explain the observed selection of phases upon delithiation and the hysterisis. Eventually, we computed kinetically-constrained precipitation driving forces in order to analyze the selection of phases upon (de)lithiation. For a preliminary model of the Si anode under cycling, we assume that silicon atoms are immobile while lithium atoms are sufficiently fast to diffuse and exchange

between different phases, ensuring a uniform lithium chemical potential. However, the value of the chemical potential may not be at equilibrium because Si diffusion may be too slow to ensure equal Si chemical potentials between phases. Therefore, we have analyzed the precipitation driving forces under the external force of a non-equilibrium and uniform chemical potential of Li (which is formally equivalent to apply a uniform over- or under-voltage). We emphasized different alloying scenarios.

We believe we could explain why the precipitation of the metastable phase $Li_{15}Si_4$ is promoted under applied voltage despite not being thermodynamically stable (e.g. vs $Li_{13}Si_4$). The nucleation of secondary phases does not depend on the final state. However, in driven systems such as a Si-anode under cycling, there are multiple possible two-phase constrained equilibria yielding the same Li-chemical potential. We believe that the one that may potentially grow at the expense of the other nucleated phases is the one with the lowest excess energy with respect to the corresponding (meta)stable two-phase equilibrium. Therefore, we inferred that under applied voltage the nucleation and growth of phases results from both the constrained nucleation driving forces and the relative difference in Gibbs free energies with respect to the closest thermodynamic (meta)stable equilibrium. Based on this two-fold energy approach, we predicted that the direct nucleation of Si during the delithiation of a crystalline Li-Si compound may be favoured.

Perspectives

Looking ahead, several promising avenues for future research and exploration emerge from the findings and insights of this study:

- The calculation of the vibrational contribution to the Gibbs free energy of the $Li_{44}Si_{18}$ phase. This calculation would provide a comprehensive understanding of the finite temperature convex hull of the line compounds, offering a complete picture. Additionally, it would facilitate a more detailed investigation of the Li_7Si_3 concentrated Li-vacancy solid solution by incorporating an additional energy parameter to better fit the interaction energy model. Note that due to the lack of symmetries in the $Li_{44}Si_{18}$ phase, applying the quasi-harmonic approximation would be computationally demanding, estimated to require approximately 1.5 million CPU hours. Nevertheless, exploring alternative computational techniques or optimization strategies could potentially overcome this computational challenge and allow for a more accurate finite temperature characterization of the $Li_{44}Si_{18}$ phase.

- The computation of vibrational contribution of pure Si, pure Li, LiSi, and $Li_{12}Si_7$ utilizing the HSE06 functional. These calculations would enable the construction of a finite temperature convex hull between Si and $Li_{12}Si_7$, providing the (meta)stability insight of LiSi at various temperatures using the HSE06 functional. However, it is important to note that the utilization of the HSE06 functional would significantly increase computational costs, particularly for the $Li_{12}Si_7$ phase, where quasi-harmonic approximation PBE calculations are already computationally expensive.

- Computing the vibrational contributions to the formation energies of the lattice point defects at finite temperatures. These contributions could explain the observed slight discrepancies between the calculated and measured OCV at 690 K. Nonetheless, it is important to note that accounting for lattice vibrations is a computational challenge. Point defects reduce the symmetry of the crystal lattice, making the quasi-harmonic approximation computationally expensive and less applicable.

- Calculation of free energies of the interfaces between Li-Si phases. These quantities would allow us to compute the critical radius and nucleation barrier which then could potentially improve our understanding of the nucleation of phases as the crystalline $Li_{15}Si_4$ over the other crystalline phases at 300 K.

- Calculating the effect of stress on the nucleation driving forces of Li-Si phases. For instance, stress can hinder nucleation by increasing the nucleation energy barriers, promote directional nucleation, or change the selection of phases.
- Accounting for the effect of an imposed gradient of Li chemical potential on the nucleation driving force to better reproduce the non-equilibrium conditions of (de)lithiation under applied-current. It was shown that above a threshold value of the gradient of solute concentration or chemical potential, the nucleation driving force of the secondary phase could be reduced or even canceled out [128].
- Calculating the migration barriers of point defects in order to compute the diffusion coefficients (since we already have the Gibbs free energy of point defect formation). This can, for example, be done using the in-house code KineCluE [129] which should be efficient for the modeling of diffusion properties of the ordered compounds not too far from perfect stoichiometry.
- Modeling the Li-induced amorphization and study the volume, energy and kinetic properties of the produced amorphous phases. We could then explore the possibility of introducing pseudo-free energies of the amorphous phases and add these phases to kinetically-constrained phase diagrams. This would allow us to have a better understanding of the amorphization process that happens at low temperatures before the nucleation of crystalline $Li_{15}Si_4$ phase upon lithiation and after $Li_{15}Si_4$ phase upon delithiation.

Ahead we mention some perspectives from experimental point of view:

- Doing neutron scattering experiments for the investigation of Li-Si compounds. In certain Li-Si phases, the use of XRD has resulted in a lack of consensus and agreement among researchers [53, 42, 43], primarily attributed to the inherent inaccuracies associated with XRD in detecting Li ordering. Neutrons, on the other hand, interact strongly with lithium atoms, their scattering patterns would provide valuable insights into their arrangement and distribution of Li within the crystal lattice.
- Performing (de)lithiation with the GITT at room temperature with very slow charging rate starting from each known crystalline phase can provide valuable insight as we already showed in Chapter 4 with the on-going work of our collaborator Magali Gauthier. We would be able to study off-stoichiometry properties of these phases while ensuring they stay crystalline which would ensure a proper comparison with our modeling.

Appendix A

Effect of negative frequencies in Li thermodynamic properties

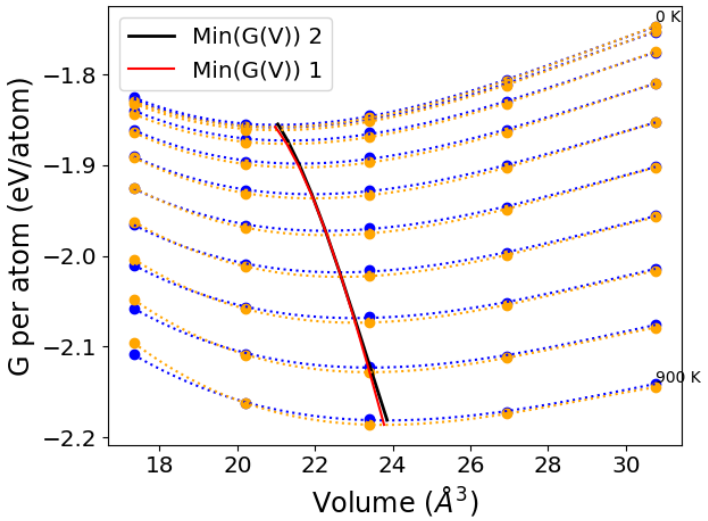

Figure A.1: Plot of the Li Gibbs free energy vs volume at steps of 100 K (from 0 to 900 K). The yellow and the blue dotted lines represent the Birch-Murnaghan equation of state of both first and second set of input parameters respectively. The red and black lines represents the minimum of G with respect to volume at each temperature using the first and second set of input parameters respectively.

For the particular case of Li, we can confirm that the negative frequencies are, indeed, artifacts. Given the low DOS that the negative frequencies have and that they are artifacts, we might as well ignore them in our calculations of thermal properties to see their effect. The results that we show ahead this section imply that we can safely take the first set of accuracy parameters and ignore the negative frequencies if we are concerned with predicting thermal properties.

We plot both Gibbs free energies using the less and more accurate set of input parameters -we ignore the negative frequencies in our calculations from the less accurate set of input parameters. The plot of relative error with respect to T (Fig. A.3) shows a good agreement in the Gibbs free energies despite

ignoring the negative frequencies. We can compare our Gibbs free energies with that of CALPHAD's [42] (in Fig. A.2).

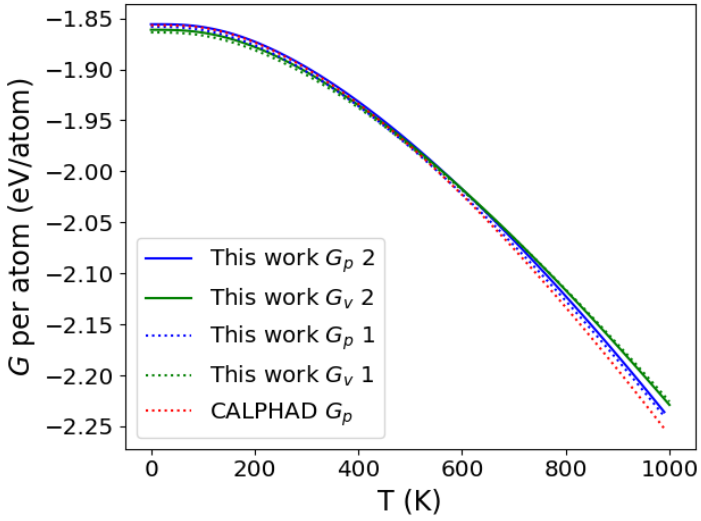

Figure A.2: Plot of the Li G_p and G_v vs temperature. Comparison with CALPHAD [42]. The 1 and 2 stand for the first and second set of accuracy parameters respectively. The fit of G_p (2) with respect to T can be found in the appendix (Sec. A).

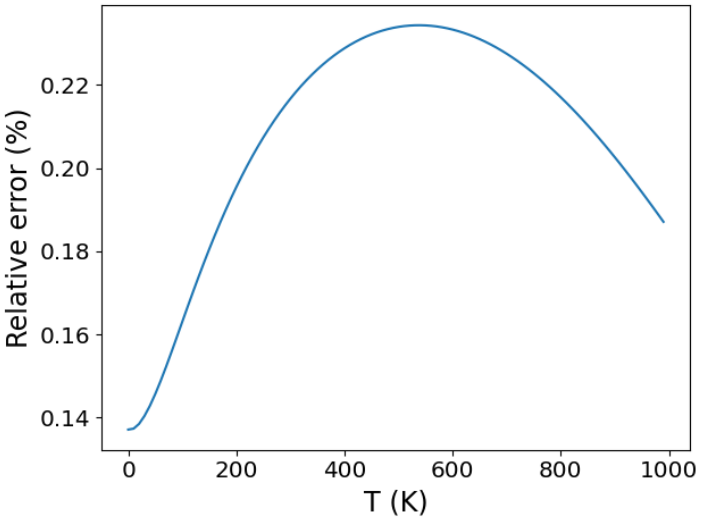

Figure A.3: Plot of the relative error of the Li Gibbs free energy using the first set of accuracy parameter vs that of the second one as a function of temperature.

A plot of the isochoric and isobaric vibrational entropy contributions from our HA and QHA phonon calculations respectively can be observed in Fig. A.4. We can observe that our more accurate S_p is

almost identical to its less accurate counter part. We can also observe that both our less (1) and more accurate (2) S_v are relatively more different.

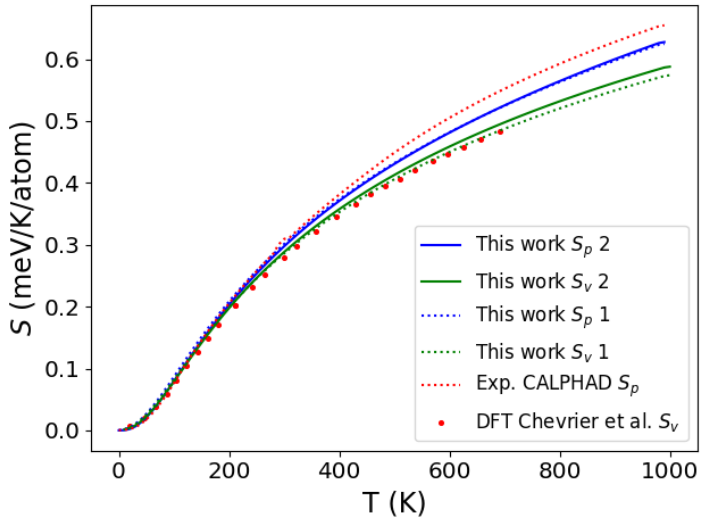

Figure A.4: Plot of the Li entropy vs temperature of Li. The 1 and 2 stand for the first and second set of accuracy parameters respectively. Comparison with CALPHAD [42], and DFT HA by Chevrier et al [41].

The heat capacity shows the most difference between Li (1) and Li (2) (Fig. A.5), we observe more the difference that is otherwise not shown with the Gibbs free energy. However, the differences is still reassuring because for both C_v and C_p it is of the order of 0.01 meV/K/atom at $T > 0$.

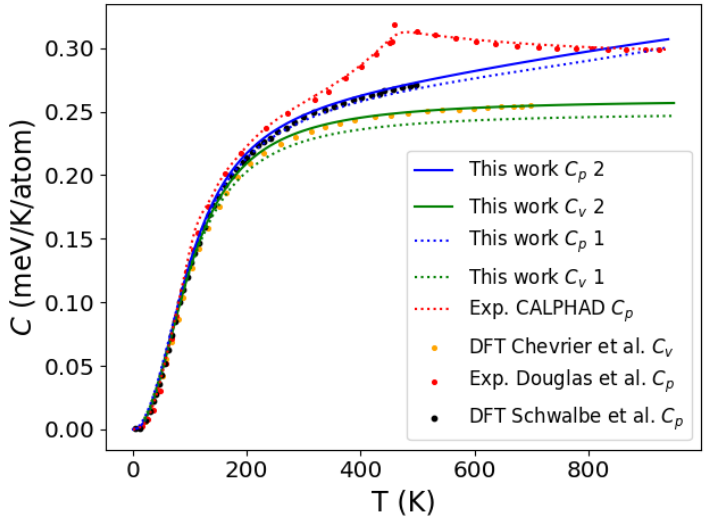

Figure A.5: Plot of the Li heat capacity vs temperature. Comparison with CALPHAD [42], DFT HA by Chevrier et al. [41], experiment by Douglas et al. [105], and DFT QHA by Schwalbe et al. [56].

Having imaginary frequencies should be of no problem for the calculation of thermodynamic properties as long as we can prove the mechanical stability of a phase with either more accurate results or from the literature. For instance the work of Gruber et al. [109] is proof that sometimes it is worth it to accept the results with negative frequencies to reduce computational time.

Appendix B

Gibbs free energy T dependent fits of ordered compounds from our studies

The inspired-by-CALPHAD G fits (in eV/atom) as a function of T (in K) from this work are listed below for each ordered compound:

$$G_{\mathrm{Li}} =$$
$$-1.85577 + 2.88679 \cdot 10^{-7}T - 1.53036 \cdot 10^{-8}T^2 - 4.80481 \cdot 10^{-11}T^4 \quad (0 \leq T < 50)$$
$$-1.8522 - 4.2227 \cdot 10^{-4}T + 1.0896 \cdot 10^{-4}T\ln(T) - 1.4993 \cdot 10^{-6}T^2 + 7.9639 \cdot 10^{-10}T^3 - \frac{2.3730 \cdot 10^{-2}}{T} \quad (50 \leq T < 120)$$
$$-1.8869 + 1.2640 \cdot 10^{-3}T - 2.2573 \cdot 10^{-4}T\ln(T) - 7.6345 \cdot 10^{-8}T^2 + 2.0612 \cdot 10^{-11}T^3 + \frac{6.7815 \cdot 10^{-1}}{T} \quad (120 \leq T < 1000)$$

$$G_{\mathrm{Si}} =$$
$$-5.30251 - 2.94321 \cdot 10^{-3}T + 5.93404 \cdot 10^{-4}T^2 - 3.19993 \cdot 10^{-6}T^4 + 3.12276 \cdot 10^{-9}T^4 \quad (0 \leq T < 50)$$
$$-5.4489 + 2.5133 \cdot 10^{-3}T - 4.3652 \cdot 10^{-4}T\ln(T) + 5.5495 \cdot 10^{-7}T^2 - 4.056 \cdot 10^{-10}T^3 + \frac{2.9321 \cdot 10^{-1}}{T} \quad (50 \leq T < 120)$$
$$-5.4169 + 1.4363 \cdot 10^{-3}T - 2.3990 \cdot 10^{-4}T\ln(T) - 2.2896 \cdot 10^{-8}T^2 + 6.8434 \cdot 10^{-12}T^3 + \frac{1.97183}{T} \quad (120 \leq T < 1000)$$

$$G_{\mathrm{Li_{12}Si_7}} =$$
$$-3.39824 - 2.32032 \cdot 10^{-8}T + 2.75195 \cdot 10^{-10}T^2 - 2.23302 \cdot 10^{-11}T^4 \quad (0 \leq T < 50)$$
$$-3.39959 + 1.23886 \cdot 10^{-4}T - 3.03255 \cdot 10^{-5}T \cdot \ln(T) + 4.92093 \cdot 10^{-7}T^2 - 4.56489 \cdot 10^{-9}T^3 + \frac{0.01187}{T} \quad (50 \leq T < 120)$$
$$-3.42938 + 1.08019 \cdot 10^{-3}T - 1.84041 \cdot 10^{-4}T \cdot \ln(T) - 1.45987 \cdot 10^{-7}T^2 + 5.75614 \cdot 10^{-11}T^3 + \frac{0.77952}{T} \quad (120 \leq T < 1000)$$

$$G_{\mathrm{Li_9Si_4}} =$$
$$-3.19777 - 1.06441 \cdot 10^{-7}T + 1.03057 \cdot 10^{-8}T^2 - 2.40938 \cdot 10^{-11}T^4 \quad (0 \leq T < 50)$$
$$-3.20077 + 2.83326 \cdot 10^{-4}T - 6.84865 \cdot 10^{-5}T \cdot \ln(T) + 9.00234 \cdot 10^{-7}T^2 - 5.70742 \cdot 10^{-9}T^3 + \frac{0.0248917}{T} \quad (50 \leq T < 120)$$
$$-3.22791 + 1.04277 \cdot 10^{-3}T - 1.77181 \cdot 10^{-4}T \cdot \ln(T) - 1.70075 \cdot 10^{-7}T^2 + 6.79896 \cdot 10^{-11}T^3 + \frac{0.757949}{T} \quad (120 \leq T < 1000)$$

$$G_{\mathrm{Li_7Si_3}} =$$

$$-3.17618 - 1.1019 \cdot 10^{-7}T + 1.02034 \cdot 10^{-8}T^2 - 2.19974 \cdot 10^{-11}T^4 \quad (0 \leq T < 50)$$

$$-3.17597 - 5.08521 \cdot 10^{-5}T + 1.4504 \cdot 10^{-5}T \cdot \ln(T) - 1.48782 \cdot 10^{-7}T^2 - 2.31181 \cdot 10^{-9}T^3 + \frac{0.000714513}{T} \quad (50 \leq T < 120)$$

$$-3.20730 + 1.06591 \cdot 10^{-3}T - 1.80866 \cdot 10^{-4}T \cdot \ln(T) - 1.55543 \cdot 10^{-7}T^2 + 5.37184 \cdot 10^{-11}T^3 + \frac{0.790117}{T} \quad (120 \leq T < 1000)$$

$$G_{\mathrm{Li_{43}Si_{18}}} =$$

$$-3.16054 - 9.51735 \cdot 10^{-8}T + 8.53505 \cdot 10^{-9}T^2 - 2.22074 \cdot 10^{-11}T^4 \quad (0 \leq T < 50)$$

$$-3.16326 + 2.62507 \cdot 10^{-4}T - 6.41490 \cdot 10^{-5}T \cdot \ln(T) + 8.83929 \cdot 10^{-7}T^2 - 5.58795 \cdot 10^{-9}T^3 + \frac{0.0221272}{T} \quad (50 \leq T < 120)$$

$$-3.19108 + 1.03639 \cdot 10^{-3}T - 1.75081 \cdot 10^{-4}T \cdot \ln(T) - 1.75163 \cdot 10^{-7}T^2 + 6.97947 \cdot 10^{-11}T^3 + \frac{0.778852}{T} \quad (120 \leq T < 1000)$$

$$G_{\mathrm{Li_5Si_2}} =$$

$$-3.12977 - 9.29205 \cdot 10^{-8}T + 8.54939 \cdot 10^{-9}T^2 - 2.09754 \cdot 10^{-11}T^4 \quad (0 \leq T < 50)$$

$$-3.13127 + 1.35594 \cdot 10^{-4}T - 3.26670 \cdot 10^{-5}T \cdot \ln(T) + 4.87621 \cdot 10^{-7}T^2 - 4.27688 \cdot 10^{-9}T^3 + \frac{0.0128793}{T} \quad (50 \leq T < 120)$$

$$-3.16087 + 1.05055 \cdot 10^{-3}T - 1.77472 \cdot 10^{-4}T \cdot \ln(T) - 1.61270 \cdot 10^{-7}T^2 + 4.94045 \cdot 10^{-11}T^3 + \frac{0.796924}{T} \quad (120 \leq T < 1000)$$

$$G_{\mathrm{Li_{13}Si_4}} =$$

$$-2.93562 + 1.21728 \cdot 10^{-7}T - 1.66941 \cdot 10^{-8}T^2 - 2.36862 \cdot 10^{-11}T^4 \quad (0 \leq T < 50)$$

$$-2.93536 - 4.95393 \cdot 10^{-5}T + 1.35626 \cdot 10^{-5}T \cdot \ln(T) - 1.39746 \cdot 10^{-7}T^2 - 2.38281 \cdot 10^{-9}T^3 \quad (50 \leq T < 120)$$

$$-2.96580 + 1.04221 \cdot 10^{-3}T - 1.77420 \cdot 10^{-4}T \cdot \ln(t) - 1.65232 \cdot 10^{-7}T^2 + 6.93195 \cdot 10^{-11}T^3 + \frac{0.76104}{T} \quad (120 \leq T < 1000)$$

$$G_{\mathrm{Li_{17}Si_4}} =$$

$$-2.75180 - 9.37906 \cdot 10^{-8}T + 8.70631 \cdot 10^{-9}T^2 - 1.82693 \cdot 10^{-11}T^4 \quad (0 \leq T < 50)$$

$$-2.74528 - 7.13966 \cdot 10^{-4}T + 1.79131 \cdot 10^{-4}T \cdot \ln(T) - 2.19927 \cdot 10^{-6}T^2 + 4.00049 \cdot 10^{-9}T^3 - \frac{0.0460207}{T} \quad (50 \leq T < 120)$$

$$-2.78308 + 1.07550 \cdot 10^{-3}T - 1.82205 \cdot 10^{-4}T \cdot \ln(T) - 1.57363 \cdot 10^{-7}T^2 + 6.12737 \cdot 10^{-11}T^3 + \frac{0.784095}{T} \quad (120 \leq T < 1000)$$

Appendix C

CIF files of this work

C.1 CIF file of $Li_{12}Si_7$

```
    # generated using pymatgen
data_Li12Si7
_symmetry_space_group_name_H-M   Pnma
_cell_length_a   8.53123800
_cell_length_b   19.62266200
_cell_length_c   14.31268200
_cell_angle_alpha   90.00000000
_cell_angle_beta   90.00000000
_cell_angle_gamma   90.00000000
_symmetry_Int_Tables_number   62
_chemical_formula_structural   Li12Si7
_chemical_formula_sum   'Li96 Si56'
_cell_volume   2396.02311375
_cell_formula_units_Z   8
loop_
 _symmetry_equiv_pos_site_id
 _symmetry_equiv_pos_as_xyz
  1  'x, y, z'
  2  '-x, -y, -z'
  3  '-x+1/2, -y, z+1/2'
  4  'x+1/2, y, -z+1/2'
  5  'x+1/2, -y+1/2, -z+1/2'
  6  '-x+1/2, y+1/2, z+1/2'
  7  '-x, y+1/2, -z'
  8  'x, -y+1/2, z'
loop_
 _atom_type_symbol
 _atom_type_oxidation_number
  Li+  1.0
  Si1.71428571-  -1.7142857142857142
loop_
 _atom_site_type_symbol
```

```
 _atom_site_label
 _atom_site_symmetry_multiplicity
 _atom_site_fract_x
 _atom_site_fract_y
 _atom_site_fract_z
 _atom_site_occupancy
  Li+  Li0  8  0.00372100  0.12500000  0.97243400  1
  Li+  Li1  8  0.10881900  0.18719400  0.65662800  1
  Li+  Li2  8  0.12289500  0.16564700  0.34041100  1
  Li+  Li3  8  0.12817800  0.14506300  0.13883900  1
  Li+  Li4  8  0.12950900  0.03157000  0.25633200  1
  Li+  Li5  8  0.12956100  0.52780300  0.43431900  1
  Li+  Li6  8  0.13043200  0.61269900  0.23651600  1
  Li+  Li7  8  0.13314000  0.50485400  0.06735800  1
  Li+  Li8  8  0.13735100  0.18890700  0.83743200  1
  Li+  Li9  8  0.13791500  0.67136400  0.47784900  1
  Li+  Li10  8  0.15755900  0.11165500  0.50508900  1
  Li+  Li11  4  0.11308000  0.75000000  0.86881000  1
  Li+  Li12  4  0.16175100  0.75000000  0.66585200  1
  Si1.71428571-  Si13  8  0.10653100  0.56501700  0.61401500  1
  Si1.71428571-  Si14  8  0.11776700  0.05060900  0.66644500  1
  Si1.71428571-  Si15  8  0.11992200  0.05314200  0.83141600  1
  Si1.71428571-  Si16  8  0.12387600  0.63215700  0.75195000  1
  Si1.71428571-  Si17  8  0.13114600  0.56082600  0.88583400  1
  Si1.71428571-  Si18  4  0.11565700  0.25000000  0.00780800  1
  Si1.71428571-  Si19  4  0.12227600  0.25000000  0.48803900  1
  Si1.71428571-  Si20  4  0.12821100  0.75000000  0.23546100  1
  Si1.71428571-  Si21  4  0.13297600  0.75000000  0.06955800  1

 ###### Interstitial sites #######
 # Li Li13  4  0.31 0.09 0.23
 # Li Li14  4  0.95 0.75 0.75
 # Li Li15  4  0.061 0.064 0.145
 # Si Si22  4  0.95 0.75 0.75
```

C.2 CIF file of Li_7Si_3

```
    # generated using pymatgen
data_Li7Si3
_symmetry_space_group_name_H-M   P3_112
_cell_length_a   7.52761214
_cell_length_b   7.52761214
_cell_length_c   17.84231328
_cell_angle_alpha   90.00000000
_cell_angle_beta   90.00000000
_cell_angle_gamma   120.00000000
_symmetry_Int_Tables_number   151
_chemical_formula_structural   Li7Si3
```

```
_chemical_formula_sum   'Li42 Si18'
_cell_volume   875.58086072
_cell_formula_units_Z   6
loop_
 _symmetry_equiv_pos_site_id
 _symmetry_equiv_pos_as_xyz
  1  'x, y, z'
  2  '-y, x-y, z+1/3'
  3  '-x+y, -x, z+2/3'
  4  '-y, -x, -z+2/3'
  5  '-x+y, y, -z+1/3'
  6  'x, x-y, -z'
loop_
 _atom_site_type_symbol
 _atom_site_label
 _atom_site_symmetry_multiplicity
 _atom_site_fract_x
 _atom_site_fract_y
 _atom_site_fract_z
 _atom_site_occupancy
  Li  Li0  6  0.19797692  0.41882908  0.37289952  1
  Li  Li1  6  0.19985906  0.09031974  0.71143697  1
  Li  Li2  6  0.21922769  0.44069037  0.51595828  1
  Li  Li3  6  0.21978707  0.10884380  0.86523613  1
  Li  Li4  6  0.53168686  0.11117821  0.95992415  1
  Li  Li5  6  0.55302434  0.11085834  0.81709133  1
  Li  Li6  3  0.22392319  0.44784637  0.66666667  1
  Li  Li7  3  0.55571353  0.11142706  0.66666667  1
  Si  Si8  6  0.22709383  0.46203092  0.10143120  1
  Si  Si9  6  0.24005389  0.11618591  0.43426484  1
  Si  Si10  6  0.54666819  0.11048421  0.23182897  1


   ###### Interstitial sites #######
 # Li Li8  3  0.22218   0.77782   0.66664
 # Si Si10 3  0.22218   0.77782   0.66664
```

C.3 CIF file of $Li_{13}Si_4$

```
    # generated using pymatgen
data_Li13Si4
_symmetry_space_group_name_H-M   Pbam
_cell_length_a   7.90356186
_cell_length_b   15.00943456
_cell_length_c   4.41386677
_cell_angle_alpha   90.00000000
_cell_angle_beta   90.00000000
_cell_angle_gamma   90.00000000
```

```
_symmetry_Int_Tables_number   55
_chemical_formula_structural   Li13Si4
_chemical_formula_sum   'Li26 Si8'
_cell_volume   523.60816304
_cell_formula_units_Z   2
loop_
 _symmetry_equiv_pos_site_id
 _symmetry_equiv_pos_as_xyz
  1  'x, y, z'
  2  '-x, -y, -z'
  3  '-x, -y, z'
  4  'x, y, -z'
  5  'x+1/2, -y+1/2, -z'
  6  '-x+1/2, y+1/2, z'
  7  '-x+1/2, y+1/2, -z'
  8  'x+1/2, -y+1/2, z'
loop_
 _atom_site_type_symbol
 _atom_site_label
 _atom_site_symmetry_multiplicity
 _atom_site_fract_x
 _atom_site_fract_y
 _atom_site_fract_z
 _atom_site_occupancy
  Li  Li0  4  0.09158420  0.75538311  0.50000000  1
  Li  Li1  4  0.09347403  0.39327086  0.50000000  1
  Li  Li2  4  0.09372641  0.19357140  0.00000000  1
  Li  Li3  4  0.15291723  0.02503682  0.00000000  1
  Li  Li4  4  0.23206042  0.84478806  0.00000000  1
  Li  Li5  4  0.24269297  0.59565722  0.50000000  1
  Li  Li6  2  0.00000000  0.50000000  0.00000000  1
  Si  Si7  4  0.07278252  0.93131645  0.50000000  1
  Si  Si8  4  0.08384910  0.66025629  0.00000000  1


     ###### Interstitial sites #######
 # Li Li8  4  0.16 0.72 0.16
 # Si Si10 4  0.16 0.72 0.16
```

C.4 CIF file of $Li_{22}Si_5$

```
    # generated using pymatgen
data_Li22Si5
_symmetry_space_group_name_H-M   F-43m
_cell_length_a   18.64489800
_cell_length_b   18.64489800
_cell_length_c   18.64489800
_cell_angle_alpha   90.00000000
```

```
_cell_angle_beta   90.00000000
_cell_angle_gamma   90.00000000
_symmetry_Int_Tables_number   216
_chemical_formula_structural   Li22Si5
_chemical_formula_sum   'Li352 Si80'
_cell_volume   6481.56731008
_cell_formula_units_Z   16
loop_
 _symmetry_equiv_pos_site_id
 _symmetry_equiv_pos_as_xyz
  1  'x, y, z'
  2  'y, -x, -z'
  3  '-x, -y, z'
  4  '-y, x, -z'
  5  'x, -y, -z'
  6  'y, x, z'
  7  '-x, y, -z'
  8  '-y, -x, z'
  9  'z, x, y'
  10  '-z, y, -x'
  11  'z, -x, -y'
  12  '-z, -y, x'
  13  '-z, x, -y'
  14  'z, y, x'
  15  '-z, -x, y'
  16  'z, -y, -x'
  17  'y, z, x'
  18  '-x, -z, y'
  19  '-y, z, -x'
  20  'x, -z, -y'
  21  '-y, -z, x'
  22  'x, z, y'
  23  'y, -z, -x'
  24  '-x, z, -y'
  25  'x+1/2, y+1/2, z'
  26  'y+1/2, -x+1/2, -z'
  27  '-x+1/2, -y+1/2, z'
  28  '-y+1/2, x+1/2, -z'
  29  'x+1/2, -y+1/2, -z'
  30  'y+1/2, x+1/2, z'
  31  '-x+1/2, y+1/2, -z'
  32  '-y+1/2, -x+1/2, z'
  33  'z+1/2, x+1/2, y'
  34  '-z+1/2, y+1/2, -x'
  35  'z+1/2, -x+1/2, -y'
  36  '-z+1/2, -y+1/2, x'
  37  '-z+1/2, x+1/2, -y'
  38  'z+1/2, y+1/2, x'
  39  '-z+1/2, -x+1/2, y'
```

```
 40  'z+1/2, -y+1/2, -x'
 41  'y+1/2, z+1/2, x'
 42  '-x+1/2, -z+1/2, y'
 43  '-y+1/2, z+1/2, -x'
 44  'x+1/2, -z+1/2, -y'
 45  '-y+1/2, -z+1/2, x'
 46  'x+1/2, z+1/2, y'
 47  'y+1/2, -z+1/2, -x'
 48  '-x+1/2, z+1/2, -y'
 49  'x+1/2, y, z+1/2'
 50  'y+1/2, -x, -z+1/2'
 51  '-x+1/2, -y, z+1/2'
 52  '-y+1/2, x, -z+1/2'
 53  'x+1/2, -y, -z+1/2'
 54  'y+1/2, x, z+1/2'
 55  '-x+1/2, y, -z+1/2'
 56  '-y+1/2, -x, z+1/2'
 57  'z+1/2, x, y+1/2'
 58  '-z+1/2, y, -x+1/2'
 59  'z+1/2, -x, -y+1/2'
 60  '-z+1/2, -y, x+1/2'
 61  '-z+1/2, x, -y+1/2'
 62  'z+1/2, y, x+1/2'
 63  '-z+1/2, -x, y+1/2'
 64  'z+1/2, -y, -x+1/2'
 65  'y+1/2, z, x+1/2'
 66  '-x+1/2, -z, y+1/2'
 67  '-y+1/2, z, -x+1/2'
 68  'x+1/2, -z, -y+1/2'
 69  '-y+1/2, -z, x+1/2'
 70  'x+1/2, z, y+1/2'
 71  'y+1/2, -z, -x+1/2'
 72  '-x+1/2, z, -y+1/2'
 73  'x, y+1/2, z+1/2'
 74  'y, -x+1/2, -z+1/2'
 75  '-x, -y+1/2, z+1/2'
 76  '-y, x+1/2, -z+1/2'
 77  'x, -y+1/2, -z+1/2'
 78  'y, x+1/2, z+1/2'
 79  '-x, y+1/2, -z+1/2'
 80  '-y, -x+1/2, z+1/2'
 81  'z, x+1/2, y+1/2'
 82  '-z, y+1/2, -x+1/2'
 83  'z, -x+1/2, -y+1/2'
 84  '-z, -y+1/2, x+1/2'
 85  '-z, x+1/2, -y+1/2'
 86  'z, y+1/2, x+1/2'
 87  '-z, -x+1/2, y+1/2'
 88  'z, -y+1/2, -x+1/2'
```

```
  89  'y, z+1/2, x+1/2'
  90  '-x, -z+1/2, y+1/2'
  91  '-y, z+1/2, -x+1/2'
  92  'x, -z+1/2, -y+1/2'
  93  '-y, -z+1/2, x+1/2'
  94  'x, z+1/2, y+1/2'
  95  'y, -z+1/2, -x+1/2'
  96  '-x, z+1/2, -y+1/2'
loop_
 _atom_site_type_symbol
 _atom_site_label
 _atom_site_symmetry_multiplicity
 _atom_site_fract_x
 _atom_site_fract_y
 _atom_site_fract_z
 _atom_site_occupancy
  Li  Li0  48  0.00578000  0.16279200  0.16279200  1
  Li  Li1  48  0.00636600  0.16131300  0.66131300  1
  Li  Li2  48  0.08561750  0.08561750  0.74970400  1
  Li  Li3  48  0.09053800  0.09053800  0.25828300  1
  Li  Li4  24  0.00000000  0.00000000  0.17239000  1
  Li  Li5  24  0.08314500  0.25000000  0.75000000  1
  Li  Li6  16  0.07148633  0.07148633  0.07148633  1
  Li  Li7  16  0.07680733  0.07680733  0.42319267  1
  Li  Li8  16  0.08284200  0.08284200  0.58284200  1
  Li  Li9  16  0.16802800  0.16802800  0.16802800  1
  Li  Li10  16  0.17340167  0.17340167  0.82659833  1
  Li  Li11  16  0.17503100  0.32496900  0.17503100  1
  Li  Li12  4  0.00000000  0.00000000  0.00000000  1
  Li  Li13  4  0.00000000  0.00000000  0.50000000  1
  Li  Li14  4  0.25000000  0.25000000  0.25000000  1
  Li  Li15  4  0.25000000  0.25000000  0.75000000  1
  Si  Si16  24  0.00000000  0.00000000  0.32415500  1
  Si  Si17  24  0.07451500  0.25000000  0.25000000  1
  Si  Si18  16  0.08808900  0.08808900  0.91191100  1
  Si  Si19  16  0.16667933  0.16667933  0.66667933  1

     ###### Interstitial sites #######
 # Li Li16  48  0.10896 0.10896 0.65343
```

C.5 CIF file of $Li_{21}Si_5$

```
    # generated using pymatgen
data_Li21Si5
_symmetry_space_group_name_H-M   F-43m
_cell_length_a   18.53249600
_cell_length_b   18.53249600
```

```
_cell_length_c   18.53249600
_cell_angle_alpha   90.00000000
_cell_angle_beta   90.00000000
_cell_angle_gamma   90.00000000
_symmetry_Int_Tables_number   216
_chemical_formula_structural   Li21Si5
_chemical_formula_sum   'Li336 Si80'
_cell_volume   6365.04890976
_cell_formula_units_Z   16
loop_
 _symmetry_equiv_pos_site_id
 _symmetry_equiv_pos_as_xyz
  1  'x, y, z'
  2  'y, -x, -z'
  3  '-x, -y, z'
  4  '-y, x, -z'
  5  'x, -y, -z'
  6  'y, x, z'
  7  '-x, y, -z'
  8  '-y, -x, z'
  9  'z, x, y'
  10  '-z, y, -x'
  11  'z, -x, -y'
  12  '-z, -y, x'
  13  '-z, x, -y'
  14  'z, y, x'
  15  '-z, -x, y'
  16  'z, -y, -x'
  17  'y, z, x'
  18  '-x, -z, y'
  19  '-y, z, -x'
  20  'x, -z, -y'
  21  '-y, -z, x'
  22  'x, z, y'
  23  'y, -z, -x'
  24  '-x, z, -y'
  25  'x+1/2, y+1/2, z'
  26  'y+1/2, -x+1/2, -z'
  27  '-x+1/2, -y+1/2, z'
  28  '-y+1/2, x+1/2, -z'
  29  'x+1/2, -y+1/2, -z'
  30  'y+1/2, x+1/2, z'
  31  '-x+1/2, y+1/2, -z'
  32  '-y+1/2, -x+1/2, z'
  33  'z+1/2, x+1/2, y'
  34  '-z+1/2, y+1/2, -x'
  35  'z+1/2, -x+1/2, -y'
  36  '-z+1/2, -y+1/2, x'
  37  '-z+1/2, x+1/2, -y'
```

```
38  'z+1/2, y+1/2, x'
39  '-z+1/2, -x+1/2, y'
40  'z+1/2, -y+1/2, -x'
41  'y+1/2, z+1/2, x'
42  '-x+1/2, -z+1/2, y'
43  '-y+1/2, z+1/2, -x'
44  'x+1/2, -z+1/2, -y'
45  '-y+1/2, -z+1/2, x'
46  'x+1/2, z+1/2, y'
47  'y+1/2, -z+1/2, -x'
48  '-x+1/2, z+1/2, -y'
49  'x+1/2, y, z+1/2'
50  'y+1/2, -x, -z+1/2'
51  '-x+1/2, -y, z+1/2'
52  '-y+1/2, x, -z+1/2'
53  'x+1/2, -y, -z+1/2'
54  'y+1/2, x, z+1/2'
55  '-x+1/2, y, -z+1/2'
56  '-y+1/2, -x, z+1/2'
57  'z+1/2, x, y+1/2'
58  '-z+1/2, y, -x+1/2'
59  'z+1/2, -x, -y+1/2'
60  '-z+1/2, -y, x+1/2'
61  '-z+1/2, x, -y+1/2'
62  'z+1/2, y, x+1/2'
63  '-z+1/2, -x, y+1/2'
64  'z+1/2, -y, -x+1/2'
65  'y+1/2, z, x+1/2'
66  '-x+1/2, -z, y+1/2'
67  '-y+1/2, z, -x+1/2'
68  'x+1/2, -z, -y+1/2'
69  '-y+1/2, -z, x+1/2'
70  'x+1/2, z, y+1/2'
71  'y+1/2, -z, -x+1/2'
72  '-x+1/2, z, -y+1/2'
73  'x, y+1/2, z+1/2'
74  'y, -x+1/2, -z+1/2'
75  '-x, -y+1/2, z+1/2'
76  '-y, x+1/2, -z+1/2'
77  'x, -y+1/2, -z+1/2'
78  'y, x+1/2, z+1/2'
79  '-x, y+1/2, -z+1/2'
80  '-y, -x+1/2, z+1/2'
81  'z, x+1/2, y+1/2'
82  '-z, y+1/2, -x+1/2'
83  'z, -x+1/2, -y+1/2'
84  '-z, -y+1/2, x+1/2'
85  '-z, x+1/2, -y+1/2'
86  'z, y+1/2, x+1/2'
```

```
  87  '-z, -x+1/2, y+1/2'
  88  'z, -y+1/2, -x+1/2'
  89  'y, z+1/2, x+1/2'
  90  '-x, -z+1/2, y+1/2'
  91  '-y, z+1/2, -x+1/2'
  92  'x, -z+1/2, -y+1/2'
  93  '-y, -z+1/2, x+1/2'
  94  'x, z+1/2, y+1/2'
  95  'y, -z+1/2, -x+1/2'
  96  '-x, z+1/2, -y+1/2'
loop_
 _atom_site_type_symbol
 _atom_site_label
 _atom_site_symmetry_multiplicity
 _atom_site_fract_x
 _atom_site_fract_y
 _atom_site_fract_z
 _atom_site_occupancy
  Li  Li0  48  0.01122400  0.34050450  0.84050450  1
  Li  Li1  48  0.01275100  0.15903800  0.15903800  1
  Li  Li2  48  0.08902800  0.24340700  0.91097200  1
  Li  Li3  48  0.09518000  0.09518000  0.26995300  1
  Li  Li4  24  0.00000000  0.00000000  0.17532500  1
  Li  Li5  24  0.07724000  0.25000000  0.75000000  1
  Li  Li6  16  0.05278000  0.05278000  0.05278000  1
  Li  Li7  16  0.06376100  0.06376100  0.43623900  1
  Li  Li8  16  0.08011100  0.08011100  0.58011100  1
  Li  Li9  16  0.16843300  0.16843300  0.16843300  1
  Li  Li10  16  0.19300000  0.19300000  0.30700000  1
  Li  Li11  16  0.19391600  0.19391600  0.80608400  1
  Si  Si12  24  0.00000000  0.00000000  0.32018500  1
  Si  Si13  24  0.07190800  0.25000000  0.25000000  1
  Si  Si14  16  0.08983400  0.08983400  0.91016600  1
  Si  Si15  16  0.16490400  0.16490400  0.66490400  1


        ###### Interstitial sites #######
 # Li Li12  4  0.047 0.952 0.822
 # Li Li13  4  0.751 0.250 0.751
 # Li Li14  4  0.5 0.5 0.5
 # Si Si16  4  0.047 0.952 0.822
```

C.6 CIF file of $Li_{17}Si_4$

```
#======================================================================
# CRYSTAL DATA
#----------------------------------------------------------------------
```

```
data_VESTA_phase_1

_chemical_name_common                  'Lithium Silicide'
_cell_length_a                         18.6563(2)
_cell_length_b                         18.6563(2)
_cell_length_c                         18.6563(2)
_cell_angle_alpha                      90.000000
_cell_angle_beta                       90.000000
_cell_angle_gamma                      90.000000
_cell_volume                           6493.465264
_space_group_name_H-M_alt              'F -4 3 m'
_space_group_IT_number                 216

loop_
_space_group_symop_operation_xyz
   'x, y, z'
   '-x, -y, z'
   '-x, y, -z'
   'x, -y, -z'
   'z, x, y'
   'z, -x, -y'
   '-z, -x, y'
   '-z, x, -y'
   'y, z, x'
   '-y, z, -x'
   'y, -z, -x'
   '-y, -z, x'
   'y, x, z'
   '-y, -x, z'
   'y, -x, -z'
   '-y, x, -z'
   'x, z, y'
   '-x, z, -y'
   '-x, -z, y'
   'x, -z, -y'
   'z, y, x'
   'z, -y, -x'
   '-z, y, -x'
   '-z, -y, x'
   'x, y+1/2, z+1/2'
   '-x, -y+1/2, z+1/2'
   '-x, y+1/2, -z+1/2'
   'x, -y+1/2, -z+1/2'
   'z, x+1/2, y+1/2'
   'z, -x+1/2, -y+1/2'
   '-z, -x+1/2, y+1/2'
   '-z, x+1/2, -y+1/2'
   'y, z+1/2, x+1/2'
   '-y, z+1/2, -x+1/2'
```

```
'y, -z+1/2, -x+1/2'
'-y, -z+1/2, x+1/2'
'y, x+1/2, z+1/2'
'-y, -x+1/2, z+1/2'
'y, -x+1/2, -z+1/2'
'-y, x+1/2, -z+1/2'
'x, z+1/2, y+1/2'
'-x, z+1/2, -y+1/2'
'-x, -z+1/2, y+1/2'
'x, -z+1/2, -y+1/2'
'z, y+1/2, x+1/2'
'z, -y+1/2, -x+1/2'
'-z, y+1/2, -x+1/2'
'-z, -y+1/2, x+1/2'
'x+1/2, y, z+1/2'
'-x+1/2, -y, z+1/2'
'-x+1/2, y, -z+1/2'
'x+1/2, -y, -z+1/2'
'z+1/2, x, y+1/2'
'z+1/2, -x, -y+1/2'
'-z+1/2, -x, y+1/2'
'-z+1/2, x, -y+1/2'
'y+1/2, z, x+1/2'
'-y+1/2, z, -x+1/2'
'y+1/2, -z, -x+1/2'
'-y+1/2, -z, x+1/2'
'y+1/2, x, z+1/2'
'-y+1/2, -x, z+1/2'
'y+1/2, -x, -z+1/2'
'-y+1/2, x, -z+1/2'
'x+1/2, z, y+1/2'
'-x+1/2, z, -y+1/2'
'-x+1/2, -z, y+1/2'
'x+1/2, -z, -y+1/2'
'z+1/2, y, x+1/2'
'z+1/2, -y, -x+1/2'
'-z+1/2, y, -x+1/2'
'-z+1/2, -y, x+1/2'
'x+1/2, y+1/2, z'
'-x+1/2, -y+1/2, z'
'-x+1/2, y+1/2, -z'
'x+1/2, -y+1/2, -z'
'z+1/2, x+1/2, y'
'z+1/2, -x+1/2, -y'
'-z+1/2, -x+1/2, y'
'-z+1/2, x+1/2, -y'
'y+1/2, z+1/2, x'
'-y+1/2, z+1/2, -x'
'y+1/2, -z+1/2, -x'
```

```
   '-y+1/2, -z+1/2, x'
   'y+1/2, x+1/2, z'
   '-y+1/2, -x+1/2, z'
   'y+1/2, -x+1/2, -z'
   '-y+1/2, x+1/2, -z'
   'x+1/2, z+1/2, y'
   '-x+1/2, z+1/2, -y'
   '-x+1/2, -z+1/2, y'
   'x+1/2, -z+1/2, -y'
   'z+1/2, y+1/2, x'
   'z+1/2, -y+1/2, -x'
   '-z+1/2, y+1/2, -x'
   '-z+1/2, -y+1/2, x'

loop_
   _atom_site_label
   _atom_site_occupancy
   _atom_site_fract_x
   _atom_site_fract_y
   _atom_site_fract_z
   _atom_site_adp_type
   _atom_site_U_iso_or_equiv
   _atom_site_type_symbol
   Si1        1.0     0.159759(8)  0.159759(8)  0.159759(8) Uani  0.006890 Si
   Si2        1.0     0.916667(8)  0.916667(8)  0.916667(8) Uani  0.006260 Si
   Si3        1.0     0.321327(11)  0.000000     0.000000    Uani  0.007010 Si
   Si4        1.0     0.570307(10)  0.250000     0.250000    Uani  0.006803 Si
   Li1        1.0     0.07410(6)   0.07410(6)   0.07410(6)  Uani  0.014900 Li
   Li2        1.0     0.30284(5)   0.30284(5)   0.30284(5)  Uani  0.012500 Li
   Li3        1.0     0.41794(7)   0.41794(7)   0.41794(7)  Uani  0.012700 Li
   Li4        1.0     0.55713(5)   0.55713(5)   0.55713(5)  Uani  0.012500 Li
   Li5        1.0     0.68687(5)   0.68687(5)   0.68687(5)  Uani  0.012300 Li
   Li6        1.0     0.83168(6)   0.83168(6)   0.83168(6)  Uani  0.013500 Li
   Li7        1.0     0.16807(8)   0.000000     0.000000    Uani  0.011800 Li
   Li8        1.0     0.07492(9)   0.250000     0.250000    Uani  0.013933 Li
   Li9        1.0     0.09068(4)   0.09068(4)   0.26186(6)  Uani  0.015633 Li
   Li10       1.0     0.09013(5)   0.09013(5)   0.76176(6)  Uani  0.016067 Li
   Li11       1.0     0.15503(4)   0.15503(4)   0.51978(6)  Uani  0.016100 Li
   Li12       1.0     0.16327(4)   0.16327(4)   0.00286(7)  Uani  0.014333 Li
   Li13       1.0     0.000000     0.000000     0.000000    Uani  0.010500 Li

loop_
   _atom_site_aniso_label
   _atom_site_aniso_U_11
   _atom_site_aniso_U_22
   _atom_site_aniso_U_33
   _atom_site_aniso_U_12
   _atom_site_aniso_U_13
   _atom_site_aniso_U_23
```

```
   Si13  0.00689  0.00689  0.00689  0.00014  0.00014  0.00014
   Si14  0.00626  0.00626  0.00626 -0.00017 -0.00017 -0.00017
   Si15  0.00649  0.00727  0.00727  0.00000  0.00000 -0.00067
   Si16  0.00671  0.00685  0.00685  0.00000  0.00000  0.00035
   Li0  0.01490  0.01490  0.01490 -0.00020 -0.00020 -0.00020
   Li1  0.01250  0.01250  0.01250  0.00090  0.00090  0.00090
   Li2  0.01270  0.01270  0.01270  0.00150  0.00150  0.00150
   Li3  0.01250  0.01250  0.01250  0.00070  0.00070  0.00070
   Li4  0.01230  0.01230  0.01230  0.00190  0.00190  0.00190
   Li5  0.01350  0.01350  0.01350 -0.00060 -0.00060 -0.00060
   Li6  0.01300  0.01120  0.01120  0.00000  0.00000  0.00020
   Li7  0.01180  0.01500  0.01500  0.00000  0.00000 -0.00070
   Li8  0.01590  0.01590  0.01510 -0.00280  0.00320  0.00320
   Li9  0.01670  0.01670  0.01480 -0.00180 -0.00020 -0.00020
   Li10  0.01570  0.01570  0.01690 -0.00160 -0.00120 -0.00120
   Li11  0.01390  0.01390  0.01520 -0.00310 -0.00050 -0.00050
   Li12  0.01050  0.01050  0.01050  0.00000  0.00000  0.00000

            ###### Interstitial sites #######
 # Li Li13  4  0.5 0.5 0.5
 # Si Si17  4  0.5 0.5 0.5
```

C.7 CIF file of $Li_{15}Si_4$

```
    # generated using pymatgen
data_Li15Si4
_symmetry_space_group_name_H-M   I-43d
_cell_length_a   10.55603184
_cell_length_b   10.55603184
_cell_length_c   10.55603184
_cell_angle_alpha   90.00000000
_cell_angle_beta   90.00000000
_cell_angle_gamma   90.00000000
_symmetry_Int_Tables_number   220
_chemical_formula_structural   Li15Si4
_chemical_formula_sum   'Li60 Si16'
_cell_volume   1176.25660323
_cell_formula_units_Z   4
loop_
 _symmetry_equiv_pos_site_id
 _symmetry_equiv_pos_as_xyz
  1  'x, y, z'
  2  'y+1/4, -x+3/4, -z+1/4'
  3  '-x, -y+1/2, z'
  4  '-y+3/4, x+3/4, -z+1/4'
  5  'x, -y, -z+1/2'
  6  'y+1/4, x+1/4, z+1/4'
  7  '-x, y+1/2, -z+1/2'
```

```
  8  '-y+3/4, -x+1/4, z+1/4'
  9  'z, x, y'
  10  '-z+1/4, y+1/4, -x+3/4'
  11  'z, -x, -y+1/2'
  12  '-z+1/4, -y+3/4, x+3/4'
  13  '-z+1/2, x, -y'
  14  'z+1/4, y+1/4, x+1/4'
  15  '-z+1/2, -x, y+1/2'
  16  'z+1/4, -y+3/4, -x+1/4'
  17  'y, z, x'
  18  '-x+3/4, -z+1/4, y+1/4'
  19  '-y+1/2, z, -x'
  20  'x+3/4, -z+1/4, -y+3/4'
  21  '-y, -z+1/2, x'
  22  'x+1/4, z+1/4, y+1/4'
  23  'y+1/2, -z+1/2, -x'
  24  '-x+1/4, z+1/4, -y+3/4'
  25  'x+1/2, y+1/2, z+1/2'
  26  'y+3/4, -x+1/4, -z+3/4'
  27  '-x+1/2, -y, z+1/2'
  28  '-y+1/4, x+1/4, -z+3/4'
  29  'x+1/2, -y+1/2, -z'
  30  'y+3/4, x+3/4, z+3/4'
  31  '-x+1/2, y, -z'
  32  '-y+1/4, -x+3/4, z+3/4'
  33  'z+1/2, x+1/2, y+1/2'
  34  '-z+3/4, y+3/4, -x+1/4'
  35  'z+1/2, -x+1/2, -y'
  36  '-z+3/4, -y+1/4, x+1/4'
  37  '-z, x+1/2, -y+1/2'
  38  'z+3/4, y+3/4, x+3/4'
  39  '-z, -x+1/2, y'
  40  'z+3/4, -y+1/4, -x+3/4'
  41  'y+1/2, z+1/2, x+1/2'
  42  '-x+1/4, -z+3/4, y+3/4'
  43  '-y, z+1/2, -x+1/2'
  44  'x+1/4, -z+3/4, -y+1/4'
  45  '-y+1/2, -z, x+1/2'
  46  'x+3/4, z+3/4, y+3/4'
  47  'y, -z, -x+1/2'
  48  '-x+3/4, z+3/4, -y+1/4'
loop_
 _atom_site_type_symbol
 _atom_site_label
 _atom_site_symmetry_multiplicity
 _atom_site_fract_x
 _atom_site_fract_y
 _atom_site_fract_z
 _atom_site_occupancy
```

```
 Li  Li0  48  0.03757034  0.87717671  0.84787494  1
 Li  Li1  12  0.00000000  0.25000000  0.87500000  1
 Si  Si2  16  0.04272246  0.95727754  0.45727754  1

          ###### Interstitial sites #######
# Li Li2  4  0 0 0.125
# Si Si3  4  0 0 0.125
```

Appendix D

XRD diffraction patterns

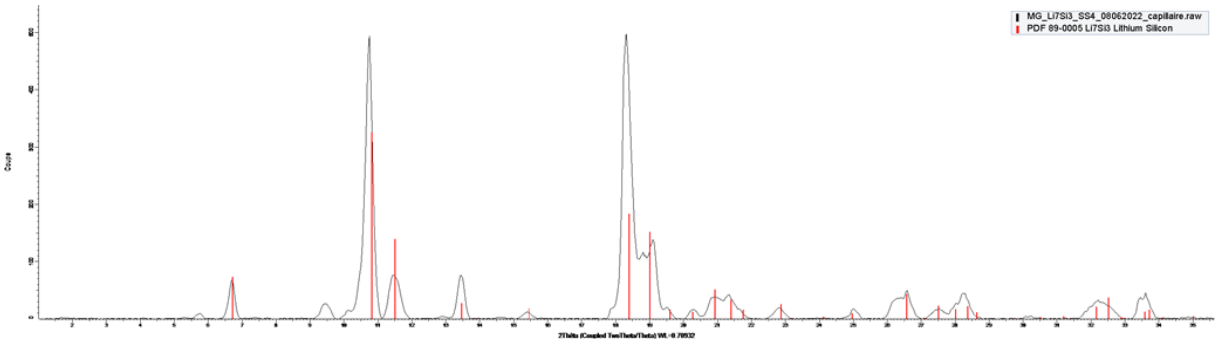

Figure D.1: Plot of the XRD patterns of powder Li_7Si_3 [Courtesy of Magali Gauthier]. The red lines represent data from ICCD database [125], and the black lines represent the results of Magali Gauthier.

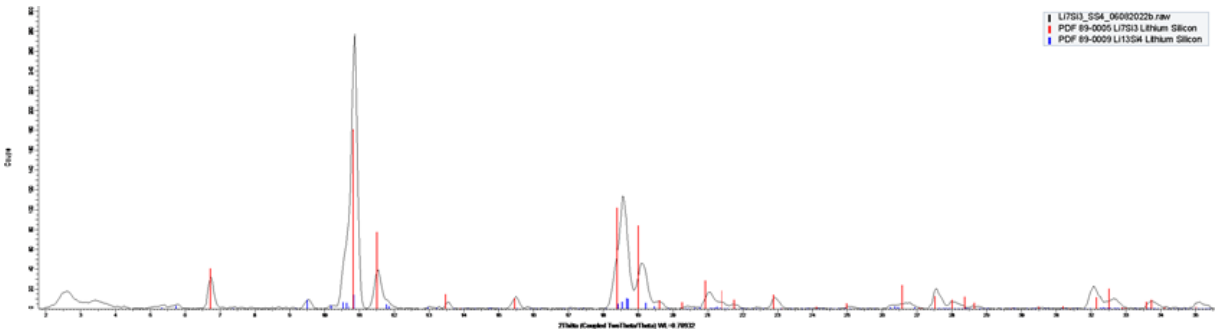

Figure D.2: Plot of the XRD 1 patterns of starting Li-Si compound in the 2 electrode delithiation. Blue lines denote the $Li_{13}Si_4$ patterns and the red lines denote the Li_7Si_3 patterns as suggested by the ICCD database [125].

Résumé en français

Les avancées dans les batteries jouent un rôle crucial dans la résolution de plusieurs défis mondiaux pressants. Tout d'abord, environ 770 millions de personnes manquent d'accès à l'électricité, principalement dans les régions en développement [1]. En améliorant la technologie des batteries, nous pouvons renforcer les systèmes de stockage et de distribution d'énergie, ce qui permet une alimentation électrique fiable dans les régions éloignées, améliorant ainsi la qualité de vie et favorisant la croissance économique de millions d'individus. Deuxièmement, les batteries ont un impact significatif sur la réduction des émissions de gaz à effet de serre. Les pays cherchant à passer de sources d'électricité riches en carbone (estimation de 45 % des émissions mondiales selon [2]) à des sources propres et renouvelables, comme le solaire et l'éolien, font face à un défi majeur en matière de stockage d'énergie. La nature intermittente de l'énergie renouvelable nécessite des méthodes efficaces pour stocker l'excès d'énergie généré pendant les périodes de pointe et la distribuer pendant les périodes de faible production. Les batteries améliorées permettent un stockage efficace de l'énergie, garantissant ainsi un approvisionnement stable et constant en électricité propre, même dans les régions dépourvues de méthodes de production d'électricité sans carbone. De plus, l'une des principales sources d'émissions actuelles provient des transports en ville à base de pétrole (estimation de 12 % des émissions mondiales selon [2]). La transition vers des véhicules électriques (VE) alimentés par des batteries efficaces et durables est une solution clé, notamment dans des pays comme la France où des sources d'électricité sans carbone (par exemple, le nucléaire) sont disponibles. C'est pourquoi, par exemple, l'Union européenne cherche à interdire complètement la vente de voitures à base de pétrole d'ici 2035 [3]. Les avancées dans la technologie des batteries permettent une autonomie accrue des VE, des temps de charge plus rapides et une durée de vie plus longue, ce qui en fait une alternative plus viable et durable aux voitures à essence conventionnelles.

La meilleure technologie actuelle et la plus utilisée dans les batteries des VE est celle au lithium-ion (Li-ion) [4]. Cependant, les performances des batteries Li-ion peuvent être améliorées grâce au développement de nouveaux matériaux d'électrode à haute densité énergétique. Au cours des deux dernières décennies, il a été démontré que dans certaines conditions, le silicium (Si) est un matériau d'électrode négative hautement prometteur car il possède une capacité théorique spécifique dix fois supérieure à celle du graphite, le matériau d'électrode négative utilisé dans les batteries commerciales [5].

La lithiation du Si par des processus électrochimiques s'est avérée difficile pour diverses raisons. Il y a une expansion volumétrique énorme allant jusqu'à 400 % du Si lorsqu'il est lithié, ce qui est connu pour causer des difficultés (par exemple, la pulvérisation du Si). Cette expansion volumétrique est due aux transformations de phase Li-Si qui peuvent dépendre de la teneur en Li, des contraintes mécaniques, des contraintes électrochimiques, etc... Des études expérimentales ont indiqué que les alliages amorphes présentent des performances cycliques supérieures par rapport à leurs homologues cristallins [6, 7]. Ces investigations ont révélé que les mécanismes responsables de la perte de capacité dans les matériaux d'anode amorphes diffèrent de ceux observés dans les phases cristallines. Dans les structures cristallines, l'introduction de lithium conduit à la formation de phases intermétalliques, entraînant une expansion inégale et des fissures. En revanche, bien que les matériaux amorphes subissent une expansion volumétrique plus importante lors de la lithiation [8], la déformation est uniforme et réversible, ce qui contraste fortement avec le comportement des phases cristallines. De plus, la formation de phases cristallines comme Li15Si4 peut poser des problèmes pour le cyclage des anodes à base de Si (par exemple, perte de capacité au fil des cycles de dé/lithiation).

Comprendre les processus d'alliage à l'échelle atomique du Si-Li, qu'ils soient cristallins ou amorphes, est essentiel pour éviter les problèmes mentionnés précédemment. Cependant, la caractérisation atomique de ces processus d'alliage a été assez difficile en raison des limitations expérimentales liées à la détermination de la structure cristallographique (par exemple, les inexactitudes des schémas de diffraction des rayons X dues au Li [9]). Avant même d'aborder la tâche difficile de modéliser les transitions d'amorphisation ou de cristallisation, nous constatons qu'il existe encore des questions ouvertes dans la littérature concernant la stabilité thermodynamique des phases cristallines. Par conséquent, il n'existe pas de diagramme de phase Li-Si largement accepté dans la littérature. De plus, il est important de souligner que la prise en compte de la modélisation théorique de la non-stœchiométrie a été négligée dans les études des systèmes Li-Si, à notre connaissance. Cette omission peut entraîner des inexactitudes lors de la création de diagrammes de phase et de leur comparaison avec les résultats expérimentaux. De plus, la modélisation théorique de la non-stœchiométrie est essentielle pour modéliser avec précision la diffusion et les transformations de phase dans ces systèmes.

Dans cette thèse, nous modélisons à l'échelle atomique les propriétés thermodynamiques des composés Li-Si cristallins en utilisant la théorie de la fonctionnelle de la densité (DFT) et des méthodes de physique statistique. Nous modélisons les défauts ponctuels et les propriétés thermodynamiques de la non-stœchiométrie des phases Li-Si. Avec l'étude de la non-stœchiométrie, cette thèse vise également à comprendre les processus de transformation de phase que subissent les phases Li-Si, qu'ils se produisent à l'équilibre ou dans le cadre de la thermodynamique contrainte (c'est-à-dire sous tension appliquée). Cela peut également aider à déterminer la stabilité de certaines phases et donc à valider leur existence.

Premier chapitre

Dans le premier chapitre, nous avons fourni un bref aperçu du principe de fonctionnement des batteries Li-ion et examiné les différents composants impliqués. Nous avons ensuite exploré les avantages potentiels de l'utilisation du silicium comme électrode négative. Bien que des progrès significatifs aient été réalisés pour améliorer les performances des électrodes à base de silicium, il reste des obstacles à surmonter avant de commercialiser des batteries Li-ion avec ces électrodes.

Nous avons également fourni suffisamment de preuves de l'importance de comprendre le processus d'alliage Li-Si dans le but d'améliorer ces systèmes. Il est important de rappeler que, contrairement à d'autres anodes comme le graphite, où nous avons une (dé)intercalation de Li, l'anode à base de Si subit une expansion/rétrécissement de volume due aux transformations de phase lors de la lithiation/délithiation. Des problèmes majeurs surviennent en raison de ces variations de volume, tels que la rupture constante et l'accumulation d'électrolyte solide et le délaminage des particules de Si de l'électrode. Les deux phénomènes entraînent une importante chute de capacité lors du cyclage de tension. Nous avons souligné dans la littérature que la formation de certaines phases comme la Li15Si4 cristalline peut poser des problèmes pour le cyclage, il est donc essentiel de comprendre sa formation par rapport à d'autres phases cristallines pour améliorer la cyclabilité des anodes à base de Si.

Nous avons mis en évidence les désaccords entre différentes études (par exemple, entre des études expérimentales ou entre des études expérimentales et théoriques) sur la stabilité des phases (c'est-à-dire les diagrammes de phase). Nous avons souligné que même les diagrammes de phase les plus récents évalués dans les systèmes Li-Si ne tiennent pas compte de la non-stœchiométrie des phases Li-Si, que nous avons montrée être importante à prendre en compte pour la cinétique des transitions de phase.

Dans ce chapitre, nous avons également présenté la méthodologie nécessaire dans le cadre de ce travail. Nous avons mis l'accent sur la relation entre les méthodes théoriques et celles de l'expérience (GITT).

Nous avons remarqué que l'évaluation du modèle thermodynamique Si-Li sur la variation de la non-stœchiométrie mesurée de la tension à circuit ouvert (OCV) [35] fait défaut, et que la contribution de la non-stœchiométrie dans les diagrammes de phase actuels des phases Li-Si [53, 42] est absente. C'est pourquoi, pour ce travail, nous avons décidé de relever le défi d'inclure la modélisation de la non-stœchiométrie des phases Li-Si afin d'avoir une meilleure compréhension et peut-être de fournir un éclairage sur les désaccords en cours dans la littérature et de répondre partiellement aux questions ouvertes sur la sélection des phases dans Si-Li lors de la (dé)lithiation.

Deuxieme chapitre

Dans le deuxieme chapitre, nous avons découvert deux nouvelles phases, les phases $Li_{43}Si_{18}$ et $Li_{44}Si_{18}$, qui, à notre connaissance, n'avaient pas été mentionnées précédemment dans la

littérature. Il est très difficile de les distinguer des phases précédemment connues Li_7Si_3 et Li_5Si_2, car elles partagent toutes la même sous-réseau de silicium et diffèrent uniquement par les lacunes de lithium dans un sous-réseau.

Nous avons constaté que la phase LiSi n'est pas stable par rapport à l'équilibre à deux phases Li-$Li_{12}Si_7$ en utilisant la fonction hybride HSE06 à 0 K. Ce résultat a joué un rôle important dans la décision d'ignorer cette phase pour le reste de ce travail.

Nous avons déduit de la comparaison avec CALPHAD que notre valeur prédite de l'énergie libre de Gibbs de Li (G_p) peut être utilisée comme référence pour les futures études de tension à circuit ouvert, malgré la négligence de la transformation de phase du solide au liquide à 453 K.

Nous avons observé l'effet de l'expansion volumique thermique incluse dans notre calcul des propriétés thermodynamiques des composés Li-Si. Elle est importante pour les phases contenant du lithium et moins importante pour le silicium pur. Cela nous donne une idée que l'expansion volumique thermique est principalement due au lithium. Une autre chose importante à noter est que l'expansion volumique thermique semble être importante à considérer après 350 K. Nous avons presque reproduit les paramètres de réseau expérimentaux à température ambiante. Et nous avons également reproduit assez bien l'expansion volumique induite par la concentration de l'expérience malgré les composés Si-Li amorphes. L'étude des structures cristallines peut donner une idée quantitative de l'expansion volumique.

Malgré l'amélioration de la tension à circuit ouvert prédite à 690 K par rapport à l'expérimentale, la contribution de l'entropie vibratoire des phases ordonnées n'est pas suffisante pour reproduire l'expérience. Nous échouons toujours à reproduire la stabilité des phases, en particulier autour de la composition Li_7Si_3. C'est ce qui a motivé notre travail sur les études de non-stœchiométrie (chapitre suivant), nous croyons qu'elles peuvent contribuer à répondre à de nombreuses questions qui existent actuellement dans la littérature, telle que la stabilité/métastabilité de la phase Li_7Si_3 ou Li_5Si_2.

Troisième chapitre

Dans ce chapitre, nous avons calculé les énergies de formation des défauts ponctuels comme moyen d'investiguer l'instabilité des phases et d'identifier les défauts ponctuels dominants dans chaque phase. Ces énergies de formation ont été utilisées conjointement avec la LTE du grand potentiel des composés Li-Si. Nous avons trouvé une corrélation entre la nature des défauts ponctuels et la composition de la phase Li-Si à 690 K. Par exemple, nous avons constaté que les défauts ponctuels du silicium deviennent plus stables aux compositions élevées de la phase Li-Si : les interstitiels de silicium ont la plus faible énergie de formation autour de $Li_{13}Si_4$ et une énergie très élevée dans toutes les autres compositions ; et les lacunes de silicium sont faciles à créer dans la phase lithiée la plus élevée, $Li_{17}Si_4$.

Nous avons utilisé la LTE pour extraire le potentiel chimique du lithium et du silicium en fonction de la composition autour de chaque composé. Cela nous a permis de comparer

nos résultats prédits avec ceux de l'expérience à 690 K. Nous avons pu comparer la tension à circuit ouvert (OCV), les énergies de formation efficaces des défauts ponctuels et le facteur thermodynamique. Remarquablement, nous avons mis en place une méthode permettant d'utiliser la LTE pour extraire les énergies de formation efficaces des défauts ponctuels à partir des valeurs expérimentales de l'OCV dans le domaine des phases à une phase unique, avec une précision de 0,03 eV.

Nous avons prédit à partir de nos comparaisons avec l'expérience quelles sont les phases les plus susceptibles d'exister à 690 K. Nous rapportons que $Li_{12}Si_7$, $Li_{43}Si_{18}$, $Li_{13}Si_4$ et $Li_{17}Si_4$ sont les phases stables, en se basant sur les similitudes avec l'expérience (par exemple, OCV, énergies de formation efficaces des défauts ponctuels, etc...).

Nous avons montré que le maximum du facteur d'amélioration thermodynamique est proportionnel à l'énergie de formation des paires Frenkel lorsque les défauts ponctuels dominants sont des interstitiels simples et des lacunes simples de la même espèce. Nous avons également prouvé que le maximum n'est pas nécessairement toujours à la stœchiométrie parfaite ($\delta = 0$ dans $Li_{a+\delta}Si_b$), comme le prétendaient autrement Wen et Huggins [35]. Nous avons prouvé que dans le cas où nous avons une paire Frenkel Li-Li comme défaut ponctuel de stœchiométrie dominante, le maximum du facteur d'amélioration thermodynamique est virtuellement à $\delta = 0$. Cependant, dans le cas où nous avons des défauts de Schottky comme défaut ponctuel de stœchiométrie dominante, nous avons montré que le maximum du facteur d'amélioration thermodynamique n'est pas à $\delta = 0$.

Les résultats de ce chapitre ne tiennent pas compte des équilibres à deux phases hors-stœchiométrie entre les phases. Cependant, à partir des énergies libres de Gibbs hors-stœchiométrie et des potentiels chimiques que nous avons obtenus dans ce chapitre, nous pouvons, dans le chapitre suivant, calculer les équilibres à deux phases entre les phases qui incluront ensuite les paliers de tension à circuit ouvert que nous pourrons comparer avec l'expérience.

Quatrieme chapitre

Dans ce chapitre, nous avons examiné le processus d'alliage des systèmes Li-Si d'un point de vue thermodynamique et thermodynamique à tension contrainte.

Nous avons montré que notre modèle de la solution solide diluée Si(Li) en équilibre avec le $Li_{12}Si_7$ est en bon accord avec les observations expérimentales. Nous avons calculé la limite de solubilité du Li dans le Si à température ambiante, qui s'avère être très faible. Nous avons également calculé la limite de solubilité de Si(Li) en équilibre avec $Li_{12}Si_7$ et montré qu'elle est également très faible. Cela suggère que le potentiel chimique du Si n'est pas affecté par l'insertion de Li dans Si(Li).

Nous avons tenté de construire le diagramme de phase en utilisant d'abord la modélisation LTE des composés hors-stœchiométriques ordonnés, y compris la concentration d'équilibre de leurs défauts de réseau. Cependant, les approximations diluées de la LTE n'ont pas pu fournir une séquence cohérente des équilibres de phase Li_7Si_3-$Li_{43}Si_{18}$-Li_5Si_2. Cela a conduit au développement d'un modèle de champ moyen de la solution solide concentrée

Li_7Si_3. À partir de ce modèle, nous avons pu extraire une température de transition ordre-désordre de $Li_{43}Si_{18}$ et $Li_{44}Si_{18}$ et découvrir qu'à des températures inférieures à 70 K, la phase ordonnée stable est en fait la $Li_{43}Si_{18}$, et au-dessus de 70 K, c'est la solution solide Li_7Si_3.

À partir de l'énergie libre de Gibbs de la solution solide concentrée et des phases ordonnées hors-stœchiométriques, nous avons construit le premier diagramme de phase rapporté incluant la hors-stœchiométrie. Notre diagramme de phase contient des informations sur la transition ordre-désordre autour de la composition Li_7Si_3. Il exclut la phase LiSi, car nos calculs hybrides DFT au chapitre 2 ont prédit que cette phase n'était pas stable à 0 K. Le diagramme de phase présenté rapporte la $Li_{17}Si_4$ comme la phase fortement lithiée. Il inclut également les phases $Li_{12}Si_7$ et $Li_{13}Si_4$, qui ont été précédemment rapportées dans tous les diagrammes de phase sans désaccord.

Nous avons ensuite pu prédire la tension à circuit ouvert (OCV) en incluant la hors-stœchiométrie. Les intervalles de composition calculés et les valeurs des paliers de l'OCV sont en bon accord avec les valeurs expérimentales rapportées à 690 K. Nous avons constaté que pour correspondre au pic de Li_7Si_3 rapporté expérimentalement à 210 K (une signature d'une transition de phase du premier ordre), nous devons légèrement surestimer la composition nominale du Li (de près de 0,9 % par rapport à celle rapportée expérimentalement). Conformément aux expériences de RMN rapportées, nous suggérons que la transition de phase du premier ordre provient d'un équilibre à deux phases entre Li_7Si_3 et $Li_{12}Si_7$ vers la phase unique Li_7Si_3.

Nous avons étudié les forces motrices de nucléation contraintes. Nous avons suggéré que pour modéliser la sélection des phases précipitées sous un potentiel chimique uniforme du Li appliqué, il est utile d'introduire le concept de force motrice de nucléation contrainte ($\Delta\Phi$) et de force motrice de relaxation (δg) de l'équilibre contraint vers son état d'équilibre. Nous avons montré que la nucléation et la croissance de $Li_{15}Si_4$ pourraient être favorisées, malgré une force motrice de nucléation légèrement inférieure que ses homologues (par exemple, SS ou $Li_{13}Si_4$). Nous avons conclu que si $Li_{15}Si_4$ se forme, elle pourrait soit se décomposer en phases stables, soit établir un équilibre métastable avec le Si. De même, la nucléation directe de Si pourrait être possible si nous délithions directement à partir d'un composé Li-Si. Nous avons conclu que le palier de 0,45 V observé expérimentalement lors de la délithiation à température ambiante pourrait être une signature de la nucléation directe de Si à partir de phases intermédiaires Li-Si.

Le lecteur peut trouver ci-dessous deux images qui montrent le résultat le plus important de ce travail : le diagramme de phase incluant la hors-stœchiométrie et la comparaison OCV à 690 K avec l'expérience.

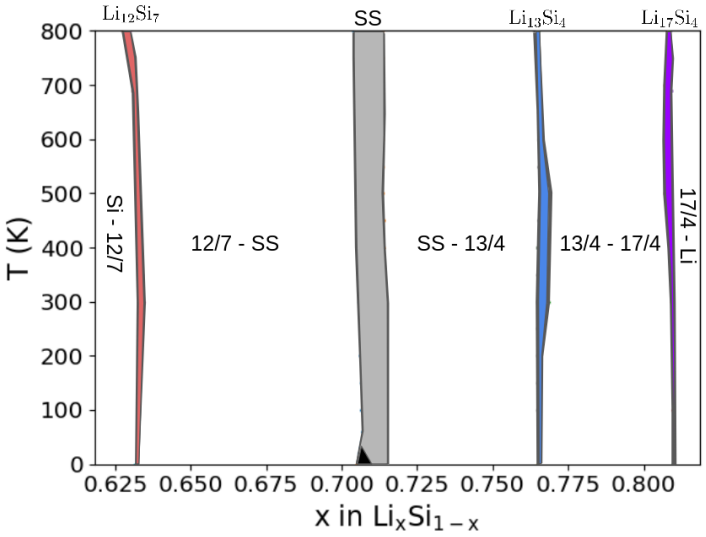

Figure D.3: Diagramme de phase du système Li-Si incluant le SS. Le diagramme de phase est zoomé entre $Li_{12}Si_7$ et $Li_{17}Si_4$, avant et après ces deux phases, nous avons les éléments purs Si et Li, respectivement. Les zones colorées représentent les domaines monophasés des composés. Pour indiquer l'équilibre à deux phases entre les composés A et B, nous mettons "A-B" dans les tracés. Nous utilisons la notation "n/m" pour désigner la phase Li_nSi_m.

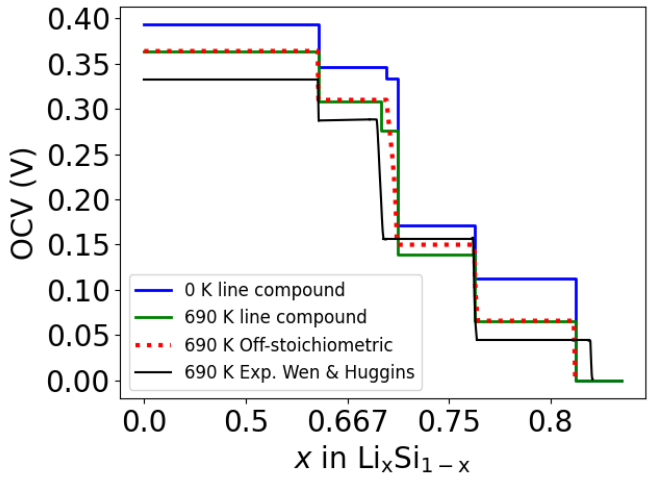

Figure D.4: Tracé de l'évolution de l'OCV en utilisant les méthodes de ce travail en fonction de la composition. Des calculs de composés linéaires à 0 K et à des températures finies à l'inclusion de la hors-stœchiométrie.

Bibliography

[1] *Access to electricity – SDG7: Data and Projections – Analysis - IEA — iea.org.* https://www.iea.org/reports/sdg7-data-and-projections/access-to-electricity. [Accessed 3-Jul-2023].

[2] *Emissions by sector — ourworldindata.org.* https://ourworldindata.org/emissions-by-sector. [Accessed 3-Jul-2023].

[3] *Policy developments – Global EV Outlook 2023 – Analysis - IEA — iea.org.* https://www.iea.org/reports/global-ev-outlook-2023/policy-developments. [Accessed 3-Jul-2023].

[4] Heide Budde-Meiwes et al. "A review of current automotive battery technology and future prospects". In: *Proceedings of the Institution of Mechanical Engineers, Part D: Journal of Automobile Engineering* 227 (May 2013), pp. 761–776. DOI: 10.1177/0954407013485567.

[5] Jin-Yi Li et al. "Research progress regarding Si-based anode materials towards practical application in high energy density Li-ion batteries". In: *Materials Chemistry Frontiers* 1.9 (2017), pp. 1691–1708. DOI: 10.1039/c6qm00302h. URL: https://doi.org/10.1039/c6qm00302h.

[6] L. Y. Beaulieu et al. "Colossal Reversible Volume Changes in Lithium Alloys". In: *Electrochemical and Solid-State Letters* 4.9 (July 2001), A137. DOI: 10.1149/1.1388178. URL: https://dx.doi.org/10.1149/1.1388178.

[7] L. Y. Beaulieu et al. "Reaction of Li with Alloy Thin Films Studied by In Situ AFM". In: *Journal of The Electrochemical Society* 150.11 (Sept. 2003), A1457. DOI: 10.1149/1.1613668. URL: https://dx.doi.org/10.1149/1.1613668.

[8] Kejie Zhao et al. "Fracture of electrodes in lithium-ion batteries caused by fast charging". In: *Journal of Applied Physics* 108.7 (Oct. 2010), p. 073517. ISSN: 0021-8979. DOI: 10.1063/1.3492617. eprint: https://pubs.aip.org/aip/jap/article-pdf/doi/10.1063/1.3492617/13192987/073517_1_online.pdf. URL: https://doi.org/10.1063/1.3492617.

[9] Hao Liu et al. "Sensitivity and Limitations of Structures from X-ray and Neutron-Based Diffraction Analyses of Transition Metal Oxide Lithium-Battery Electrodes". In: *Journal of The Electrochemical Society* 164.9 (June 2017), A1802. DOI: 10.1149/2.0271709jes. URL: https://dx.doi.org/10.1149/2.0271709jes.

[10] Marco Piccolino, Marco Bresadola, and Nicholas Wade. "177The Controversy Between Galvani and Volta Over Animal Electricity: The Second STAGE". In: *Shocking Frogs: Galvani, Volta, and the Electric Origins of Neuroscience*. Oxford University Press, Nov. 2013. ISBN: 9780199782161. DOI: 10.1093/acprof:oso/9780199782161.003.0007. eprint: https://academic.oup.com/book/0/chapter/143064292/chapter-ag-pdf/46384530/book_2646_section_143064292.ag.pdf. URL: https://doi.org/10.1093/acprof:oso/9780199782161.003.0007.

[11] Aldo da Rosa. "Chapter 18 - Storage of Energy". In: *Fundamentals of Renewable Energy Processes (Third Edition)*. Ed. by Aldo da Rosa. Third Edition. Boston: Academic Press, 2013, pp. 821–862. ISBN: 978-0-12-397219-4. DOI: https://doi.org/10.1016/B978-0-12-397219-4.00018-7. URL: https://www.sciencedirect.com/science/article/pii/B9780123972194000187.

[12] A.J. Bard, G. Inzelt, and F. Scholz. *Electrochemical Dictionary*. Springer Berlin Heidelberg, 2012. ISBN: 9783642295508. URL: https://books.google.fr/books?id=sOTEs76vAFkC.

[13] François Cardarelli. "Less common nonferrous metals". In: *Materials Handbook: A Concise Desktop Reference* (2008), pp. 213–454.

[14] A.H. Thompson, F.R. Gamble, and C.R. Symon. "The verification of the existence of TiS2". In: *Materials Research Bulletin* 10.9 (1975), pp. 915–919. ISSN: 0025-5408. DOI: https://doi.org/10.1016/0025-5408(75)90071-9. URL: https://www.sciencedirect.com/science/article/pii/0025540875900719.

[15] D.F. Shriver et al. "Structure and ion transport in polymer-salt complexes". In: *Solid State Ionics* 5 (1981). Proceedings of the International Conference on Fast Ionic Transport in Solids, pp. 83–88. ISSN: 0167-2738. DOI: https://doi.org/10.1016/0167-2738(81)90199-5. URL: https://www.sciencedirect.com/science/article/pii/0167273881901995.

[16] D. W. Murphy, J. Broadhead, and B. C. H. Steele, eds. *Materials for Advanced Batteries*. Springer US, 1980. DOI: 10.1007/978-1-4684-3851-2. URL: https://doi.org/10.1007/978-1-4684-3851-2.

[17] M. Lazzari and B. Scrosati. "A Cyclable Lithium Organic Electrolyte Cell Based on Two Intercalation Electrodes". In: *Journal of The Electrochemical Society* 127.3 (Mar. 1980), p. 773. DOI: 10.1149/1.2129753. URL: https://dx.doi.org/10.1149/1.2129753.

[18] Wangda Li, Bohang Song, and Arumugam Manthiram. "High-voltage positive electrode materials for lithium-ion batteries". In: *Chem. Soc. Rev.* 46 (10 2017), pp. 3006–3059. DOI: 10.1039/C6CS00875E. URL: http://dx.doi.org/10.1039/C6CS00875E.

[19] Qiongqiong Lu et al. "Carbon materials for stable Li metal anodes: Challenges, solutions, and outlook". In: *Carbon Energy* 3.6 (Sept. 2021), pp. 957–975. DOI: 10.1002/cey2.147. URL: https://doi.org/10.1002/cey2.147.

[20] Ji Heon Ryu et al. "Failure Modes of Silicon Powder Negative Electrode in Lithium Secondary Batteries". In: *Electrochemical and Solid-State Letters* 7.10 (Sept. 2004), A306. DOI: 10.1149/1.1792242. URL: https://dx.doi.org/10.1149/1.1792242.

[21] WJ Weydanz, Margret Wohlfahrt-Mehrens, and Robert A Huggins. "A room temperature study of the binary lithium–silicon and the ternary lithium–chromium–silicon system for use in rechargeable lithium batteries". In: *Journal of power sources* 81 (1999), pp. 237–242.

[22] Bo Gao et al. "Alloy formation in nanostructured silicon". In: *Advanced Materials* 13.11 (2001), pp. 816–819.

[23] Hui Wu and Yi Cui. "Designing nanostructured Si anodes for high energy lithium ion batteries". In: *Nano Today* 7.5 (2012), pp. 414–429. ISSN: 1748-0132. DOI: https://doi.org/10.1016/j.nantod.2012.08.004. URL: https://www.sciencedirect.com/science/article/pii/S1748013212000977.

[24] Harald Schmidt et al. "Volume expansion of amorphous silicon electrodes during potentiostatic lithiation of Li-ion batteries". In: *Electrochemistry Communications* 115 (2020), p. 106738. ISSN: 1388-2481. DOI: https://doi.org/10.1016/j.elecom.2020.106738. URL: https://www.sciencedirect.com/science/article/pii/S1388248120300898.

[25] Jang Wook Choi and Doron Aurbach. "Promise and reality of post-lithium-ion batteries with high energy densities". In: *Nature Reviews Materials* 1.4 (Mar. 2016). DOI: 10.1038/natrevmats.2016.13. URL: https://doi.org/10.1038/natrevmats.2016.13.

[26] Martin Winter. "The solid electrolyte interphase–the most important and the least understood solid electrolyte in rechargeable Li batteries". In: *Zeitschrift für physikalische Chemie* 223.10-11 (2009), pp. 1395–1406.

[27] Cao Cuong Nguyen and Seung-Wan Song. "Interfacial structural stabilization on amorphous silicon anode for improved cycling performance in lithium-ion batteries". In: *Electrochimica Acta* 55.8 (2010), pp. 3026–3033.

[28] Loıc Baggetto, Rogier AH Niessen, and Peter HL Notten. "On the activation and charge transfer kinetics of evaporated silicon electrode/electrolyte interfaces". In: *Electrochimica acta* 54.24 (2009), pp. 5937–5941.

[29] Xuming Chen, Hanyi Zhang, and Tianhao Zhao. "Silicon-metal and silicon-metal oxides composite anodes material for lithium-ion batteries". In: *Journal of Physics: Conference Series* 2399.1 (Dec. 2022), p. 012016. DOI: 10.1088/1742-6596/2399/1/012016. URL: https://doi.org/10.1088/1742-6596/2399/1/012016.

[30] Qitao Shi et al. "A review of recent developments in Si/C composite materials for Li-ion batteries". In: *Energy Storage Materials* 34 (2021), pp. 735–754. ISSN: 2405-8297. DOI: https://doi.org/10.1016/j.ensm.2020.10.026. URL: https://www.sciencedirect.com/science/article/pii/S2405829720304037.

[31] Uday Kasavajjula, Chunsheng Wang, and A. John Appleby. "Nano- and bulk-silicon-based insertion anodes for lithium-ion secondary cells". In: *Journal of Power Sources* 163.2 (2007). Selected Papers presented at the FUEL PROCESSING FOR HYDROGEN PRODUCTION SYMPOSIUM at the 230th American Chemical SocietyNational Meeting Washington, DC, USA, 28 August – 1 September 2005, pp. 1003–1039. ISSN: 0378-7753. DOI: https://doi.org/10.1016/j.jpowsour.2006.09.084. URL: https://www.sciencedirect.com/science/article/pii/S037877530602026X.

[32] Zhixin Xu et al. "Electrolytes for advanced lithium ion batteries using silicon-based anodes". In: *J. Mater. Chem. A* 7 (16 2019), pp. 9432–9446. DOI: 10.1039/C9TA01876J. URL: http://dx.doi.org/10.1039/C9TA01876J.

[33] S-C Lai. "Solid lithium-silicon electrode". In: *Journal of The Electrochemical Society* 123 (1976), p. 1196.

[34] Ram A. Sharma and Randall N. Seefurth. "Thermodynamic Properties of the Lithium-Silicon System". In: *Journal of The Electrochemical Society* 123.12 (Dec. 1976), p. 1763. DOI: 10.1149/1.2132692. URL: https://dx.doi.org/10.1149/1.2132692.

[35] C. John Wen and Robert A. Huggins. "Chemical diffusion in intermediate phases in the lithium-silicon system". In: *Journal of Solid State Chemistry* 37.3 (1981), pp. 271–278. ISSN: 0022-4596. DOI: https://doi.org/10.1016/0022-4596(81)90487-4. URL: https://www.sciencedirect.com/science/article/pii/0022459681904874.

[36] H. Okamoto. "The Li-Si (Lithium-Silicon) system". In: *Bulletin of Alloy Phase Diagrams* 11.3 (June 1990), pp. 306–312. DOI: 10.1007/bf03029305. URL: https://doi.org/10.1007/bf03029305.

[37] M. H. Braga∗, L. F. Malheiros, and I. Ansara. "Thermodynamic assessment of the Li-Si system". In: *Journal of Phase Equilibria* 16.4 (Aug. 1995), pp. 324–330. DOI: 10.1007/bf02645289. URL: https://doi.org/10.1007/bf02645289.

[38] H. Okamoto. "Li-Si (Lithium-Silicon)". In: *Journal of Phase Equilibria and Diffusion* 30.1 (Jan. 2009), pp. 118–119. DOI: 10.1007/s11669-008-9431-8. URL: https://doi.org/10.1007/s11669-008-9431-8.

[39] Linda A. Stearns et al. "Lithium monosilicide (LiSi), a low-dimensional silicon-based material prepared by high pressure synthesis: NMR and vibrational spectroscopy and electrical properties characterization". In: *Journal of Solid State Chemistry* 173.1 (2003), pp. 251–258. ISSN: 0022-4596. DOI: https://doi.org/10.1016/S0022-4596(03)00045-8. URL: https://www.sciencedirect.com/science/article/pii/S0022459603000458.

[40] Jürgen Evers, Gilbert Oehlinger, and Gerhard Sextl. "High-Pressure Synthesis of LiSi: Three-Dimensional Network of Three-Bonded Si- Ions". In: *Angewandte Chemie International Edition in English* 32.10 (1993), pp. 1442–1444. DOI: https://doi.org/10.1002/anie.199314421. eprint: https://onlinelibrary.wiley.com/doi/pdf/10.1002/anie.199314421. URL: https://onlinelibrary.wiley.com/doi/abs/10.1002/anie.199314421.

[41] V.L. Chevrier, J.W. Zwanziger, and J.R. Dahn. "First principles study of Li–Si crystalline phases: Charge transfer, electronic structure, and lattice vibrations". In: *Journal of Alloys and Compounds* 496.1 (2010), pp. 25–36. ISSN: 0925-8388. DOI: https://doi.org/10.1016/j.jallcom.2010.01.142. URL: https://www.sciencedirect.com/science/article/pii/S0925838810001969.

[42] Peisheng Wang et al. "Thermodynamic analysis of the Li–Si phase equilibria from 0 K to liquidus temperatures". In: *Intermetallics* 42 (2013), pp. 137–145. ISSN: 0966-9795. DOI: https://doi.org/10.1016/j.intermet.2013.06.003. URL: https://www.sciencedirect.com/science/article/pii/S0966979513001763.

[43] Daniel Thomas et al. "The heat capacity and entropy of lithium silicides over the temperature range from (2 to 873)K". In: *The Journal of Chemical Thermodynamics* 64 (2013), pp. 205–225. ISSN: 0021-9614. DOI: https://doi.org/10.1016/j.jct.2013.05.018. URL: https://www.sciencedirect.com/science/article/pii/S0021961413001730.

[44] William W. Tipton et al. "Structures, phase stabilities, and electrical potentials of Li-Si battery anode materials". In: *Phys. Rev. B* 87 (18 May 2013), p. 184114. DOI: 10.1103/PhysRevB.87.184114. URL: https://link.aps.org/doi/10.1103/PhysRevB.87.184114.

[45] Andrew J. Morris, C. P. Grey, and Chris J. Pickard. "Thermodynamically stable lithium silicides and germanides from density functional theory calculations". In: *Phys. Rev. B* 90 (5 Aug. 2014), p. 054111. DOI: 10.1103/PhysRevB.90.054111. URL: https://link.aps.org/doi/10.1103/PhysRevB.90.054111.

[46] Irais Valencia-Jaime et al. "Novel crystal structures for lithium–silicon alloy predicted by minima hopping method". In: *Journal of Alloys and Compounds* 655 (2016), pp. 147–154. ISSN: 0925-8388. DOI: https://doi.org/10.1016/j.jallcom.2015.09.101. URL: https://www.sciencedirect.com/science/article/pii/S092583881531077X.

[47] Ji Y. Kwon, Ji Heon Ryu, and Seung M. Oh. "Performance of electrochemically generated Li21Si5 phase for lithium-ion batteries". In: *Electrochimica Acta* 55.27 (2010). EMERGING TRENDS AND CHALLENGES IN ELECTROCHEMISTRY, pp. 8051–8055. ISSN: 0013-4686. DOI: https://doi.org/10.1016/j.electacta.2010.01.054. URL: https://www.sciencedirect.com/science/article/pii/S0013468610001325.

[48] M.N. Obrovac and Leif Christensen. "Structural changes in silicon anodes during lithium insertion/extraction". In: *Electrochemical and Solid-State Letters* 7.5 (2004). Cited by: 1629, A93–A96. DOI: 10.1149/1.1652421. URL: https://www.scopus.com/inward/record.uri?eid=2-s2.0-2342577530&doi=10.1149%2f1.1652421&partnerID=40&md5=67c4ebd93956df18f25df4d7814a4ad3.

[49] Michael Zeilinger et al. “Single Crystal Growth and Thermodynamic Stability of Lisub17/subSisub4/sub”. In: *Chemistry of Materials* 25.9 (Apr. 2013), pp. 1960–1967. DOI: 10.1021/cm400612k. URL: https://doi.org/10.1021/cm400612k.

[50] Michael Zeilinger et al. “Stabilizing the Phase Li15Si4 through Lithium–Aluminum Substitution in Li15–xAlxSi4 (0.4 ¡ x ¡ 0.8)—Single Crystal X-ray Structure Determination of Li15Si4 and Li14.37Al0.63Si4”. In: *Chemistry of Materials* 25.20 (2013), pp. 4113–4121. DOI: 10.1021/cm402721n. eprint: https://doi.org/10.1021/cm402721n. URL: https://doi.org/10.1021/cm402721n.

[51] Michael Zeilinger et al. “Revision of the Li–Si Phase Diagram: Discovery and Single-Crystal X-ray Structure Determination of the High-Temperature Phase Li4.11Si”. In: *Chemistry of Materials* 25.22 (2013), pp. 4623–4632. DOI: 10.1021/cm4029885. eprint: https://doi.org/10.1021/cm4029885. URL: https://doi.org/10.1021/cm4029885.

[52] Michael Zeilinger and Thomas F. Fässler. “Revision of the Li13Si4 structure”. In: *Acta Crystallographica Section E: Structure Reports Online* 69.12 (2013). Cited by: 17; All Open Access, Gold Open Access, Green Open Access, pp. i81–i82. DOI: 10.1107/S1600536813029759. URL: https://www.scopus.com/inward/record.uri?eid=2-s2.0-84889640901&doi=10.1107%2fS1600536813029759&partnerID=40&md5=b2459a2fa9f5a1d7ef6c218e3b688002.

[53] M. Helena Braga, Adam Debski, and Władysław Gasior. “Li–Si phase diagram: Enthalpy of mixing, thermodynamic stability, and coherent assessment”. In: *Journal of Alloys and Compounds* 616 (2014), pp. 581–593. ISSN: 0925-8388. DOI: https://doi.org/10.1016/j.jallcom.2014.06.212. URL: https://www.sciencedirect.com/science/article/pii/S0925838814017009.

[54] Sven Dupke et al. “Structural characterization of the lithium silicides Li15Si4, Li13Si4, and Li7Si3 using solid state NMR”. In: *Phys. Chem. Chem. Phys.* 14 (18 2012), pp. 6496–6508. DOI: 10.1039/C2CP24131E. URL: http://dx.doi.org/10.1039/C2CP24131E.

[55] Song-Mao Liang et al. “Thermodynamics of Li-Si and Li-Si-H phase diagrams applied to hydrogen absorption and Li-ion batteries”. In: *Intermetallics* 81 (2017), pp. 32–46. ISSN: 0966-9795. DOI: https://doi.org/10.1016/j.intermet.2017.02.024. URL: https://www.sciencedirect.com/science/article/pii/S0966979516306276.

[56] Sebastian Schwalbe et al. “Mechanical, elastic and thermodynamic properties of crystalline lithium silicides”. In: *Computational Materials Science* 134 (2017), pp. 48–57. ISSN: 0927-0256. DOI: https://doi.org/10.1016/j.commatsci.2017.03.028. URL: https://www.sciencedirect.com/science/article/pii/S0927025617301490.

[57] Jing Li and J. R. Dahn. “An In Situ X-Ray Diffraction Study of the Reaction of Li with Crystalline Si”. In: *Journal of The Electrochemical Society* 154.3 (Jan. 2007), A156. DOI: 10.1149/1.2409862. URL: https://dx.doi.org/10.1149/1.2409862.

[58] Julien Danet et al. “Valence electron energy-loss spectroscopy of silicon negative electrodes for lithium batteries”. In: *Phys. Chem. Chem. Phys.* 12 (1 2010), pp. 220–226. DOI: 10.1039/B915245H. URL: http://dx.doi.org/10.1039/B915245H.

[59] Etienne Radvanyi et al. “Study of lithiation mechanisms in silicon electrodes by Auger Electron Spectroscopy”. In: *J. Mater. Chem. A* 1 (16 2013), pp. 4956–4965. DOI: 10.1039/C3TA10212B. URL: http://dx.doi.org/10.1039/C3TA10212B.

[60] MN Obrovac and LJ Krause. “Reversible cycling of crystalline silicon powder”. In: *Journal of the Electrochemical Society* 154.2 (2006), A103.

[61] Meng Gu et al. “Electronic Origin for the Phase Transition from Amorphous LixSi to Crystalline Li15Si4”. In: *ACS Nano* 7.7 (2013). PMID: 23795599, pp. 6303–6309. DOI: 10.1021/nn402349j. eprint: https://doi.org/10.1021/nn402349j. URL: https://doi.org/10.1021/nn402349j.

[62] Matthew T. McDowell et al. "25th Anniversary Article: Understanding the Lithiation of Silicon and Other Alloying Anodes for Lithium-Ion Batteries". In: *Advanced Materials* 25.36 (2013), pp. 4966–4985. DOI: https://doi.org/10.1002/adma.201301795. eprint: https://onlinelibrary.wiley.com/doi/pdf/10.1002/adma.201301795. URL: https://onlinelibrary.wiley.com/doi/abs/10.1002/adma.201301795.

[63] M. J. Chon et al. "Real-Time Measurement of Stress and Damage Evolution during Initial Lithiation of Crystalline Silicon". In: *Phys. Rev. Lett.* 107 (4 July 2011), p. 045503. DOI: 10.1103/PhysRevLett.107.045503. URL: https://link.aps.org/doi/10.1103/PhysRevLett.107.045503.

[64] S. Huang et al. "Stress generation during lithiation of high-capacity electrode particles in lithium ion batteries". In: *Acta Materialia* 61.12 (2013), pp. 4354–4364. ISSN: 1359-6454. DOI: https://doi.org/10.1016/j.actamat.2013.04.007. URL: https://www.sciencedirect.com/science/article/pii/S1359645413002796.

[65] Pierre Bernard et al. "Electrochemical analysis of silicon nanoparticle lithiation – Effect of crystallinity and carbon coating quantity". In: *Journal of Power Sources* 435 (2019), p. 226769. ISSN: 0378-7753. DOI: https://doi.org/10.1016/j.jpowsour.2019.226769. URL: https://www.sciencedirect.com/science/article/pii/S0378775319307402.

[66] H.B. Callen. *Thermodynamics and an Introduction to Thermostatistics*. Wiley, 1991. ISBN: 9780471862567. URL: https://books.google.fr/books?id=m%5C_39DwAAQBAJ.

[67] P. Hohenberg and W. Kohn. "Inhomogeneous Electron Gas". In: *Phys. Rev.* 136 (3B Nov. 1964), B864–B871. DOI: 10.1103/PhysRev.136.B864. URL: https://link.aps.org/doi/10.1103/PhysRev.136.B864.

[68] W. Kohn and L. J. Sham. "Self-Consistent Equations Including Exchange and Correlation Effects". In: *Phys. Rev.* 140 (4A Nov. 1965), A1133–A1138. DOI: 10.1103/PhysRev.140.A1133. URL: https://link.aps.org/doi/10.1103/PhysRev.140.A1133.

[69] John P. Perdew, Kieron Burke, and Matthias Ernzerhof. "Generalized Gradient Approximation Made Simple". In: *Phys. Rev. Lett.* 77 (18 Oct. 1996), pp. 3865–3868. DOI: 10.1103/PhysRevLett.77.3865. URL: https://link.aps.org/doi/10.1103/PhysRevLett.77.3865.

[70] Jochen Heyd, Gustavo E. Scuseria, and Matthias Ernzerhof. "Hybrid functionals based on a screened Coulomb potential". In: *The Journal of Chemical Physics* 118.18 (Apr. 2003), pp. 8207–8215. ISSN: 0021-9606. DOI: 10.1063/1.1564060. eprint: https://pubs.aip.org/aip/jcp/article-pdf/118/18/8207/10847843/8207_1_online.pdf. URL: https://doi.org/10.1063/1.1564060.

[71] G. Kresse and D. Joubert. "From ultrasoft pseudopotentials to the projector augmented-wave method". In: *Phys. Rev. B* 59 (3 Jan. 1999), pp. 1758–1775. DOI: 10.1103/PhysRevB.59.1758. URL: https://link.aps.org/doi/10.1103/PhysRevB.59.1758.

[72] P. E. Blöchl. "Projector augmented-wave method". In: *Phys. Rev. B* 50 (24 Dec. 1994), pp. 17953–17979. DOI: 10.1103/PhysRevB.50.17953. URL: https://link.aps.org/doi/10.1103/PhysRevB.50.17953.

[73] Atsushi Togo. "First-principles Phonon Calculations with Phonopy and Phono3py". In: *J. Phys. Soc. Jpn.* 92.1 (2023), p. 012001. DOI: 10.7566/JPSJ.92.012001.

[74] John M Ziman. *Electrons and phonons: the theory of transport phenomena in solids*. Oxford university press, 2001.

[75] Gyaneshwar P Srivastava. *The physics of phonons*. Routledge, 2019.

[76] Duane C Wallace. "Thermodynamics of crystals". In: *American Journal of Physics* 40.11 (1972), pp. 1718–1719.

[77] Martin T Dove. *Introduction to lattice dynamics*. 4. Cambridge university press, 1993.

[78] François Ducastelle. "Order and Phase Stability in Alloys." In: (1991).

[79] Thomas Schuler et al. "Equilibrium Vacancy Concentration Driven by Undetectable Impurities". In: *Phys. Rev. Lett.* 115 (1 June 2015), p. 015501. DOI: 10.1103/PhysRevLett.115.015501. URL: https://link.aps.org/doi/10.1103/PhysRevLett.115.015501.

[80] Thomas Schuler et al. "Ab initio investigation of phosphorus and hydrogen co-segregation and embrittlement in -Fe twin boundaries". In: *Applied Surface Science* 492 (2019), pp. 919–935. ISSN: 0169-4332. DOI: https://doi.org/10.1016/j.apsusc.2019.04.025. URL: https://www.sciencedirect.com/science/article/pii/S0169433219310177.

[81] Emmanuel Clouet and Maylise Nastar. "Classical nucleation theory in ordering alloys precipitating with $L1_2$ structure". In: *Phys. Rev. B* 75 (13 Apr. 2007), p. 132102. DOI: 10.1103/PhysRevB.75.132102. URL: https://link.aps.org/doi/10.1103/PhysRevB.75.132102.

[82] Ryoichi Kikuchi. "A Theory of Cooperative Phenomena". In: *Phys. Rev.* 81 (6 Mar. 1951), pp. 988–1003. DOI: 10.1103/PhysRev.81.988. URL: https://link.aps.org/doi/10.1103/PhysRev.81.988.

[83] A.F. Kohan et al. "Computation of alloy phase diagrams at low temperatures". In: *Computational Materials Science* 9.3 (1998), pp. 389–396. ISSN: 0927-0256. DOI: https://doi.org/10.1016/S0927-0256(97)00168-7. URL: https://www.sciencedirect.com/science/article/pii/S0927025697001687.

[84] A.T. Dinsdale. "SGTE data for pure elements". In: *Calphad* 15.4 (1991), pp. 317–425. ISSN: 0364-5916. DOI: https://doi.org/10.1016/0364-5916(91)90030-N. URL: https://www.sciencedirect.com/science/article/pii/036459169190030N.

[85] Taufiq Hidayat et al. "Thermodynamic reevaluation of the Fe–O system". In: *Calphad* 48 (2015), pp. 131–144. ISSN: 0364-5916. DOI: https://doi.org/10.1016/j.calphad.2014.12.005. URL: https://www.sciencedirect.com/science/article/pii/S0364591614001023.

[86] Anton Van der Ven, Jishnu Bhattacharya, and Anna A. Belak. "Understanding Li Diffusion in Li-Intercalation Compounds". In: *Accounts of Chemical Research* 46.5 (2013). PMID: 22584006, pp. 1216–1225. DOI: 10.1021/ar200329r. eprint: https://doi.org/10.1021/ar200329r. URL: https://doi.org/10.1021/ar200329r.

[87] I. Courtney and J. Tse. "Ab initio calculation of the lithium-tin voltage profile". English. In: *Physical Review B - Condensed Matter and Materials Physics* 58.23 (1998). Cited By :245, pp. 15583–15588. URL: www.scopus.com.

[88] W. Weppner and R. A. Huggins. "Determination of the Kinetic Parameters of Mixed-Conducting Electrodes and Application to the System Li3Sb". In: *Journal of The Electrochemical Society* 124.10 (Oct. 1977), p. 1569. DOI: 10.1149/1.2133112. URL: https://dx.doi.org/10.1149/1.2133112.

[89] P. Novák. "CuO cathode in lithium cells—II. Reduction mechanism of CuO". In: *Electrochimica Acta* 30.12 (1985), pp. 1687–1692. ISSN: 0013-4686. DOI: https://doi.org/10.1016/0013-4686(85)87015-8. URL: https://www.sciencedirect.com/science/article/pii/0013468685870158.

[90] P. L. Taberna et al. "High rate capabilities Fe3O4-based Cu nano-architectured electrodes for lithium-ion battery applications". In: *Nature Materials* 5.7 (June 2006), pp. 567–573. DOI: 10.1038/nmat1672. URL: https://doi.org/10.1038/nmat1672.

[91] V. I. Kalikmanov. "Classical Nucleation Theory". In: *Nucleation Theory*. Dordrecht: Springer Netherlands, 2013, pp. 17–41. ISBN: 978-90-481-3643-8. DOI: 10.1007/978-90-481-3643-8_3. URL: https://doi.org/10.1007/978-90-481-3643-8_3.

[92] Donghee Chang et al. "Elucidating the origins of phase transformation hysteresis during electrochemical cycling of Li–Sb electrodes". In: *J. Mater. Chem. A* 3 (37 2015), pp. 18928–18943. DOI: 10.1039/C5TA06183K. URL: http://dx.doi.org/10.1039/C5TA06183K.

[93] Yasumasa Okada and Yozo Tokumaru. "Precise determination of lattice parameter and thermal expansion coefficient of silicon between 300 and 1500 K". In: *Journal of Applied Physics* 56.2 (1984), pp. 314–320. DOI: 10.1063/1.333965. eprint: https://doi.org/10.1063/1.333965. URL: https://doi.org/10.1063/1.333965.

[94] Wan Si Tang, Jean-Noël Chotard, and Raphaël Janot. "Synthesis of Single-Phase LiSi by Ball-Milling: Electrochemical Behavior and Hydrogenation Properties". In: *Journal of The Electrochemical Society* 160.8 (May 2013), A1232. DOI: 10.1149/2.089308jes. URL: https://dx.doi.org/10.1149/2.089308jes.

[95] Reinhard Nesper, Hans Georg von Schnering, and Jan Curda. "Li12Si7, eine Verbindung mit trigonal-planaren Si4-Clustern und isometrischen Si5-Ringen". In: *Chemische Berichte* 119.12 (1986), pp. 3576–3590. DOI: https://doi.org/10.1002/cber.19861191207. eprint: https://chemistry-europe.onlinelibrary.wiley.com/doi/pdf/10.1002/cber.19861191207. URL: https://chemistry-europe.onlinelibrary.wiley.com/doi/abs/10.1002/cber.19861191207.

[96] Hans Georg von Schnering et al. "Li12Si7, a Compound Having a Trigonal Planar Si4 Cluster and Planar Si5 Rings". In: *Angewandte Chemie International Edition in English* 19.12 (1980), pp. 1033–1034. DOI: https://doi.org/10.1002/anie.198010331. eprint: https://onlinelibrary.wiley.com/doi/pdf/10.1002/anie.198010331. URL: https://onlinelibrary.wiley.com/doi/abs/10.1002/anie.198010331.

[97] Ursula Frank, Wiking Müller, and Herbert Schäfer. "Zur Kenntnis der Phase Li13Si4/On the Phase Li13Si4". In: *Zeitschrift für Naturforschung B* 30.1-2 (1975), pp. 10–13.

[98] Reinhard Nesper and Hans Georg von Schnering. "Li21Si5, a Zintl phase as well as a Hume-Rothery phase". In: *Journal of Solid State Chemistry* 70.1 (1987), pp. 48–57. ISSN: 0022-4596. DOI: https://doi.org/10.1016/0022-4596(87)90176-9. URL: https://www.sciencedirect.com/science/article/pii/0022459687901769.

[99] H. Axel, Herbert Schäfer, and Armin Weiss. In: *Zeitschrift für Naturforschung B* 21.2 (1966), pp. 115–117. DOI: doi:10.1515/znb-1966-0204. URL: https://doi.org/10.1515/znb-1966-0204.

[100] Josef Zemann. "Crystal structures,2nd edition. Vol. 1by R. W. G. Wyckoff". In: 1965.

[101] J. Paier et al. "Screened hybrid density functionals applied to solids". In: *The Journal of Chemical Physics* 124.15 (Apr. 2006). 154709. ISSN: 0021-9606. DOI: 10.1063/1.2187006. eprint: https://pubs.aip.org/aip/jcp/article-pdf/doi/10.1063/1.2187006/15383909/154709_1_online.pdf. URL: https://doi.org/10.1063/1.2187006.

[102] I. Barvík. "To the magnetic properties of Li2·33Si". In: *Czechoslovak Journal of Physics* 33.12 (Dec. 1983), pp. 1338–1346. DOI: 10.1007/bf01590223. URL: https://doi.org/10.1007/bf01590223.

[103] *Materials Project*. https://materialsproject.org/. Accessed: 2023.

[104] Xavier Gonze, Gian-Marco Rignanese, and Razvan Caracas. In: *Zeitschrift für Kristallographie - Crystalline Materials* 220.5-6 (2005), pp. 458–472. DOI: doi:10.1524/zkri.220.5.458.65077. URL: https://doi.org/10.1524/zkri.220.5.458.65077.

[105] Thomas B. Douglas et al. "Lithium: Heat Content from 0 to 900°, Triple Point and Heat of Fusion, and Thermodynamic Properties of the Solid and Liquid1". In: *Journal of the American Chemical Society* 77.8 (1955), pp. 2144–2150. DOI: 10.1021/ja01613a031. eprint: https://doi.org/10.1021/ja01613a031. URL: https://doi.org/10.1021/ja01613a031.

[106] P. Flubacher, A. J. Leadbetter, and J. A. Morrison. "The Heat Capacity of Pure Silicon and Germanium and Properties of Their Vibrational Frequency Spectra". In: *Philosophical Magazine* 4.39 (1959), pp. 273–294. DOI: 10.1080/14786435908233340.

[107] Janghyuk Moon et al. "Ab initio and kinetic Monte Carlo simulation study of lithiation in crystalline and amorphous silicon". In: *Journal of Power Sources* 272 (2014), pp. 1010–1017. ISSN: 0378-7753. DOI: https://doi.org/10.1016/j.jpowsour.2014.09.004. URL: https://www.sciencedirect.com/science/article/pii/S0378775314014104.

[108] Hyunwoo Kim et al. "On the nature and behavior of Li atoms in Si: a first principles study". In: *The Journal of Physical Chemistry C* 114.41 (2010), pp. 17942–17946.

[109] Thomas Gruber, Silvia Bahmann, and Jens Kortus. "Metastable structure of $Li_{13}Si_4$". In: *Phys. Rev. B* 93 (14 Apr. 2016), p. 144104. DOI: 10.1103/PhysRevB.93.144104. URL: https://link.aps.org/doi/10.1103/PhysRevB.93.144104.

[110] Peter Atkins and Julio de Paula. *Atkins' Physical Chemistry*. 11th. Oxford, UK: Oxford University Press, 2018.

[111] Silvia Bahmann and Jens Kortus. "EVO—Evolutionary algorithm for crystal structure prediction". In: *Computer Physics Communications* 184.6 (2013), pp. 1618–1625. ISSN: 0010-4655. DOI: https://doi.org/10.1016/j.cpc.2013.02.007. URL: https://www.sciencedirect.com/science/article/pii/S0010465513000519.

[112] H. G. VON SCHNERING et al. "ChemInform Abstract: STRUCTURE AND PROPERTIES OF LITHIUM SILICIDE (LI14SI6(LI2.33SI)), THE PURPLE PHASE IN THE LITHIUM-SILICON SYSTEM". In: *Chemischer Informationsdienst* 11.36 (1980). DOI: https://doi.org/10.1002/chin.198036006. eprint: https://onlinelibrary.wiley.com/doi/pdf/10.1002/chin.198036006. URL: https://onlinelibrary.wiley.com/doi/abs/10.1002/chin.198036006.

[113] James Griego, Mark A Rodriguez, and Daniel Edward Wesolowski. *Phase Transition Behavior of a Processed Thermal Battery*. Tech. rep. Sandia National Lab.(SNL-NM), Albuquerque, NM (United States), 2012.

[114] A. Debski, W. Gasior, and A. Góral. "Enthalpy of formation of intermetallic compounds from the Li–Si system". In: *Intermetallics* 26 (2012), pp. 157–161. ISSN: 0966-9795. DOI: https://doi.org/10.1016/j.intermet.2012.04.001. URL: https://www.sciencedirect.com/science/article/pii/S0966979512001495.

[115] A. Debski et al. "Enthalpy of formation of the Li22Si5 intermetallic compound". In: *Thermochimica Acta* 551 (2013), pp. 53–56. ISSN: 0040-6031. DOI: https://doi.org/10.1016/j.tca.2012.10.015. URL: https://www.sciencedirect.com/science/article/pii/S0040603112005102.

[116] V. L. Chevrier, J. W. Zwanziger, and J. R. Dahn. "First principles studies of silicon as a negative electrode material for lithium-ion batteries". In: *Canadian Journal of Physics* 87.6 (2009), pp. 625–632. DOI: 10.1139/P09-031. eprint: https://doi.org/10.1139/P09-031. URL: https://doi.org/10.1139/P09-031.

[117] H. Mehrer. *Diffusion in Solids: Fundamentals, Methods, Materials, Diffusion-Controlled Processes*. Springer Series in Solid-State Sciences. Springer Berlin Heidelberg, 2007. ISBN: 9783540714880. URL: https://books.google.fr/books?id=IUZVffQLFKQC.

[118] Aiping Wang et al. "Review on modeling of the anode solid electrolyte interphase (SEI) for lithium-ion batteries". In: *npj Computational Materials* 4.1 (Mar. 2018). DOI: 10.1038/s41524-018-0064-0. URL: https://doi.org/10.1038/s41524-018-0064-0.

[119] Jong-Won Song et al. "Communication: Singularity-free hybrid functional with a Gaussian-attenuating exact exchange in a plane-wave basis". en. In: *J Chem Phys* 138.24 (June 2013), p. 241101.

[120] G. Makov and M. C. Payne. "Periodic boundary conditions in ab initio calculations". In: *Phys. Rev. B* 51 (7 Feb. 1995), pp. 4014–4022. DOI: 10.1103/PhysRevB.51.4014. URL: https://link.aps.org/doi/10.1103/PhysRevB.51.4014.

[121] Roger Keith Crouch and T.E. Gilmer. "Thermal ionization energy of lithium and lithium-oxygen complexes in single-crystal silicon". In: *Journal of Physics and Chemistry of Solids* 30.8 (1969), pp. 2037–2043. ISSN: 0022-3697. DOI: https://doi.org/10.1016/0022-3697(69)90182-6. URL: https://www.sciencedirect.com/science/article/pii/0022369769901826.

[122] R. L. Aggarwal et al. "Excitation Spectra of Lithium Donors in Silicon and Germanium". In: *Phys. Rev.* 138 (3A May 1965), A882–A893. DOI: 10.1103/PhysRev.138.A882. URL: https://link.aps.org/doi/10.1103/PhysRev.138.A882.

[123] E.M. Pell. "Solubility of lithium in silicon". In: *Journal of Physics and Chemistry of Solids* 3.1 (1957), pp. 77–81. ISSN: 0022-3697. DOI: https://doi.org/10.1016/0022-3697(57)90051-3. URL: https://www.sciencedirect.com/science/article/pii/0022369757900513.

[124] Magali Gauthier. "Electrodes négatives à base de silicium pour accumulateurs au lithium : mécanisme réactionnel à l'échelle nanométrique et optimisation des performances". 2013NANT2056. PhD thesis. 2013, 1 vol. (229 p.) URL: http://www.theses.fr/2013NANT2056/document.

[125] Apr. 2023. URL: https://www.icdd.com/pdf-4/.

[126] Mats Hillert. "The compound energy formalism". In: *Journal of Alloys and Compounds* 320.2 (2001). Materials Constitution and Thermochemistry. Examples of Methods, Measurements and Applications. In Memoriam Alan Prince, pp. 161–176. ISSN: 0925-8388. DOI: https://doi.org/10.1016/S0925-8388(00)01481-X. URL: https://www.sciencedirect.com/science/article/pii/S092583880001481X.

[127] A. Dworkin and H. Cailleau. "Heat capacity of biphenyl around its phase transitions at low temperature". In: *Journal de Physique Lettres* 41.4 (1980), pp. 83–85. DOI: 10.1051/jphyslet:0198000410408300. URL: https://doi.org/10.1051/jphyslet:0198000410408300.

[128] P. J. Desré and A. R. Yavari. "Suppression of crystal nucleation in amorphous layers with sharp concentration gradients". In: *Phys. Rev. Lett.* 64 (13 Mar. 1990), pp. 1533–1536. DOI: 10.1103/PhysRevLett.64.1533. URL: https://link.aps.org/doi/10.1103/PhysRevLett.64.1533.

[129] Thomas Schuler, Luca Messina, and Maylise Nastar. "KineCluE: A kinetic cluster expansion code to compute transport coefficients beyond the dilute limit". In: *Computational Materials Science* 172 (2020), p. 109191. ISSN: 0927-0256. DOI: https://doi.org/10.1016/j.commatsci.2019.109191. URL: https://www.sciencedirect.com/science/article/pii/S0927025619304902.